BISTABLE MOLECULAR MATERIALS: TRIAZOLE-BASED COORDINATION CHEMISTRY OF FIRST ROW TRANSITION METALS

Andrea Moneo Corcuera

UNIVERSITAT ROVIRA i VIRGILI

Bistable Molecular Materials: Triazole-based Coordination Chemistry of First Row Transition Metals

ANDREA MONEO CORCUERA

DOCTORAL THESIS
2019

DOCTORAL THESIS

Bistable Molecular Materials: Triazole-based coordination chemistry of first row transition metals

Andrea Moneo Corcuera

Supervised by

Prof. Dr. José Ramón Galán Mascarós

Institut Català d'Investigació Química (ICIQ)

Tarragona, 2019

Prof. Dr. José Ramón Galán Mascarós, Group Leader of the Institut Català d'Investigació Química (ICIQ) and Research Professor of Institució Catalana de Recerca i Estudis Avançants (ICREA),

CERTIFIES that the present study, entitled **"Bistable Molecular Materials: triazole-based coordination chemistry of first row transition metals"**, presented by Andrea Moneo Corcuera for the award of the PhD degree in Chemistry, has been carried out under my supervision at the Institut Català d'Investigació Química (ICIQ).

Tarragona, 4th November 2019

PhD Thesis supervisor

Prof. Dr. José Ramón Galán Mascarós

Table of contents

Chapter 2. Structure and Magnetism of first-row transition metal trimers

Chapter 3. Tuning the SCO Behavior of the polyanionic Fe^{II} trimer via cation exchange

Chapter 4. Molecular Magnetic Memory in Isolated SCO Fe^{II} Trimer

Chapter 5. Nanostructuring the SCO Fe^{II} Trimer on Surfaces

Summary

Considerable effort is being made to design new molecules with controllable properties due to their diverse applicability, especially in device miniaturization. One of the most demanding perspective in this field is the use of magnetic molecules as active elements in devices for information storage and signal processing. Spin Crossover (SCO) molecules are suitable for such applications, since they are able to display magnetic bistability in response to an external stimulus. However, the fragility of the SCO phenomena during the processing and nano-structuration processes have limited their development for nano-technological applications. Thus, the search of molecular material with proper and robust SCO properties at the nanoscale is one of the main challenge in this research field.

In this Doctoral thesis, we have explored the basic molecular magnetism through the coordination chemistry with a di-anionic triazole ligand (**L**$^{-2}$ = 4-(1,2,4-triazol-4-yl)ethanedisulfonate) and first-raw transition metal ions. In particular, we describe the synthesis and crystal structure of linear trimers $[NH_2Me_2]_6[M_3(\mu\text{-}\mathbf{L})_6(H_2O)_6]$ (M = Mn^{II}, Co^{II}, Ni^{II}, Fe^{II} and Cu^{II}) with the analysis of their magnetic behavior. Special emphasis was devoted to study the thermal-induced SCO phenomena of such Fe^{II} trimer within different environments and dimensions. In bulk, the SCO behavior was modulated towards more abrupt spin transition by manipulating the connectivity between trimers via simple cationic exchange. In highly diluted systems (in solid state and in liquid solution), the hysteretic behavior do not present apparent dilution effect, and indeed, it is still maintained in systems where the cooperative have been reduced down to single molecule level. This surprisingly results open the opportunity to exploit the active-SCO molecule as molecular memory. As a first approach to incorporate this molecule in nano-sized devices, we deposit $[NH_2Me_2]_6[M_3(\mu\text{-}\mathbf{L})_6(H_2O)_6]$ complex onto diverse surfaces, obtaining nanometer-thick films with SCO bistability onto silica surface and well-ordered molecular arrays onto gold surface.

Publication

The results of this PhD Thesis have delivered the following publication:

Moneo, Andrea, David Nieto-Castro, Cristina Sáenz de Pipaón, Veronica Gomez, Pilar Maldonado-Illescas, and Jose Galan-Mascaros. "Tuning the spin crossover behavior of the polyanion $[(H_2O)_6Fe_3(\mu\text{-}L)_6]^{6-}$: The case of the cesium salt (L^{2-} = (1, 2, 4-triazol-4-yl) ethanedisulfonate)." *Dalton Transactions,* **2018**, vol. 47, no 34, p. 11895 - 11902.

(Accepted 5th June, published on-line)

Abbreviations

SCO	Spin Crossover
LS	Low Spin
HS	High Spin
CFT	Crystal Field Theory
10Dq	Ligand Field Strength
P	Pairing Energy
ΔE_{HL}	Zero-point energy difference
K_B	Boltzmann constant
T	Temperature
χ_m	Magnetic susceptibility
Y_{HS}	High Spin Fraction
TIESST	Temperature-Induced Excited Spin- State trapping
LIESST	Light-Induced Excited-Spin State Trapping
LD-CISSS	Light-driven coordination-induced spin-state switching
LD-LISC	Ligand-Driven-Light-Induced Spin Change
LD-LIVT	Ligand-Driven Light-Induced Valence Tautomerism
4-Ettrz	4-ethyl-l,2,4-triazole
Hyetrz	4-(2"- hydroxy-ethyl)-1,2,4-triazole
Iptrz	4-Isopropyl-1,2,4-triazole
Bntrz	(Benzyl)-1,2,4-triazole
L	Ligand: 4-(1,2,4-triazol-4-yl)ethanedisulfonate

TIESST	Temperature-Induced Excited Spin- State trapping
LIESST	Light-Induced Excited-Spin State Trapping
LD-CISSS	Light-driven coordination-induced spin-state switching
LD-LISC	Ligand-Driven-Light-Induced Spin Change
$T_{1/2}(\uparrow)$	Transition Temperatures in the heating branch
$T_{1/2}(\downarrow)$	Transition Temperatures in the cooling branch
d	Distance
M	Magnetization
C	Curie constant
g	g-factor
β	Bohr magneton
Φ	Weiss Constant
N	Avogadro`s number
H	Magnetic Field
kJ	Kilojoule
Ms	Saturation Magnetization
F	Ferromagnetic
AF	Anti-Ferromagnetic
E_a	Activation Energy
S	Spin
J	Magnetic Coupling parameter
fac	Facial
R_a	Average roughness

UV-VIS	Ultra Violet-Visible
Abs	Absorbance
SMMs	Single Molecule Magnets
PXRD	Powder X Ray Diffraction
SCXRD	Single Crystal X Ray Diffraction
IR	Infrared
SQUID	Super quantum interference device
ICP-OES	Inductively coupled plasma optical emission spectrometry
EDX	Energy-dispersive X-ray spectroscopy
TGA	Thermogravimetric analysis
DSC	Differential Scanning Calorimetry
ESEM	Environment Electron Scanning microscopy
AFM	Atomic Force Microscopy
STM	Scanning Tunneling Microscopy
1D/2D/3D	One, Two and Three Dimensional, respectively

UNIVERSITAT ROVIRA I VIRGILI
BISTABLE MOLECULAR MATERIALS: TRIAZOLE-BASED COORDINATION CHEMISTRY OF FIRST ROW TRANSITION METALS
Andrea Moneo Corcuera

Chapter 1

General Introduction

1.1. Magnetic molecular material

Inorganic network solids participate considerably in our technological society, representing one of the most used materials for advancing technologies. The development and design of novel and improved materials with interesting magnetic, optical and/or electrical properties have important implications in multiple areas of technology, as for example magnetic imaging, magneto-optics or information storage application.[1,2] However, these solid state materials typically lose their properties at the nanoscale in the miniaturization process through common top-down approach.[3–5]

Molecular materials have been considered as a plausible alternative to overcome this size limitation,[6–10] being good candidates for molecular-based components for data storage devices.[11–15] In addition to their intrinsic molecular properties (e.g. molecular dimensions, optical transparency or low density), molecular compounds are more advantageous because their properties can be in principle finely modulated by synthetic design with high synthetic versatility. Optical,[16,17] electric[18,19] or magnetic[20,21] molecular materials have been widely explored, opening the way to prepare also multifunctional materials able to combine those properties.[22–25]

In particular, magnetic molecular material have attached great interest, attempting to understand the correlations between molecular geometry and magnetic features. Indeed, the rational design of molecular architectures to predict appropriate magnetic behavior is still an open research field. In this direction, large variety of original compounds have been synthesized containing several types of metal ions, organic fragments and/or bridging ligands (obtaining multinuclear compounds, clusters, chains, two- or three-dimensional architectures).[26] These materials exhibit large diversity of magnetic properties, including light-weight room

temperature magnets,[27,28] single-molecule magnets,[29–33] or photo-active magnets.[34–37]

Another important type of materials in this field are switchable magnetic compounds. They can adapt their physicochemical properties (magnetic behavior) as a consequence of a change in their electronic configuration in response to an external perturbation. Several switchable molecules have already been investigated, as for example, spin crossover (SCO), valence tautomerism or metal-to-metal charge transfer (MMCT) complexes. All of them contribute significantly to inaugurate the use of molecules as building blocks for the fabrication of electronic devices and/or molecular memories. Indeed, some preliminary advances have been already obtained in molecular switching, data storage and signal processing.[38]

This chapter focuses on the spin crossover phenomenon, a spectacular example of bistability in molecule-based materials and the major subject of this thesis.

1.2. Spin Crossover (SCO) phenomenon

1.2.1. Discovery of SCO phenomenon

Spin crossover (SCO) phenomenon in metal-organic complexes arises from the switch between the low spin (LS) ground state and the high spin (HS) excited state, low enough in energy to be populated due to the particular crystal field imposed by a variety of ligands. In this case, the HS state may be populated by external stimuli such as temperature, light, pressure or magnetic field. The change of the spin state also provokes additional changes, due to the different electronic structure, typically associated to a different population of anti-bonding and non-bonding orbitals.

Thus, spin transition complexes can be found in nature, being a relevant process in biology[39,40] and geology.[41,42] The SCO phenomenon plays an important role in the chemical reactivity of metallo– (as in the case of cytochrome P450)[43] or hem-derived enzymes (as hemoglobin, where the spin transition is crucial for efficient oxygen transport).[44] The SCO phenomenon is also present in minerals and geological processes, being especially connected to pressure effects on spin transition.

In synthetic systems, SCO has been recognized since the 1930s, when Cambi and co-workers observed a significant magnetic moment change as a function of temperature for an iron(III) ditiocarbamate complex.[45,46] Simultaneously, Pauling and co-workers published similar anomalous magnetic behaviour in ferrihemoglobin hydroxides. [47] Around twenty years later, Orgel attributed these anomalous magnetic properties to an equilibrium between HS and LS state.[48] In 1964, Baker and Bobonich synthesized the two first iron (II) SCO complexes, $[Fe(phen)_2(NCS)_2]$ and $[Fe(bipy)_2(NCS)_2]$ (phen: 1,10-phenanthroline, bipy:2,2-bipyridine) and reported their “unusual cooperative magnetic behavior”.[49] Three years later, Konig and Madeja carried out detailed magnetic and Mössbauer spectroscopic studies on these complexes and attributed the origin of such

cooperative magnetic behaviour to a spin transition induced by the temperature.[50] This represented a starting point for further development of this research field. In fact, since then, numerous thermal induced SCO Fe^{II} and Fe^{III} compounds have been reported.[48,51,52,53]

Nowadays, it is well-known that not only temperature but also light, pressure or magnetic field can induce spin state switching. The first example of light as external stimulus to promote the spin transition was reported in 1984 as the so-called Light Induced Excited Spin State Trapping (LIESST) phenomenon.[54] In these experiments, green light could induce the spin transition from LS to HS state at low temperature.

Although iron (II) complexes are the most common SCO complexes, other coordination compounds of 3d transition metal such as Co^{II},[55] Co^{III},[56], Cr^{II},[57] Mn^{II},[58] or Mn^{III},[59] can also display spin crossover behavior.

1.2.2. Principle of molecular spin state switching

The spin crossover phenomenon for d^4-d^7 transition metal ions can be rationalized on the basis of crystal field theory, and can be predicted using Tanabe-Sugano diagrams, following the ligand field strength.

Crystal Field Theory

The Crystal Field Theory (CFT) was firstly proposed by the physicist Hans Bethe in 1929,[60] and six year later, J. H. Van Vleck introduced some modifications taking into account the covalent bonding in paramagnetic anisotropy.[61]

CFT describes the electronic distribution in the valence shell (*d* or *f* orbitals) of transition metal ions in coordination complexes (see the schematic representation of 3d orbitals in Figure 1.1).

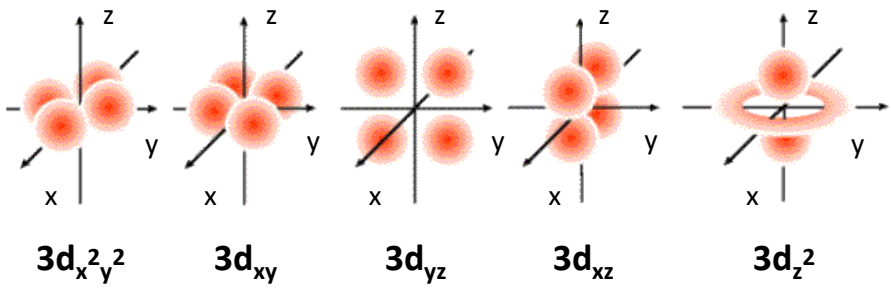

Figure 1.1. *Representation of 3d-orbitals. d_{x2-y2}: lobes lie on x and y axes; d_{xy}: lobes between x and y axes; d_{yz}: lobes between y and z axes; d_{xz}: lobes between x and z axes; d_{x2}: two lobes on the z axes and a donus-shape ring on the xy plane around the other lobes.*

This theory is based on an electrostatic model to describe the interaction between the metal ion and the coordinated ligands, whose anisotropic field affects the atomic orbitals of the central metal. Firstly, considering the situation of a free and gaseous metal ion, there are no electrostatic interactions between the orbitals from the metal center and the ligands, and hence, this model supposes that the metal ion d orbitals are degenerated. In coordination complexes, the electrostatic interaction between the electrons from the ligands and the d-electrons cause a splitting in energy of the d orbitals, depending on the crystal field symmetry. For octahedral complexes, where the ligands are oriented along the cartesian axes, the five 3d orbitals are splitted into two sets: three t_{2g} degenerate orbitals (d_{xy}, d_{yz} and d_{xz}), which are lower in energy and the remaining two degenerate e_g orbitals (d_z^2 and $d_{x^2-y^2}$), which are higher in energy. The energy gap between these orbitals subsets is symbolized by the parameter called Ligand Field Strength, 10Dq.[62]

The electronic distribution of $3d^4$-$3d^7$ transition metal ions is determined by the relationship between 10Dq and the electron-electron repulsion energy, often referred as spin-pairing energy, P. In strong ligand fields, when the 10Dq is greater than P, the electrons tend to occupy preferably the non-bonding orbitals, t_{2g}, and the metal complex adopts the LS configuration. In weak ligand field, the 10Dq is

smaller than P energy, the d electrons follow Hund's first rule of maximum multiplicity and the metal complex adopts the HS configuration. As an example, Figure 1.2 shows a schematic representation of the two possible electronic ground state for Fe^{II} ion under an octahedral symmetry. In this case, the low spin state exhibit $t_{2g}^6e_g^0$ electronic configuration ($^1A_1$ state) with no unpaired electrons (S = 0, diamagnetic) and the high spin state present $t_{2g}^4e_g^2$ configuration ($^5T_{2g}$ state) with four unpaired electrons (S = 2, paramagnetic).

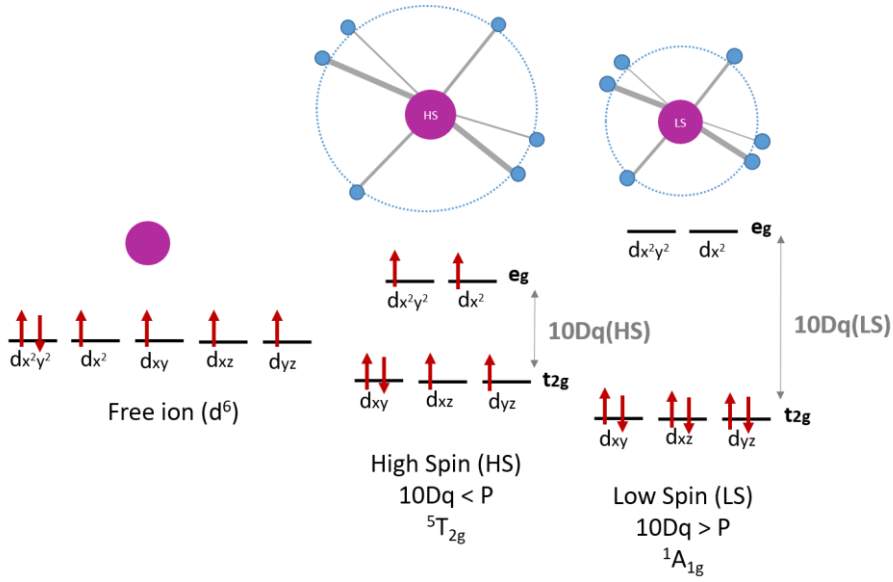

Figure 1.2. *Schematic representation of electronic distribution in splitted d-orbitals in an octahedral environment. The case of Fe^{II} ion with $3d^6$ electronic configuration.*

The possibility to induce a spin transition between LS and HS state by applying external stimuli is directly associated to intermediate ligand field strength, where 10Dq and P energy values are comparable (10Dq ≈ P). Based in this concept, the SCO phenomenon may be considered an intra-ionic electron transfer between e_g and t_{2g} orbitals, Figure 1.3.

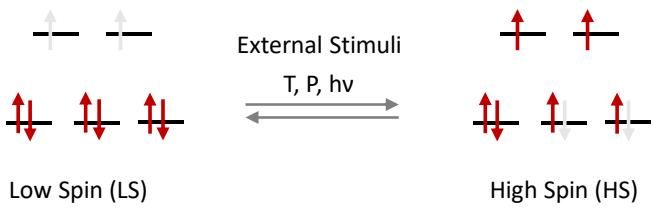

Figure 1.3. *Schematic representation of $3d^6$ electronic distribution during the spin transition in octahedral Fe^{II} complexes.*

Factors influencing ligand field splitting energy, 10Dq.

The ligand field splitting energy plays a relevant role in spin crossover phenomenon at transition coordination complexes. The strength of 10Dq is strongly influenced by the ligand nature and structural parameters.

Regarding the ligand nature, in general terms, the π-donor ligands cause lower fields in comparison with the ligands with more π-acceptor character. The spectrochemical series (Figure 1.4) classifies several ligands as a function of the ligand field strength that they produce.[63] Therefore, the chemical design of the coordinated ligands is a strategy to control in advance the spin state of the metal ion and also to promote the spin switching phenomenon.

$I^- < Br^- < S_2^- < SCN^- < Cl^- < NO_3^- < N_3^- < F^- < OH^- < C_2O_4^{2-} < H_2O < NCS^- <$ CH_3CN < pyridine (py)< NH_3 < ethylenediamine(en) < 2,2'-bipyridine (bipy) < 1,10-phenanthroline (phen) < NO_2^- < PPh_3 < CN^- < CO.

Figure 1.4. *Classification of several coordinated ligands in function of the ligand field strength that they can generate (from low to high ligand field strength).*

Not only the ligand nature but also structural parameters, especially the metal-ligand distance, are determinant for the ligand field strength.[64,65] Indeed, the HS state involve substantially larger metal-ligand bond length than LS state, due to the electrons populating the antibonding e_g orbitals. In the case of Fe^{II} ion, the

differences in Fe-N bond lengths between LS and HS states are between 0.1 - 0.3 Å . Therefore, the potential energy of both spin state correlates with radius, R parameter, Figure 1.5.

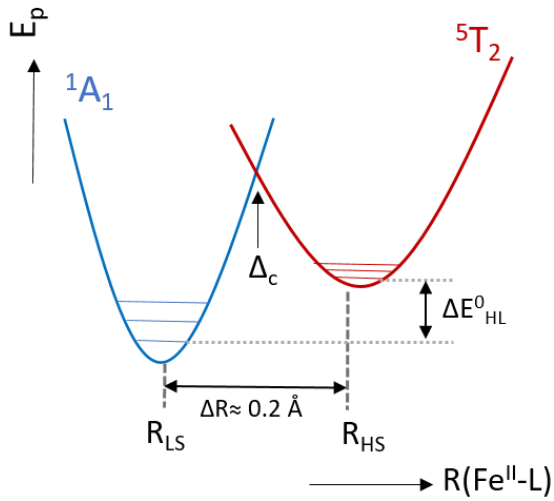

Figure 1.5. *Potential energy representation of the HS ($^5T_{2g}$) and LS state ($^1A_{1g}$) depending on the metal-to-ligand distance (R) for an octahedral Fe^{II} complex. The vibrational energy levels are represented as horizontal straight lines inside the potential wells.*

The HS-potential well is shifted to longer metal-ligand distances compared to the LS-potential well. This horizontal displacement averages around 0.2 Å in Fe^{II} complexes, which accounts for 5 - 15% differences in bond length. On the other hand, LS-potential well is lower in energy, as the ground state. The difference in energy between the lowest vibrational levels of the HS and LS state (zero-point energy difference, ΔE_{HL}) is an important parameter for the occurrence of spin transition. For intermediate ligand field, ΔE_{HL} may be small enough to induce excited state (HS) population pumping energy into the system (thermal, light irradiation) or by external effects modifying the energy diagram (pressure).

Thermally induced spin crossover phenomenon is expected when ΔE_{HL} is in the order of magnitude of thermal accessible energy, K_BT [65] ($\Delta E^0_{HL} \approx K_BT \approx 200$ cm^{-1} at 295 K). At very low temperature, the SCO center is in the LS ground state. When the temperature increases, the thermal energy is transformed into vibrational energy and the excited vibrational levels are populated. According to Franck-Condon principle, the spin transition from LS to HS state can occur from the crossing point (Δ_c) of both potential wells, where the HS successor and LS precursor state have the same geometry. Since SCO is an endothermic process, the transition from low to high spin state is considered an entropy-driven process (greater electronic and vibrational contributions in HS state), favoring the population of the HS state at high temperatures.[62,66]

Tanabe-Sugano Diagrams

The repulsion between d-electrons of a transition metal ion involves different electronic states, characterized by a spin multiplicity, *2S+1*, and an orbital moment, *L*. These states are symbolized with ^{2S+1}L terms and their energies are calculated from the Racah parameters of the electron-electron repulsion, B and C.[62] Tanabe-Sugano diagrams, for a given electronic configuration d^n, represent the energy of the electronic states (vertical axis) respect to the ligand field strength (horizontal axis), Figure 1.6.

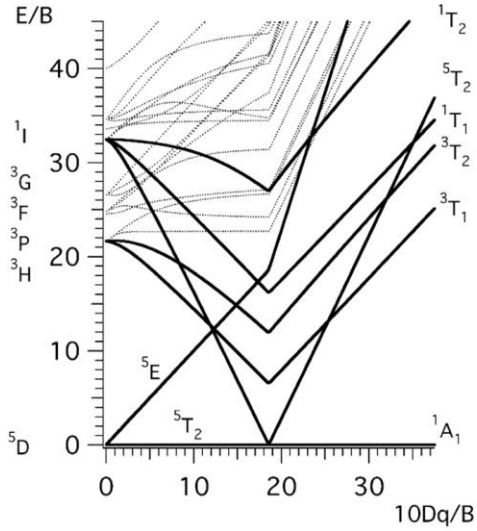

Figure 1.6. *Simplified Tanabe-Sugano diagram for a $3d^6$ metal ion in octahedral environment.*[62]

For d^6 transition metal ion and weak ligand field, the coordination complex is in the ground high spin ($^5T_{2g}$) state, which arises from ^5D state in the free metal ion. The HS ground state remains stable until critical ligand field strength, Δ_c. Such value corresponds to the crossing point of the two potential wells in configurational coordinate diagrams (see Figure 1.5) and is related to the magnitude of the P energy. While at ligand fields higher than Δ_c, the low spin ($^1A_{1g}$) state becomes the ground state.

According to Franck-Condon principle, the vertical allowed d-d transitions of this diagram are reflected in the absorption spectra. The electronic spectra of HS species show an absorption band in the near-infrared range, which arise from the $^5T_{2g} \rightarrow {}^5E_g$ transition. The LS species exhibit two absorption bands in the UV-visible range: the near-ultraviolet band is attributed to $^1A_{1g} \rightarrow {}^1T_{2g}$ transition and the visible band corresponds to $^1A_{1g} \rightarrow {}^1T_{1g}$ transition. Thus, the LS-HS transition results in a visible thermochromism for ^6d species, typically from pink-violet (LS) to colorless (HS), providing an additional and rapid detection of the spin transition.

1.2.3. Detection of the spin transition

The spin state transition is accompanied by significant variation in the chemical and physical properties that depend on the electronic distribution of the 3d orbitals. Predominantly, optical, vibrational, magnetic and structural properties reveal notorious changes during the spin crossover process. The quantification of these molecular changes enables to detect the spin transition and determine the external-stimuli dependence in the SCO complex. In this section, we show an overview of the physical experimental techniques that can be used to follow the main molecular changes that occur during the spin transition, see Table 1.1.

Table 1.1. *Overview of the physical experimental techniques commonly used to detect the spin transition.*

Experimental Techniques	Detected property
Magnetic measurements (Evans´s NMR Method; SQUID)	Magnetic susceptibility Effective magnetic moment
Optical Spectroscopy (UV-vis absorption)	d-d transitions Metal to Ligand Charge Transfer
Vibrational Spectroscopy (FIR; Raman)	Metal-ligand vibrational frequencies
Mössbauer Spectroscopy	Isomer shift/Electric quadrupole splitting Electronic state of metal centers
X-Ray Diffraction (PXRD, SCXRD)	Metal-Ligand distance
Calorimetric Measurements (DSC)	Heat Capacity Crystallographic phase transitions

Magnetic Measurements

The number of unpaired electrons is directly related to the magnetic susceptibility (χ) of the material. For Fe^{II} ion, the high spin state exhibits four unpaired electrons (S = 2) and the low spin state is diamagnetic with no unpaired electrons (S = 0). For thermally induce SCO complexes, the magnetic susceptibility measurements as a function of temperature, $\chi(T)$, have been the main characterization method to follow the spin switching process. The relation between the magnetic susceptibility and the LS-HS fractions can be expressed as

$$\chi(T) = \gamma_{HS}(T)\cdot\chi_{HS} + (1-\gamma_{HS}(T))\cdot\chi_{LS} \qquad \text{Equation 1.1}$$

where γ_{HS} in the molar fraction of the SCO centers in HS state, whereas χ_{HS} and χ_{LS} are the magnetic susceptibility for each species. Therefore, from $\chi(T)$ data the spin transition curves, $\gamma_{HS}(T)$, can be estimated. The magnetic studies can be performed in liquid state by Evans NMR method [67] or by magnetic susceptometer (SQUID) in the solid state.

Optical Spectroscopy

Most SCO complexes present thermochromism as a typical feature of SCO phenomena. The major subject in this thesis, iron(II) SCO complexes with 1,2,4-triazole ligands look generally colorless in the HS state and purple in the LS state. This color change opens the possibility to follow the spin crossover process by means of optical reflectance and UV-vis absorption spectroscopy. Since absorbance is proportional to concentration, the population of each spin species can be quantified by this methods. Temperature-dependent UV-vis spectroscopy has been used in this thesis to monitor spin transitions in solution.

Vibrational Spectroscopy

The increment in the population of the antibonding e_g orbitals in the HS state results in a weakening of the metal-donor bonds, which is reflected in the far-infrared (FIR)

region between 250 and 500 cm^{-1} of vibrational spectrum. Therefore, FIR and Raman spectroscopy can be employed to qualitatively recognize the spin crossover behavior.

Mossbauer Spectroscopy

^{57}Fe Mossbauer spectroscopy is a highly sensitive technique to probe the oxidation state and the spin state of coordination Fe(II) complexes,[68] since it is element specific. Important parameters arising from the hyperfine interaction between the nucleus and the surrounded electronic/magnetic field, vary significantly with electronic configuration. The Mössbauer spectra is proportional to the fraction of spin state, enabling easy quantification.

X-Ray Diffraction Method

The variation of metal-ligand bond length during the spin switching process affects the crystal lattice parameters in the solid state,[69,70] provoking in some cases phase transitions beyond cell expansion. Thus, the spin transition can be monitored by X-ray diffraction methods. Powder X-ray diffraction (PXRD) provides information about the changes in cell parameters and symmetry, while single crystal X-ray diffraction (SCXRD) may be able to determine the chemical structure of each metal center in the solid, albeit disorder issues, along additional changes in intermolecular interactions (hydrogen bonding, π-stacking…).

Calorimetric measurements

As previously mentioned, the spin transition from LS to HS state is an entropy-driven process. The higher entropy in HS state arises from a higher spin multiplicity and larger intermolecular vibrations. Therefore, SCO phenomena may be detected by thermodynamic parameters: enthalpy ($\Delta H = H_{HS} - H_{LS}$) and entropy ($\Delta S = S_{HS} - S_{LS}$). In the solid state, crystallographic phase transitions will also contribute to these parameters, and can be easily detected by calorimetry.[71] Generally, the enthalpy

and entropy variations in SCO materials are in the 10-20 kJ mol^{-1} and 50-80 KJ mol^{-1} K^{-1} range, respectively.[72] Differential Scanning Calorimetry offers heat capacity data, which is directly related to enthalpy and entropy parameters.

Other techniques

Other specific techniques for structural characterization, such as X-ray absorption (XAS), or spin characterization (EPR) are also helpful to extract additional information in SCO systems. Within this group, XAS near edge structure (XANES) and extended XAS fine structure (EXAFS) are very powerful methods to offer information about the local structure and variations upon spin transition.

1.3. Light-induced Spin State Change

Photo-inducted spin state change was firstly observed by McGarvey and Lawthers in 1982. They studied the perturbation of the equilibrium between the singlet (^{1}A) and quintuplet (^{5}T) states in Fe^{II} complexes in solution by pulsed laser irradiation.[73] Later, in 1984, Descurtins et al. discovered a Fe^{II} SCO compound, $[Fe(ptz)_6](BF_4)_2$ ptz:1-propyltetrazole, that was photo-converted into the metastable long-live HS state in solid state at sufficiently low temperatures.[74,75] This phenomenon, called Light-Induced Excited-Spin State Trapping (LIESST) effect, was deeply studied by Hauser et. al, finding also the reverse process (reverse-LIESST).[76]

These phenomena and their mechanisms are today well-understood, Figure 1.7.[77,78] Regarding the direct process, typically green light (≈514 nm) at low temperatures can stimulate the spin allowed $^1A_1 \rightarrow {}^1T_1$ transition, with $^1T_1$-lifetimes in the nanosecond range (≈50 ns). A fast relaxation processes over two successive crossing steps through $^3T_1$ and $^3T_2$ intermediate states, populates the metastable $^5T_2$ high spin state. The $^5T_2 \rightarrow {}^1A_1$ transition is symmetry forbidden and can only occur by thermal tunneling, resulting in a very long lifetime for the trapped HS state at low temperatures (usually below 50 K). The metastable HS state can be converted back to the ground LS state by warming up or by irradiation of red light (≈ 820 nm), promoting the opposite transition. The latter phenomenon is called reverse-LIESST, and it is achieved by a first excitation from $^5T_2$ to ^{5}E state with consecutive crossing processes ,$^5E \rightarrow {}^3T_1 \rightarrow {}^1A_1$.

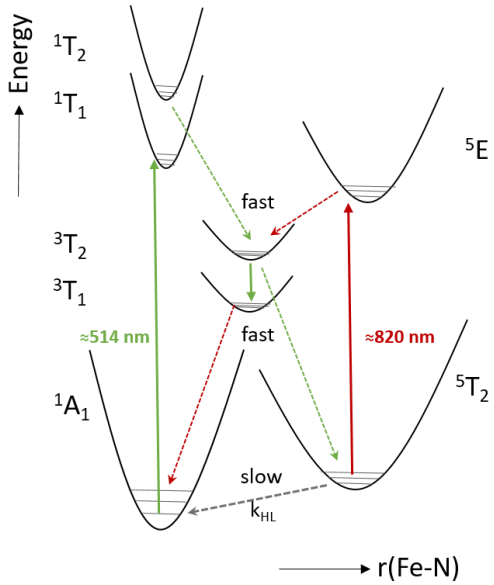

Figure 1.7. *Schematic mechanism of LIESST (green) and reverse-LIESST (red) phenomenon for a SCO d^6 complex. Spin allowed d–d transitions promoted by light irradiation are denoted by full black arrows and the relaxation processes are denoted by dotted arrows.*

The photo-control of the spin state supposes a promising approach to use photo-switchable SCO compounds as optically-sensitive memory materials. However, the LIESST effect depends on very low temperatures, since high temperatures promote faster relaxation of the photo-induced HS state, clearly limitating room temperature applications.[79]

Alternative strategies for photo-induced spin transition have been investigated in order to overcome such disadvantage in the LIESST effect. For example, some solid materials have shown photo-induced spin conversion within the thermal hysteresis region, due to a transition in the macroscopic phase by a laser pulse irradiation.[80–82] Another example is the phenomenon called Ligand-Driven Spin Change, where the light is used to produce a photo-isomerization of the coordinated ligand with subsequent spin transition of the metal center, as a result of a change in the coordination mode, called Light-driven coordination-induced spin-state switching

(LD-CISSS) [83,84] or a change in the ligand field strength, called Ligand-Driven-Light-Induced Spin Change (LD-LISC)[85–87] (Figure 1.8).

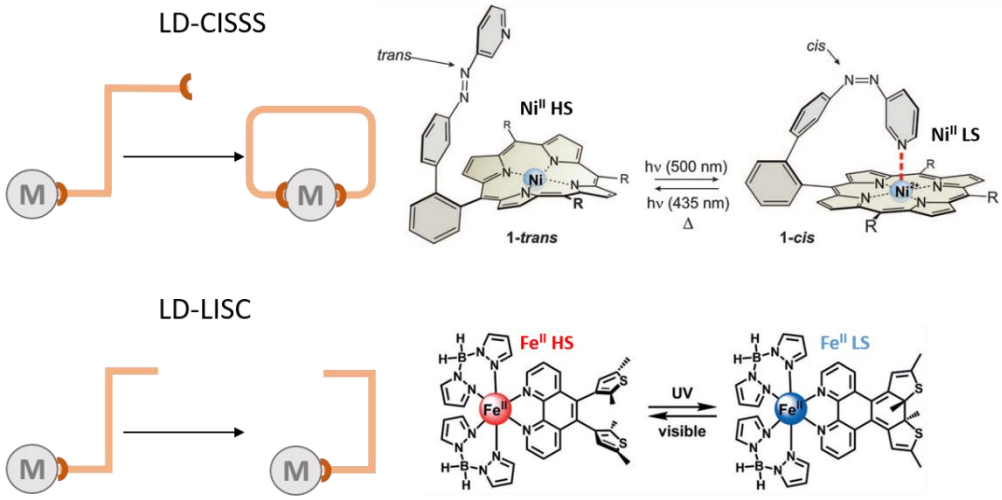

Figure 1.8. *Schematic representation of LD-CISS and LD-LISC with a corresponding example: (Top) Ni-porphyrin complex with reversible cis-trans photoisomerization of azopyridine moiety. (Bottom) Fe^{II} complex with photoisomerizable diarylethene ligand.*

1.4. Pressure-induced Spin State Change

The spin transition is also very sensitive to an applied external pressure because of the molecular volume difference between HS and LS species. The applied pressure favors shorter metal-ligand distance, stronger ligand field and an increase in the zero-point energy separation $\Delta E°_{HL}$ (see schematic illustration for Fe^{II} complexes, Figure 1.9). So, an externally applied pressure stabilizes the LS state, as firstly confirmed by Ewald et al. in their pressure-dependent studies on iron(III) complexes.[88]

Therefore, the pressure have large influence on SCO behavior, typically shifting the thermal spin transition toward higher temperatures (by stabilizing the LS ground state) and also accelerating relaxation processes.[89,90] In some examples, applied pressure can induce spin state switching in materials that are HS in ambient conditions. Firstly, Drickamer and coworkers observed experimental evidences of a pressure-induced HS → LS conversion for $[Fe(phen)_2(NCS)_2]$ complex.[91] More recently, M.L. Boillot et. al. reported a comparative XANES analysis for several $iron^{II}$ SCO compounds, showing a pressure-induced structural phase transition.[88] Another remarkable example was the memory effect of a cyanide-bridged Fe^{II} SCO polymer, $Fe(pyrazine)[Ni(CN)_4]\cdot 2H_2O$, reported by Azzedine group.[92] This complex exhibits a reproducible piezo-hysteresis loop at room temperature with characteristic spin transition pressures of $P_{1/2}\uparrow$=1350 bar and $P_{1/2}\downarrow$=650 bar through compression and decompression processes, respectively.

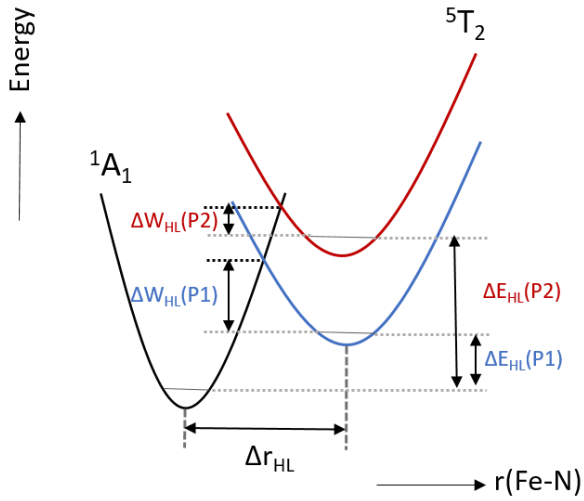

Figure 1.9. *Scheme of the pressure effect on the potential walls for HS and LS state of a Fe^{II} complex.*

The pressure effect on the spin conversion between two different electronic states would enable the implementation of this type of SCO materials in devices for piezo-electric memory or pressure sensors.[92,93]

1.5. Thermally-induced Spin State Change

Temperature is often used as an external perturbation to induce a spin state switching in SCO complexes. Indeed, the work presented in this thesis is mainly focused on thermally induced SCO phenomena. This section introduces the different thermal SCO behaviors from theoretical (section 1.5.1) and experimental point of views (section 1.5.2), and also the chemical modulation of the SCO behavior (section 1.5.3).

1.5.1. Thermodynamical aspects of the spin transition

Considering the system as an assembly of isolated non-interacting SCO centers, the spin transition can be described in the basis of a simple thermodynamic model as an equilibrium between two different phases. Under common experimental conditions (isothermal and isobaric) the thermodynamic function applied to this system is the Gibbs free energy (G) difference between HS and LS phases,

$$\Delta G = G_{HS} - G_{LS} = \Delta H - T \cdot \Delta S \qquad \text{Equation 1.2}$$

Where ΔH and ΔS are the enthalpy difference ($H_{HS} - H_{LS}$) and the entropy variation ($S_{HS} - S_{LS}$) during a spin transition, respectively. According to this equation, at low temperatures, the Gibbs free energy variation is dominated by enthalpy factor and the LS state is the stable state. Upon increasing the temperature, the entropy term becomes more significant, being the dominant factor at high temperatures. In this case, the stable state is the more degenerated HS state. There is an equilibrium temperature ($T_{1/2}$) in which the Gibbs free energy (G) difference is cero (i.e. $G_{HS} = G_{LS}$) and the proportion of LS and HS molecules are the same. The equilibrium temperature is defined by Equation 1. 3,

$$T_{1/2} = {}^{\Delta H}/_{\Delta S} \qquad \text{Equation 1.3}$$

ΔH can be divided into an electronic (ΔH_{el}) and a vibrational (ΔH_{vibr}) contribution. Apart from a few particular examples,[94] in most SCO complexes, the general ΔH is principally given by electronic enthalpy variation, ΔH_{el}. Conversely, the vibrational part of entropy variation contribute significantly to the SCO system. The electronic entropy contribution during the spin transition, is attributed to the change in the total spin momentum, S, (ΔS_{el}^{spin}) and the change in angular orbital momentum, L, (ΔS_{el}^{orb}),

$$\Delta S_{el}^{spin} = N_A k_B \ln \frac{2S_{HS}+1}{2S_{LS}+1} \qquad \text{Equation 1.4}$$

$$\Delta S_{el}^{orb} = N_A k_B \ln \frac{2L_{HS}+1}{2L_{LS}+1} \qquad \text{Equation 1.5}$$

Where N_A is Avogadro's number and k_B is the Boltzmann constant.

For Fe^{II} SCO complexes, heat capacity data reveals a remarkable difference between ΔS values (40-80 $J{\cdot}K^{-1}{\cdot}mol^{-1}$) and ΔS_{el} values ($\Delta S_{el} \approx \Delta S_{el}^{spin}$= 12-15 $JK^{-1}mol^{-1}$).[95] This highlights the large contribution of the vibrational entropy in SCO system, which arises mainly from the difference of the metal-ligand distances and the octahedral distortion between the HS and LS state.

However, cooperativity between SCO centers is crucial in a spin transition process in the solid state, when all centers belong to the crystal lattice, and intermolecular interactions may play a significant role. Slitcher and Drickramer[96] took into account the cooperativity in the thermodynamical model, describing the free energy as,

$$G = n_{HS}G_{HS} + (1 - n_{HS})G_{HS} + \Gamma n_{HS}(1 - n_{HS}) - TS_{mix} \qquad \text{Equation 1.6}$$

Where *Γ* represents the intermolecular interaction between active SCO centers.

The high spin fraction as a function of temperature (Equation 1. 7) can be obtained from first derivate of free energy expression and considering the thermal and pressure equilibrium, ($\delta G/\delta n_{HS/P,T} = 0$)

$$T = \frac{\Delta H + \Gamma(1-2n_{HS})}{N_A k_B \ln(^{1-n_{HS}}/_{n_{HS}})}$$ Equation 1.7

According to this equation, the spin transition curve n_{HS}(T) depends strongly on the magnitude of cooperativity. Therefore, at low cooperativity, $\Gamma < 2RT_{eq}$, the spin transition curves would be gradual, as it happens in solution. On the other hand, with stronger cooperative effects, the spin transition shows abrupt character ($\Gamma \approx 2RT_{eq}$) and at very strong cooperativity ($\Gamma > 2RT_{eq}$) the spin transition curve would present a maximum and a minimum, opening the appearance of a thermal hysteresis loop, Figure 1.10.

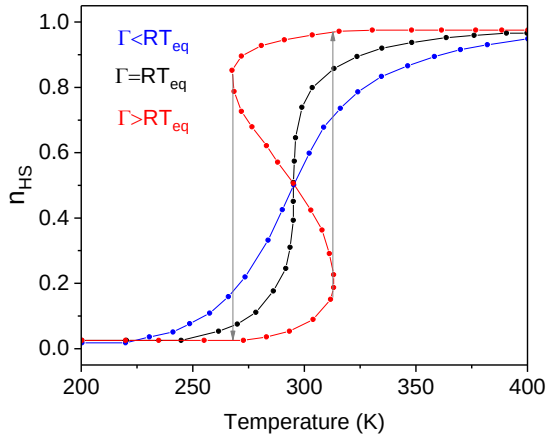

Figure 1.10. *Representation of spin transition curves, n_{HS} vs T plots, simulated according to equation 1.7 with different cooperativity values.*

1.5.2. Thermal spin transition behaviors

Variable temperature measurements of SCO systems gives the spin transition curve, γ_{HS}(T), from which is possible to determine the fraction of the HS or LS state at any temperature. Although the origin of the SCO phenomenon is molecular, the γ_{HS}(T) curves depend deeply on intermolecular interactions. Therefore, these curves provide information about the nature of the spin transition and the degree of cooperativity between SCO centers. The extent of cooperativity can be interpreted

in terms of the propagation of the spin change throughout the solid lattice, due to elastics interactions between SCO centers.[92]

There are different variants of spin transition curves (Figure 1.11), indicating the peculiarities of thermally induced SCO behaviors in terms of cooperativity. The gradual spin transition curve follows the Boltzmann distribution for thermal equilibrium between vibronic levels of both spin states.[97] Such behavior is characteristic of SCO system in solution, where the transition takes places essentially at molecular level without lattice interactions. On the other hand, for solid systems, the gradual curve is the most common SCO behavior in the case of short-range propagation in weak-cooperative solid systems, and until 1964 it was the only trend observed. Baker and coworkers reported for the first time that an abrupt spin transition curve, appearing when strong cooperativity is effective in the solid lattice.[49] Additionally, the transition can also occur in several steps (**c**), suggesting the presence of different crystallographic SCO metal centers.[98,99] In other cases, the transition can be also incomplete with residual HS or LS fraction due to the presence of inactive SCO centers.

The SCO behavior with thermal hysteresis has attracted great interest due to their potential implication in information storage applications. In such SCO systems, two transition temperatures ($T_{1/2}\uparrow$ in the heating branch and $T_{1/2}\downarrow$ in the cooling branch) determine the width of the hysteresis loop, within which the SCO compound presents bistability. The spin state at a given temperature is dependent on the immediate thermal history of the complex, conferring a memory effect within a certain temperature range. The first SCO complex with thermal hysteresis, $[Fe(4,7\text{-}(CH_3)_2\text{-phen})_2(NCS)_2]$, was discovered by Konich and Ritter in 1976.[100] Afterwards, hysteretic SCO systems have been widely observed and studied.[101–105]

The hysteresis can be interpreted as a kinetic effect, because of the difference in energy between both spin states, which precludes a fast equilibrium between

them.[105] Typically, the activation energy barrier for the transition is originated either by a crystallographic phase transition or by the propagation of intramolecular structural changes through the lattice, as mediated by intermolecular interactions.

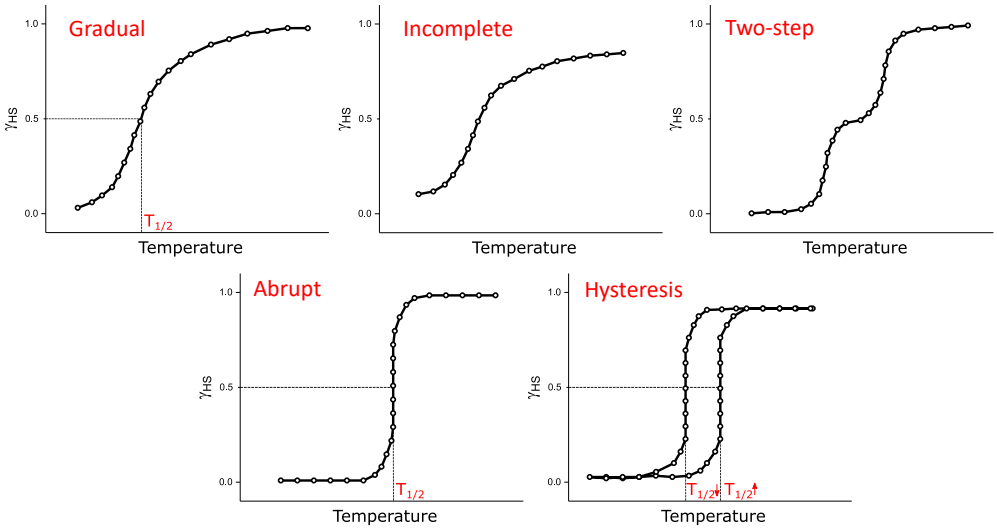

Figure 1.11. *Representation of different experimental spin transition curves of thermally-induced SCO complexes.*

1.5.3. Chemical Influences on thermal SCO behavior

The different spin transition curves shown in the previous section can be modulated though modifications of the external and/or internal coordination sphere of the SCO complexes. This section deals with the effect of chemical modifications (metal dilution, counter ions, or non-coordinating molecules) in the SCO behavior.

Metal dilution effects

The dilution of SCO complexes into isostructural lattices strongly affect the propagation of the spin transition through the lattice. In such experiments, the SCO active metal centers (e.g., Fe(II)) are partially replaced by isostructural non-SCO-active ions (e.g., Zn^{II}, or Cu^{II}) to progressively decrease interactions between SCO centers. The result of these studies[106–109] reveals a shift in transition temperatures,

and a flattening of population curves, with one of the spin states becoming dominant, and the only populated state above critical doping levels. The displacement of the transition temperatures can be correlated to the influence of the inactive metal ions sizes that change the internal "chemical pressure" in the system. For example in Zn/Fe dilutions, r (Zn^{II}) > r (Fe_{LS}^{II}), the larger dopant metal ions induce a "negative pressure" in the crystal lattice and consequently stabilize the larger HS state (downshifting the $T_{1/2}$). Remarkably, the thermal hysteresis also becomes narrower through the metal dilution and it disappears above a certain dopant concentration. This critical doping is typically very low, with 10-20% doping content being enough to vanish the SCO behavior. Two representative examples of metal diluted SCO systems was reported by Andreas Hauser et. al. [110] (Figure 1.12, left) and by Jean-François Létard et. al.[111] (Figure 1.12, right). The maximum threshold value was observed for $[Fe_xCo_{1-x}(4,4'\text{-bis-1,2,4-triazole})_2(NCS)_2]\cdot H_2O$ single mixed-crystals, with hysteresis disappearing above 64% Co^{II} content.[112]

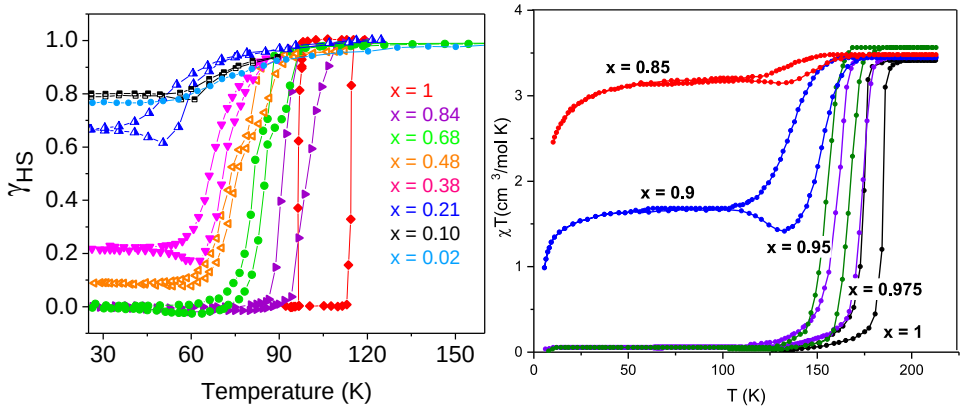

Figure 1.12. *(Left) HS fraction vs T plots obtained from optical absorption spectroscopy for* $[Zn_{1-x}Fe_x(bbtr)_3](ClO_4)_2$. *(Right) Thermal magnetic susceptibility measurements for* $[Fe_xMn_{1-x}(bpp)_2](BF_4)_2$ *series.*

Non-coordinated anions and solvents effects

The variation in non-coordinated counteranions and/or solvation molecules of SCO species can affect their spin transition properties, generally through modifications in the crystal structure (crystal lattice, "chemical pressure", H-bonding network, etc…). These changes are directly reflected on the cooperativity degree between the SCO centers, and hence in the SCO properties. Numerous examples of anion and solvents effects on SCO properties have been reported in the literature, going from shifts in transition temperatures or hysteresis loop, to (dis)appearance of SCO phenomena. However, such influence is not totally predictable since many weak parameters may affect the solid state behavior. In these section we will describe some representative examples of counter-anion and solvent effects reported in the literature.

The anion effects were firstly observed for $[Co(trpy)_2]^{2+}$ salts (trpy: terpyridine), and later for Fe^{II} salts, as $[Fe(2\text{-pic})_3]^+$ (2-pic: 2-Aminomethylpyridine). The magnetic behavior of $[Fe(pic)_3]X_2 \cdot EtOH$ ($X=Cl^-$, Br^-, I^-) salts shows drastic changes, from complete and abrupt in the chloride salt to an incomplete transition in the iodine salt, Figure 1.13 left.[113, 114, 115]

Another example is the series of 1D- $[Fe(NH_2trz)_3]X \cdot nH_2O$ polymers. The SCO behavior depends on the counterions, as found for the series of fluorinated inorganic anions X = TiF_6^{2-}, ZrF_6^{2-}, SnF_6^{2-}, GeF_6^{2-}, TaF_7^{2-}, Figure 1.13 right.[116]

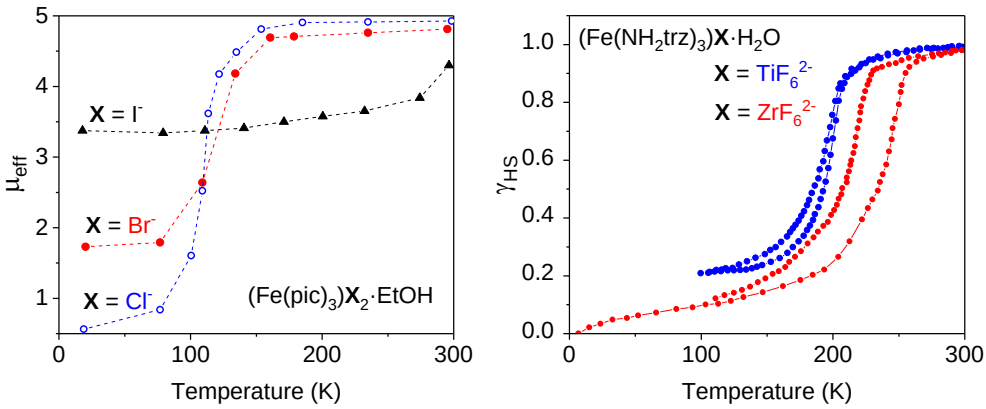

Figure 1.13. *Examples of non-coordinated anion (X) effect on the SCO properties of cationic SCO Fe^{II} species: (Left) $[Fe(pic)_3]X_2 \cdot EtOH$ salts[113] and (Right) $[Fe(NH_2trz)_3]X \cdot H_2O$.[116]*

The uncoordinated solvent molecules that participate in the crystal lattice could have large influence in the spin crossover behavior. The effect of the solvent content/nature has been widely studied including several cases, since it may modify and mediate crystal packing, intermolecular interactions, and even the ligand field strength at the metal center.[117–120]

J.A. Real et. al. analyzed the solvent influence in the crystal structure and magnetic behavior of $[Fe(tap)_2(NCS)_2] \cdot nCH_3CN$ (n =½, 1), (tap: tetraazaphenanthrene) systems.[118] Higher acetonitrile content in the crystal packing (from *0.5*·CH_3CN to *1*·CH_3CN) induces a shortening in metal-to-ligand bond distances, affecting the SCO behavior: paramagnetic for n=0.5 and thermal-induced LS-HS state conversion for n=1, Figure 1.14 left. On the contrary, in $[Fe(dppFc)_2](BF_4)_2 \cdot 2Et_2O$,[119] lower diethyl ether content induces LS stabilization and the appearance of a complete spin transition for $[Fe(dppFc)_2](BF_4)_2 \cdot Et_2O$ (Figure 1.14 right).

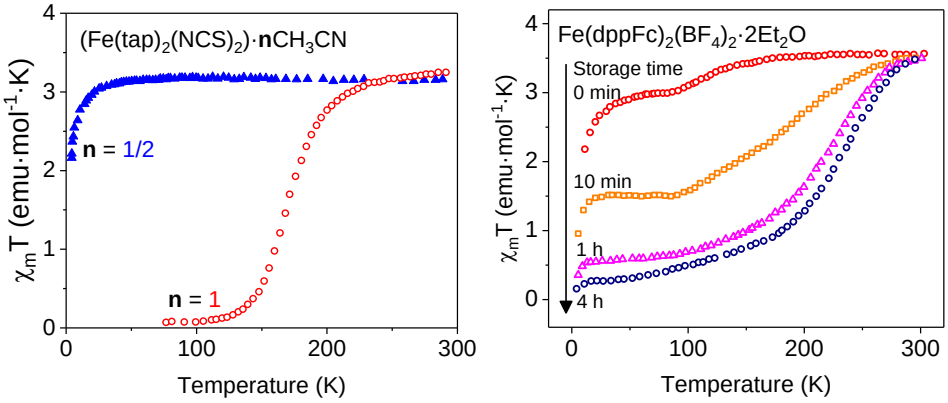

Figure 1.14. *Magnetic susceptibility measurements for (Left) [Fe(tap)₂(NCS)₂]·nCH₃CN (n =½ and 1)* [118] *and (Right) for [Fe(dppFc)₂](BF₄)₂·2Et₂O after different storage times.*[119]

In the same direction, C.J. Kepert et al. synthetized a molecular nanoporous framework material, $Fe_2(azpy)_4(NCS)_4 \cdot x(guest)$, (azpy: trans-4,4- azopyridine), that undergoes spin crossover behavior influenced by the reversible adsorption/desorption of guest molecules (ethanol or 1-propanol), Figure 1.15 right.[121] The sorbed phases display SCO behavior due to H-bond between the guest molecules and the thiocyanate sulfur atoms from the coordinating ligands, Figure 1.15 left.

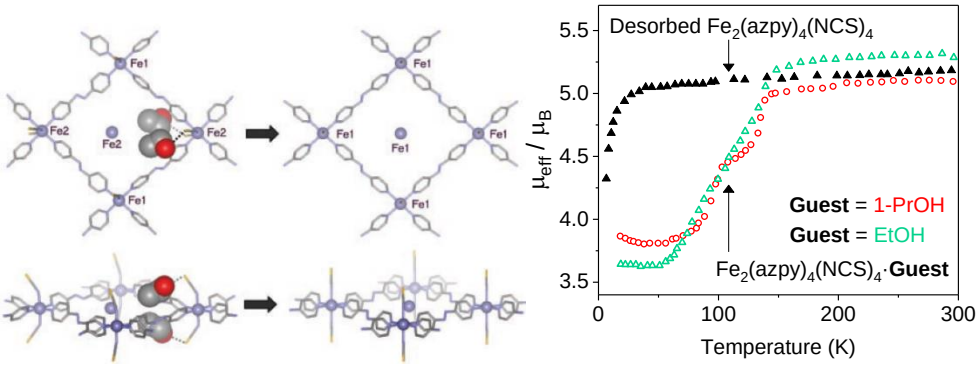

Figure 1.15. *(Left) Representation of the desorption process for Fe₂(azpy)₄(NCS)₄·2EtOH. (Right) The magnetic behavior of both adsorbed and desorbed system for EtOH and PrOH solvents.*

Ligand Effects

The ligand nature is at the core of the SCO phenonema. Thus, ligand substitution or chemical modifications are common strategies to modify or tune the SCO behavior of known materials

Ligand replacement strongly modifies the ligand field strength. A representative example of ligand substitution is the $Fe(phen)_3^{+2}$ / $[Fe(NCS)_2(phen)_2]$ (phen = 1,10-phenanthroline) system, Figure 1.16 left. The $[Fe(phen)_3]X_2$ compound is LS state, while the substitution of one bidentate phen ligand by two thiocyanato groups (NCS^-) weakens the ligand field strength sufficiently to present a thermal LS-HS conversion with a transition temperature around 180 K. The same effect was observed by the replacement with the weaker field $NCSe^-$ ligand, reaching a transition temperature around 230 K for $Fe(NCSe)_2(phen)_2$.[122] Substitution by every weak ligand field anions: X = Cl^-, Br^-, I^- or N_3^- yields HS complexes $Fe(X)_2(phen)_2$,[49] Figure 1.16 right.

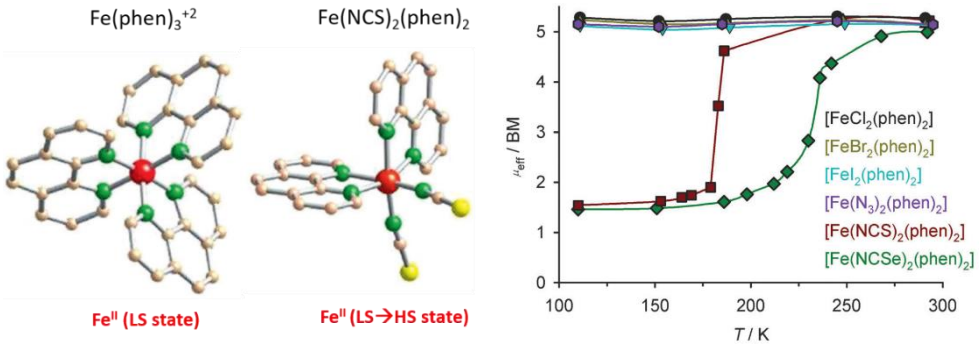

Figure 1.16. *(Left) Crystal structure of $Fe(phen)_3^{+2}$ and $Fe(NCS)_2(phen)_2$ molecules and the corresponding spin state.*[123] *(Right) Magnetic moment measurements for $Fe(X)_2(phen)_2$ (X = Cl, Br, I, N_3, NCS, NCSe) systems.*[124]

Similar effect in the modulation of crystal field strength can be observed by chemical modification of the coordinating ligands. This can be illustrated with the series Fe(2-X-phen)$_3^{+2}$ (X= H, CH_3, CH_3O and Cl) complexes.[125–128] The incorporation of different

functional groups in the 2–position of phen ligands involves an steric hindrance effect and the consequent elongation of the Fe-N bond. This causes a weakening in the crystal field (HS stabilization). $\gamma_{HS}(T)$ at a given temperature progressively increases in the order H < CH_3O < CH_3 < Cl, resulting in LS state in $Fe(phen)_3^{+2}$, promoting the appearance of SCO phenomenon in $Fe(2\text{-}CH_3\text{-}phen)_3^{+2}$ and $Fe(2\text{-}CH_3O\text{-}phen)_3^{+2}$, and HS state in $Fe(2\text{-}Cl\text{-}phen)_3^{+2}$, Figure 1.17 left. This can be explained in terms of both steric and electronic influence of the substituent in the coordinating N-atom.

In order to investigate the role of coordination steric barriers on SCO behavior, substituents at no adjacent positions to coordinating N-atom were introduced in the SCO $[Fe(NCS)_2(phen)_2]$ complex, Figure 1.17 right. The SCO behavior of $[Fe(NCS)_2(4\text{-}CH_3\text{-}phen)_2]$ and $[Fe(NCS)_2(4,7\text{-}CH_3\text{-}phen)_2]$ complexes were analyzed, observing no influence in the SCO behavior.[129,130]

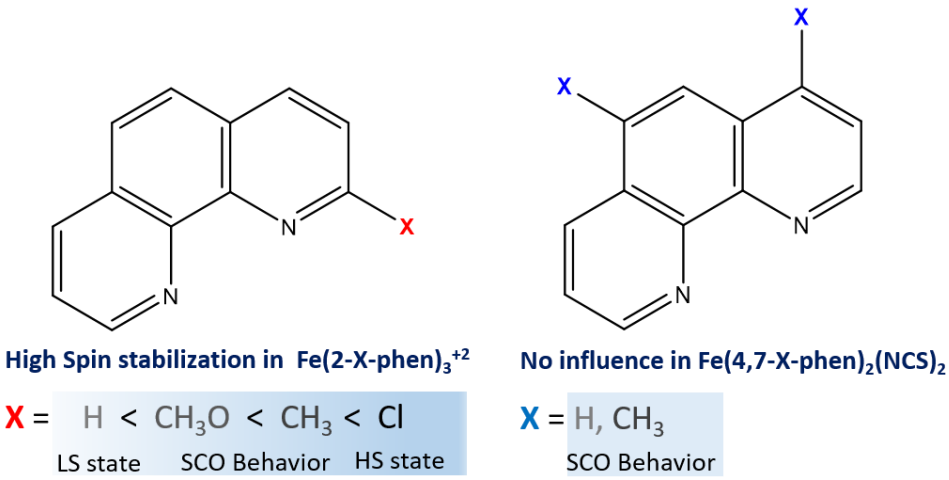

Figure 1.17. *Influence of the substituent position in the ligand field strength of the phen ligand. (Left) Functional group at 2-positions of phen ligand and (Right) Substituents in no adjacent positions to coordinating N-atoms.*

1.6. Thermally-Induced in SCO Fe^{II} Complexes

As already mentioned in section 1.2, the first examples of thermal SCO phenomenon was observed in mononuclear compounds of iron (III) [45,46] and iron (II) [50]. Later, it was well known that the cooperative interaction between SCO metal centers can tune the SCO properties, leading to abrupt ST process and large hysteresis loop. However, the control of cooperativity in such mononuclear compounds is difficult. One strategy to enhance cooperativity, and therefore memory effect, is the formation of polymeric architectures where metal centers are connected through covalent bonds.[131,132] One of the most successful examples was achieved with 1,2,4-triazole ligands, due to its capacity to form infinite 1D chain structures with metal cations. Additional studies in funcitionalized 1,2,4-triazole ligand types also yielded 1D discrete chains, particularly trimers. This section describe some examples of polynuclear SCO complexes based on 1,2,4 triazole and the 4-functionalized-1,2,4-triazole, focusing the attention on trinuclear SCO complexes and particularly in a polyanionic iron (II) complex (complex used in the thesis; section 1.6.3.1.)

1.6.1. Triazole Ligands

As mentioned before, the spin crossover phenomenon requires a ligand field strength (Δ_0) comparable to the pairing energy (P) to induce the switching between low spin to high spin state through a minor external perturbation. 1,2,4-triazole based-ligands often provide a ligand field strength at Fe^{II} centers that is adequate for the occurrence of SCO.[133] The 1,2,4-triazole ligand can coordinate to transition metal centers through their nitrogen donor atoms with strong tendency to act as a bridge ligand in $\mu_{1,2}$- or $\mu_{1,4}$-or even $\mu_{1,2,4}$ bridging modes, see Figure 1.18.

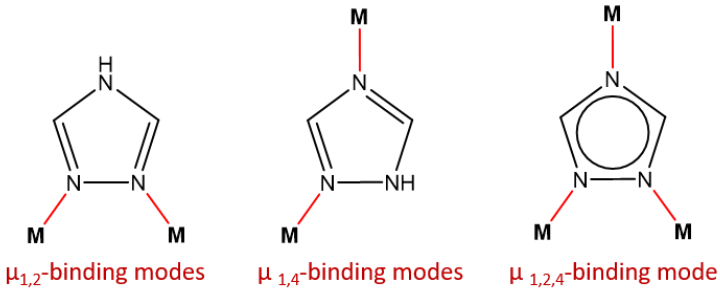

Figure 1.18. *Coordination modes of 1,2,4-triazole ligand to link two or three metal centers.*

The N_1,N_2-1,2,4-triazol bridge is the one favoring SCO behavior, since it provides appropriate ligand field strength. Additionally, this short and rigid bridge also favors effective spin transition propagation when compared with more flexible links.[134] This also means that the functionalization of the triazole in the N_4 position offers interesting opportunities for SCO tuning, being possible to modulate the SCO properties and the cooperativity with the nature of the 4-substituyent.

1.6.2. Polymeric SCO complexes based on 4-R-1,2,4-triazole

The family of polymeric Fe II complexes of formula $[Fe(4\text{-}R\text{-}1,2,4\text{-triazole})_3]^{2+}$ have been widely studied due to their interesting SCO properties: abrupt ST curve and wide hysteresis around room temperature[135–137]. For instance, $[Fe(NH_2trz)_3](NO_3)_2$ and $[Fe(Htrz)_2(trz)](BF_4)$ polymers reveal SCO behavior with transition temperatures of $T_{1/2}\uparrow$ = 348 K, $T_{1/2}\downarrow$ = 313 K [137] and $T_{1/2}\uparrow$ = 383 K, $T_{1/2}\downarrow$ = 345 K [138,139], respectively. The synthesis and magnetic measurements were reproduced in our group, see Figure 1.19.

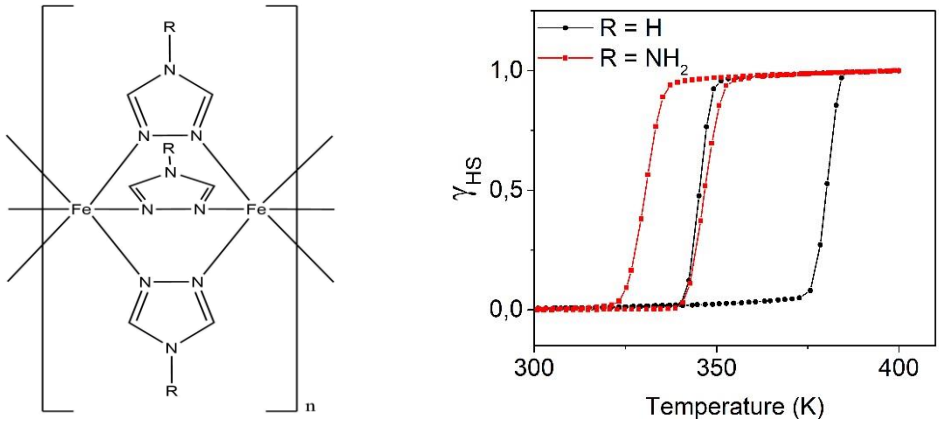

Figure 1.19. *(Left) General chemical structure of $[Fe(Rtrz)_3]^{2+}$polymers. (Right) Magnetic susceptibility measurements of $[Fe(Htrz)_2(trz)](BF_4)$ and $[Fe(NH_2trz)_3](NO_3)_2$ compounds.*

However, the crystallization of these polymers is very difficult due to the fast precipitation from solution yielding polycrystalline solids. Indeed, the crystal structure was obtained only recently for $[Fe(NH_2trz)_3](NO_3)_2{\cdot}2H_2O$ polymer.[140] Thus, structural information cannot be obtained from single crystal X-ray diffraction data, and other techniques such as EXAFS or LAXS (large-angle x-ray scattering) are helpful.

In certain synthetic conditions and with some triazole-derivatives, the 1D chain does not grow, and discrete polynuclear systems such as dimers, trimers or higher, are obtained. These species can be crystallized, allowing for easier structural characterization.

1.6.3. Trinuclear Complexes based on 4-R-1,2,4-triazole

In the SCO trinuclear Fe^{II} complexes, the Fe^{II} ions are connected through two triply 4(R)-1,2,4-triazole bridges, Figure 1.20. Their chemical structure present a central FeN_6 octahedral center and the terminal Fe(II) ions are coordinated by 3N donors from the triazole ligands and three mono anions and/or solvent molecules to complete the octahedral surrounding.

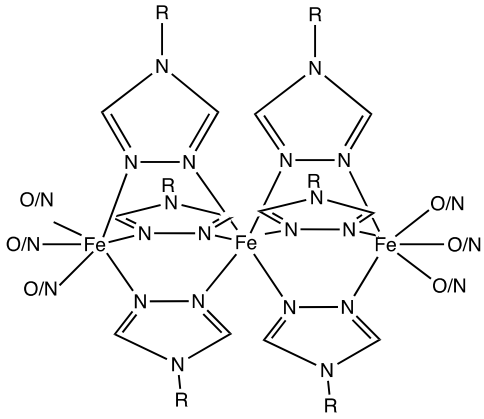

Figure 1.20. *Representation of the general chemical structure of trinuclear triply-triazol bridged SCO Fe^{II} complex.*

The SCO properties of these complexes can be drastically tuned by changing the coordinating anion/solvent molecules and the *R* group in the triazole ligand. Many different 4-(R)-1,2,4-triazole ligands have been successfully used to form active-SCO trinuclear Fe(II) complexes. Here, we explain some examples of this complexes with neutral triazole ligands, Figure 1.21.

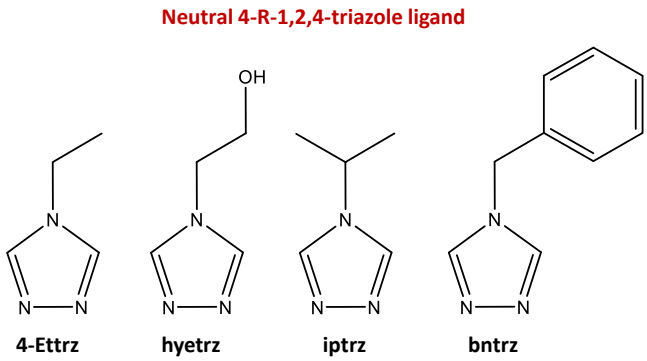

Figure 1.21. *(Left) Neutral 4-R-1,2,4-triazole ligands to form cationic SCO Fe^{II} trimers.*

Most reported SCO trinuclear complexes have cationic overall charge with neutral ligands. In 1983, Reedijk and coworkers published the first linear trimer Fe(II) complex, $[(Fe_3(\mathbf{4\text{-}Ettrz})_6(H_2O)_6)](CF_3SO_3)_6$.[141] Magnetic measurements and Mössbauer spectroscopy revealed an abrupt spin transition of one-third of the iron ions around 203 K. Later, Gütlich and coworkers synthetized a derivated Fe(II) trimer, $[Fe_3(\mathbf{hyetrz})_6(H_2O)_6](CF_3SO_3)_6$. Its magnetic behavior exhibits more gradual ST and the transition temperature was shifted towards higher temperatures, $T_{1/2}$=290K.[142] The change in the magnetic properties was attributed to the introduction of hydroxyl moiety that create H-bonds network. The anion effect was studied by Haasnoot and co-workers on the $[Fe_3(\mathbf{iptrz})_6(H_2O)_6]X_6{\cdot}xH_2O$ complexes, with X=p-toluenesulfonate (Tos) or trifluoromethanesulfonate (Trifl) anions.[143] Both complexes exhibited a gradual ST of the central iron ion centered at 242 K and 187 K, for the Tos and Trifl anions, respectively. In 2017, Marchivie and co-workers reported the first example of SCO Fe (II) trinuclear complex, $[Fe_3(\mathbf{bntrz})_6(\mathbf{tcnset})_6]$, tcnset=1,1,3,3-tetracyano-2-thioethylpropenide, that shows a complete and sharp one-step spin transition above room temperature ($T_{1/2}$=318K).[144]

Iron (II) trimer based on anionic triazole ligands

Our group has focused on the search for anionic triazole ligands to obtain overall anionic SCO complexes. With this purpose, we synthetized sulfonated 1,2,4-triazole derivatives: 4-(1,2,4-triazol-4-yl)ethanesulfonate ligand and 4-(1,2,4-triazol-4-yl)ethanedisulfonate, Figure 1.22.

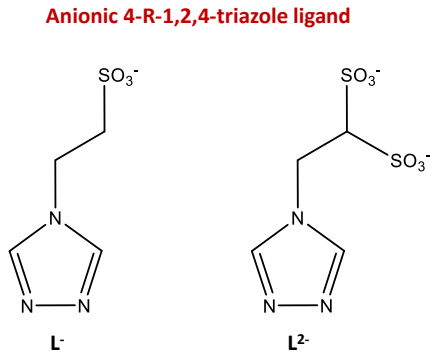

Figure 1.22. *Anionic ligand to form neutral and anionic SCO Fe^{II} trimers.*

In 2014, we reported the hysteretic SCO behavior of an iron (II) trimer, $[Fe_3(L)_6(H_2O)_6]_8H_2O$ (L^{-1} = 4-(1,2,4-triazol-4-yl)ethanesulfonate) [145] exhibiting thermal hysteresis at very high temperature with $T_{1/2}\uparrow$=350 K and $T_{1/2}\downarrow$=343 K, Figure 1.23. Typically, only polymeric architectures have memory effect at such high temperatures due to the covalent interaction between SCO centers. However, the neutral character of this complex and the highly polarity of the ligand can explain its particular SCO behavior, since neutral SCO systems do not need counter-ions, allowing shorter intermolecular distances between SCO molecules in the solid state.

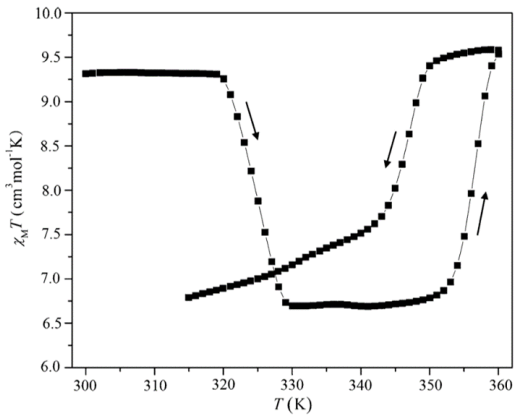

Figure 1.23. *Magnetic susceptibility measurements for $[Fe_3(\mathbf{L})_6(H_2O)_6]_8H_2O$ (L^{-1} = 4-(1,2,4-triazol-4-yl)ethanesulfonate).*

This thesis is manly focused on the study and processing of the first polyanionic Fe^{II} SCO complex ,$[Fe_3(\mu\text{-}\mathbf{L})_6(H_2O)_6]^{6-}$ $\mathbf{L}^{2-}$ =4-(1,2,4-triazol-4-yl)ethanedisulfonate, firstly isolated as the dymethil ammonium salt, $(Me_2NH_2)_6[Fe_3(\mu\text{-}L)_6(H_2O)_6]$ (Complex **1**) by our group.[146]

The crystal structure revealed the trinuclear polyanion $[Fe_3(\mu\text{-}\mathbf{L})_6(H_2O)_6]^{6-}$ (Figure 1.24) formed by a linear array of octahedral Fe (II) ions (Fe1−Fe2− Fe1) connected by two triple μ-triazole bridges. The terminal Fe1 ions completes its N_3O_3 hexacoordination with three H_2O molecules in *fac* conformation. The central Fe2 ion is octahedral coordinated with 6N donors from the ligands, forming the active SCO FeN6 site. The metal-to-ligand distances at 100 K indicate Fe_1 is in high spin (with an average Fe_1-N=2.13 Å) and Fe_2 is in low spin at 100 K (with average Fe_2−N = 1.99 Å). The sulfonate moieties participate in hydrogen bonded network between the trimers (Figure 1.25).

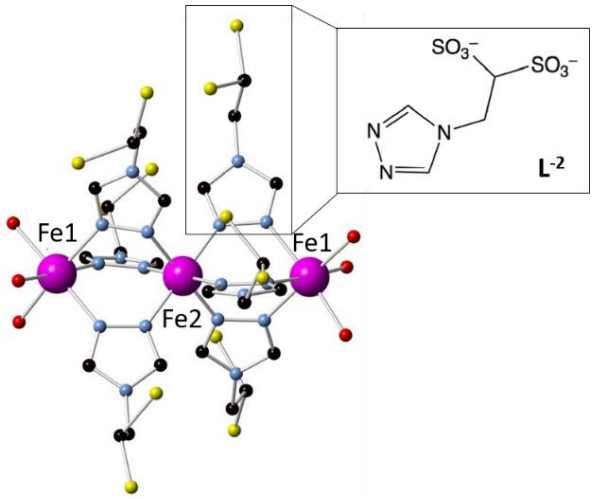

Figure 1.24. *Molecular structure of $[Fe_3(\mu\text{-}\mathbf{L})_6(H_2O)_6]^{6-}$ ($\mathbf{L}^{2-}$ = 4-(1,2,4-triazol-4-yl)ethanedisulfonate). Color code: Fe = purple; S = yellow; O = red; N = blue; C = black. H and Oxigen from the ligand are omitted for clarity.*

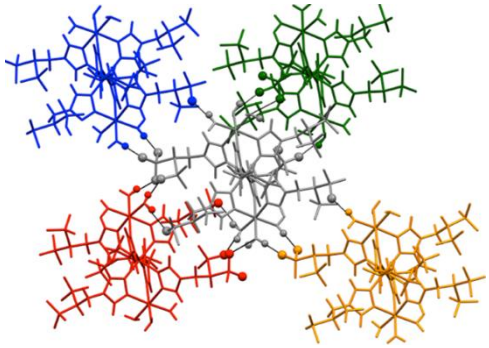

Figure 1.25. *H-bond interactions between $[Fe_3(\mu\text{-}\mathbf{L})_6(H_2O)_6]^{6-}$ trimers.*

The trimer remains in HS-LS-HS configuration at room temperature (Figure 1.26). Above 360 K, a partial spin transition starts with a 90 K-wide thermal hysteresis loop ($T_{1/2}(\uparrow)$ = 400 K, $T_{1/2}(\downarrow)$ = 310 K).

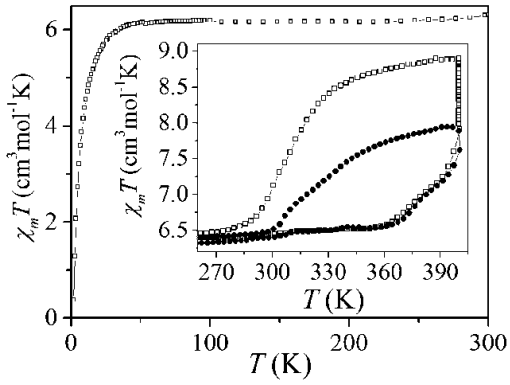

Figure 1.26. *Magnetic measurements for complex **1** in the 2–300 K range and in the 270–400 K range (inset). Scan rate ≈ 0.1 K min^{-1}.*

The thermal hysteresis of this complex changes remarkably with the temperature rate (Figure 1.27 left). The heating branch does not show notorious changes, whereas the cooling branch is very sensitive to scan rate, becoming significantly quenched at scan rates as slow as 5 K·min^{-1}. With faster cooling rate, 10 K min^{-1}, and the 57% of the complexes are trapped as HS-HS-HS configuration. Following the method defined by Letard et al, a characteristic T_{TIESST} = 250 K was determined (TIESST temperature-induced excited spin- state trapping), Figure 1.27 right. This is the highest temperature reported for a thermally quenched SCO system, even higher than the values displayed by Prussian blue analogues.[147]

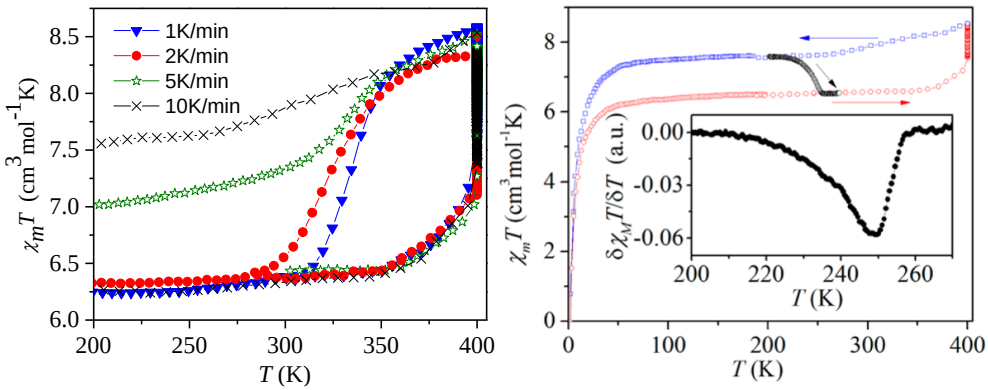

Figure 1.27. *(Left) Scan rate dependence of thermal hysteresis for the Fe^{II} trimer. (Right) heating up to 400 K and cooling down at 10 K min^{-1}, and warming up again at 0.3 K min^{-1}. Inset: δ(χmT)/δT vs T curve for the latter warming process.*

Spin transition kinetics of this complex[148] showed isothermal relaxation curves with exponential character,[147] typically associated to non-cooperative systems, Figure 1.28 left. The non-cooperative character of the relaxation process agrees with the weak intermolecular interactions in the crystal lattice and the gradual ST curve. Moreover, the relaxation process above T_{TIESST} becomes temperature independent, Figure 1.28 right. A high activation energy (E_a = 6370 ± 1442 cm^{-1}) was estimated.

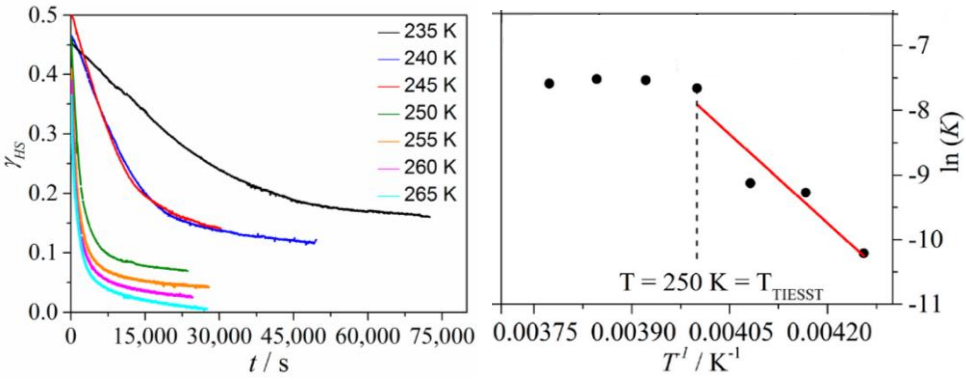

Figure 1.28. *(Left) Relaxation curves at different temperatures of the trapped HS fraction of* ***1****. (Right) Variation of equilibrium constant (K) as a function of T^{-1}.*

1.7. Implementation of SCO on devices

The fascinating physicochemical changes of SCO complexes have been explored in devices for photonic, mechanical or electronic applications.

As first step, numerous efforts have been done towards processing of SCO materials. As discussed before, SCO behavior depends on multiple parameters, including anions, solvent, intermolecular interactions, all of them tentative to be affected by processing. Nano-structuration, integration into composite functional networks or deposition/patterning onto surfaces have been studied, finding strong dependence of SCO properties in size-reduction, or molecule-surface interaction.[92] The strong size influence in the SCO properties is analyzed in section 1.7.1.

1.7.1. SCO phenomenon at the nanoscale. Size Reduction Effect.

A decrease in dimension typically leads to an inevitable change in the SCO phenomenon.[149] Indeed, the size reduction involves a reduction of domain size, decreasing cooperativity,[150] which directly impacts ST behavior.

A large variety of SCO nanomaterials such as nanoparticles, nanocomposites, continuous or nano-patterned thin films have been studied. The most common observations are: A) Shrinking in the thermal hysteresis loop upon size reduction. B) Downshift in transition temperatures, as a consequence of the HS stabilization. C) Incomplete spin transition curve with residual inactive fraction, predominantly HS fraction.

In 2008, J.A. Real et al.[151] and T. Mallah et al.[152] reported nanoparticles of the 3D SCO polymer, [Fe(pyrazine)$Pt(CN)_4$], where SCO behavior at the nanoscale significantly differs from bulk[153], Figure 1.29 left. Very small nanoparticles (< 14 nm) showed a significant downshift in transition temperatures, shrinking of hysteresis width, and incomplete spin transition. Below 7 nm, hysteresis loop disappears, Figure 1.29 right. When these nanoparticles are coated by silica, the differences in

comparison to bulk are less pronounced due to higher cooperativity provided by the rigid matrix.[154]

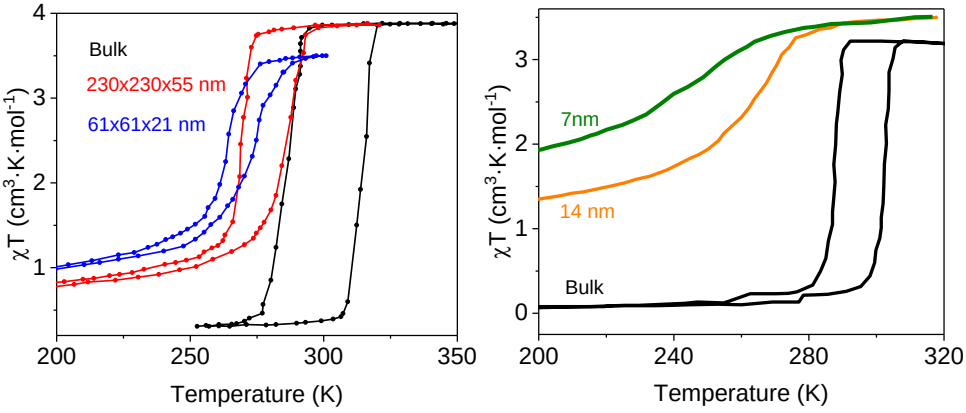

Figure 1.29. *Magnetic susceptibility measurements for [Fe(pyrazine)Pt(CN)$_4$] in bulk and different-sizes nanoparticles: (Left) average size of 230x230x55 nm and 61x 61x21 nm,*[151] *(Right) 14 nm and 7 nm-nanoparticles* [152]

Similar size reduction effects have been also observed for other SCO nanoparticles,[155-157] where hysteresis notoriously decreases below a critical minimum size, until disappearing.

SCO behavior remains at smaller sizes in the triazole 1D polymers series. For example, Coronado et al. reported a relatively large hysteresis in nanoparticles below 10 nm in [Fe(Htrz)$_2$(trz)](BF$_4$) [158,159], Figure 1.30. Upon size reduction, these NPs preserve memory effect even below 4 nm (24 K of hysteresis loop). This unexpected SCO behavior at the nanoscale is attributed to the high cooperativity and low dimensionality of this particular SCO polymer. Nanoparticles of this compound were introduced in porous silica matrix, obtaining ultra-small (≈3.2 ± 0.5 nm) nanoparticles with 65 K wide hysteresis above room temperature. The wider hysteresis in comparison with the previous cases is attributed to the role of rigid silica matrix.[103] Other examples of thermal hysteresis preserved at the nanoscale

were found in different materials [154,157,160,161], with the best results found in the 1,2,4-triazole-based triazole chains.

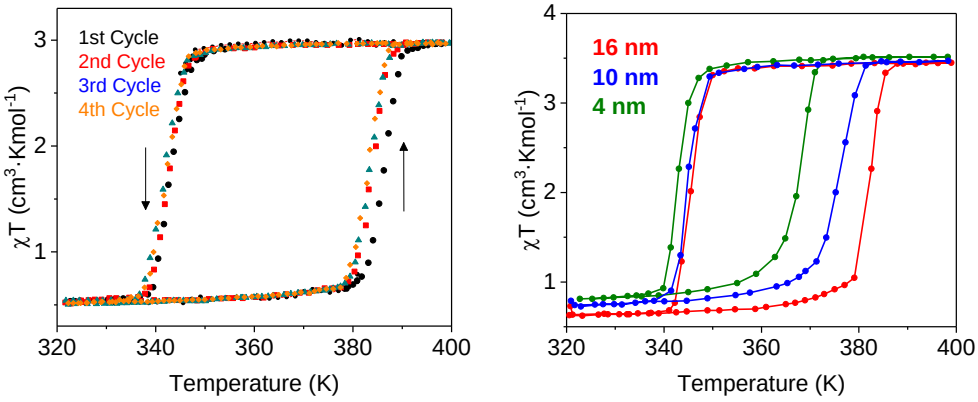

Figure 1.30. *Magnetic thermal hysteresis of [Fe(Htrz)$_2$(trz)](BF$_4$) nanoparticles. (Left) Successive thermal cycles for ≈15 nm NPs. (Right) Thermal cycles for nanoparticles of 16, 10 and 4 nm.*

Overall, the SCO behavior at the nanoscale is not easily predictable due to the large diversity observed. Indeed, other factors such as defects, particle shape, residual stresses, surface/interface effects or matrix effect can also interfere on SCO behavior.

1.7.2. Deposition of SCO materials onto surfaces

The fabrication of SCO-based devices often involves the deposition of the SCO materials onto surfaces, preferably as high-quality and homogeneous SCO film. A large number of film fabrication techniques such as Langmuir–Blodgett,[162,163] layer-by-layer assembly,[164] high-vacuum sublimation,[165–169] spin coating,[170] drop casting[171] or lithography techniques[172] have been successfully used to create mono/multi-layer and nanometer/micrometer thick films. Despite the difficulty to maintain the SCO properties at the nanoscale and to avoid undesirable surface effect on the SCO behavior, several thin films based on SCO materials can be found in the literature in which the ST is preserved.

For example, 3D-SCO coordination polymers, [Fe- (pyrazine){M(CN)4}] (M=Ni, Pd, or Pt) were successfully deposited onto a surface by layer-by-layer assembly (Figure 1.31 left). This multilayer thin films display thermally-induced SCO phenomenon as observed in the bulk material. The spin transition in the multilayers is less abrupt, but the thermal hysteresis is maintained around room temperature (Figure 1.31 right).[164]

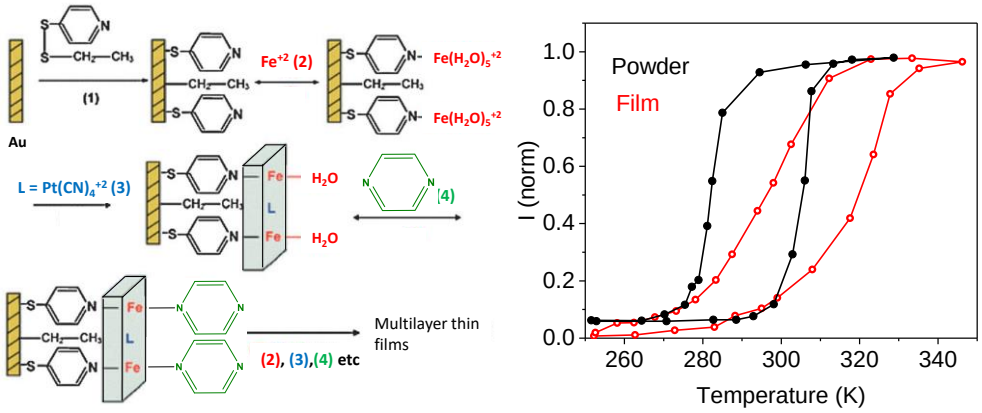

Figure 1.31. (Left) *Scheme of the assembly of [Fe(pyrazine){Pt(CN)$_4$}] multilayer. (Right) Normalized Raman intensity vs temperature plots for powder and film samples.*

Other interesting examples of ultrathin SCO films were fabricated by high-vacuum sublimation techniques with sub-monolayer control of the thickness and high purity. P. Rosa et. al. used neutral Fe(II) SCO complexes, Fe(H_2B(pz)$_2$)$_2$(bipy)], to form microcrystalline and smooth 300 nm-thick films[173], with similar features to bulk (Figure 1.32 left). Sub-monolayers of this complex maintain thermally and light-induced SCO behavior, with no bistability, Figure 1.32 right.[174]

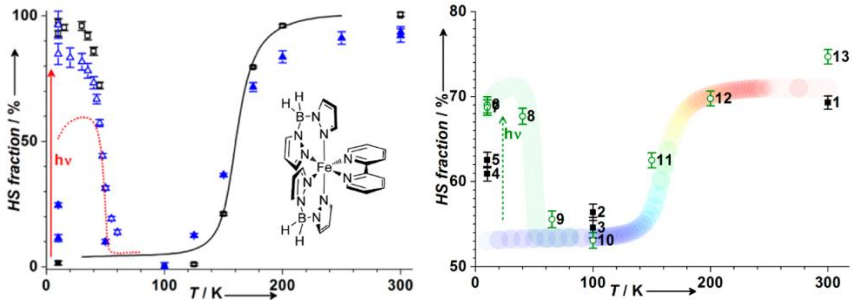

Figure 1.32. (Left) *HS fraction vs T plots for $Fe(H_2B(pz)_2)_2(bipy)]$ in bulk (black points) and the 300 nm thick film before and after illumination (full and empty blue triangles, respectively). (Right) HS fraction for the sub-monolayer of $Fe(H_2B(pz)_2)_2(bipy)]$ before and after irradiation.*[174]

Another remarkable example of a SCO sub-monolayer was published by K. Bairagi and coworkers.[175] The molecular complex, $[Fe^{II}((3, 5\text{-}(CH_3)_2Pz)_3BH)_2]$ Pz:1,4 – pyyrazolyl, were deposited on gold substrate under high-vacuum, forming molecular islands onto the surface. Their characterization was performed by Scanning Tunneling Microscopy (STM) and Scanning Tunneling Spectroscopy (STS) at 4.6 K. The blue light irradiation promotes the LS to HS switching of the molecules and the excited HS molecules relax back after 9 hours without irradiation (Figure 1.33 and Figure 1.34), studying the dynamics and the propagative effects of the spin transition at molecular level.

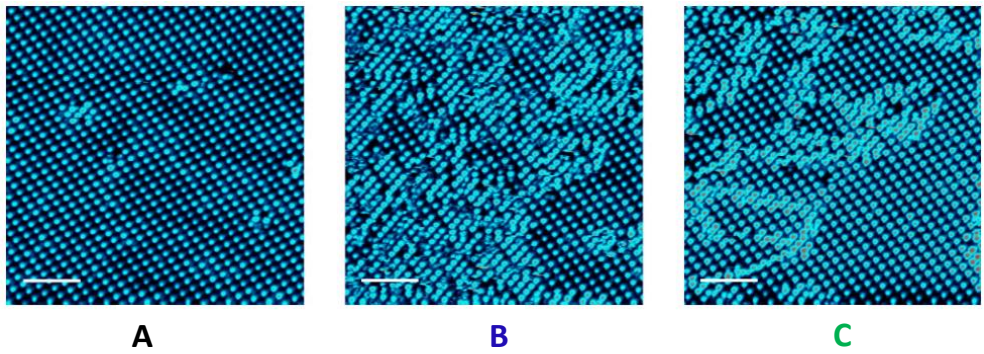

Figure 1.33. *STM images (scale bar 10 nm) for the sub-monolayer of $Fe(H_2B(pz)_2)_2(bipy)$]. (Left) The initial state of the isolated molecules. (Middle) After blue light irradiation during 9 hours and (Right) the relaxed molecules after 9 hours without laser exposure.*

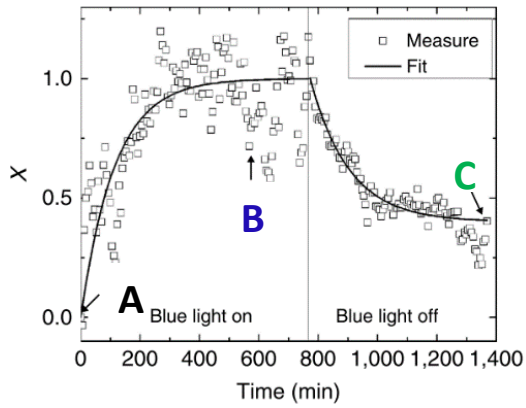

Figure 1.34. *Time evolution of the normalized intensity for sub-monolayer of $Fe(H_2B(pz)_2)_2(bipy)$] (open squares) and their corresponding fitting (full line). The arrows correspond with the STM images shown in Figure 1.33.*

1.8. THESIS OBJECTIVE AND OUTLINE

Molecular materials are a plausible alternative to overcome the miniaturization limitations in current technological materials. Data storage applications may exploit molecular compounds able to exhibit switchable magnetic/electronic properties. Particularly, spin crossover system are one of the most attractive magnetic switches given their very high working temperatures, being their implementation into devices one of the main scientific challenges in this research area.

The objective of this PhD project will be the synthesis, processing and characteriation of complexes with the dianionic ligand 4-(1,2,4-triazol-4-yl)ethanedisulfonate (L), focussing on the Fe^{II} complex, already known to display thermally-induced spin state with slow kinetics and large thermal hysteresis. Special emphasis will be devoted to to determine the effect of nanostructuration in the SCO of the $[Fe_3(\mu\text{-}\mathbf{L})_6(H_2O)_6]^{6-}$ polyanionic complex.

- In Chapter 2, we present the linear trimers $[NH_2Me_2]_6[M_3(\mu\text{-}\mathbf{L})_6(H_2O)_6]$ (M = Mn^{II}, Co^{II}, Ni^{II}, Fe^{II} and Cu^{II}), with the analyses of their magnetic properties.
- Chapter 3 includes the counter-cation influence on the crystal structure and SCO behavior of the polyanionic Fe^{II} trimer, $[Fe_3(\mu\text{-}\mathbf{L})_6(H_2O)_6]^{6-}$. The cesium derivative was obtained as single crystals as the $Cs_6[Fe_3(\mu\text{-}\mathbf{L})_6(H_2O)_6]$ salt, with distinct crystal structure and different SCO properties in comparison to dimethyl ammonium salt.
- Chapter 4 deals with dilution effects in the SCO properties of the , $[Fe_3(\mu\text{-}\mathbf{L})_6(H_2O)_6]^{6-}$ trimers. In the solid state with Zn^{II} dopant, but also in liquid solution. These dilution strategies reduce the cooperativity in the systems, down to the single molecule level. The perseverance of magnetic bistability in these non-cooperative systems opens unique opportunities to exploit this SCO-active molecules in molecular memories.

- In Chapter 5, the results obtained with the $[NH_2Me_2]_6[Fe_3(\mu\text{-}\mathbf{L})_6(H_2O)_6]$ salt s deposited onto silica and gold surfaces are highlighted. On the one hand, we achieved homogeneous film deposition on silica with controllable thickness, maintaining hysteretic SCO behavior at the nanoscale. On the other hand, a nanostructured sub-monolayer have been obtained on gold surface with potential perspectives for future applications.

In summary, in this thesis we explore the basic molecular magnetism though coordination chemistry with a dianionic triazole ligand, focusing on dimension and size-dependence for the spin crossover phenomena: bulk, molecular and onto surfaces.

1.9. References

1. Miller, J. S. Molecular Materials I. Molecular materials mimic inorganic network solids. *Adv. Mater.* **2**, 98–99 (2004).

2. Gatteschi, D. *Magnetic Molecular Materials | D. Gatteschi | Springer*.

3. Dey, P. Nath, T. K. Effect of grain size modulation on the magneto- and electronic-transport properties of La0.7 Ca0.3 Mn O3 nanoparticles: The role of spin-polarized tunneling at the enhanced grain surface. *Phys. Rev. B - Condens. Matter Mater. Phys.* **73**, 1–14 (2006).

4. Vassil Skumryev, Stoyan Stoyanov, Yong Zhang, George Hadjipanayis, Dominique Givord, J. N. Beating the superparamagnetic limit with exchange bias. *Nature* **423**, 19–22 (2003).

5. Vaz, C. A. F., Bland, J. A. C., Lauhoff, G. Magnetism in ultrathin film structures. *Reports Prog. Phys.* **71**, 056501 (2008).

6. De Ruiter, G., Van Der Boom, M. E. Sequential logic and random access memory (RAM): A molecular approach. *J. Mater. Chem.* **21**, 17575–17581 (2011).

7. Lindsey, J. S., Bocian, D. F. Molecules for Charge-Based Information Storage. **44**, 638–650 (2011).

8. Jean-Francois Lutz. Writing on Polymer Chains. *Acc. Chem. Res.* **46**, 2696–2705 (2013).

9. Natterer, F. D. Yang, K., Paul W., Willke P., Choi T., Greber T., Heinrich A. J., Lutz C. P. Reading and writing single-atom magnets. *Nature* **543**, 226–228 (2017).

10. Pilarczyk, K., Daly, B., Podborska, A., Kwolek, P., Silverson, V.A.D., de Silva, A. P., Szaciłowski, K. Coordination chemistry for information acquisition and processing. *Coord. Chem. Rev.* **325**, 135–160 (2016).

11. Raman, K. V., Kamerbeek, A. M., Mukherjee, A., Atodiresei, N., Sen, T. K., Lazić, P., Caciuc, V., Michel, R., Stalke, D., Mandal, S. K., Blügel, S., Münzenberg, M., Moodera, J. S. Interface-engineered templates for molecular spin memory devices. *Nature* **493**, 509–513 (2013).

12. Varghese, S., Elemans, J. A. A. W., Rowan, A. E., Nolte, R. J. M. Molecular computing: paths to chemical Turing machines. *Chem. Sci.* **6**, 6050–6058 (2015).

13. Castellano, M. Ruiz-García, R., Cano, J., Ferrando-Soria, J., Pardo, E., Fortea-Pérez, F. R., Stiriba, S. E., Barros, W. P., Stumpf, H. O., Cañadillas-Delgado, L., Pasán, J., Ruiz-Pérez, C., de Munno, G., Armentano, D., Journaux, Y., Lloret, F., Julve, M. Metallosupramolecular approach toward multifunctional magnetic devices for

molecular spintronics. *Coord. Chem. Rev.* **303**, 110–138 (2015).

14. Dunbar, K. R. Special issue on new horizons for magnetic solids based on molecules: From high-Tc magnets to nanomagnets to devices. *J. Solid State Chem.* **159**, 251–252 (2001).

15. Ma, L., Chen, C., Agnolet, G., Nie, J., Zhao, H., Dunbar, K. R. Electric transport properties of Mn12-acetate films measured with self-assembling tunnelling junction. *J. Phys. D. Appl. Phys.* **42**, (2009).

16. Wu, H., Chen, Y., Liu, Y. Reversibly Photoswitchable Supramolecular Assembly and Its Application as a Photoerasable Fluorescent Ink. *Adv. Mater.* **29**, (2017).

17. Gallardo, I., Guirado, G., Hernando, J., Morais, S., Prats, G. A multi-stimuli responsive switch as a fluorescent molecular analogue of transistors. *Chem. Sci.* **7**, 1819–1825 (2016).

18. Finniss, G. M., Canadell, E., Campana, C., Dunbar, K. R. Unprecedented Conversion of a Compound with Metal-Metal Bonding into a Solvated Molecular Wire. *Angew. Chem. Int. Ed. Engl.* **35**, 2771–2774 (1996).

19. Jurow, M., Schuckman, A. E., Batteas, J. D., Drain, C. M. Porphyrins as molecular electronic components of functional devices. *Coord. Chem. Rev.* **254**, 2297–2310 (2010).

20. Wang, X. Y., Avendaño, C., Dunbar, K. R. Molecular magnetic materials based on 4d and 5d transition metals. *Chem. Soc. Rev.* **40**, 3213–3238 (2011).

21. Ferrando-Soria, J. Vallejo, J., Castellano, M., Martínez-Lillo, J., Pardo, E., Cano, J., Castro, I., Lloret, F., Ruiz-García, R., Julve, M. Molecular magnetism, quo vadis? A historical perspective from a coordination chemist viewpoint. *Coord. Chem. Rev.* **339**, 17–103 (2017).

22. Pinkowicz, D., Southerland, H. I., Avendaño, C., Prosvirin, A., Sanders, C., Wernsdorfer, W., Pedersen, K. S., Dreiser, J., Clérac, R., Nehrkorn, J., Simeoni, G. G., Schnegg, A., Holldack, K., Dunbar, K. R.Cyanide Single-Molecule Magnets Exhibiting Solvent Dependent Reversible 'on' and 'off' Exchange Bias Behavior. *J. Am. Chem. Soc.* **137**, 14406–14422 (2015).

23. Wu, D. Q. Shao, D., Wei, X. Q., Shen, F. X., Shi, L., Kempe, D., Zhang, Y. Z., Dunbar, K. R., Wang, X. Y. Reversible On-Off Switching of a Single-Molecule Magnet via a Crystal-to-Crystal Chemical Transformation. *J. Am. Chem. Soc.* **139**, 11714–11717 (2017).

24. Galán-Mascarós, J. R. Coronado, E., Goddard, P.A., Singleton, J., Coldea, A. I., Wallis, J. D., Coles, S. J., Alberolá, A. A chiral ferromagnetic molecular metal. *J. Am. Chem.*

Soc. **132**, 9271–9273 (2010).

25. Phan, H., Benjamin, S. M., Steven, E., Brooks, J. S., Shatruk, M. Photomagnetic response in highly conductive iron(II) spin-crossover complexes with TCNQ radicals. *Angew. Chemie - Int. Ed.* **54**, 823–827 (2015).

26. E. Coronado, P. Delhaes, D. G., J. S. M. New Magntic Properties emerging from zero- and one-dimensional molecular materials. 289–307 (1996).

27. Ferlay, S., Mallah, T., Ouahes, R., Veillet, P., Verdaguer, M. Room Temperature Organometallic Magnet. *Nature* **378**, 701–703 (1995).

28. Hatlevik, Ø., Buschmann, W. E., Zhang, J., Manson, J. L., Miller, J. S. Enhancement of the magnetic ordering temperature and air stability of a mixed valent vanadium hexacyanochromate(III) magnet to 99°C (372 K). *Adv. Mater.* **11**, 914–918 (1999).

29. Qian, K. Huang, X. C., Zhou, C., You, X. Z., Wang, X.Y., Dunbar, K. R. A single-molecule magnet based on heptacyanomolybdate with the highest energy barrier for a cyanide compound. *J. Am. Chem. Soc.* **135**, 13302–13305 (2013).

30. Saber, M. R., Dunbar, K. R. Trigonal bipyramidal 5d-4f molecules with SMM behavior. *Chem. Commun.* **50**, 2177–2179 (2014).

31. Woods, T. J., Ballesteros-Rivas, M. F., Gómez-Coca, S., Ruiz, E., Dunbar, K. R. Relaxation Dynamics of Identical Trigonal Bipyramidal Cobalt Molecules with Different Local Symmetries and Packing Arrangements: Magnetostructural Correlations and ab inito Calculations. *J. Am. Chem. Soc.* **138**, 16407–16416 (2016).

32. Brown, A. J., Pinkowicz, D., Saber, M. R., Dunbar, K. R. A trigonal-pyramidal Erbium(III) single-molecule magnet. *Angew. Chemie - Int. Ed.* **54**, 5864–5868 (2015).

33. Fang, M. Zhao, H., Prosvirin, A. V., Pinkowicz, D., Zhao, B., Cheng, P., Wernsdorfer, W., Brechin, E. K., Dunbar, K. R. Squaring the cube: A family of octametallic lanthanide complexes including a Dy8 single-molecule magnet. *Dalt. Trans.* **42**, 14693–14701 (2013).

34. Aguilà, D., Prado, Y., Koumousi, E. S., Mathonière, C., Clérac, R. Switchable Fe/Co Prussian blue networks and molecular analogues. *Chem. Soc. Rev.* **45**, 203–224 (2016).

35. Liu, T. Zheng, H., Kang, S., Shiota, Y., Hayami, S., Mito, M., Sato, O., Yoshizawa, K., Kanegawa, S., Duan, C. A light-induced spin crossover actuated single-chain magnet. *Nat. Commun.* **4**, 1–7 (2013).

36. Ohkoshi, S. I., Imoto, K., Tsunobuchi, Y., Takano, S., Tokoro, H. Light-induced spin-crossover magnet. *Nat. Chem.* **3**, 564–569 (2011).

37. Mathonière, C., Lin, H. J., Siretanu, D., Clérac, R., Smith, J. M. Photoinduced single-molecule magnet properties in a four-coordinate iron(II) spin crossover complex. *J. Am. Chem. Soc.* **135**, 19083–19086 (2013).

38. Kahn, O. Molecular Magnetism. *Journal of Chemical Education* **72**, (2009).

39. Scheidt, W. R., Reed, C. A. Spin-State/Stereochemical Relationships in Iron Porphyrins: Implications for the Hemoproteins. *Chem. Rev.* **81**, 543–555 (1981).

40. Weiss, R., Gold, A., Terner, J. Cytochromes c‘: Biological Models for the S = 3/2, 5/2 Spin-State Admixture?. *Chem. Rev.* **106**, 2550–2579 (2006).

41. Womes, M., Jumas, J. C., Olivier-Fourcade, J., Aubertin, F., Gonser, U. High spin (5T2)-low spin (1A1) equilibrium of iron (II) in M2FeSn3S8 thiospinels (M = Cu, Ag). *Chem. Phys. Lett.* **201**, 555–558 (1993).

42. Farber, D. L. Antonangeli, D., Hoesch, M., Ryerson, F. J., Siebert, J., Aracne, C. M., Bosak, A., Fiquet, G., Krisch, M., Badro, *J.* Spin Crossover in Ferropericlase at High Pressure: A Seismologically Transparent Transition? *Science (6013).* **331**, 64–67 (2011).

43. Sason, S., Devesh, K., Samuël, P. de V., Ahmet, A., Walter, T. Theoretical Perspective on the Structure and Mechanism of Cytochrome P450 Enzymes. *Chemical Reviews* **105**, (2005).

44. Perutz, M. F., Fermi, G., Luisi, B., Shaanan, B., Liddington, R. C. Stereochemistry of Cooperative Mechanisms in Hemoglobin. *Acc. Chem. Res.* **20**, 309–321 (1987).

45. Cambi, L., Szegö, L. The magnetic susceptibility of complex compounds. *Berichte der Dtsch. Chem. Gesellschaft* **64**, 2591–2598 (1931).

46. Cambi, L., Szegö, L. The magnetic susceptibility of complex compounds (II Report). *Berichte der Dtsch. Chem. Gesellschaft* **66**, 656–661 (1933).

47. Coryell, C. D., Stitt, F., Pauling, L. The Magnetic Properties and Structure of Ferrihemoglobin (Methemoglobin) and Some of its Compounds. *J. Am. Chem. Soc.* **59**, 633–642 (1937).

48. L.E. Orgel. Quelques Problemes de Chimie Minerales. *10 Conf. Chim. Bruxelles* 289 (1956).

49. Baker, W. A., Bobonich, H. M. Magnetic Properties of Some High-Spin Complexes of Iron(II). *Inorg. Chem.* **3**, 1184–1188 (1964).

50. Konig, E., Madeja, K. T-A Equilibria in some iron (II)-bis (1,10-phenanthroline) complexes. *Inorg. Chem.* **6**, 48–55 (1965).

51. Goodwin, H. A. Spin Transitions in six-coordinate iron(II) complexes. *Coord. Chem.*

Rev. **18**, 293–325 (2002).

52. Weber, B., Jäger, E. G. Structure and magnetic properties of iron(II/III) complexes with N 2O22- coordinating schiff base like ligands. *Eur. J. Inorg. Chem.* 465–477 (2009).

53. Gütlich, P., Gaspar, A. B., Garcia, Y. Spin state switching in iron coordination compounds. *Beilstein J. Org. Chem.* **9**, 342–391 (2013).

54. Decurtins, S., Gütlich, P., Köhler, C. P., Spiering, H., Hauser, A. Light-induced excited spin state trapping in a transition-metal complex: The hexa-1-propyltetrazole-iron (II) tetrafluoroborate spin-crossover system. *Chem. Phys. Lett.* **105**, 1–4 (1984).

55. Hayami, S. Murata, K., Urakami, D., Kojima, Y., Akita, M., Inoue, K., Dynamic structural conversion in a spin-crossover cobalt(II) compound with long alkyl chains. *Chem. Commun.* 6510–6512 (2008).

56. Klaeui, W., Eberspach, W., Guetlich, P. Spin-crossover cobalt(III) complexes: steric and electronic control of spin state. *Inorg. Chem.* **26**, 3977–3982 (2005).

57. Halepoto, D. M. Holt, D., Larkworthy, L. F., Povey, D. C., Smith, G. W., Leigh, G. J. Spin crossover in chromium(II) complexes. *Polyhedron* **8**, 1821–1822 (1989).

58. Scheuermayer, S., Tuna, F., Bodensteiner, M., Scheer, M., Layfield, R. A. Spin crossover in phosphorus- and arsenic-bridged cyclopentadienyl- manganese(II) dimers. *Chem. Commun.* **48**, 8087–8089 (2012).

59. Morgan, G. G., Murnaghan, K. D., Müller-Bunz, H., McKee, V., Harding, C. J. A manganese(III) complex that exhibits spin crossover triggered by geometric tuning. *Angew. Chemie - Int. Ed.* **45**, 7192–7195 (2006).

60. Bethe, H. A. Splitting of terms in crystals. *Annals of Physics*. **3**, 133–206 (1929).

61. Vleck, J. H. Van. Theory of the Variations. *Phys. Rev.* **173**, 208–215 (1932).

62. Hauser, A. Ligand Field Theoretical Considerations. *Adv Polym Sci.* 49–58 (2004).

63. König, E. Some aspects of the chemistry of bis(2,2'-dipyridyl) and bis(1,10-phenanthroline) complexes of iron(II). *Coord. Chem. Rev.* **3**, 471–495 (2002).

64. Hauser, A. Intersystem crossing in the $[Fe(ptz)_6](BF_4)_2$ spin crossover system (ptz=1-propyltetrazole). *J. Chem. Phys.* **94**, 2741–2748 (1991).

65. Gutlich P., Hauser, A., Spiering, H. Thermal and Optical Switching of Iron (II) Complexes. *J. Chem. Eng. Japan* **33**, 2024–2054 (1994).

66. Real, J. A., Gaspar, A. B., Carmen Muñoz, M. Thermal, pressure and light switchable spin-crossover materials. *Dalt. Trans.* 2062–2079 (2005).

67. Evans, D. F. The Determination of the Pararnagnetic Susceptibility. *J. Chem. Soc.* 2003–2005 (1959).

68. Fultz B. Mössbauer Spectrometry. *Characterization of materials*. 1-20 (2012).

69. Guionneau, P., Marchivie, M., Bravic, G., Létard, J.-F., Chasseau, D. Structural Aspects of Spin Crossover. Example of the $[Fe^{II}Ln(NCS)_2]$ Complexes. *Top Curr Chem* **234**, 97–128 (2004).

70. Kusz, J., Gütlich, P., Spiering, H. Structural Investigations of Tetrazole Complexes of Iron (II) List of Abbreviations in Spin Crossover Research. *Top Curr Chem* 129–153 (2004).

71. König, E., Kulshreshtha, S. K., Ritter, G., Waigel, J., Goodwin, H. A. The discontinuous high-spin ($^5T_2$ ⇌ low-spin ($^1A_1$) transition in solid bis(1,10-phenanthroline-2-carbaldehyde phenylhydrazone)iron(ii) bis(tetrafluoroborate): Hysteresis effects, concurrent crystallographic phase change, entropy of the transition, and effect of pressure. *Inorg. Chem.* **23**, 1896–1902 (1984).

72. König, E. Nature and dynamics of the spin-state interconversion in metal complexes. *Struct. Bond.* **76**, 51–152 (1991).

73. Mcgarvey, J. J., Lawthers, I. Photochemically-induced Perturbation of the 1A-5T Equilibrium in FeII Complexes by Pulsed Laser Irradiation in the Metal-to-ligand Charnge-transfer Absorption Band. *J. Chem. Soc., Chem. Commun.* 906–907 (1982).

74. Decurtins, S., Gtitlich, P., Kohler, C. P., Spiering, H., Hauser, A. Light-Induced Excited Spin State Trapping in a transition-Meal Complex: the Hexa-1-Propyltetrazole-Iron (II) Tetrafluoroborate Spin-Crossover System. *Chem. Phys. Lett.* **105**, 1 (1984).

75. Gutlich, P., Decurtins, S., Hasselbach, K. M., Spiering, H., Hauser, A. Light-Induced Excited-Spin-State Trapping in Iron(II) Spin-Crossover Systems. Optical Spectroscopic and Magnetic Susceptibility Study. *Inorg. Chem.* **24**, 2174–2178 (1985).

76. Hauser, A. Reversibility of light-induced excited spin state trapping in the $Fe(ptz)_6(BF_4)_2$, and the $Zn_{1-x}Fe_x(ptz)_6(BF_4)_2$ spin-crossover systems. *Chem. Phys. Lett.* **124**, 543–548 (1986).

77. Varret, F., Boukheddaden, K., Codjovi, E., Enachescu, C., Linarès, J. On the Competition Between Relaxation and Photoexcitations in Spin Crossover Solids under Continuous Irradiation. *Top. Curr. Chem* 199–229 (2004).

78. Hauser, A. Light-Induced Spin Crossover and the High-Spin→Low-Spin Relaxation. *Top. Curr. Chem* 155–198 (2004).

79. Létard, J.F., Guionneau, P., Goux-Capes, L. Towards Spin Crossover Applications. *Top Curr Chem* **1**, 221–249 (2004).

80. Bonhommeau, S. Molnár, G., Galet, A., Zwick, A., Real, J.A., McGarvey, J. J., Bousseksou, A. One shot laser pulse induced reversible spin transition in the spin-crossover complex [Fe($C_4H_4N_2$){Pt(CN)$_4$}] at room temperature. *Angew. Chemie - Int. Ed.* **44**, 4069–4073 (2005).

81. Cobo, S. Ostrovskii, D., Bonhommeau, S, Vendlier, L., Molnár, G., Salmon, L., Tanaka, K., Bousseksou*, A.* Spin Transition at Room Temperature in Single Crystals of Fe^{II} (pyrazine)(Pt(CN)$_4$). *J. Am. Chem. Soc.* **130**, 9019–9024 (2008).

82. Fouché, O. Degert, J., Jonusauskas, G., Daro, N., Létard, J. F. & Freysz, E. Mechanism for optical switching of the spin crossover [Fe(NH_2-trz)$_3$]$(Br)_2$·3H_2O compound at room temperature. *Phys. Chem. Chem. Phys.* **12**, 3044–3052 (2010).

83. Venkataramani, S. Jana, U., Dommaschk, M., Sönnichsen, F. D., Tuczek, F., Herges, R. Magnetic Bistability of Molecules. Science. **331**, 445–449 (2011).

84. Heitmann, G., Schütt, C., Herges, R. Spin State Switching in Solution with an Azoimidazole-Functionalized Nickel(II)-Porphyrin. *European J. Org. Chem.* **2016**, 3817–3823 (2016).

85. Estrader, M. Salinas Uber, J., Barrios, L.A., Garcia, J., Lloyd-Williams, P., Roubeau, O., Teat, S. J., Aromí, G. A Magneto-optical Molecular Device: Interplay of Spin Crossover, Luminescence, Photomagnetism, and Photochromism. *Angew. Chemie - Int. Ed.* **56**, 15622–15627 (2017).

86. Nihei, M., Suzuki, Y., Kimura, N., Kera, Y., Oshio, H. Bidirectional photomagnetic conversions in a spin-crossover complex with a diarylethene moiety. *Chem. - A Eur. J.* **19**, 6946–6949 (2013).

87. Takahashi, K. Hasegawa, Y., Sakamoto, R., Nishikawa, M., Kume, S., Nishibori, E., Nishihara, H. Solid-state ligand-driven light-induced spin change at ambient temperatures in bis(dipyrazolylstyrylpyridine)iron(II) complexes. *Inorg. Chem.* **51**, 5188–5198 (2012).

88. Ewald, A. H., Martin, R. L., Sinn, E., White, A. H. Electronic Equilibrium between the 6Ai and 2T2 States in Iron(III) Dithio Chelates. *Inorg. Chem.* **8**, 1837–1846 (1969).

89. Jeftić, J., Hauser, A. Pressure study of the thermal spin transition and the high-spin → low-spin relaxation in the R3 and P1 crystallographic phases of [$Zn_{1-x}Fe_x$(ptz)$_6$]$(BF_4)_2$ single crystals (x = 0.1, 0.32, and 1; ptz = 1-n-propyltetrazole). *J. Phys. Chem. B* **101**, 10262–10270 (1997).

90. Schenker, S., Hauser, A., Wang, W., Chan, I. Y. Matrix effects on the high-spin → low-spin relaxation in [M_{1-x}Fex(bpy)$_3$]$(PF_6)_2$ (M = Cd, Mn and Zn, bpy = 2,2'-bipyridine). *Chem. Phys. Lett.* **297**, 281–286 (1998).

91. Drickamer, H. G. Electronic transformations in transition metal compounds at high pressure. *Angew. Chemie* **86**, 61–70 (1974).

92. Bouseksou, A., Molnár, G., Matouzenko, G. Switching of molecular spin states in inorganic complexes by temperature, pressure, magnetic field and light: Towards molecular devices. *Eur. J. Inorg. Chem.* 4353–4369 (2004).

93. Garcia, Y., Ksenofontov, V., Gütlich, P. Spin transition molecular materials: New sensors. *Hyperfine Interact.* **139**–**140**, 543–551 (2002).

94. Mun, M. C. Le, S., Salmon, L., Tuchagues, J., Bousseksou, A., Real, J.A. Mass Effect on the Equienergetic High-Spin/Low-Spin States of Spin-Crossover in 4,4'-Bipyridine-Bridged Iron(II) Polymeric Compounds: Synthesis, Structure, and Magnetic, Mössbauer, and Theoretical Studies. *Inorg. Chem.* **41**, 6997–7005 (2002).

95. Kulshreshtha, S. K., Iyer, R. M., König, E., Ritter, G. The nature of spin-state transitions in Fe(II) complexes. *Chem. Phys. Lett.* **110**, 201–204 (1984).

96. Slichter, C. P., Drickamer, H. G. Pressure-Induced Electronic Changes in Compounds of Iron. *J. Chem. Phys.* **56**, 2142–2160 (1972).

97. Gütlich, P., Garcia, Y., Goodwin, H. A. Spin crossover phenomena in Fe(II) complexes. *Chem. Soc. Rev.* **29**, 419–427 (2000).

98. Romstedt, H., Hauser, A., Spiering, H. High-spin → low-spin relaxation in the two-step spincrossover compound $[Fe(pic)_3]Cl_2EtOH$ (pic = 2-picolylamine). *J. Phys. Chem. Solids* **59**, 265–275 (1998).

99. Piñeiro-López, L. Valverde-Muñoz, F. J., Seredyuk, M., Muñoz, M. Ca., Haukka, M., Real, J. A.. Guest Induced Strong Cooperative One- and Two-Step Spin Transitions in Highly Porous Iron(II) Hofmann-Type Metal-Organic Frameworks. *Inorg. Chem.* **56**, 7038–7047 (2017).

100. Sams, J. R., Scott, J. C., Tsin, T. B. Tris [2-(2'-pyridyl)benzimidazole]iron(II) complexes. Some new examples of $^5T_2$ - $^1A_1$ spin equilibria. *Chem. Phys. Lett.* **18**, 451–453 (1973).

101. Weber, B., Bauer, W. & Obel, J. An iron(II) spin-crossover complex with a 70 K wide thermal hysteresis loop. *Angew. Chemie - Int. Ed.* **47**, 10098–10101 (2008).

102. Weber, B., Kaps, E. S., Obel, J., Achterhold, K., Parak, F. G. Synthesis and characterization of a dinuclear iron(II) spin crossover complex with wide hysteresis. *Inorg. Chem.* **47**, 10779–10787 (2008).

103. Durand, P. Pillet, S., Bendeif, E., Carteret, C., Bouazaoui, M., Hamzaoui, H., Capoen, B., Salmon, Li., Hébert, S., Ghanbaja, J., Aranda, L., Schaniel, D. Room temperature bistability with wide thermal hysteresis in a spin crossover silica nanocomposite. *J. Mater. Chem. C.* **1**, 1933–1942 (2013).

104. Lochenie, C. Bauer, W., Railliet, A.P., Schlamp, S., Garcia, Y., Weber, B. Large Thermal Hysteresis for Iron (II) Spin Crossover Complexes with N-(Pyrid-4-yl)isonicotinamide. *Inorg. Chem.* **53**, 11563-11572 (2014).

105. Brooker, S. Spin crossover with thermal hysteresis: Practicalities and lessons learnt. *Chem. Soc. Rev.* **44**, 2880–2892 (2015).

106. Ganguli, P., Gütlich, P., Müller, E. W. Effect of Metal Dilution on the Spin-Crossover Behavior in $[Fe_xM_{1-x}(phen)_2(NCS)_2]$ (M = Mn, Co, Ni, Zn). *Inorg. Chem.* **21**, 3429–3433 (1982).

107. Hauser, A., Gutlich, P., Spiering, H. High-Spin → Low-Spin Relaxation Kinetics and Cooperative Effects in the $[Fe(ptz)_6](BF_4)_2$ and $[Zn_{1-x}Fe_x(ptz)_6](BF_4)_2$ (ptz=1-Propyltetrazole) Spin-Crossover Systems. *Inorg. Chem.* **25**, 4245–4248 (1986).

108. Martin, J. P., Zarembowitch, J., Dworkin, A., Haasnoot, J. G., Codjovi, E. Solid-State Effects in Spin Transitions: Influence of Iron(II) Dilution on the Magnetic and Calorimetric Properties of the Series $[Fe_xNi_{1-X}(4,4'\text{-bis}(1,2,4\text{-triazole}))_2(NCS)_2]\cdot H_2O$. *Inorg. Chem.* **33**, 2617–2623 (1994).

109. Paradis, N., Chastanet, G., Létard, J. F. When stable and metastable HS states meet in spin-crossover compounds. *Eur. J. Inorg. Chem.* **2012**, 3618–3624 (2012).

110. Chakraborty, P., Bronisz, R., Hauser, A., Krivokapic, I., Enachescu, C. Low-Spin→High-Spin Relaxation Dynamics in the Highly Diluted Spin-Crossover System $[Fe_xZn_{1-x}(bbtr)_3](ClO_4)_2$. *Inorg. Chem.* **50**, 1856–1861 (2011).

111. Paradis, N., Chastanet, G., Varret, F., Létard, J. F. Metal dilution of cooperative spin-crossover compounds: When stable and metastable high-spin states meet. *Eur. J. Inorg. Chem.* **2013**, 968–974 (2013).

112. Haasnoot, J. G. Martin J. P., Zarembowitch J., Bousseksou A., Dworkin A., Haasnoot J. G., Varret F.. Solid State Effects on Spin Transitions: Magnetic, Calorimetric, and Mossbauer-Effect Properties of $[Fe_xCo_{1-x}(4,4'\text{-bis-}1,2,4\text{-triazole})_2(NCS)_2]$.cntdot.$H_2O$ Mixed-Crystal Compounds. *Inorg. Chem.* **33**, 6325–6333 (1994).

113. Renovitch, A.G., Baker, W.A. Spin Equilibrium in Tris(2-aminomethylpyridine)iron(II) halides. *J. Am. Chem. Soc.* **89**, 6377–6378 (1967).

114. Köppen, H. Müller, E.W., Köhler, C.P., Spiering, H., Meissner, E., Gütlich, P. Unusual spin-transition anomaly in the crossover system $[Fe\ (2\text{-pic})_3]Cl_2\cdot EtOH$. *Chem. Phys. Lett.* **91**, 348–352 (1982).

115. Wiehl, L., Kiel, G., Köhler, C. P., Spiering, H., Gütlich, P. Structure Determination and Investigation of the High-Spin Low-Spin Transition of [Fe(2-pic),]Br2.EtOH. *Inorg. Chem.* **25**, 1565–1571 (1986).

116. Dîrtu, M. M. Rotaru, A., Gillard, D., Linares, J., Codjovi, E., Tinant, B., Garcia, Y. Prediction of the spin transition temperature in FeII one-dimensional coordination polymers: An anion based database. *Inorg. Chem.* **48**, 7838–7852 (2009).

117. Sorai, M., Ensling, J., Hasselbach, K. M., Gütlich, P. Mössbauer effect study on low-spin $^1A_1 \rightleftharpoons$ high spin $^5T_2$ transition in $[Fe(2\text{-pic})_3]Cl_2$. *Chem. Phys.* **20**, 197–208 (1977).

118. Real, J. A., Muñoz, M. C., Andrés, E., Granier, T., Gallois, B. Spin-Crossover Behavior in the $Fe(Tap)_2(NCS)_2 \cdot nCH_3CN$ System (tap=1,4,5,8-Tetraazaphenanthrene; n=1,1/2).Crystal Structures and Magnetic Properties of Booth Solvates. *Inorg. Chem.* **33**, 3587–3594 (1994).

119. Nihei, M., Han, L., Oshio, H. Magnetic bistability and single-crystal-to-single-crystal transformation induced by guest desorption. *J. Am. Chem. Soc.* **129**, 5312–5313 (2007).

120. Hostettler, M., Törnroos, K. W., Chernyshov, D., Vangdal, B., Bürgi, H. B. Challenges in engineering spin crossover: Structures and magnetic properties of six alcohol solvates of iron(II) tris(2-picolylamine) dichloride. *Angew. Chemie - Int. Ed.* **43**, 4589–4594 (2004).

121. Halder, G. J., Kepert, C. J., Moubaraki, B., Murray, K. S., Cashion, J. D. Guest-dependent spin crossover in a nanoporous molecular framework material. *Science.* **298**, 1762–1765 (2002).

122. König, E., Madeja, K. Unusual magnetic behaviour of some iron(II)-bis-(1,10-phenanthroline) complexes. *Chem. Commun.* 61–62 (1966).

123. Gütlich, P. Fifty years of Mössbauer spectroscopy in solid state research - Remarkable achievements, future perspectives. *Journal of Inorganic and General Chemistry* **638**, 15–43 (2012).

124. Halcrow, M. A. The foundation of modern spin-crossover. *Chem. Commun.* **49**, 10890–10892 (2013).

125. Goodwin, H. A., Sylva, R. N. The Magnetic Properties of the Tris(2-Methyl-1, 10-Phenanthroline)Iron(II) Ion. *Aust. J. Chem.* **21**, 83–90 (1968).

126. Fleisch, J., Gutlich, P., Hasselbach, K. M., Muller, W. High spin-low spin transition in substituted phenanthroline complexes of Iron (II). *J. Phys. I* 659–662 (1974).

127. Fleisch, J., Gütlich, P., Hasselbach, K. M. Mössbauer effect study of the electronic ground state of iron(II)in tris(2-chlorophenanthroline)iron(II) perchlorate. *Inorganica Chim. Acta.* **17**, 51–54 (1976).

128. Fleisch, J., Gütlich, P., Hasselbach, K. M. Thermally Induced Spin Transition in Tris(2-methoxy-1,10-phenanthroline) iron(II) Perchlorate. Variable-Temperature

Mössbauer, Magnetic Susceptibility, and Far-Infrared Measurements. *Inorg. Chem.* **16**, 1979–1984 (1977).

129. Fallis, A. ^{57}Fe Mossbauer effect and magnetism down to 0.98K in the high-spin ($^5T_2$) to or from low- spin ($^1A_1$) system dithiocyanato bis(4-methyl-1, 10-phenanthroline) iron (II). *J. Phys. C Solid State Phys* **10**, 603–615 (1977).

130. König, E., Ritter, G., Irler, W. Consistent changes of X-Ray peak profiles and Mossbauer area fractions associated with hysteresis of the spin state transition. *Chem. Phys. Lett.* **66**, 336–339 (1979).

131. Kahn, O., Codjovi, E. Iron(II)-1,2,4-triazole spin transition molecular materials. *Philos. Trans. R. Soc. A Math. Phys. Eng. Sci.* **354**, 359–379 (1996).

132. Hogue, R. W., Singh, S., Brooker, S. Spin crossover in discrete polynuclear iron(ii) complexes. *Chem. Soc. Rev.* **47**, 7303–7338 (2018).

133. Haasnoot, J. G. 1,2,4-Triazoles as Ligands for Iron(II) High Spin ↔ Low Spin Crossovers. *Magn. A Supramol. Funct.* 299–321 (1996).

134. Roubeau, O. Triazole-based one-dimensional spin-crossover coordination polymers. *Chem. - A Eur. J.* **18**, 15230–15244 (2012).

135. Kahn, O., Kröber, J., Jay, C. Spin Transition Molecular Materials for displays and data recording. *Adv. Mater.* **4**, 718–728 (1992).

136. Kröber, J., Codjovi, E., Kahn, O., Grolière, F., Jay, C. A Spin Transition System with a Thermal Hysteresis at Room Temperature. *J. Am. Chem. Soc.* **115**, 9810–9811 (1993).

137. Kahn, O., Martinez, C. J. Spin-Transition Polymers: From Molecular Materials Toward Memory Devices. *Science.* **279**, 44–48 (1998).

138. Kröber, J., Audiere, J.-P., Claude, R., Codjovi, E., Kahn, O. Spin Transitions and Thermal Hystereses in the. *Chem. Mater.* **2**, 1404–1412 (1994).

139. Sugiyarto, K. H., Goodwina, H. A. Cooperative Spin Transitions in Iron (II) Derivatives of 1 , 2 , 4-Triazole. 263–277 (1994).

140. Grosjean, A. Daro, N., Kauffmann, B., Kaiba, A., Létard, J. F., Guionneau, P. The 1-D polymeric structure of the $[Fe(NH_2trz)_3](NO_3)_2{\cdot}nH_2O$ (with n=2) spin crossover compound proven by single crystal investigations. *Chem. Commun.* **47**, 12382–12384 (2011).

141. Vos, G., Fdbre, R. A., Graaff, R. A. G. De, Haasnoot, J. G., Reedijk, J. Unique High Spin Transition of the Central Ion in a Linear, Trinuclear Iron (II) Triazalo Compound. *Am. Chem. Soc.* **105**, 1682–1683 (1983).

142. Garcia, Y. Guionneau, P., Bravic, G., Chasseau, D., Howard, J.A.K., Kahn, O.,

Ksenofontov, V., Reiman, S., Gütlich, P. Synthesis, crystal structure, magnetic properties and 57Fe Mossbauer spectroscopy of the new trinuclear $[Fe_3$(4-(2'-hydroxyethyl)-1,2,4-triazole$)_6(H_2O)_6](CF_3SO_3)_6$ spin crossover. *Eur. J. Inorg. Chem.* **3**, 0–7 (2000).

143. Kolnaar, J. J. A. van Dijk, G., Kooijman, H., Spek, A. L., Ksenofontov, V. G., Gütlich, P., Haasnoot, J. G., Reedijk, J. Synthesis, Structure, Magnetic Behavior, and Mössbauer Spectroscopy of Two New Iron(II) Spin-Transition Compounds with the Ligand 4-Isopropyl-1,2,4-triazole. X-ray Structure of $[Fe_3$(4-isopropyl-1,2,4-triazole$)_6(H_2O)_6]$(tosylate) $_6 \cdot 2H_2O$. *Inorg. Chem.* **36**, 2433–2440 (2002).

144. Pittala, N. Thétiot, F., Charles, C., Triki, S., Boukheddaden, K., Chastanet, G., Marchivie, M. An unprecedented trinuclear FeII triazole-based complex exhibiting a concerted and complete sharp spin transition above room temperature. *Chem. Commun.* **53**, 8356–8359 (2017).

145. Gómez, V., Benet-Buchholz, J., Martin, E., Galán-Mascarós, J. R. Hysteretic spin crossover above room temperature and magnetic coupling in trinuclear transition-metal complexes with anionic 1,2,4-triazole ligands. *Chem. - A Eur. J.* **20**, 5369–5379 (2014).

146. Gómez, V., Sáenz De Pipaón, C., Maldonado-Illescas P. Waerenborgh, J. C., Martin, E., Benet-Buchholz, J., Galán-Mascarós, J. R. Easy Excited-State Trapping and Record High TTIESST in a Spin-Crossover Polyanionic Fe^{II} Trimer. *J. Am. Chem. Soc.* **137**, 11924–11927 (2015).

147. Carbonera, C., Dei, A., Sangregorio, C., Létard, J. F. Optically switchable behaviour of a dioxolene adduct of a cobalt-macrocycle complex. *Chem. Phys. Lett.* **396**, 198–201 (2004).

148. Sáenz de Pipaón, C., Maldonado-Illescas, P., Gómez, V., Galán-Mascarós, J. Spin Transition Kinetics in the Salt $[H_2N(CH_3)_2]_6[Fe_3(L)_6(H_2O)_6]$ (L = 4-(1,2,4-triazol-4-yl)ethanedisulfonate). *Magnetochemistry* **2**, 20 (2016).

149. Kawamoto, T., Abe, S. Thermal hysteresis loop of the spin-state in nanoparticles of transition metal complexes: Monte Carlo simulations on an Ising-like model. *Chem. Commun.* **1**, 3933–3935 (2005).

150. Molnár, G., Rat, S., Salmon, L., Nicolazzi, W., Bousseksou, A. Spin Crossover Nanomaterials: From Fundamental Concepts to Devices. *Adv. Mater.* **30**, 1–23 (2018).

151. Boldog, I. Gaspar, A. B., Martínez, V., Pardo-Ibañez, P., Ksenofontov, V., Bhattacharjee, A., Gütlich, P., Real, J. A. Spin-crossover nanocrystals with magnetic, optical, and structural bistability near room temperature. *Angew. Chemie - Int. Ed.*

47, 6433–6437 (2008).

152. Volatron, F. Catala, L., Rivière, E., Gloter, Al., Stéphan, O., Mallah, T. Spin-crossover coordination nanoparticles. *Inorg. Chem.* **47**, 6584–6586 (2008).

153. Niel, V., Martinez-Agudo, J. M., Muñoz, M. C., Gaspar, A. B., Real, J. A. Cooperative spin crossover behavior in cyanide-bridged Fe(II)-M(II) bimetallic 3D Hofmann-like networks (M = Ni, Pd, and Pt). *Inorg. Chem.* **40**, 3838–3839 (2001).

154. Raza, Y. Volatron, F., Moldovan, S., Ersen, O., Huc, V., Martini, C., Brisset, F., Gloter, A., Stéphan, O., Bousseksou, A., Catala, L., Mallah, T. Matrix-dependent cooperativity in spin crossover Fe(pyrazine)$Pt(CN)_4$ nanoparticles. *Chem. Commun.* **47**, 11501–11503 (2011).

155. Forestier, T. Kaiba, A., Pechev, S., Denux, D., Guionneau, P., Etrillard, C., Daro, N., Freysz, E., Létard, J. F. Nanoparticles of $[FeNH_2\text{-}trz_3]Br_2\text{-}3H_2O$ (NH_2-trz=2-Amino-l,2,4-triazole) prepared by the reverse micelle technique: Influence of particle and coherent domain sizeson spin-crossover properties. *Chem. - A Eur. J.* **15**, 6122–6130 (2009).

156. Martínez, V. Boldog, I., Gaspar, A. B., Ksenofontov, V., Bhattacharjee, A., Gütlich, P., Real, J. A. Spin crossover phenomenon in nanocrystals and nanoparticles of $[Fe(3\text{-}py)_2M(CN)_4]$ (M^{II}=Ni, Pd, Pt) two-dimensional coordination polymers. *Chem. Mater.* **22**, 4271–4281 (2010).

157. Peng, H. Tricard, S., Félix, G., Molnár, G., Nicolazzi, W., Salmon, L., Bousseksou, A.. Re-appearance of cooperativity in ultra-small spin-crossover $[Fe(pz)\{Ni(CN)_4\}]$ nanoparticles. *Angew. Chemie - Int. Ed.* **53**, 10894–10898 (2014).

158. Coronado, E., Galán-Mascarós, J. R., Monrabal-Capilla, M., García-Martínez, J., Pardo-Ibáñez, P. Bistable spin-crossover nanoparticles showing magnetic thermal hysteresis near room temperature. *Adv. Mater.* **19**, 1359–1361 (2007).

159. Giménez-Marqués, M., García-Sanz De Larrea, M. L., Coronado, E. Unravelling the chemical design of spin-crossover nanoparticles based on iron(II)-triazole coordination polymers: Towards a control of the spin transition. *J. Mater. Chem. C* **3**, 7946–7953 (2015).

160. Galán-Mascarós, J. R. Coronado, E., Forment-Aliaga, A., Monrabal-Capilla, M., Pinilla, Cienfuegos, E., Ceolin, M. Tuning size and thermal hysteresis in bistable spin crossover nanoparticles. *Inorg. Chem.* **49**, 5706–5714 (2010).

161. Prins, F., Monrabal-Capilla, M., Osorio, E. A., Coronado, E., Van Der Zant, H. S. J. Room-temperature electrical addressing of a bistable spin-crossover molecular system. *Adv. Mater.* **23**, 1545–1549 (2011).

162. Bodenthin, Y., Pietsch, U., Möhwald, H., Kurth, D. G. Inducing spin crossover in metallo-supramolecular polyelectrolytes through an amphiphilic phase transition. *J. Am. Chem. Soc.* **127**, 3110–3114 (2005).

163. Ruaudel-Teixier, A., Barraud, A., Coronel, P., Kahn, O. Spin transition in a magnetic Langmuir-Blodgett film. *Thin Solid Films* **160**, 107–115 (1988).

164. Cobo, S., Molnár, G., Real, J. A., Bousseksou, A. Multilayer sequential assembly of thin films that display room-temperature spin crossover with hysteresis. *Angew. Chemie - Int. Ed.* **45**, 5786–5789 (2006).

165. Shi, S. Schmerber, G., Arabski, J., Beaufrand, J. B., Kim, D. J., Boukari, S., Bowen, Kemp, N. T. Viart, N., Rogez, G., Beaurepaire, E., Aubriet, H., Petersen, J., Becker, C. , Ruch, D. Study of molecular spin-crossover complex $Fe(phen)_2(NCS)_2$ thin films. *Appl. Phys. Lett.* **95**, 2–5 (2009).

166. Gopakumar, T. G. Matino, F., Naggert, H., Bannwarth, A., Tuczek, F., Berndt, R. Electron-induced spin crossover of single molecules in a bilayer on gold. *Angew. Chemie - Int. Ed.* **51**, 6262–6266 (2012).

167. Miyamachi, T. Gruber, M., Davesne, V., Bowen, M., Boukari, S., Joly, L., Scheurer, F., Rogez, G., Yamada, T. K., Ohresser, P., Beaurepaire, E., Wulfhekel, W. Robust spin crossover and memristance across a single molecule. *Nat. Commun.* **3**, 936–938 (2012).

168. Shalabaeva, V. Rat, S., Manrique-Juarez, M. D., Bas, A.C., Vendier, L., Salmon, L., Molnár, G., Bousseksou, A. Vacuum deposition of high-quality thin films displaying spin transition near room temperature. *J. Mater. Chem. C* **5**, 4419–4425 (2017).

169. Ossinger, S. Naggert, H.M Kipgen, L., Jasper-Toennies, T., Rai, A., Rudnik, J., Nickel, F., Arruda, L. M., Bernien, M., Kuch, W., Berndt, R. Tuczek, F. Vacuum-Evaporable Spin-Crossover Complexes in Direct Contact with a Solid Surface: Bismuth versus Gold. *J. Phys. Chem. C* **121**, 1210–1219 (2017).

170. Matsuda, M., Tajima, H. Thin film of a spin crossover complex [Fe(dpp)2](BF4)2. *Chem. Lett.* **36**, 700–701 (2007).

171. Galyametdinov, Y. Ksenofontov, V., Prosvirin, A., Ovchinnikov, I., Ivanova, G., Gütlich, P., Haase, W. First example of coexistence of thermal spin transition and liquid-crystal properties. *Angew. Chemie - Int. Ed.* **40**, 4269–4271 (2001).

172. Akou, A. Bartual-Murgui, C., Abdul-Kader, K., Lopes, M., Molnár, G., Thibault, C., Vieu, C., Salmon, L., Bousseksou, *A.* Photonic gratings of the metal-organic framework $\{Fe(bpac)[Pt(CN)_4]\}$ with synergetic spin transition and host-guest properties. *Dalt. Trans.* **42**, 16021–16028 (2013).

173. Palamarciuc, T. Oberg, J. C., El Hallak, F., Hirjibehedin, C. F., Serri, M., Heutz, S., Létard, J. F., Rosa, P. Spin crossover materials evaporated under clean high vacuum and ultra-high vacuum conditions: From thin films to single molecules. *J. Mater. Chem.* **22**, 9690–9695 (2012).

174. Warner, B. Oberg, J. C., Gill, T. G., Hallak, F., Hirjibehedin, C. F., Serri, M., Heutz, S., Arrio, M. A., Sainctavit, P., Mannini, M., Poneti, G., Sessoli, R., Rosa, P. Temperature- and light-induced spin crossover observed by X-ray spectroscopy on isolated Fe(II) complexes on gold. *J. Phys. Chem. Lett.* **4**, 1546–1552 (2013).

175. Bairagi, K. Iasco, O., Bellec, A., Kartsev, A., Li, D., Lagoute, J., Chacon, C., Girard, Y., Rousset, S., Miserque, F., Dappe, Y.J., Smogunov, A., Barreteau, C., Boillot, M. L., Mallah, T., Repain, V. Molecular-scale dynamics of light-induced spin cross-over in a two-dimensional layer. *Nat. Commun.* **7**, 1–7 (2016).

UNIVERSITAT ROVIRA I VIRGILI
BISTABLE MOLECULAR MATERIALS: TRIAZOLE-BASED COORDINATION CHEMISTRY OF FIRST ROW TRANSITION METALS
Andrea Moneo Corcuera

Chapter 2

Structure and Magnetism of first-row transition metal trimers

Abstract

The dianionic 4-(1,2,4-triazol-4-yl) ethanedisulfonate ligand (**L**) was reacted with first row transition metals to obtain polyanionic trimers with general formula $[M_3(\mu\text{-}\mathbf{L})_6(H_2O)_6]^{6-}$, M = Mn^{II}, Fe^{II}, Co^{II}, Ni^{II} and Cu^{II}. All these complexes were isolated in solid state as the corresponding dimethyl ammonium salt, as polycrystalline solids and/or single crystals. In this chapter we present the synthesis, structure and magnetic properties of these complexes. Their chemical structure has been determined by single-crystal X-ray diffraction data and confirmed via Pawley fits from powder X-Ray diffractograms. The polyanionic part of all complexes show the same structural framework, which consist of a linear array of metal (II) ions linked by triple N_1-N_2-triazole bridges. The magnetic properties suggested dominant intramolecular antiferromagnetic interactions, showing negatives values of the Weiss constant in the Curie-Weiss fitting of their magnetic susceptibility data. The experimental data was modeled to a simple isotropic Hamiltonian for a centrosymmetric linear trimer, considering negligible all magnetic interactions except those promoted by the direct M–N–N–M triazole bridges:

$$H = -2J\, s_2\, (s_1 + s_3)$$

J values found: – 0.25 K for Mn^{II}, – 3.5 K for Ni^{II} and – 30 K for Cu^{II}. In the case of the Fe^{II} derivative, the low spin (S = 0) ground state configuration for the central Fe^{II} cation yields negligible intramolecular exchange between the two terminal high spin Fe^{II} (S = 2) centers.

2.1. Introduction

Molecular-based materials have been proposed as a plausible alternative for actual solid state materials due to their optical,[1,2] electric[3,4] or magnetic[5] properties. These materials have been studied with excellent perspectives because they can combine their properties, allowing to prepare multifunctional materials. This is particularly true in magnetic materials, able to mimic and even surpass the performance of solid state magnetic materials. The metal-organic materials have great interest in the context of molecular-based magnetism[6,7] due to their promising molecular magnetic performances.[8–11] Some unique examples include light-weight room temperature magnets,[12,13] single molecule magnets[14–18] or photoactive magnets.[19–22]

The chemical design of the organic ligands supposes an attractive strategy to synthetize novel coordination polynuclear metal complexes with desirable and tailor-made magnetic properties[23–28] as well as multifunctional materials with combined properties. [29–31]

In particular, 1,2,4-triazole and its derivatives are interesting bridging ligands to form stable metallic structures with different dimensionalities, such as discrete polynuclear metal complexes,[32,33] 1D/2D polymers[34–36] or 3D metal-organic-frameworks (MOFs),[37–39] due to its capacity to form N_1-N_2 bridges between metal centers. The N_1-N_2-1,2,4-triazole bridges offer short and conjugated diatomic pathway to propagate an effective magnetic superexchange between metal centers. Moreover, the nitrogen donor atoms of the triazole ring can support the suitable ligand field for spin transition in ferrous complexes,[40–42] which suppose an potential approach to molecule-based data storage application.[43–45] On the other hand, 1,2,4-triazole plays a relevant role in the biochemistry field by mimicking enzymatic reactions due to their geometrical similarity to imidazoles.[46] For these reasons, discrete polynuclear complexes with derivated-1,2,4-triazole are especially relevant

for the study of magnetic interaction between the metal centers. In recent years, a large number of polynuclear compounds based on 1,2,4-triazole and its derivatives have been synthetized and investigated [46–49] to further understand the magnetic superexchange coupling.

The chemical nature of the triazole substituents allow to have a control over the structure of these complexes, and hence upon their magnetic properties.[36,50] One of the most developed magnetic materials are those based on 4-functionalized 1,2,4-triazoles. This type of triazole functionalization do not sterically hindered to the N1-N2 bridging coordination mode and can confer different structural motifs to the coordination complexes. In the literature, the most common functionalized group in the family of 4-functionalized-1,2,4-triazole are pyridines,[51–53] triazol,[35,54] tetrazoles,[55] aromatic rings[56] or alkyl tails.[57] All of them lead to the formation of neutral ligands, and therefore the synthesis of cationic coordination metal complexes.

On the contrary, with the strategy to form anionic polynuclear complexes, we recently synthetized a dianionic triazole ligand (**L^{-2}** = 4-(1,2,4-triazol-4-yl)ethanedisulfonate) with two sulfonated groups at the 4-position, which confer high polar and anionic character. The coordination of this dianionic ligand with iron (II) ions led to the formation of a polyanionic Fe^{II} trinuclear complex (**1**) with spin transition above room temperature.[58]

We synthetize structural analogs with a series of other first-row transition metal ions (Mn^{II}, Co^{II}, Ni^{II}, or Cu^{II}). Here, we present the synthesis, crystal structure and magnetic properties of these complexes.

2.2. Results

2.2.1. Synthesis

The ligand, $\mathbf{L^{2-}}$ =4-(1,2,4-triazol-4-yl)ethanedisulfonate and the corresponding perchlorate metal salt were dissolved in water in a 2.5:1 molar ratio, leading to the formation of polyanionic linear trinuclear complexes with the formula $[M_3(\mu\text{-}L)_6(H_2O)_6]^{-6}$ (M= Mn^{II} (**1**), Fe^{II} (**2**), Co^{II} (**3**), Ni^{II} (**4**), or Cu^{II} (**5**)), see Experimental section for the detailed procedure. These complexes were isolated in solid state as the corresponding dimethyl ammonium salt by slow ethanol vapor diffusion into the aqueous mixture reaction, Figure 2.1. This crystallization process yielded needle-shape crystals for (**1**) – (**4**) compounds, with distinct colors depending on the metal content: purple for Fe^{II}, white for Mn^{II}, orange for Co^{II}, and blue-purple for Ni^{II} (Figure 2.2). The high quality of these crystals enabled us to determine their crystal structure from single crystal X-Ray diffraction data. We could not isolate (**5**) as single crystals, although highly crystalline powder was obtained, and their crystal structure was determined by Pawley refinement of the powder X-Ray diffractogram.

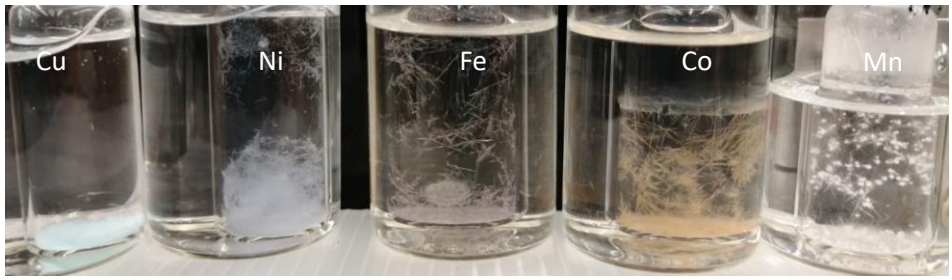

Figure 2.1. *Picture of (**1**) – (**5**) complexes in the synthesis solution after seven days in ethanol vapor flow.*

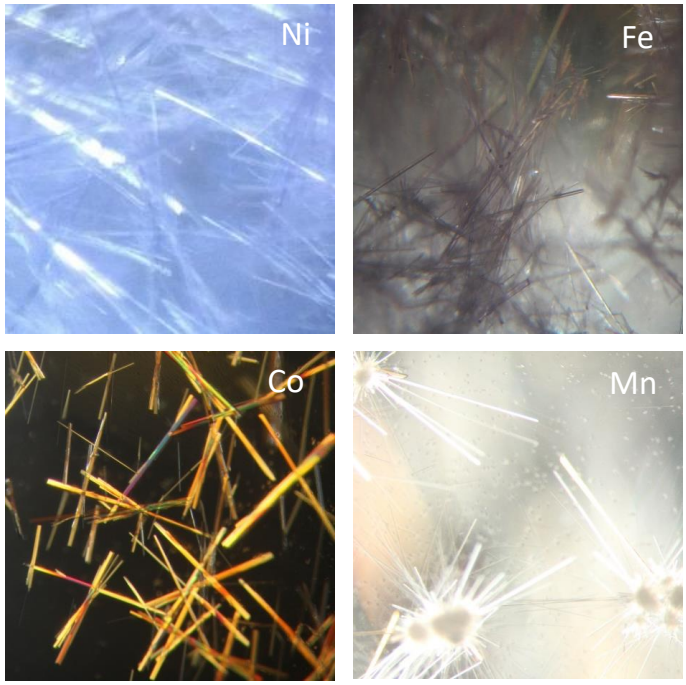

Figure 2.2. *Images from an optical microscope of (**1**) – (**4**) single crystals in the synthesis solution.*

2.2.2. Single Crystal Structure

Single Crystal X-Ray Diffraction data were collected at 100 K. Crystallographic refinement showed that the Mn^{II}, Fe^{II}, Co^{II} and Ni^{II} compounds contain the same polyanionic trinuclear units, crystallizing in the triclinic P–1 space group, (Table 2.1). The trimers are formed by linear array of three metal centers connected by six triazole ligands through two triple N_1-N_2 bridges, Figure 2.3. The central metal ion is an MN_6 octahedral center and the terminal metal ions are MN_3O_3 coordinated with three nitrogen from the bridging triazole ligands and three oxygen from three terminal water molecules completing the octahedral geometry in *fac* configuration. The coordination geometry of the metal centers for each complex is summarized in Table 2.2. The metal-ligand bonding distances for Mn^{II}, Co^{II} and Ni^{II} trimers indicate high spin configuration for all positions, terminal and central [average M-N (Å)= 2.239 for Mn^{II}, 2.121 for Co^{II} and 2.064 for Ni^{II}]. These are in good agreement with the corresponding metal ion radii in HS state [r (Mn^{II}_{HS}) = 97 pm, r (Co^{II}_{HS}) = 88 pm and r (Ni^{II}_{HS}) = 83 pm]. In contrast, the Fe^{II} trimer exhibits distinct distances for the terminal centers (average M-N = 2.13 Å) and the central one (average M-N = 1.99 Å), suggesting LS configuration for the latter.[58]

Table 2.1. *Crystallographic data at 100 K for $(Me_2NH_2)_6[M_3(\mu\text{-}L)_6(H_2O)_6]$ complexes.*

	M = Mn	M = Fe	M = Co	M = Ni
Formula	$C_{36}H_{90}Mn_{3.6}N_{24}O_{42}S_{12}$	$C_{36}H_{100}Fe_3N_{24}O_{47}S_{12}$	$C_{36}H_{90}Co_3N_{24}O_{42}S_{12}$	$C_{36}H_{90}Ni_3N_{24}O_{42}S_{12}$
	$[+xH_2O]$		$[+xH_2O]$	$[+xH_2O]$
Formula weigh	1873.16	2173.66	1816.26	1815.60
T(K)	100(2)	100(2)	100(2)	100(2)
Crystal system	Triclinic	Triclinic	Triclinic	Triclinic
Space group	P -1	P-1	P -1	P -1
Crystal size	0.05x0.10x0.30	0.20x0.04x0.02	0.30x0.04x0.02	0.01x0.01x0.30
a(Å)	14.377(3)	14.287(5)	14.2894(4)	14.1984(17)
b(Å)	15.477(3)	15.1581(6)	15.2780(4)	15.2235(16)
c(Å)	21.517(6)	21.3262(9)	21.3682(6)	21.239(2)
α(°)	80.249(8)	80.3780(14)	80.9239(9)	81.620(4)
β(°)	85.449(8)	84.2804(13)	84.9700(9)	85.252(4)
γ(°)	87.090(7)	83.7729(14)	83.7924(10)	83.570(4)
V (Å^3)	4700.6(18)	4492.5(3)	4567.7(2)	4502.8(9)
Z	2	2	2	2
ρ_{calcd} (g cm^{-3})	1.323	1.607	1.321	1.339
μ (mm^{-1})	0.824	0.860	0.895	0.982
F (000)	1884	2260	1842	1848
Refl. collected	65160	64559	72710	45072
Ind.reflections	23493	23819	23388	13182
Abs. correction	Empirical	Empirical	Empirical	Empirical
θ range (°)	2.26-28.07	1.37-29.15	1.356-29.192	2.26-23.38
Index ranges	$-19 \le h \le 19$	$-19 \le h \le 18$	$-14 \le h \le 19$	$-16 \le h \le 16$
	$-21 \le k \le 21$	$-20 \le k \le 20$	$-12 \le k \le 20$	$-17 \le k \le 12$
	$-29 \le l \le 29$	$-19 \le l \le 29$	$-29 \le l \le 29$	$-23 \le l \le 23$
Data/restr/para.	23493/ 0/929	23819/3588/2115	23388/2700/1451	13182/2163/1339
Goodnesss-of-fit	1.040	1.047	1.041	1.049
R1 (I>2σ(I))	0.0863	0.0740	0.0627	0.0597
wR2 (I>2σ(I))	0.2480	0.2217	0.1721	0.1521

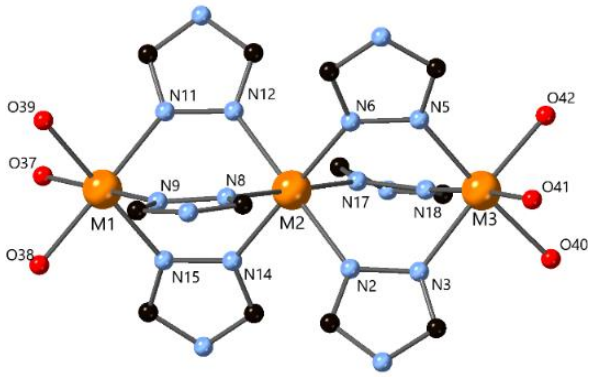

Figure 2.3. *Labeling structure for the general framework of (**1**) - (**5**) complexes. H atoms of coordinating molecules have been omitted.*

Table 2.2. *Metal-Nitrogen Bond Length for $(Me_2NH_2)_6[M_3(\mu\text{-}L)_6(H_2O)_6]$ complexes.*

	M-N Bond Length (Å)			
Bond	**M = Mn**	**M = Fe**	**M = Co**	**M = Ni**
M1-N11	2.258(4)	2.156(2)	2.120(3)	2.048(6)
M1-N9	2.239(4)	2.149(2)	2.119(3)	2.053(5)
M2-N12	2.221(4)	1.985(2)	2.114(3)	2.066(5)
M2-N8	2.210(4)	1.882(2)	2.114(3)	2.064(6)
M2-N14	2.230(4)	2.006(2)	2.125(3)	2.094(5)
M2-N6	2.221(4)	1.993(2)	2.113(3)	2.062(5)
M2-N17	2.255(4)	1.999(2)	2.149(3)	2.095(6)

The Fe^{II}, Co^{II} and Ni^{II} compounds are isostructural, with similar cell parameters and analogous unit cell contents, including six dimethyl ammonium counter cations per trimer, Figure 2.4 left. However, the Mn^{II} compound crystallizes with a slightly different packing, including an additional cation position for Mn^{II} counter cations with a 0.6 occupation factor. This position is coordinated to three oxygen atoms from sulfonated groups from a trimer and three water molecules, Figure 2.4 right. The low occupancy factor indicates delocalization of the Mn^{II} cation among several positions. This also brings a lower occupancy for the dimethyl ammonium cations that are also disordered.

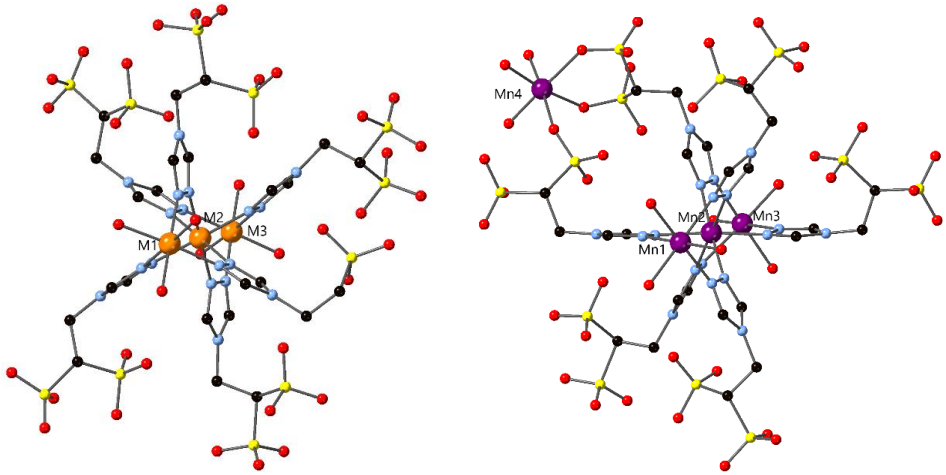

Figure 2.4. *Chemical structure of the polyanionic part for Fe^{II}, Co^{II} and Ni^{II} complexes (left) and for Mn^{II} complex (right). Hydrogen atoms are omitted for clarity. Color code: M (Ni, Co or Fe) = orange; Mn = purple, S = yellow; O = red; N = blue; C = black.*

Regarding the crystallographic packing, the trimers are oriented parallel to *c* axis, forming *zig-zag* chains, Figure 2.5. The intra-chain interactions are directed by multiple H-bonds [d(O…H) = 1.9 - 2.5 Å] between coordinated water molecules and sulfonated groups of the adjacent trimers. The chains of trimers are connected to each other along *a* and *b* axis by additional intramolecular H-bonding interactions [d(O…H) = 1.9 - 2.5 Å for Fe^{II}, Co^{II} and Ni^{II}complexes; d(O…H) = 2.3 - 2.5 Å for Mn^{II} complex]. The dimethyl ammonium cations and water molecules are disordered in the interstices between these chains.

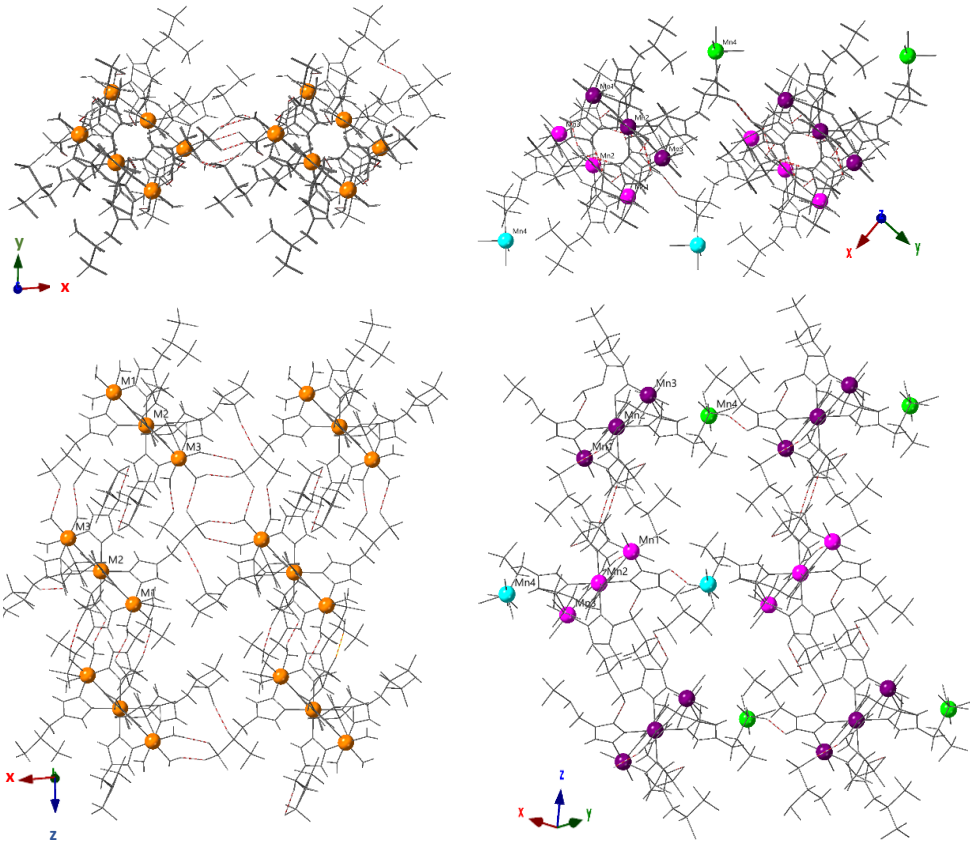

Figure 2.5. *Packing diagrams showing the arrangement of the trimers in Fe^{II}, Co^{II} and Ni^{II} complexes (left) and in Mn^{II} complex (right). Different color of manganese ions to note the zig-zag chains of trimers (Mn with 0.6 occupancy are represented in blue/green color). H-bonded interactions (1.9 – 2.5 Å) are represented by dotted red lines.*

2.2.3. Further structural characterization in bulk

We confirmed the phase purity of the compounds when obtained as polycrystalline samples in bulk from powder X-ray diffraction data. Pawley refinements were carried out on experimental diffractograms (Figure 2.6), obtaining refined cell parameters for each powder sample (Table 2.3). The refined cell parameters for Fe^{II}, Co^{II}, and Ni^{II} compounds are in good agreement with single crystal data, confirming the materials present a single crystallographic phase. The XRD for the Cu^{II} compound indicates this material is isostructural to this series, although we could not obtain single crystals. The refined cell parameters from the powder XRD for the Mn^{II} sample revealed some small differences with the single crystal, particularly for the γ parameter (γ = 84.98º) in between the single crystal value (γ = 87.09º) and the one found in the Fe^{II}, Co^{II}, Ni^{II} and Cu^{II} series (γ ≈ 83º). This suggests that the presence of Mn^{II} counter cations, at the origin of the differences in crystal structure, is variable depending on preparation. Our efforts to obtain a pure phase, without additional Mn^{II} counter cations were not successful.

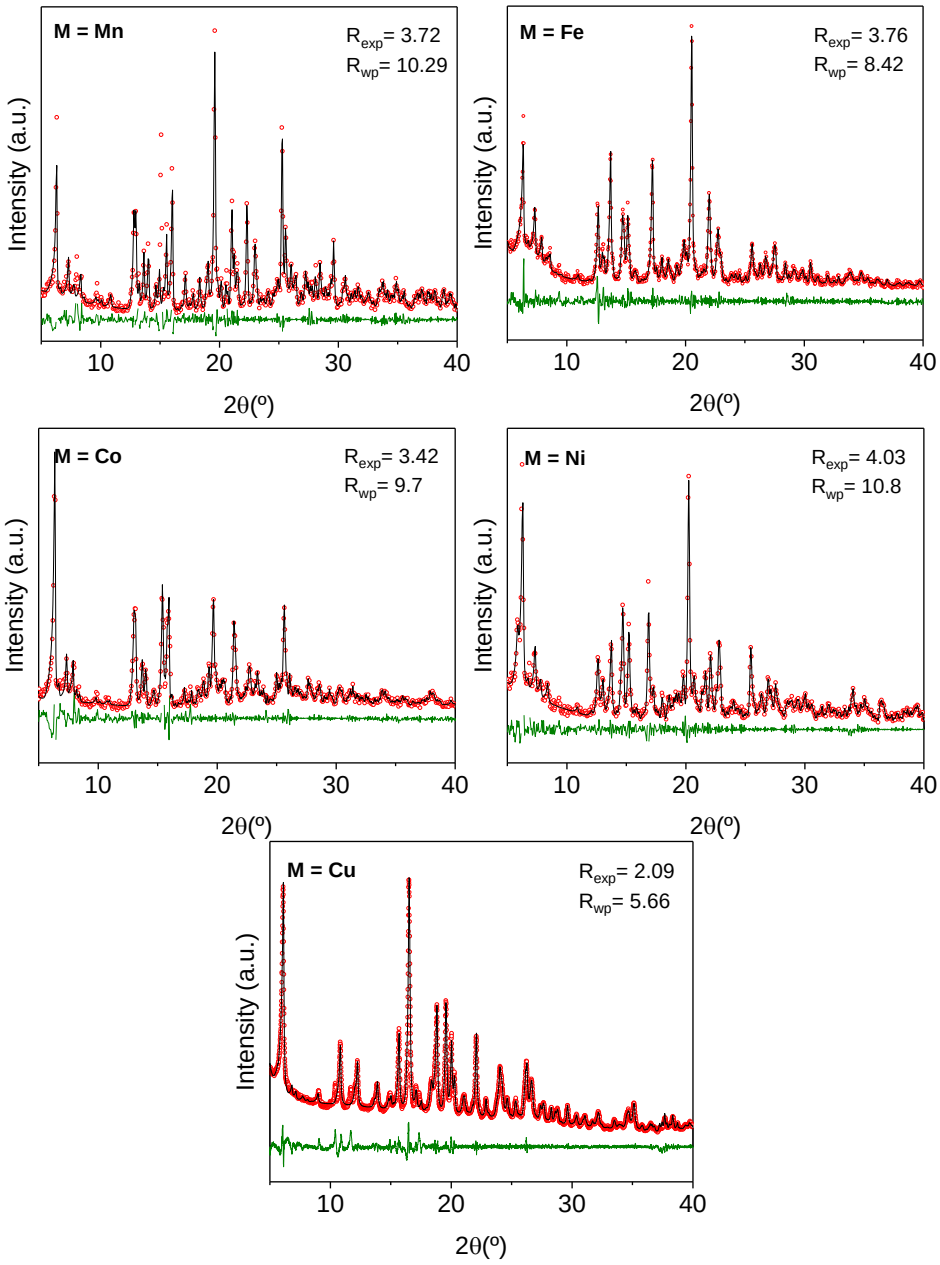

Figure 2.6. *Pawley refinement (black line) of experimental XRD patterns (red circles). The difference between fitting and experimental data (green line).* R_{exp} *and* R_{wp} *show the goodness of the fitting.*

Table 2.3. *Cell parameters and cell volume obtained from Pawley refinement of experimental PXRD pattern shown in Figure 2.6.*

Cell Parameters	M = Mn	M = Fe	M = Co	M = Ni	M = Cu
a (Å)	14.21(2)	14.16(1)	14.10(1)	14.19(1)	14.573(5)
b (Å)	15.48(2)	15.14(2)	15.44(2)	15.22(2)	14.966(5)
c (Å)	21.62(5)	21.35(1)	21.31(2)	21.23(2)	21.216(5)
α (º)	80.89(13)	80.51(1)	80.99(8)	81.62(5)	81.15(1)
β (º)	85.39(18)	84.27(7)	84.62(11)	85.25(7)	84.51(2)
γ (º)	84.98(10)	83.59(8)	83.57(19)	83.57(7)	83.53(3)
V (Å^3)	4670(10)	4474(10)	4541(11)	4502(8)	4528(10)

Fourier Transform Infrared (FTIR) spectrometry was performed for all these complexes in order to have supplementary structural information. All the compounds showed identical IR spectra (Figure 2.7) which again support the same chemical structure for all linear metal trimers. The 400 - 700 cm^{-1} region of the IR spectra is attributed to the metal–ligand stretching vibrations (M-N and M-O vibration modes). The band at 1200 cm^{-1} and 1650 cm^{-1} can be assigned to S=O and C=N stretching, respectively. The bands at 3491 cm^{-1} (OH stretching) and at 1630 cm^{-1} (H-OH bending) evidence the presence of coordinated water molecules. Noteworthy, although single crystal structural data for Cu^{II} compound was not obtained, IR and PXRD results reveal the same chemical structure as analogues Mn^{II}, Fe^{II}, Co^{II} and Ni^{II} complexes.

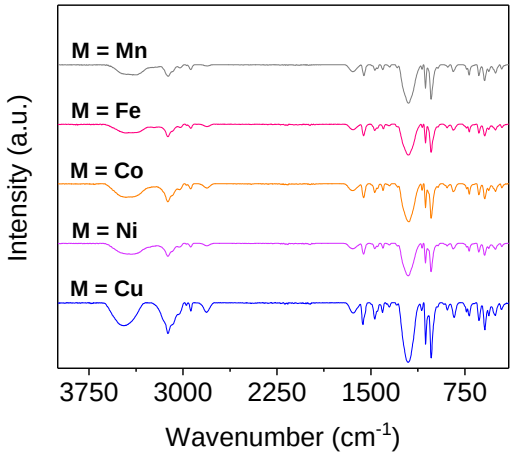

Figure 2.7. *IR spectra for* $(Me_2NH_2)_6[M_3(\mu\text{-}L)_6(H_2O)_6]$ *complexes.*

2.2.4. Magnetic Properties

In this section, we present the magnetic properties of these linear transition metal trimers, $(Me_2NH_2)_6$ $[M_3(\mu\text{-}L)_6(H_2O)_6]$ (M^{II} = Mn (**1**), Fe (**2**), Co (**3**), Ni (**4**) and Cu (**5**)), focusing on the analysis of the dominant magnetic intramolecular interactions between the paramagnetic metal centers to establish the corresponding magneto-structural correlations.

Variable Temperature Magnetic Susceptibility data

Single crystals or crystalline powders of (**1**) – (**5**) compounds were handpicked and grained for magnetic measurements. Magnetic susceptibility measurements were performed in the 300-2 K range, with an applied magnetic field of 0.1T, Figure 2.8.

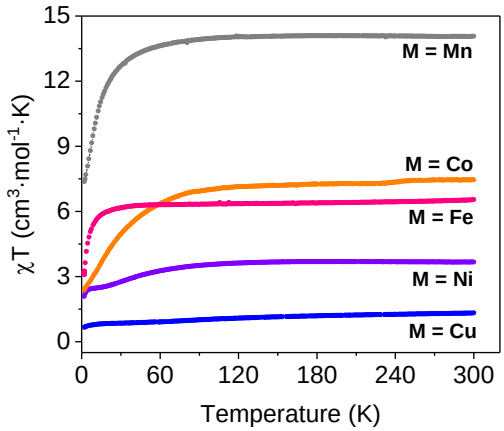

Figure 2.8. *$\chi_m T$ versus T plots for $(Me_2NH_2)_6$ [**M_3**$(\mu\text{-}L)_6(H_2O)_6$] complexes.*

The $\chi_m T$ product at room temperature is in good agreement with the expected values for magnetically diluted high spin samples with g ≈ 2, Table 2.4, according to the Equation 2.1 (detailed information in Annex I):

$$\chi T_{theoretical} = \frac{N g^2 \beta^2}{3 k_B} S(S+1) \qquad \text{Equation 2.1}$$

Where N is the Avogadro`s number, g is the g-factor (g = 2 for ideal isotropic situation), k_B is the Boltzmann constant, β is the Bohr magneton and S is the total spin.

Table 2.4. *Comparison of theoretical and experimental $\chi_m T$ product for **1** – **5** complexes. The data was calculated with g=2.*

Metal	S (HS ion)	$\chi_m T$ theoretical Per HS ion	$\chi_m T$ theoretical Per trimer	$\chi_m T$ experimental ($cm^3 \cdot mol^{-1} \cdot K$)
Mn^{II}	5/2	4.37	13.12	14.07
Fe^{II}	2	3	9	6.3
Co^{II}	3/2	1.87	5.6	7.4
Ni^{II}	1	1	3	3.66
Cu^{II}	1/2	0.37	1.2	1.32

There are two exceptions, the Fe^{II} complex where the value corresponds to only two HS Fe^{II} ions (S = 2) and one LS Fe^{II} ion (S = 0), and the Co^{II} complex that exhibits larger values (g > 2) as result of the high magnetic anisotropy typically found in octahedral Co^{II} ions. In all the cases, the $\chi_m T$ product remains essentially constant when the temperature decreases, down to ≈ 60 K. Below this temperature $\chi_m T$ decreases suggesting the presence of weak antiferromagnetic interactions (intramolecular), in addition to other possible contributions (zero field splitting or intermolecular interactions).

The thermal dependence of the susceptibility data at high temperatures (above 50 K, to minimize the participation of additional contributions) can be fitted to a Curie-Weiss Law (Equation 2.2 and Figure 2.9), obtaining the parameters shown in Table 2.5. All Weiss constants (θ value) are negative, suggesting dominant antiferromagnetic (AF) spin-spin coupling.

$$\chi = \frac{C}{(T-\theta)} \qquad \text{Equation 2.2}$$

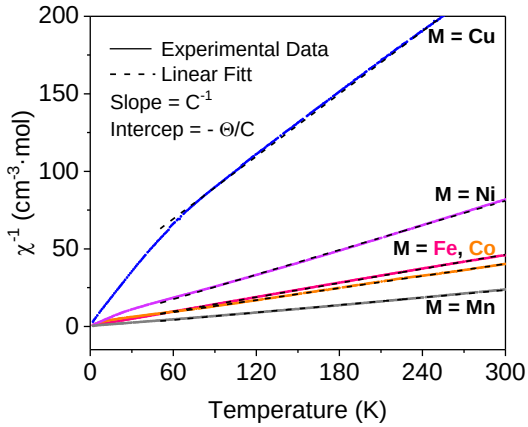

Figure 2.9. *X^{-1} vs T plots for $(Me_2NH_2)_6$ $[M_3(\mu\text{-}L)_6(H_2O)_6]$. The data have been measured at a magnetic field of 1000 Oe.*

Table 2.5. *Magnetic Curie-Weiss parameters obtained from X^{-1} vs T plots.*

Metal	θ (K)	C (emu·K·mol^{-1})
Fe^{II}	-3.54	6.5
Mn^{II}	-1.17	14.12
Co^{II}	-11.28	7.72
Ni^{II}	-6.23	3.77
Cu^{II}	-43.20	1.487

These high temperature data can also be modelled with a simple isotropic Hamiltonian (Equation 2.3) as a first approximation, considering the intermolecular interactions and/or zero field splitting contributions as negligible.

$$H = -2J\, s_2\, (s_1 + s_3) \qquad \text{Equation 2.3}$$

Where S are the spins of the different metal centers and J is the magnetic exchange constant expressed in kelvins, which measure the character and strength of the spin–spin interactions.

In this model we also assumed that the exchange pathway between the neighboring metals are identical ($J = J_{12} = J_{23}$) and that the coupling between terminal metal centers is negligible ($J_{13} = 0$), [59] Figure 2.10.

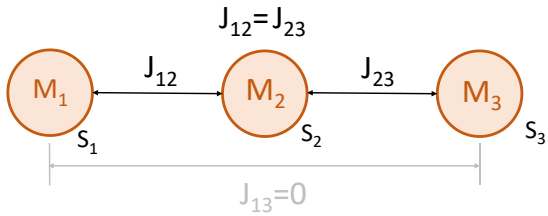

Figure 2.10. *Centrosymmetrical model of linear trinuclear complexes*

From this Hamiltonian, the energy levels for each compound were calculated and the susceptibility data reproduced with the MAGPPACK package.[60,61] Two compounds were not modeled, the Fe^{II} derivative (the LS ground state of the central Fe center makes $J = 0$), and the Co^{II} derivative, due to its high single-ion anisotropy. This isotropic model (see Annex I for detailed information) was satisfactory for the rest of the series (Mn^{II} ($^6A_{1g}$) Ni^{II} ($^3A_{2g}$) and Cu^{II} ($^2T_{2g}$)), obtaining the best fit parameters (J and g) for each complex, Figure 2.11.

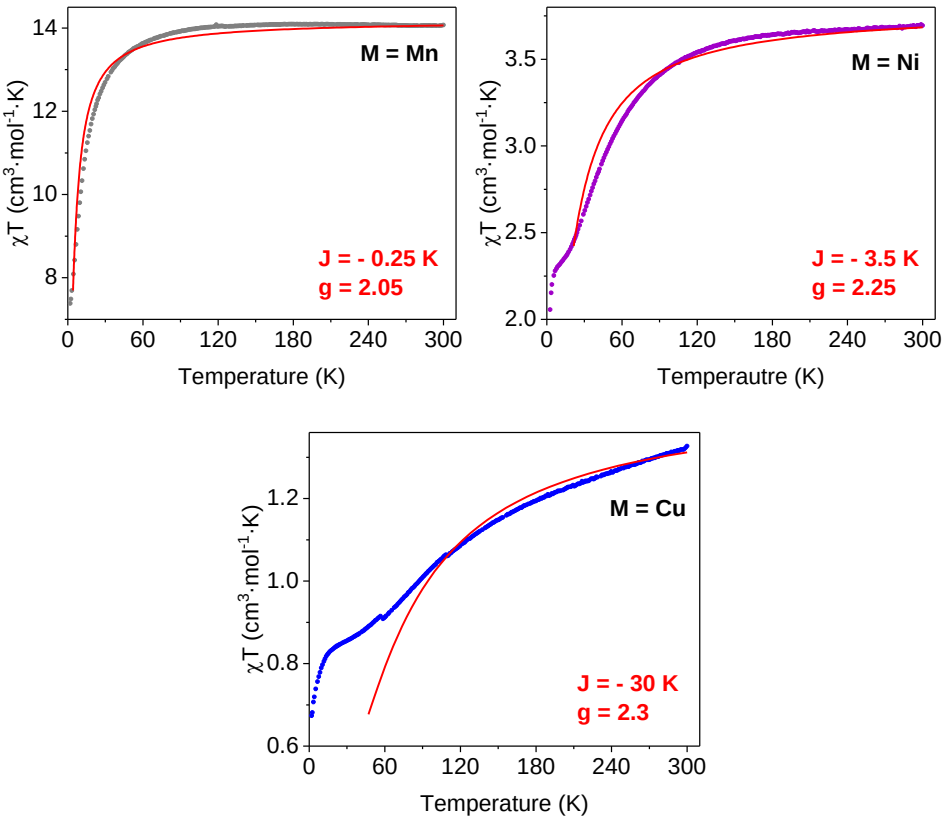

Figure 2.11. *Thermal dependence of $\chi_m T$ for Mn^{II}, Ni^{II} and Cu^{II} complexes and their corresponding best fit (red line) from MAGPACK software.*

In the Mn^{II} compound, the $\chi_m T$ product at 300 K is 14.07 $cm^3 \cdot mol^{-1} \cdot K$, in agreement to the presence of three Mn^{II} ions (13.12 $cm^3 \cdot mol^{-1} \cdot K$ for g=2). This value remains constant above 70 K, and at lower temperatures the $\chi_m T$ decrease rapidly to reach 7.38 $cm^3 \cdot mol^{-1} \cdot K$ at 2 K. The best fitting parameters from magnetic exchange calculations within 300 - 2 K range are g = 2.05 and J = - 0.26 K, which is in the same order than those J values previously published for linear trinuclear Mn^{II} complexes.[62,63]

In the Ni^{II} compound reveals a χ_mT value of 3.66 $cm^3 \cdot mol^{-1} \cdot K$ at 300K, which is consistent with the presence of three high spin Ni (II) ions with S = 1 (3 $cm^3 \cdot mol^{-1} \cdot K$, for g = 2). This χ_mT value remains constant above 140 K, when it starts to decrease quickly until 2.5 $cm^3 \cdot mol^{-1} \cdot K$ at 10 K. At lower temperatures, a small decrease in χ_mT appears, reaching a value of 2.0 $cm^3 \cdot mol^{-1} \cdot K$ at 2K. The best fitting in the 300 - 100 K range was obtained with g = 2.25 and J = - 3.5 K. Such J value is slightly lower than those from -13.8 to -6.7 K in analogues triazole-bridge linear Ni^{II} trimers.[59,64–66]

In the Cu^{II} complex, the χ_mT product at 300 K is 1.32 $cm^3 \cdot mol^{-1} \cdot K$ at 300 K, which is in good agreement with the spin-only value for three Cu^{II} ions S = 1/2 (1.125 $cm^3 \cdot mol^{-1} \cdot K$, for g = 2). On cooling process, it decrease gradually to reach around 0.81 $cm^3 \cdot mol^{-1} \cdot K$ at 15 K. Below 15 K, the χ_mT product abruptly decrease until 0.66 $cm^3 \cdot mol^{-1} \cdot K$ at 2 K. The high temperature regime can be well-modelled by MAGPACK with J = - 30 K, g = 2.3. The value of J parameter are in good agreement with previous reported values in the literature for Cu^{II} trimers, where the magnetic exchange only occur through one side of the triazole bridge.[67]

The Co^{II} compound cannot be appropriately modeled with the simple isotropic model used for the rest of the compounds due to the orbitally non-degenerate ground state. The ground state of free Co(II) ion is 4F, but under an octahedral crystal field symmetry, the orbital degeneracy is removed by giving one $^4A_{2g}$ and two ^4T levels.[68] Moreover, the large distorted octahedral environment of Co^{II} ions involve a large orbital contribution in the ground $^4T_1$ state, which is generally split into an orbital singlet ground state and an orbital doublet excited state[9]. The modeling for Co complexes requires a modified Lines approximation, a fictitious spin 5/3**s** (**s** = 1/2)).[69,70] In the literature, some analogue linear Co(II) trinuclear complexes with triazole ligands have been modelled, presenting J value between – 6.9 K [59] and – 4 K.[64]

Low temperature data

The intra-trimer magnetic coupling explains the high temperature magnetic data. However, the low-temperature data deviates from this simple model, pointing towards additional contributions, which makes a complex problem to model since it is difficult to differentiate all contributions of the data. In addition to the previously mention, we also found paramagnetic impurities, with the χT product for most compounds tending to a plateau at very low temperatures, incompatible with the isolated trimer models.

We also measured the field-dependence of the magnetization (M) at low temperature (2 K) for **1**- **5** complexes, Figure 2.12.

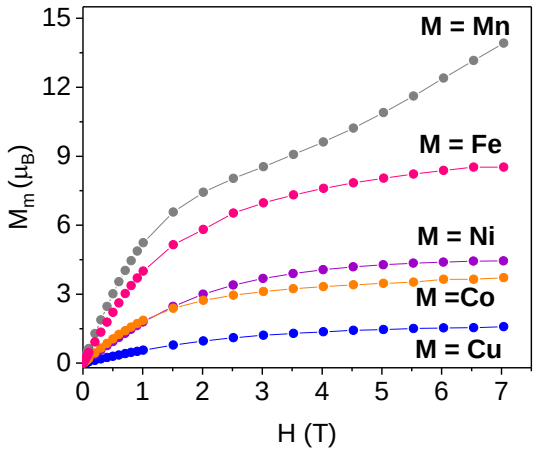

Figure 2.12. *Magnetization (M) vs magnetic field (H) plots at 2 K for all compounds.*

All the complexes show similar tendency in the *M vs H* curve. At lower applied field, the magnetization is lineally proportional to magnetic field, effectively described by Curie Law (M = χ · H). When the magnetic field becomes larger, the magnetization tends to a saturation value, Ms, generally described as Equation 2.4,

$$M_{S(\mu_B)} = N \cdot g \cdot S \qquad \text{Equation 2.4}$$

Where N is the number of centers with a spin (S) and g-factor (g).

We compared the experimental magnetization at 7 T with the expected value for the ferromagnetic (F) state population with g = 2, shown in Table 2.6.

Table 2.6. S*aturation magnetization from the experimental data and from equation 2.4 with g = 2 for ferromagnetic (N = 3) and antiferromagnetic (N = 1) state population.*

Metal	$M_{S\ (experimental)}$	$M_{S\ (F)}$	$M_{S\ (AF)}$
Mn^{II}	14	15	5
Fe^{II}	8.5	8	2
Co^{II}	3.7	9	4
Ni^{II}	4.3	6	3
Cu^{II}	1.5	3	1

The Mn^{II} and Fe^{II} complexes present similar magnetization values than the expected values for all spins aligned, while Co^{II}, Ni^{II} and Cu^{II} complexes exhibit significantly lower magnetization values in comparison with their corresponding theoretical saturation magnetization. These results can be explained by the energy diagrams for each trimer (Figure 2.13), where the energy states for Mn^{II}, Ni^{II} and Cu^{II} complexes with respect to the AF ground state were calculated according to Equation 6.19 (see Annex I and Table 6.1) and taking into account the J values determined from experimental χT vs T data (– 0.25 K for Mn^{II}, – 3.5 K for Ni^{II} and – 30 K for Cu^{II} complex).

Mn^{II} complex exhibits the lowest energy gap, making easier the population of excited states by the Zeeman effect. The same is expected for the iron complex where J = 0, facilitating typical paramagnetic behavior and reaching saturation. On the other hand, Ni^{II} and Cu^{II} complexes show stronger antiferromagnetic coupling (J) and higher energy difference between antiferro- and ferro- magnetic states. Thus, saturation is more difficult to achieve at 2 K. In the Co complex, the strong single-

ion anisotropy also contributes to the magnetization behavior, making the data more complex to analyze.

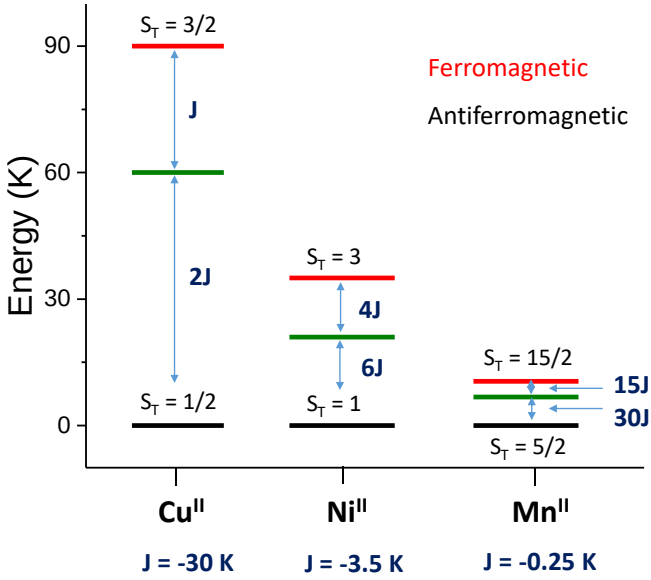

Figure 2.13. *Energy Diagram for Mn^{II}, Ni^{II} and Cu^{II} trimers with those J values determined from experimental χT vs T data.*

2.3. Discussion

The anionic 4-(1,2,4-triazol-4-yl)ethanedisulfonate ligand acts as a N-N-bridge between metal centers, promoting selectively the formation of linear trinuclear metal complexes. We have obtained analog trimeric structures with several first-raw transition metal ions (Fe^{II}, Mn^{II}, Co^{II}, Ni^{II} and Cu^{II}). Such high selectivity for trimers synthesis could arise from the remarkable bulky and anionic nature of the ligand that could confer huge steric hindrance and electrostatic repulsion in triazole-bridge polymeric structures.

Regarding the magnetic properties, all these N-N-triazole-bridge trinuclear compounds exhibit antiferromagnetic behavior. The magnetic coupling between intra-trimer metal centers, defined by J, have been determined from experimental χT *vs* T data according to isotropic Hamiltonian, obtaining J values of - 0.25 K for Mn^{II}, - 3.5 K for Ni^{II} and - 30 K for Cu^{II} complex.

On one hand, the antiferromagnetic character of J is highly determined by the ligand structure and bridging mode. In a simple polarization model, the number of atoms forming the bridge between metals may predict anti-ferromagnetic interactions (Figure 2.14), as we found in our compounds. This is also in good agreement with previous N-N-triazole-bridged polynuclear complexes in the literature.[62,71,32]

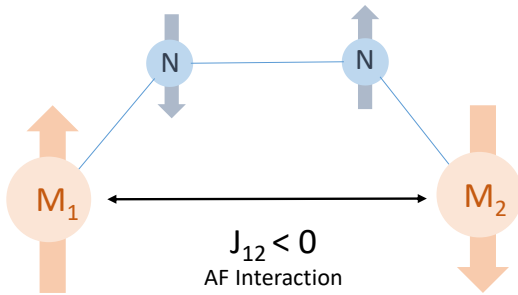

Figure 2.14. *Representation of Antiferromagnetic (AF) super-exchange through N-N-Bridges*.

Beyond this very simple model, magnetic orbital overlapping can better explain the magnetic super-exchange.[75] It is possible to relate the magnitude and sign of magnetic super exchange to the orbital symmetry of the magnetic system. Typically, orthogonality of the magnetic orbitals with no overlap favor ferromagnetic interactions, whereas orbital mixing tends to favor electron pairing: antiferromagnetic interactions. Indeed, the AF coupling is proportional to the overlap integral between magnetic orbitals.

This is easy to observe in the trinuclear Cu^{II} compounds, since the axially elongated z^2 orbital is not magnetic and we expect the unique unpaired electron in dx^2y^2 type magnetic orbital. Thus, the magnetic coupling is minimized if Cu atoms were exclusively connected through N-N-bridges in axial position (dx^2y^2orbital would be perpendicular to the triazole ring).[76–79] The *fac* triply bridged connectivity precludes this possibility. Still, in this case only one of the bridges does not participate of an axial Cu^{II} position (Figure 2.15),[67] resulting in a weak antiferromagnetic interaction (J = – 30 K) when compared with J value between - 70 K [80] and - 107 K [67] found in other complexes where more bridges favor orbital overlap.

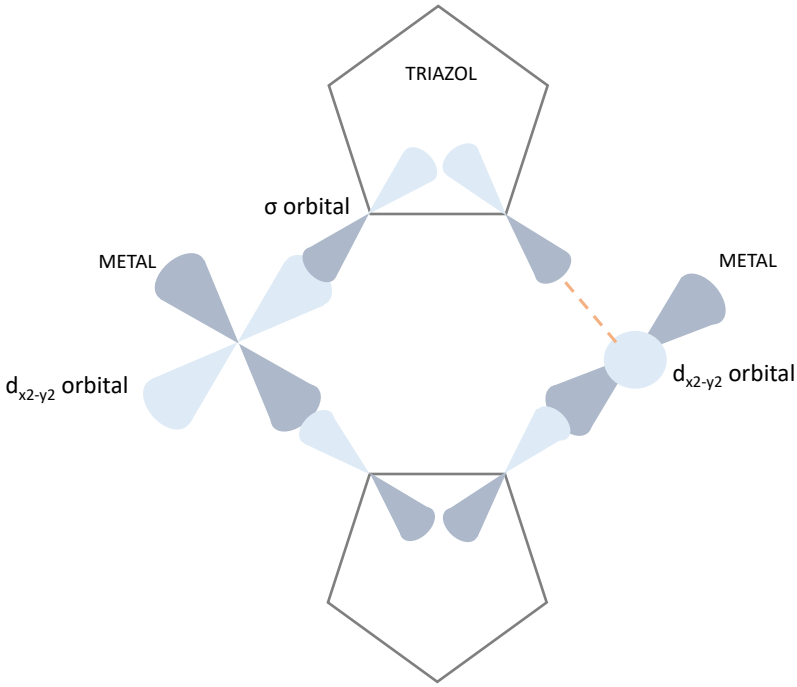

Figure 2.15. *Magnetic molecular orbitals representation in triazole-bridges complexes. The triazole (pentagon) in the bottom exhibit the σ overlap for an efficient AF exchange propagation. The triazole in the top present an absence of orbital overlapping (orange line).*

Analogous distorted bridging is found in the rest of the series, justifying the weaker magnetic coupling (J = – 0.25 K for Mn^{II} and J = - 3.5 K for Ni^{II}) in comparison with other μ^2-triazole trinuclear complexes in the literature (≈ –1 K for Mn^{II} [62] and – 14 K for Ni^{II}).[59,64–66]

2.4. Conclusions

A series of analogous linear trinuclear complexes ,$(Me_2NH_2)_6$ $[M_3(\mu\text{-}\mathbf{L})_6(H_2O)_6]$ (M= Fe^{II}, Mn^{II}, Co^{II}, Ni^{II} and Cu^{II}), have been synthetized by the reaction of the ligand $\mathbf{L^{-2}}$ = 4-(1,2,4-triazol-4-yl)ethanedisulfonate with the corresponding metal (II) perchlorate salts in 2.5:1 molar ratio. Crystallographic data shows the same molecular structure for all the complexes, formed by three metal ions linked by triply N-N-triazole bridges. The Fe complex shows a conformation of Fe^{II}_{HS}-Fe^{II}_{LS}-Fe^{II}_{HS} at 100 K, while the other metal trimers exhibit HS configuration for all metal centers. Magnetic susceptibility studies showed dominant intra-trimer antiferromagnetic interactions between terminal and central positions, as expected from N_1,N_2-triazole-bridge polynuclear complexes. The magnetic exchange parameter, J, was obtained from the fitting of the thermal dependence of the magnetic susceptibility based on a general isotropic model for centrosymmetric linear trimers with negligible intermolecular interactions. We observed slightly lower *J* values for these compounds compared with those values for other analogous trimers in the literature that we related to the local distortion of metal octahedral.

2.5. Experimental

2.5.1. Synthesis

$(Me_2NH_2)_6L$ (L^{2-}= 4-(1,2,4-triazol-4-yl)ethanedisulfonate) was synthetized as previously reported:[58] N,Ndimethylformamide azine (3.0 g, 21.0 mmol) and 2-aminoethane-1,1-disulfonic acid (1.44 g, 7.0 mmol) are dissolved in 15 mL of water, and the pH is adjusted at 6.0 with HCl. The solution is heated at 92°C overnight under stirring. The solvent is removed under vacuum and after that, EtOH was added obtaining a white precipitate. The product is removed by filtration as a white solid, washed with diethyl ether and dried in air.

$(Me_2NH_2)_6$ $[Mn_3(\mu\text{-}L)_6(H_2O)_6]$ (**1**). $Mn(ClO_4)_2$ (0.029g; 0.115 mmol) and $(Me_2NH_2)_6$**L** (0.1g ;0.287 mmol) were dissolved in 2 ml of water. The crystals of this complex were isolated by slow vapor diffusion on this reaction mixture. IR (ATR): ν= 3420, 3114, 1632, 1205, 1020, 838, 716, 636, 592, 505. Elemental Analysis experimental and calculated for $C_{24}H_{42}Mn_3N_{18}O_{42}S_{12}$ (1873.16 g/mol) ($\%_{exp}$; %calc): C (16.99%; 15.37 %), H (3.91%; 1.6 %) N (14.27%; 13.45 %), S (17.31%; 20.5 %).

$(Me_2NH_2)_6$ $[Fe_3(\mu\text{-}L)_6(H_2O)_6]$ (**2**) was synthetized as previously reported.[58] $Fe(ClO_4)_2{\cdot}6H_2O$ (0.0212 g, 0.058 mmol) and $(Me_2NH_2)_6$**L** (0.05 g, 0.144 mmol) were both dissolved in water and then mixed (total volume 2 ml). Slow vapor diffusion on this aqueous reaction solution led to the formation of crystals of **2** after few days. IR (ATR): ν=3420, 3121, 1653, 1204, 1020, 844, 715, 639, 595, 505. Elemental Analysis experimental and calculated for $C_{24}H_{42}N_{18}Fe_3O_{42}S_{12}$ (2173.66 g/mol) ($\%_{exp}$; $\%_{calc}$): C (13.24%; 14.86 %), H (1.93%; 1.31%) N(11.59%; 12.68 %), S (17.6%; 18.19%).

$(Me_2NH_2)_6$ $[Co_3(\mu\text{-}L)_6(H_2O)_6]$ (**3**). $Co(ClO_4)_2{\cdot}6H_2O$ (0.02112 g, 0.050 mmol) and $(Me_2NH_2)_6$**L** (0.05g, 0.144 mmol) were dissolved and mixed in 2ml of water. Afterwards, crystallization was induced with the same procedure than compound 2, obtaining orange crystals of **3** after few days. IR (ATR): v=3440, 3118, 1643, 1204, 1017, 841, 716, 636, 589, 505. Elemental Analysis experimental and calculated for $C_{24}H_{42}Co_3\ N_{18}O_{42}S_{12}$ (1816.26) ($\%_{exp}$; $\%_{calc}$): C (17.28 %; 15.80 %), H (4.04%; 2.31 %) N (14.10%; 13.87 %), S (16.51%; 21.14 %).

$(Me_2NH_2)_6$ $[Ni_3(\mu\text{-}L)_6(H_2O)_6]$ (**4**). $Ni(ClO_4)_2{\cdot}6H_2O$ (0.0212 g, 0.058 mmol) and $(Me_2NH_2)_6$**L** (0.05 g, 0.144 mmol) were both dissolved in water and then mixed (total volume 2 ml). Slow vapor diffusion on this aqueous reaction solution led to the formation of crystals of **4** after few days. IR (ATR): v=3420, 3121, 1653, 1204, 1020, 844, 715, 639, 595, 505. Elemental Analysis experimental and calculated for $C_{24}H_{42}N_{18}Ni_3O_{42}S_{12}$ (1815.60 g/mol) ($\%_{exp}$; $\%_{calc}$): C (16.08%; 15.86 %), H (4.09%; 2.31%) N(15.42%; 13.88 %), S (16.14%; 21.19%).

$(Me_2NH_2)_6$ $[Cu_3(\mu\text{-}L)_6(H_2O)_6]$, (**5**). $Cu(ClO_4)_2{\cdot}6H_2O$ (0.0213 g, 0.058 mmol) and $(Me_2NH_2)_6$**L** (0.05 g, 0.144 mmol) were both dissolved in water and then mixed (total volume 2 ml). Afterwards, ethanol was added to the aqueous reaction solution, isolating the compound **1** as a blue powder. Crystals of **1** suitable for X-ray diffraction was not obtained. IR (ATR): v=3467, 3119, 1643, 1205, 1020, 837, 712, 639, 589, 510. Elemental Analysis experimental and calculated for $C_{24}H_{42}N_{18}Cu_3O_{42}S_{12}$ (1829.85g/mol) ($\%_{exp}$; $\%_{calc}$): C (19.3% ;15.73%), H (4.61% ;2.29%) N(15.53% ;13.77%), S (16.61%; 20.98%).

2.5.2. Physical methods

Thermogravimetric analysis (TGA) was performed using a TGA/SDTA851 Mettler Toledo with a MT1 microbalance. The experiments were carried out from 20 to 500 ^{o}C to examine the stability of the samples and the presence of crystallization water molecules (Figure 2.16). All compounds were stable above 300 ^{o}C and the loss of twelve crystallization water were estimated.

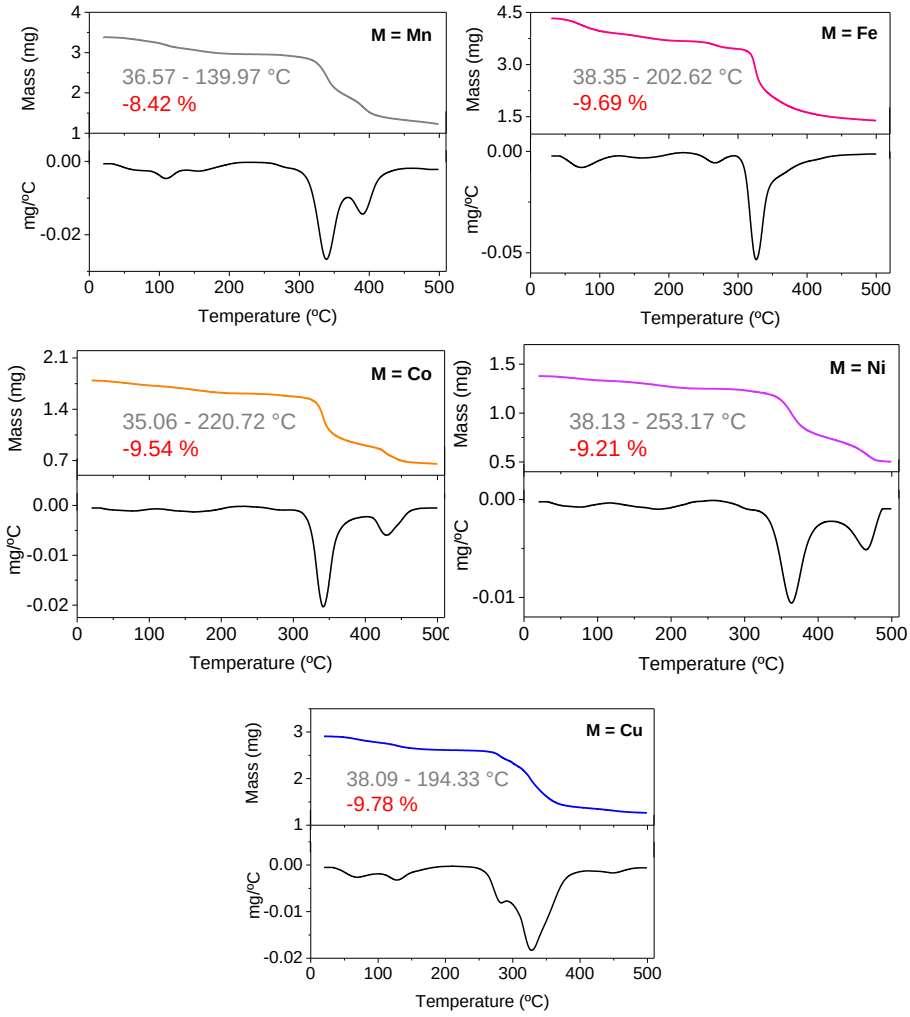

Figure 2.16. *TGA analysis for **1** - **5** compounds from 20 ^{o}C to 500 ^{o}C under inert atmosphere. Scan rate 1 ^{o}C/min.*

Inductively coupled plasma optical emission spectrometry (ICP-OES) was used to carry out elemental analysis with Agilent 755-ES inductively coupled plasma optical emission spectrometer at University of Valladolid.

Infrared spectroscopy (IR) spectra were collected with a FTIR Bruker spectrometer model Alpha equipped with an ATR accessory.

Single crystal X-ray diffraction (SCXRD) measurements were performed on a Bruker-Nonius diffractometer with an APPEX 2 4K CCD area detector at 100 K. The total electron density in the unit cell was split up into t0wo parts with associated contributions to $F_h = F_h1 + F_h2$. F_h1 is associated with the main molecule of interest, $(Me_2NH_2)_6$ $[M_3 (\mu\text{-}L)_6 (H_2O)_6]$, and F_h2 with the region where the non-coordination water molecules are disordered. The SQUEEZE approach[81] was used to determine the contribution from the F_h2 region. Crystal data of **1** - **5** are given in Table 2.1 and supplementary data for Fe complex can be obtained with CCDC 1016539 code.

X-ray powder diffraction (PXRD) measurements were made using a Siemens D5000 diffractometer (Bragg-Brentano parafocusing geometry and vertical θ-θ goniometer) fitted with a curved graphite diffracted-beam monochromator, incident and diffracted -beam Soller slits, a 0.06° receiving slit and scintillation counter as a detector. The angular 2θ diffraction range was between 5 and 40°. The data were collected with an angular step of 0.05° at 10 s per step and sample rotation. A low background Si (510) wafer was used as sample holder. Cu kα radiation was obtained from a copper X-ray tube operated at 40 kV and 30 mA. The obtained XPRD patterns were analysed by Pawley profile analysis using the Topas software [82] and a Chebyshev function of seven terms was used to fit the background.

Magnetic measurements were carried out on grained solid powders with a Quantum Design MPMS-XL SQUID magnetometer (Quantum Design, Inc, San Diego, CA, USA). Variable temperature magnetic susceptibility measurements were carried out under an applied field of 1000 Oe at 1 $K \cdot min^{-1}$ between 300 and 2 K. Variable field magnetization measurements were carried out at 2 K from 0 to 7 T.

2.6. References

1. Wu, H., Chen, Y., Liu, Y. Reversibly Photoswitchable Supramolecular Assembly and Its Application as a Photoerasable Fluorescent Ink. *Adv. Mater.* **29**, (2017).

2. Gallardo, I., Guirado, G., Hernando, J., Morais, S., Prats, G. A multi-stimuli responsive switch as a fluorescent molecular analogue of transistors. *Chem. Sci.* **7**, 1819–1825 (2016).

3. Finniss, G. M., Canadell, E., Campana, C., Dunbar, K. R. Unprecedented Conversion of a Compound with Metal-Metal Bonding into a Solvated Molecular Wire. *Angew. Chem. Int. Ed. Engl.* **35**, 2771–2774 (1996).

4. Jurow, M., Schuckman, A. E., Batteas, J. D., Drain, C. M. Porphyrins as molecular electronic components of functional devices. *Coord. Chem. Rev.* **254**, 2297–2310 (2010).

5. Wang, X. Y., Avendaño, C., Dunbar, K. R. Molecular magnetic materials based on 4d and 5d transition metals. *Chem. Soc. Rev.* **40**, 3213–3238 (2011).

6. Hill, S., Edwards, R. S., Aliaga-Alcalde, N., Christou, G. Quantum Coherence in an Exchange-Couped Dimer of Single-Molecule Magnets. *Science (80-.).* **302**, 1015–1018 (2003).

7. Bagai, R., Christou, G. The Drosophila of single-molecule magnetism: [Mn12O 12(O2CR)16(H2O)4]. *Chem. Soc. Rev.* **38**, 1011–1026 (2009).

8. Miller, J. S., Drillon, M. *Magnetism: Molecules to Materials*. *Magnetism: Molecules to Materials* **1**–**5**, (2003).

9. Kahn, O. Molecular Magnetism. *Journal of Chemical Education* **72**, (2009).

10. Ferrando-Soria, J. Vallejo, J., Castellano, M., Martínez-Lillo, J., Pardo, E., Cano, J.Castro, I., Lloret, F., Ruiz-García, R., Julve, M.. Molecular magnetism, quo vadis? A historical perspective from a coordination chemist viewpoint. *Coord. Chem. Rev.* **339**, 17–103 (2017).

11. Miller, J. S. Molecular Materials I. Molecular materials mimic inorganic network solids. *Adv. Mater.* **2**, 98–99 (2004).

12. Ferlay, S., Mallah, T., Ouahes, R., Veillet, P., Verdaguer, M. Room Temperature Organometallic Magnet. *Nature* **378**, 701–703 (1995).

13. Hatlevik, Ø., Buschmann, W. E., Zhang, J., Manson, J. L., Miller, J. S. Enhancement of the magnetic ordering temperature and air stability of a mixed valent vanadium hexacyanochromate(III) magnet to 99°C (372 K). *Adv. Mater.* **11**, 914–918 (1999).

14. Qian, K. Huang, X.C., Zhou, C., You, X. Z., Wang, X. Y., Dunbar, K. R. A single-molecule magnet based on heptacyanomolybdate with the highest energy barrier for a cyanide compound. *J. Am. Chem. Soc.* **135**, 13302–13305 (2013).

15. Saber, M. R., Dunbar, K. R. Trigonal bipyramidal 5d-4f molecules with SMM behavior. *Chem. Commun.* **50**, 2177–2179 (2014).

16. Woods, T. J., Ballesteros-Rivas, M. F., Gómez-Coca, S., Ruiz, E., Dunbar, K. R. Relaxation Dynamics of Identical Trigonal Bipyramidal Cobalt Molecules with Different Local Symmetries and Packing Arrangements: Magnetostructural Correlations and ab inito Calculations. *J. Am. Chem. Soc.* **138**, 16407–16416 (2016).

17. Brown, A. J., Pinkowicz, D., Saber, M. R., Dunbar, K. R. A trigonal-pyramidal Erbium(III) single-molecule magnet. *Angew. Chemie - Int. Ed.* **54**, 5864–5868 (2015).

18. Fang, M. Zhao, H., Prosvirin, A. V., Pinkowicz, D., Zhao, B., Cheng, P.,Wernsdorfer,W., Brechin, E. K., Dunbar, K. R. Squaring the cube: A family of octametallic lanthanide complexes including a Dy8 single-molecule magnet. *Dalt. Trans.* **42**, 14693–14701 (2013).

19. Aguilà, D., Prado, Y., Koumousi, E. S., Mathonière, C., Clérac, R. Switchable Fe/Co Prussian blue networks and molecular analogues. *Chem. Soc. Rev.* **45**, 203–224 (2016).

20. Liu, T., Zheng, H., Kang, S., Shiota, Y., Hayami, S., Mito, M., Sato, O., Yoshizawa, K., Kanegawa, S., Duan, C. A light-induced spin crossover actuated single-chain magnet. *Nat. Commun.* **4**, 1–7 (2013).

21. Ohkoshi, S. I., Imoto, K., Tsunobuchi, Y., Takano, S., Tokoro, H. Light-induced spin-crossover magnet. *Nat. Chem.* **3**, 564–569 (2011).

22. Mathonière, C., Lin, H. J., Siretanu, D., Clérac, R., Smith, J. M. Photoinduced single-molecule magnet properties in a four-coordinate iron(II) spin crossover complex. *J. Am. Chem. Soc.* **135**, 19083–19086 (2013).

23. Galán-Mascarós, J. R. Coronado, E., Goddard, P. A., Singleton, J., Coldea, A. I., Wallis, J. D., Coles, S. J., Alberolá, A. A chiral ferromagnetic molecular metal. *J. Am. Chem. Soc.* **132**, 9271–9273 (2010).

24. Wu, D. Q. Shao, D., Wei, X. Q., Shen, F. X., Shi, L., Kempe, D., Zhang, Y. Z., Dunbar, K.R., Wang, X.Yi. Reversible On-Off Switching of a Single-Molecule Magnet via a Crystal-to-Crystal Chemical Transformation. *J. Am. Chem. Soc.* **139**, 11714–11717 (2017).

25. Pardo, E. Ruiz-García, R., Lloret, F., Faus, J., Julve, M., Journaux, Y., Novak, M. A. Delgado, F. S., Ruiz-Pérez, C. Ligand design for heterobimetallic single-chain

magnets: Synthesis, crystal structures, and magnetic properties of MIICuII (M = Mn, Co) chains with sterically hindered methyl-substituted phenyloxamate bridging ligands. *Chem. - A Eur. J.* **13**, 2054–2066 (2007).

26. Ruiz, E., Rodríguez-Fortea, A., Alvarez, S. Tailor-Made Strong Exchange Magnetic Coupling through Very Long Bridging Ligands: Theoretical Predictions. *Inorg. Chem.* **42**, 4881–4884 (2007).

27. Kurmoo, M. Magnetic metal-organic frameworks. *Chem. Soc. Rev.* **38**, 1353–1379 (2009).

28. Ouellette, W., Prosvirin, A. V., Whitenack, K., Dunbar, K. R., Zubieta, J. A thermally and hydrolytically stable microporous framework exhibiting single-chain magnetism: Structure and properties of $[Co_2(H_{0.67}bdt)_3]\cdot 20H_2O$. *Angew. Chemie - Int. Ed.* **48**, 2140–2143 (2009).

29. Phan, H., Benjamin, S. M., Steven, E., Brooks, J. S., Shatruk, M. Photomagnetic response in highly conductive iron(II) spin-crossover complexes with TCNQ radicals. *Angew. Chemie - Int. Ed.* **54**, 823–827 (2015).

30. Ohkoshi, S. I., Tokoro, H. Photomagnetism in cyano-bridged bimetal assemblies. *Acc. Chem. Res.* **45**, 1749–1758 (2012).

31. Train, C. Gheorghe, R., Krstic, V., Chamoreau, L. M., Ovanesyan, N. S., Rikken, G., Gruselle, M., Verdaguer, M. Strong magneto-chiral dichroism in enantiopure chiral ferromagnets. *Nat. Mater.* **7**, 729–734 (2008).

32. Shakirova, O. G. Lavrenova, L. G., Shvedenkov, Y. G., Berezovskii, G. A., Naumov, D. Y., Sheludyakova, L. A., Dolgushin, G. V., Larionov, S. V. Synthesis and physicochemical study of Iron(II), Cobalt(II), Nickel(II), and Copper(II) complexes with 4-(2-Pyridyl)-1,2,4-triazole. *Russ. J. Coord. Chem. Khimiya* **30**, 473–479 (2004).

33. Hogue, R. W., Singh, S., Brooker, S. Spin crossover in discrete polynuclear iron(ii) complexes. *Chem. Soc. Rev.* **47**, 7303–7338 (2018).

34. Grosjean, A. Daro, N., Kauffmann, B., Kaiba, A., Létard, J. F., Guionneau, P. The 1-D polymeric structure of the $[Fe(NH_2trz)_3](NO_3)_2\cdot nH_2O$ (with n = 2) spin crossover compound proven by single crystal investigations. *Chem. Commun.* **47**, 12382–12384 (2011).

35. Fe, M. I. I. Garcia, Y., Bravic, G., Gieck, C., Chasseau, D., Tremel, W. Crystal Structure, Magnetic Properties , and ^{57}Fe Mossbauer Spectroscopy of the Two-Dimensional Coordination Polymers. **44**, 9723–9730 (2005).

36. Roubeau, O. Triazole-based one-dimensional spin-crossover coordination polymers. *Chem. - A Eur. J.* **18**, 15230–15244 (2012).

37. Ouellette, W., Yu, M. H., O'Connor, C. J., Hagrman, D., Zubieta, J. Hydrothermal chemistry of the copper-triazolate system: A microporous metal-organic framework constructed from magnetic $\{Cu_3(\mu_3\text{-}OH)(triazolate)_3\}^{2+}$ building blocks, and related materials. *Angew. Chemie - Int. Ed.* **45**, 3497–3500 (2006).

38. Wang, Y., Cheng, P., Song, Y., Liao, D. Z., Yan, S. P. Self-assembly and anion-exchange properties of a discrete cage and 3D coordination networks based on cage structures. *Chem. - A Eur. J.* **13**, 8131–8138 (2007).

39. Naik, A. D. Dĭrtu, M. M., Léonard, A., Tinant, B., Marchand-Brynaert, J., Su, B. L., Garcia, Y. Engineering three-dimensional chains of porous nanoballs from a 1,2,4-triazole-carboxylate supramolecular synthon. *Cryst. Growth Des.* **10**, 1798–1807 (2010).

40. Garcia, Y. Guionneau, P., Bravic, G., Chasseau, D., Howard, J.A.K., Kahn, O., Ksenofontov, V., Reiman, S., Gütlich, P. Synthesis, crystal structure, magnetic properties and ^{57}Fe Mossbauer spectroscopy of the new trinuclear $[Fe_3(4\text{-}(2'\text{-hydroxyethyl})\text{-}1,2,4\text{-triazole})_6(H_2O)_6](CF_3SO_3)_6$ spin crossover. *Eur. J. Inorg. Chem.* **3**, 0–7 (2000).

41. Kitchen, J. A., Brooker, S. Spin crossover in iron(II) complexes of 3,5-di(2-pyridyl)-1,2,4-triazoles and 3,5-di(2-pyridyl)-1,2,4-triazolates. *Coord. Chem. Rev.* **252**, 2072–2092 (2008).

42. Kitchen, J. A. White, N. G., Boyd, M., Moubaraki, B., Murray, K. S., Boyd, P. D.W., Brooker, S. Iron(II) tris-[N4-substituted-3,5-di(2-pyridyl)-1,2,4-triazole] complexes: Structural, magnetic, NMR, and density functional theory studies. *Inorg. Chem.* **48**, 6670–6679 (2009).

43. Molnár, G., Rat, S., Salmon, L., Nicolazzi, W., Bousseksou, A. Spin Crossover Nanomaterials: From Fundamental Concepts to Devices. *Adv. Mater.* **30**, 1–23 (2018).

44. Manrique-Juarez, M. D. Mathieu, F., Shalabaeva, V., Cacheux, J., Rat, S., Nicu, L., Leïchlé, T., Salmon, L., Molnár, G., Bousseksou, A. A Bistable Microelectromechanical System Actuated by Spin-Crossover Molecules. *Angew. Chemie - Int. Ed.* **56**, 8074–8078 (2017).

45. Senthil Kumar, K., Ruben, M. Emerging trends in spin crossover (SCO) based functional materials and devices. *Coord. Chem. Rev.* **346**, 176–205 (2017).

46. Haasnoot, J. G. Mononuclear, oligonuclear and polynuclear metal coordination compounds with 1,2,4-triazole derivatives as ligands. *Coord. Chem. Rev.* **200–202**, 131–185 (2000).

47. Depree, C. V., Beckmann, U., Heslop, K., Brooker, S. Monomeric, trimeric and polymeric assemblies of dicopper(II) complexes of a triazolate-containing Schiff-base macrocycle. *Dalt. Trans.* **15**, 3071–3081 (2003).

48. Klingele, M. H., Moubaraki, B., Cashion, J. D., Murray, K. S., Brooker, S. The first X-ray crystal structure determination of a dinuclear complex trapped in the [low spin-high spin] state: [FeII2(PMAT) 2](BF4)4·DMF. *Chem. Commun.* **2**, 987–989 (2005).

49. Meng, Z. S. Yun, L., Zhang, W. X., Hong, C. G., Herchel, R., Ou, Y. C., Leng, J. D., Peng, M. X., Lin, Z. J., Tong, M. L. Reactivity of 4-amino-3,5-bis(pyridin-2-yl)-1,2,4-triazole, structures and magnetic properties of polynuclear and polymeric Mn(II), Cu(II) and Cd(II) complexes. *Dalt. Trans.* **2**, 10284–10295 (2009).

50. Aromí, G., Barrios, L. A., Roubeau, O., Gamez, P. Triazoles and tetrazoles : Prime ligands to generate remarkable coordination materials. *Coord. Chem. Rev.* **255**, 485–546 (2011).

51. Tahli, A., MacLaren, J. K., Boldog, I., Janiak, C. Synthesis and crystal structure determination of 0D-, 1D- and 3D-metal compounds of 4-(pyrid-4-yl)-1,2,4-triazole with zinc(II) and cadmium(II). *Inorganica Chim. Acta* **374**, 506–513 (2011).

52. Li, W., Li, M. X., Shao, M., Wang, Z. X., Liu, H. J. Ferromagnetic and mixed-valence copper coordination polymers assembled by polycarboxylates and 2,6-bis(1,2,4-triazolyl)pyridine. *Inorg. Chem. Commun.* **11**, 954–957 (2008).

53. Ding, B. Yi, L., Wang, Y., Cheng, P., Liao, D. Z., Yan, S. P., Jiang, Z. H., Song, H. B., Wang, H. G. Synthesis of a series of 4-pyridyl-1,2,4-triazole-containing cadmium(ii) luminescent complexes. *J. Chem. Soc. Dalt. Trans.* **60**, 665665–675675 (2006).

54. Garcia, Y. Kahn, O., Rabardel, L., Chansou, B., Salmon, L., Tuchagues, J. P. Two-Step Spin Conversion for the Three-Dimensional Compound Tris(4,4'-bis-1,2,4-triazole)iron(II) Diperchlorate. *Inorg. Chem.* **38**, 4663–4670 (1999).

55. Boland, Y. Tinant, B., Safin, D. A., Marchand-Brynaert, J., Clérac, R., Garcia, Y. A metal-organic framework made of an asymmetric 1,2,4-triazole and tetrazole ligand. *CrystEngComm* **14**, 8153–8155 (2012).

56. Drabent, K., Ciunik, Z., Ozarowski, A. X-ray Crystal Structures, Electron Paramagnetic Resonance, and Magnetic Studies on Strongly Antiferromagnetically Coupled Mixed. *Inorg. Chem.* **47**, 3358–3365 (2008).

57. Roubeau, O. Alcazar Gomez, J. M., Balskus, E., Kolnaar, J. J.A., Haasnoot, J. G., Reedijk, J. Spin-transition behaviour in chains of FeII bridged by 4-substituted 1,2,4-triazoles carrying alkyl tails. *New J. Chem.* **25**, 144–150 (2001).

58. Gómez, V. Sáenz De Pipaón, C., Maldonado-Illescas, P., Waerenborgh, J. C., Martin,

E., Benet-Buchholz, J., Galán-Mascarós, J. R. Easy Excited-State Trapping and Record High TTIESST in a Spin-Crossover Polyanionic FeII Trimer. *J. Am. Chem. Soc.* **137**, 11924–11927 (2015).

59. Yang, J. Ma, Y. S., Tang, X. Y., Shen, L., Yuan, R. X., Zhuz, D. R. Two linear trinuclear clusters with bridging triazole:crystal structure and magnetism. *J. Coord. Chem.* **64**, 3291–3302 (2011).

60. Properties, B. M., Neutron, I. Software News and Updates. *J. Comput. Chem.* **2**, 665–672 (2000).

61. Borrás-Almenar, J. J., Clemente-Juan, J. M., Coronado, E., Tsukerblat, B. S. High-Nuclearity Magnetic Clusters: Generalized Spin Hamiltonian and Its Use for the Calculation of the Energy Levels, Bulk Magnetic Properties, and Inelastic Neutron Scattering Spectra. *Inorg. Chem.* **38**, 6081–6088 (1999).

62. Vos, G., Haasnoot, J. G., Verschoor, G. C., Reedijk, J., Schaminee, P. E. L. Linear trinuclear coordination compounds with 4-ethyl-1,2,4-triazole. Structure and magnetic properties. *Inorganica Chim. Acta* **105**, 31–39 (1985).

63. Baca, S. G. Sevryugina, Y., Clérac, R., Malaestean, I., Gerbeleu, N., Petrukhina, M. A. Linear trinuclear manganese(II) complexes: Crystal structures and magnetic properties. *Inorg. Chem. Commun.* **8**, 474–478 (2005).

64. Tong, Y. Z. Wang, Q. L., Si, M., Qi, J., Yan, S. P., Yang, G. M., Cheng, P., Liao, D. Z. Crystal structure, spectroscopy and magnetism of trinuclear nickel(II), cobalt(II) complexes and their solid solution. *Polyhedron* **30**, 3151–3157 (2011).

65. Siddiqui, K. A., Mehrotra, G. K., Mrozinski, J., Butcher, R. J. Anion assisted self-assembly of a Ni(II) complex into metallo-supramolecular network involving H-bonded synthons as nodes. *J. Mol. Struct.* **964**, 18–26 (2010).

66. Ding, B. Yi, L., Shen, W. Z., Cheng, P., Liao, D. Z., Yan, S. P., Jiang, Z. H. Synthesis, crystal structure and magnetic properties of N1,N2-bridged polynuclear Ni(II) complexes. *J. Mol. Struct.* **784**, 138–143 (2006).

67. Aznar, E. Ferrer, S., Borrás, J., Lloret, F., Liu-González, M., Rodríguez-Prieto, H., García-Granda, S. Coordinative versatility of guanazole [3,5-diamino-1,2,4-triazole]: Synthesis, crystal structure, EPR, and magnetic properties of a dinuclear and a linear trinuclear copper(II) complex containing small bridges and triazole ligands. *Eur. J. Inorg. Chem.* 5115–5125 (2006).

68. Dumestre, F. Soula, B., Galibert, A-M., Fabre, P.-L. F., Bernardinelli, G., Donnadieu, C., Castan, P. Synthesis and characterization of cobalt(II) complexes of croconate and dicyanomethylene-substituted derivatives. *J. Chem. Soc., Dalt. Trans.* **30**, 4131–4137 (1998).

69. Lines, M. E. Orbital angular momentum in the theory of paramagnetic clusters. *J. Chem. Phys.* **55**, 2977–2984 (1971).

70. Oka, Y., Inoue, K. Structures and Magnetic Properties of a New Cobalt(II) Linear Trimer with Phenylcinnamic Acid. *Chem. Lett.* **33**, 402–403 (2004).

71. Gómez, V., Benet-Buchholz, J., Martin, E., Galán-Mascarós, J. R. Hysteretic spin crossover above room temperature and magnetic coupling in trinuclear transition-metal complexes with anionic 1,2,4-triazole ligands. *Chem. - A Eur. J.* **20**, 5369–5379 (2014).

72. Papaefstathiou, G. S. Perlepes, S. P., Escuer, A., Vicente, R., Font-Bardia, M., Solans, X. Unique Single-Atom Binding of Pseudohalogeno Ligands to Four Metal Ions Induced by Their Trapping into High-Nuclearity Cages *Angew. Chem. Int. Ed. Engl.* **40**, 884–886 (2001).

73. Papaefstathiou, G. S. Escuer, A., Vicente, R., Font-Bardia, M., Solans, X., Perlepes, S. P. Reactivity in polynuclear transition metal chemistry as a means to obtain high-spin molecules: Substitution of μ4-OH− by η1,μ4-N3− increases nine times the ground-state S value of a nonanuclear nickel(II) cage. *Chem. Commun.* **1**, 2414–2415 (2001).

74. Stamatatos, T. C. Papaefstathiou, G. S., Macgillivray, L. R., Escuer, A., Vicente, R., Ruiz, E., Perlepes, S.P. Ferromagnetic Coupling in a 1D Coordination Polymer Containing a Organic Ligand Obtained from the Solid State. *Inorg. Chem.* **46**, 8843–50 (2007).

75. Slangen, P. M., van Koningsbruggen, P. J., Goubitz, K., Haasnoot, J. G., Reedijk, J. Isotropic Magnetic Exchange Interaction through Double μ-1,2,4-Triazolato-N1,N2 Bridges: X-ray Crystal Structure, Magnetic Properties, and EPR Study of Bis(μ-3-pyridin-2-yl-1,2,4-triazolato-N′,N1,N2)(sulfato-O)aquacopper(II)diaquacopper(II) Trihydrate. *Inorg. Chem.* **33**, 1121–1126 (1994).

76. Bencini A Gatteschi, D., Zanchini C. Haasnoot, J. G., Prins, R., Reedijk, J. EPR Spectra of Binuclear Triazolato- and Imidazolato-Bridged Copper(II) Complexes Including the Four-Copper Form of Bovine Erythrocyte Superoxide Dismutase. *Inorg. Chem.* **24**, 2812–2815 (1985).

77. Slangen, P. M. van Koningsbruggen, P. J., Haasnoot, J. G., Jansen, J., Gorter, S., Reedijk, J., Kooijman, H., Smeets, W.J.J., Spek, A. L. Synthesis, characterization, crystal structures and magnetic properties of di- and polynuclear bis(μ-3-pyridin-2-yl-1,2,4- triazolato)copper(II) compounds containing N-methylimidazole, pyrazole or 4,4′-bipyridine as co-ligands. *Inorganica Chim. Acta* **212**, 289–301 (1993).

78. Garcia, Y. Garcia, Y., van Koningsbruggen, P. J., Bravic, G., Guionneau, P., Chasseau,

D.,Cascarano, G. L., Moscovici, J., Lambert, K., Michalowicz, A., Kahn, O. Synthesis, Crystal Structure, EXAFS, and Magnetic Properties of catena -Poly[μ-tris(4-(2-hydroxyethyl)-1,2,4-triazole- N 1 , N 2)copper(II)] Diperchlorate Trihydrate: Relevance with the Structure of the Iron(II) 1,2,4-Triazole Spin Transition Molecular. *Inorg. Chem.* **36**, 6357–6365 (1997).

79. Oudenniel, W. M. E. K., Graaff, R. A. G. De, Haasnoot, J. G., Prins, R., Reedijk, J. Magnetic and Spectroscopic Properties of Copper(II) Compounds with Alkyl-Disubstituted Triazoles. X-ray Structure of Bis[4amino-3,5-bis(aminomethyl)- 1,2,4-triazole-,N',N1,N2,N''bis[aqua bromo copper(II)] Dibromide-2- Water-Methanol. **28**, 1128–1133 (1989).

80. Ding, B., Huang, Y. Q., Liu, Y. Y., Shi, W., Cheng, P. Synthesis, structure and magnetic properties of a novel 1D coordination polymer {[Cu2(amtrz)4(1,1-μ-NCS)2](ClO4)2 · H2O}n. *Inorg. Chem. Commun.* **10**, 7–10 (2007).

81. Spek, A. L. PLATON SQUEEZE: a tool for the calculation of the disordered solvent contribution to the calculated structure factors . *Acta Crystallogr. Sect. C Struct. Chem.* **71**, 9–18 (2015).

82. Coelho, A. A., Evans, J., Evans, I., Kern, A., Parsons, S. The TOPAS symbolic computation system. *Powder Diffr.* **26**, S22–S25 (2011).

UNIVERSITAT ROVIRA I VIRGILI
BISTABLE MOLECULAR MATERIALS: TRIAZOLE-BASED COORDINATION CHEMISTRY OF FIRST ROW TRANSITION METALS
Andrea Moneo Corcuera

Chapter 3

Tuning the SCO Behavior of the polyanionic Fe^{II} trimer via cation exchange

Abstract

The magnetic behavior of the polyanionic iron (II) trimer $[Fe_3(\mu\text{-}L)_6(H_2O)_6]^{6-}$ (L^{2-}= (1,2,4-triazol-4-yl)ethanedisulfonate), as the corresponding dimethylammonium salt (**1**), exhibits an interesting thermally-induced spin crossover (SCO) behavior. The spin transition occurs above room temperature, with a dynamic and wide thermal hysteresis over 85 K. In addition, it presents a temperature-induced excited spin state trapping (TIESST) phenomena at 250 K, the highest temperatures reported so far. Taking advantage of the anionic nature of this trinuclear complex, we have substituted the dimethylammonium cations by monovalent heavy alkali metal cations (Cesium and Rubidium) via simple methathesis reactions. The cation exchange resulted in $Cs_6[Fe_3(\mu\text{-}L)_6(H_2O)_6]$ and $Rb_6[Fe_3(\mu\text{-}L)_6(H_2O)_6]$ salts, with different crystal packing and SCO features relative to the dimethyl ammonium salt. Both compounds present more abrupt spin transition above room temperature, but narrower hysteresis loop (over 50 K for the cesium salt and 60 K for the rubidium salt). Albeit these differences, TIESST is observed with almost identical characteristic temperature (T_{TIESST} ≈ 250 K), an additional experimental evidence supporting the molecular-origin of the TIESST behavior in these materials.

3.1. Introduction

One of the main challenges in molecular material science is the design of molecules with bistability to be utilized for information processing and storage.[1–5] The bistability in this context may be defined as a property of a molecular system that allows it to exist in two different electronic states over a certain range of external perturbation. The most well-known example is the spin crossover phenomena involving the switching between the low spin (LS) and the high spin (HS) metastable excited state in octahedral $3d^4$-$3d^7$ transition metal complexes.[6–12] Such spin conversion is controlled through an external stimulus such as temperature, pressure, light or magnetic field. Several transition metal centers, e.g. $Co^{II/III}$, $Mn^{II/III}$, $Ni^{II/III}$ or Cr^{II}, are able to display this phenomena [13–19]. However, most studies in this field have been focused on Fe^{II} compounds, where the switching between LS and HS states (Fe^{II}_{LS} (S=0); Fe^{II}_{HS} state (S = 2)) brings drastic magnetic variation and some additional changes including spectroscopic properties and molecular volume.[20,21] In the solid state, these materials may show true memory effect. For example, Fe^{II} complexes have shown interesting features such as wide thermal hysteresis,[22] ultrafast photoinduced spin switching,[23–25] or bistability in electromechanical properties.[26,27]Due to these reasons, SCO materials could be promising candidates for the implementation of SCO molecules into molecular electronics, data storage and display devices.[22,26,28–31]

In this direction, numerous effort have thus been directed to prepare SCO materials with proper features for real applications: abrupt spin transition and bistability at ambient conditions. From a synthetic point of view, the spin transition and thermal hysteretic behavior can be tuned at and well above room temperature by controlling the local coordination environment of the metal ion (i.e. ligands in the first coordination sphere) and its external sphere,[32–36] being also of primary importance in order to probe structure-magnetic properties relation.

Alternatively, a common strategy to optimize the SCO behavior consist in the modulation of cooperative forces between SCO centers, taking the advantage of the lattice-dynamic role in the spin transition.[37–39] Indeed, the manipulation of non-covalent interactions between SCO units is used to promote different solid-state cooperativity. For example, a simple change in solvent content (desorption/absorption or solvent change) or non-coordinated counter-ions may drastically change the magnetic properties in a large range of SCO materials, as observed in the case of metal organic frameworks,[40] coordination polymers[41] or mononuclear complexes.[42–47]

As mentioned in the first chapter, our group is interested in anionic SCO complexes, that are very scarce in comparison with cationic or neutral ones.[48] Among the series of polyanionic first-row transition metal complexes described in Chapter 2, the iron (II) analogue $(Me_2NH_2)_6[Fe_3(\mu\text{-}\mathbf{L})_6(H_2O)_6]$ L^{-2}:4-(1,2,4-triazol-4-yl)ethanedisulfonate (**1**), exhibits an additional SCO behavior.[49,50] Its molecular structure is formed by a linear array of three octahedral Fe(II) centers, bridged by two triple 1,2,4-triazole bridges. The crystallographic packing of this complex consist in anionic trimers connected by H-bonds, whereas the dimethyl ammonium cations and water molecules are disordered in the interstices. In the solid state, as the corresponding dimethyl ammonium $(Me_2NH_2)^+$ salt, a thermally induced spin transition from LS to HS state above room temperature was found for the central Fe(II), with a hysteresis cycle of 85 K at very slow scan rate (1 K·min^{-1}). A characteristic T_{TIESST} of 250 K was determined, which is the highest T_{TIESST} reported up to date. [51]

Taking the advantage of the interesting SCO behavior of **1** and the high influence of crystal structure in the spin transition phenomena, we studied how the substitution of the dimethyl ammonium cations by other cation type might influence the bistability and switchability of these trimeric units. By analogy to counter-anion effects in cationic SCO complexes.[41–43,52–54]

In this chapter, we describe how simple metathesis in aqueous solution of **1** with an excess of a Cs^+ or Rb^+ salts yields the corresponding Cs^+ (**1-Cs**) or Rb^+ (**1-Rb**) salts , that we were able to isolate as single crystals. These salts present distinct magnetic features, confirming that the nature and size of the cations induces different crystallographic packing, affecting the SCO behavior.

3.2. Results

3.2.1. Synthesis and crystal structure

Single crystals of **1-Cs** and **1-Rb** compounds were obtained by ethanol slow vapor diffusion into an aqueous solution of **1** with a 20-fold excess of cesium chloride and rubidium chloride, respectively (see detailed procedure in the experimental section). This reaction yields pink needle-like single crystal of **1-Cs** and **1-Rb**, Figure 3.1.

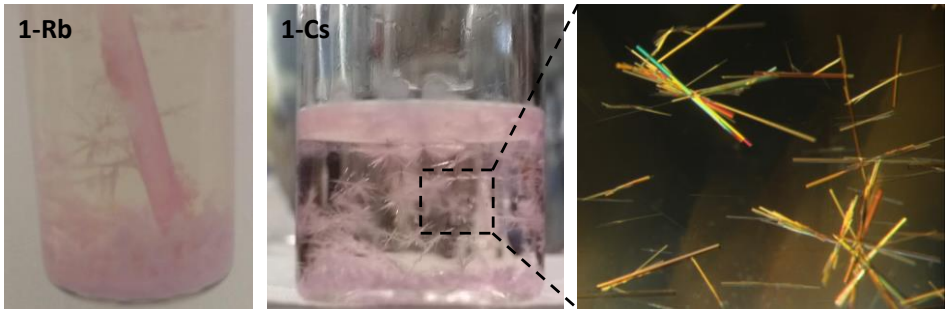

Figure 3.1. *Picture of **1-Rb** and **1-Cs** crystals in aqueous solution after the ethanol vapor diffusion. (Right) Image from an optical microscope, evidencing the needle-like shape of the crystals.*

The crystal structure of both complexes was determined by single crystal X-Ray Diffraction (SCXRD) data. These single crystals contain the same trinuclear polyanion, $[Fe_3(\mu\text{-}L)_6(H_2O)_6]^{6-}$ (Figure 3.2) than the parent compound (**1**),[49] where all dimethylammonium cations have been substituted by Cs^+/Rb^+ cations. The metal to ligand distances obtained at 100 K reveal the spin state of the metal centers to be high spin (HS) for terminal Fe1 position (average Fe1-N distance: 2.19 Å for **1-Cs** and 2.16 Å for **1-Rb**) and low spin (LS) for central Fe2 positions (average Fe2-N distance: 1.97 Å for **1-Cs** and 1.98 Å for **1-Rb**), see Table 3.1.

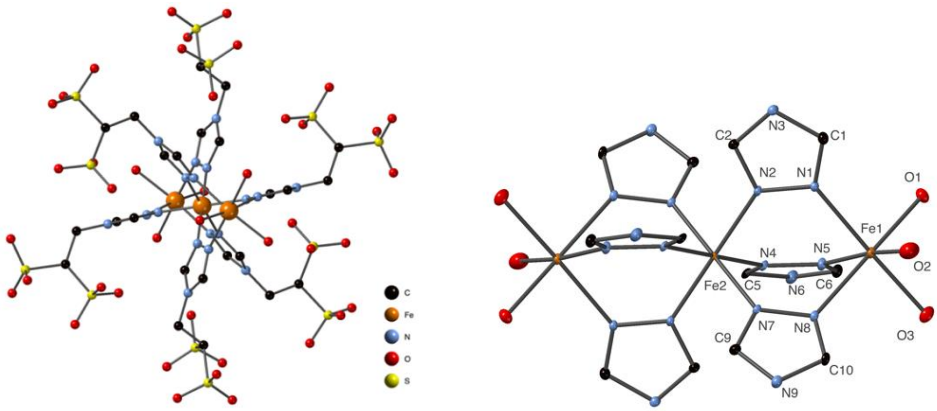

Figure 3.2. *(Left) Molecular structure of* $[Fe_3(\mu\text{-}L)_6(H_2O)_6]^{6-}$ *anionic part. (Right) Labelled ORTEP representation of the core trimer showing the triple triazole-bridges and terminal water molecules. (H atoms have been omitted for clarity).*

Table 3.1. *Selected bond lengths (Å) of* ***1-Cs*** *and* ***1-Rb*** *complexes.*

Bond Length (Å)	1-Cs	1-Rb
Fe1-O1	2.076(5)	2.054(3)
Fe1-O2	2.173(6)	2.130(2)
Fe1-O3	2.098(6)	2.1651(4)
Fe1-N1	2.174(6)	2.166(2)
Fe1-N5	2.184(7)	2.150(2)
Fe1-N8	2.199(6)	2.164(2)
Fe2-N7	1.961(6)	1.997(2)
Fe2-N4	1.968(6)	1.971(2)
Fe2-N2	1.976(6)	1.974(2)

This polyanionic unit crystallizes with six monovalent cations (Cs^+ or Rb^+) and non-coordinating water molecules in a monoclinic (C2/c) symmetry for **1-Cs** or triclinic (P–1) symmetry for **1-Rb** (see crystallographic data in Table 3.2).

Table 3.2. *Crystallographic data for **1-Cs** and **1-Rb** single crystals.*

	1-Cs	1-Rb
Chemical formula	$C_{24}H_{68}Cs_6Fe_3N_{18}O_{55}S_{12}$	$C_{24}H_{40}Rb_6Fe_3N_{18}O_{52}S_{12}[+xH_2O]$
Formula weigh	2838.69	2477.83
T(K)	100(2)	100(2)
Crystal system	Monoclinic	Triclinic
Space group	C2/c	P -1
Crystal size	0.01x0.02x0.4	0.4x0.02x0.01
a(Å)	34.4273(12)	11.2345(3)
b(Å)	11.4107(4)	14.5696(3)
c(Å)	26.1316(9)	15.2673(4)
α(°)	90	73.673(2)
β(°)	128.2290(8)	84.148(2)
γ(°)	90	70.911(2)
V (Å^3)	8064.0(5)	2266.2(1)
Z	4	1
ρ_{calcd} (g cm^{-3})	2.338	1.815
μ (mm^{-1})	3.631	4.064
F (000)	5512	1356
Reflections collected	38646	35096
Indep. Reflections	9659	14444
Abs. correction	Empirical	Empirical
θ range (°)	1.583-28.010	1.898-31.659
Index ranges	-45 ≤ h ≤ 44	-15 ≤ h ≤ 16
	-14 ≤ k ≤ 12	-21 ≤ k ≤ 20
	-32 ≤ l ≤ 34	-22 ≤ l ≤ 21
Data/restr/para.	9659/ 921/585	14444/0/533
Goodnesss-of-fit	1.028	1.023
R1 (I>2σ(I))	0.0684	0.0438
wR2 (I>2σ(I))	0.1988	0.1145

Despite these differences, both complexes present comparable crystallographic packing. The cations and anions form segregated layers, following an ABAB stacking pattern. (Figure 3.3 for **1-Cs** and Figure 3.4 for **1-Rb**). The cations layer are localized close to the sulfonated groups of the anionic layer.

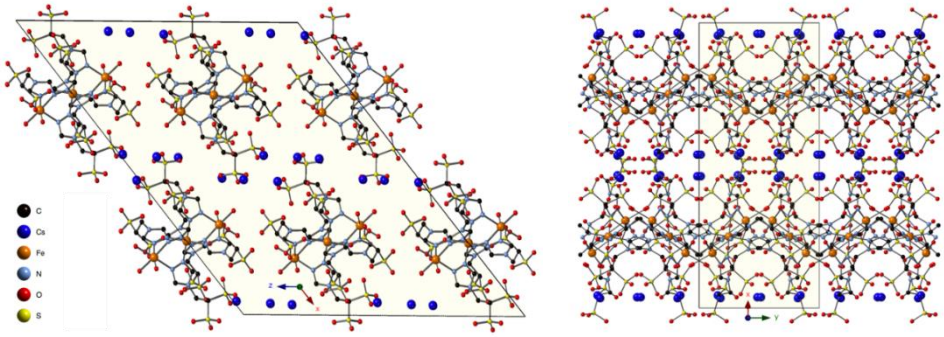

Figure 3.3. *Projection of the crystal structure of **1-Cs** on the ac plane (left) and the ab plane (right), showing the stacking of alternating layers along the a axis.*

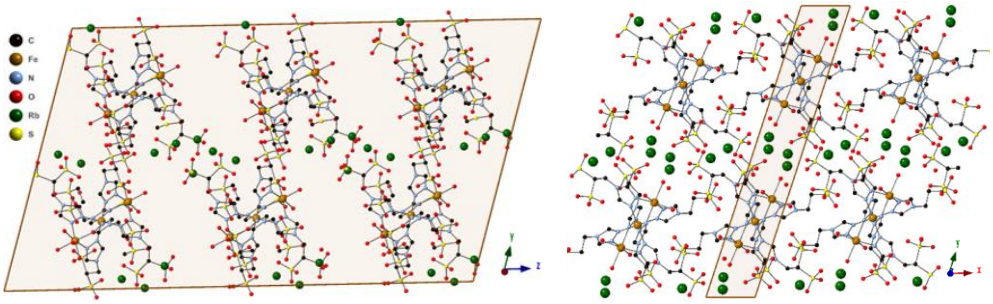

Figure 3.4. *Stacking of alternatives anionic and cationic layers of **1-Rb** along the b axis in the bc plane (left) and in the ab plane (right). (Solvation water molecules and H atoms have been omitted for clarity).*

Along the anionic layer, the adjacent trimers are connected by Hydrogen-interactions, in which participate the oxygen atoms from the sulfonated groups and from the coordinated water molecules, Figure 3.5. The cesium and rubidium salts present multiple intermolecular H-bond interactions with very short H-bond contacts in the range of 2.69 - 2.95 Å. The **1-Cs** compound presents a pseudo-hexagonal structure of the anionic layers, with each trimer surrounded by six near neighbors. The **1-Rb** compound shows a less dense intralayer H-bonded network with each trimer surrounded by four neighbors. The sulfonate groups that do not participate in these H-interactions point towards the cation layers.

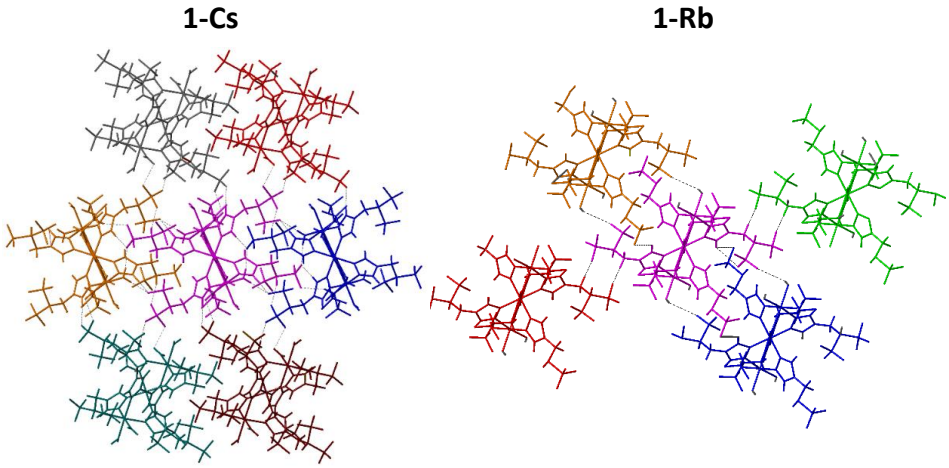

Figure 3.5. *Top view of the anionic layer for 1-Cs and 1-Rb complexes, showing the arrangements of the trimers and their closest H-contacts (dotted lines). Trimers are in a different color for clarity.*

The cationic layers in **1-Cs** are formed by two parallel planes of cations separated by 2.1(1) Å, while **1-Rb** shows two zig-zag planes of Rb^+ cations separated by 2.7(1) Å, Figure 3.6 top. In both compounds, each cation has short contacts with both adjacent anionic layers, connecting them by $Cation^+ \cdots {}^-O_3S$ and $Cation^+ \cdots OH_2$ distances in the 2.9 - 3.4 Å range. There are three crystallographic cationic positions in both salts, with different coordination modes, Figure 3.6 bottom. In the cesium salt, Cs1 is heptacoordinated, surrounded by three SO_3 groups in monodentate coordination mode, and four water molecules. Cs2 is octacoordinated, by six SO_3 groups (one acting as bidentate ligand) and one water molecule. And Cs3 is heptacoordinated to four SO_3 groups (one acting as bidentate ligand), and two water molecules. In the Rb salt, Rb1 is octacoordinated by six SO_3 groups (two in bidentate coordination mode) and two water molecules. Rb2 is hexacoordinated by four SO_3 groups and two water molecule. And Rb3 is tetracoordinated surrounded by three sulfonate groups and one water molecule, see summarized data in Table 3.3.

Noteworthy, these interactions allows to communicate the trimers between layers with direct O···Cation^{+}···O contacts.

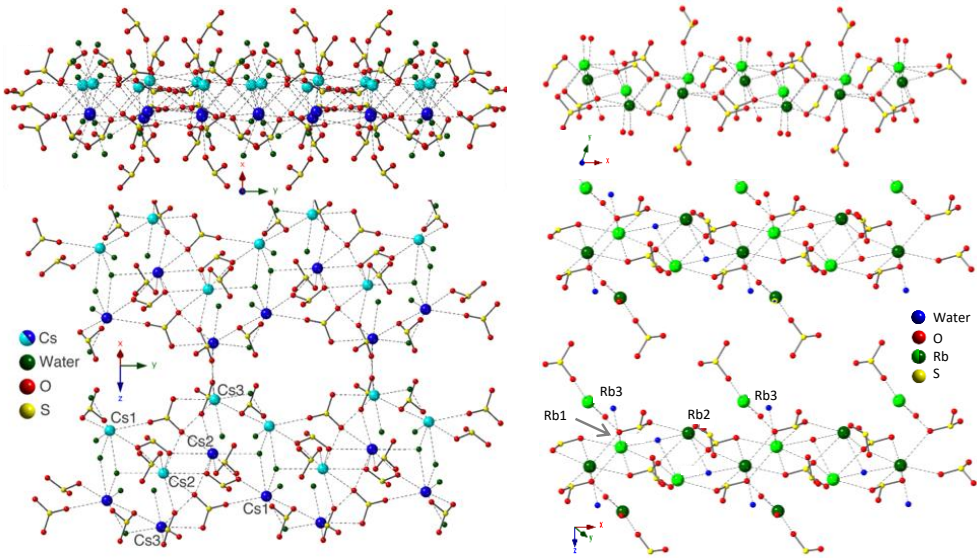

Figure 3.6. *Side and top views of the cationic layer, showing the Cation^{+}···O contacts in the range of 2.9 - 3.4 Å, as dotted lines. The cations are represented in two colors, to highlight the two cationic planes.*

Table 3.3. *Summarized data of the different crystallographic cations in **1-Cs** and **1-Rb**.*

Crystallographic Positions	1-Cs	1-Rb
Cation 1	Heptacoordinated 3 Cs^{+}…OSO_3	Sixcoordinated 6 Rb^{+}…OSO_3
Cation 2	Octacoordinated 6 Cs^{+}…OSO_3	Octacoordinated 4 Rb^{+}…OSO_3
Cation 3	Heptacoordinated 4 Cs^{+}…OSO_3	Tetracoordinated 3 Rb^{+}…OSO_3

Powder X-Ray diffraction data of the polycrystalline samples are in good agreement with the theoretical pattern obtained from the single crystal structures, confirming the single crystallographic phase of these compounds (Figure 3.7). Indeed, a Pawley-fitting with TOPAS software was carried out on the experimental powder X-ray pattern, obtaining similar refined-lattice parameters than the values obtained from SCXRD data, Table 3.4. This evidences that the crystal structures of one single crystal is also retained in a bulk samples of grained-crystals, with non-evidences of crystalline impurities.

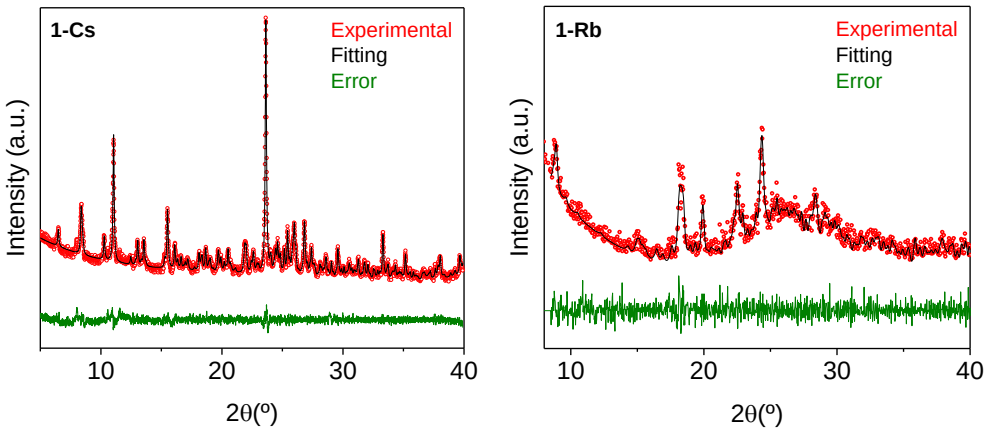

Figure 3.7. *Experimental XRD and their corresponding Pawley fit for **1-Cs** (left) and **1-Rb** (right). (R_{wp}=4.29 and R_{exp}=2.95 for **1-Cs**; R_{wp}=9.43 and R_{exp}=4.73 for **1-Rb**).*

Table 3.4. *Lattice parameters and cell volume from PXRD pattern and SCXRD data.*

	1-Cs		1-Rb	
Cell Parameters	PXRD	SCXRD	PXRD	SCXRD
a(Å)	34.26(4)	34.427(1)	11.15(7)	11.234(3)
b(Å)	11.38(1)	11.4107(4)	14.64(6)	14.569(3)
c(Å)	26.13(3)	26.1316(9)	15.23(7)	15.267(4)
α(°)	90	90	74.4(2)	73.673(2)
β(°)	127.98(1)	128.2290(8)	83.1(3)	84.148(2)
γ(°)	90	90	70.1(3)	70.911(2)
V (Å^3)	8030(2)	8064.0(5)	2256(22)	2266.2(1)

3.2.2. Magnetic Measurements

The magnetic properties of grained single crystals of **1-Cs** and **1-Rb** were studied in the 200 - 400 K range. Dehydration/hydration effect in the magnetic cycles have been discarded by proper dehydrating the sample (purging cycles and heating) before the measurements.

Cesium Salt

Thermal dependence of magnetic susceptibility of **1-Cs** (Figure 3.8) shows a thermally-induced spin transition above room temperature. The $\chi_m T$ product at room temperature is 6.0 $cm^3 \cdot mol^{-1} \cdot K$, in good agreement with two HS Fe^{II} centers per trimer. At very slow temperature scan rate (0.3 $K \cdot min^{-1}$), this value remains constant in the 200 - 350 K temperature range. Above 350 K, $\chi_m T$ shows a sharp increase, indicating the existence of a spin transition. This transition to the HS-HS-HS state is two step, first a sharp increase to 8.1 $cm^3 \cdot mol^{-1} \cdot K$ at 354 K, with a $T_{1/2}(\uparrow)$ = 352 K, and a second more gradual increase reaching 9.2 $cm^3 \cdot mol^{-1} \cdot K$ at 400 K. This second regime shows slow kinetics, and at 400 K (the highest T available in our set-up), about 140 min are needed to reach saturation (see Figure 3.8 inset). According to these values, about 2/3 of the SCO centers participate in the abrupt process, but all anions reach the thermally induced HS – HS – HS state after the gradual transition is over. When temperature is decreased at the same scan rate (0.3 $K \cdot min^{-1}$), a thermal hysteresis cycle opens for both regimes. The gradual step closes just below 300 K, where the abrupt transition drives the compound back to the ground state with $T_{1/2}(\downarrow)$ = 305 K. This creates a thermal hysteresis cycle of 47 K for the abrupt regime. We assign the gradual regime to a less-cooperative contribution that could be due to defects in the crystal, surface effects, or to the appearance of two crystallographically distinct trimers upon the abrupt step.

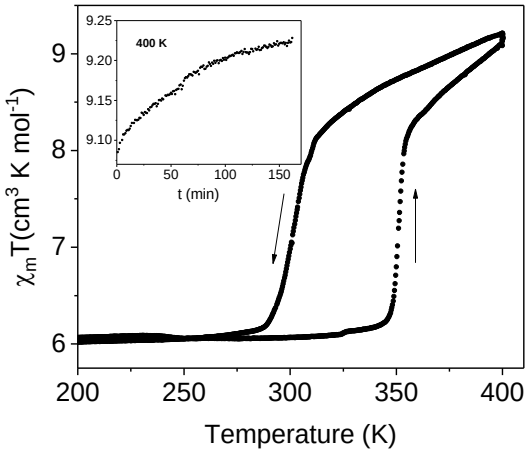

Figure 3.8. *$\chi_m T$ vs T plot for* **1-Cs** *during the heating and cooling processes at 0.3 K·min^{-1}. The sample was kept at 400 K for 140 minutes to reach saturation (inset).*

The hysteresis cycle in **1-Cs** is very sensitive to the scan rate (Figure 3.9 left), as in the dimethyl ammonium salt.[36,55] The hysteresis width changes from 47 K at 0.3 K·min^{-1} to 65 K at 2 K·min^{-1}. The effect upon the cooling branch is particularly significant, and the signature of temperature induced excited spin state trapping (TIESST) is already apparent. At faster cooling rates, the compound is not able to relax to the ground state, trapping a portion of molecules in the HS-HS-HS state. About 8% at 2·K min^{-1} (low temperature value of 6.25 cm^3 K·mol^{-1}), 40% at 5 K·min^{-1}, and 52 % at 10 K·min^{-1}. A characteristic T_{TIESST} = 245 K was estimated following the method established by Letard et al[56], Figure 3.9 right.

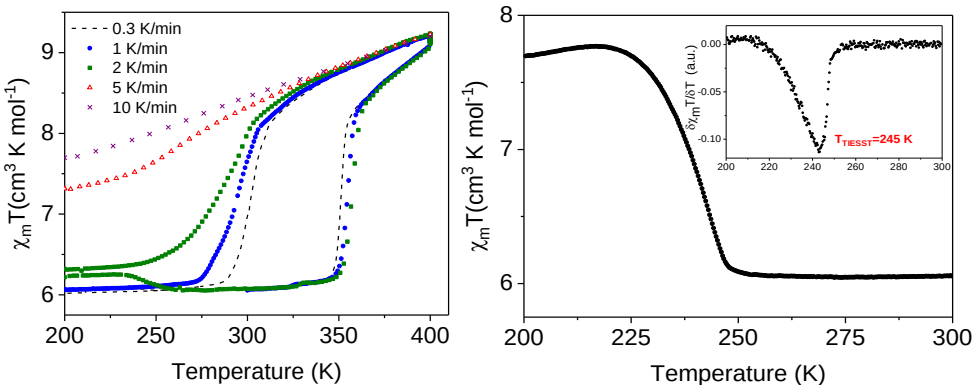

Figure 3.9. *(Left)Thermal hysteresis cycles for compound **1-Cs** at different scan rates. (Right) Heating branch (at 0.3 K min^{-1}) after trapping the sample via fast cooling. (Inset) Derivate of the heating data that allows to extract the T_{TIESST}.*

Rubidium Salt

The $\chi_m T$ product at room temperature for **1-Rb** is 6.3 cm^3·mol^{-1}·K, Figure 3.10. Upon heating, a gradual spin transition starts immediately, becoming abrupt above 375 K, $T_{1/2}(\uparrow)$ = 390 K. At 400 K, saturation is reached after 100 minutes, accounting for ≈76 % of the trimers in HS-HS-HS ($\chi_m T$ = 8.3 cm^3·mol^{-1}·K), Figure 3.10 inset. Upon cooling down the sample, a wide hysteresis cycle appears. This spin conversion occurs also in two steps, as an abrupt process down to 320 K with $T_{1/2}(\downarrow)$ = 325 K, with a hysteresis loop of 55 K, and a second gradual step that closes at ≈250 K.

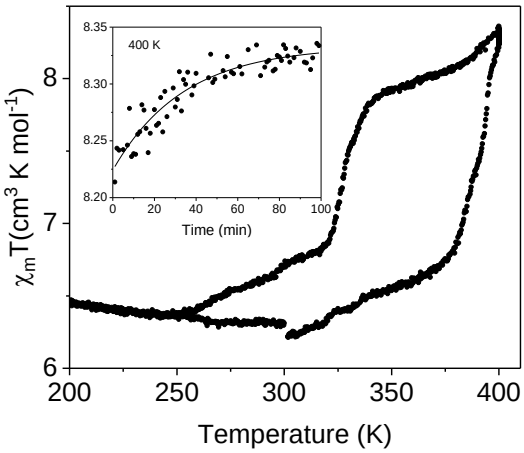

Figure 3.10. *Thermal dependence of the magnetic susceptibility for **1-Rb** sample during the heating and cooling processes at 0.3 K·min^{-1}. The sample was kept at 400 K for 100 minutes to reach saturation (inset).*

In this case, the hysteresis cycle does not show significant scan rate dependence below 5 K·min^{-1}. At faster scan rates, the transition temperature, $T_{1/2}\downarrow$, shifts to lower temperatures, resulting in wider hysteresis loops (87 K at 5 K·min^{-1} and 100 K at 10 K·min^{-1}). However, the metastable HS-HS-HS excited state is not easily trapped by rapid cooling. Only 16 % of the SCO Fe^{II} centers are trapped in the HS state after cooling down at 10 K·min^{-1}. Despite this, the characteristic TIESST temperature is in good agreement with the dimethyl ammonium and cesium salt, giving a value around 250 K, Figure 3.11 right.

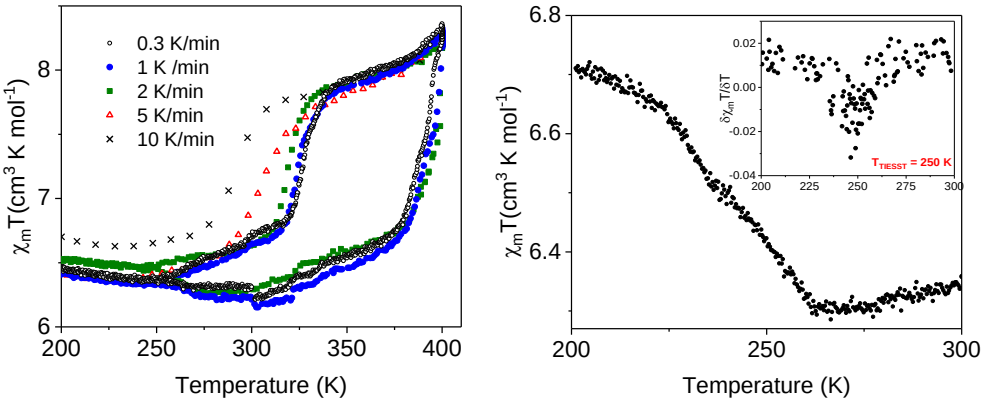

Figure 3.11. *(Left) Thermal hysteresis cycles at different scan rates for **1-Rb**. (Right) χT evolution by warming the sample at 0.3 K·min^{-1} trapping the sample via fast cooling (scan rate 10 K·min^{-1}). (Inset) The derivate of the curve that allows to extract the TIESST temperature.*

3.2.3. Further characterization

The dehydration process and the stability of the samples was studied by thermogavimetric analysis (TGA) from 25 to 300ºC, Figure 3.12. Interstitial solvent molecules are lost upon heating below 130°C (first step), and the bound water molecules start to be removed above 160°C (second step). The gravimetric plateau above 220°C, stable at least up to 300°C, correspond to a total weight loss around 8.7 % for both samples, indicating that not all water molecules are lost even at such high temperatures. In addition, it also reveals that these complexes shows very high thermal stability, with no decomposition of the organic matter in this temperature range.

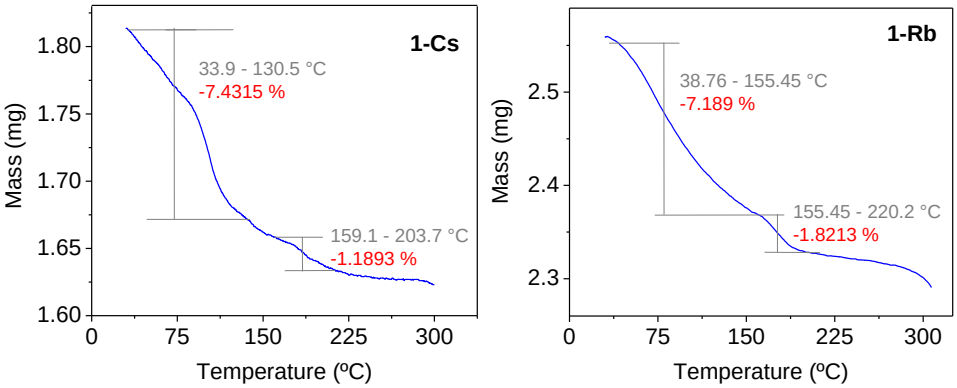

Figure 3.12. *TGA analysis for **1-Cs** and **1-Rb** from 25 to 300ºC at 1 C^{o}·min^{-1}.*

Differential Scanning Calorimetry (DSC) analysis within 20 – 120ºC temperature range (Figure 3.13) detected some dehydration processes during the first heating. But successive cycles did not show any feature that could be assigned to a crystallographic phase transition associated to spin transition.

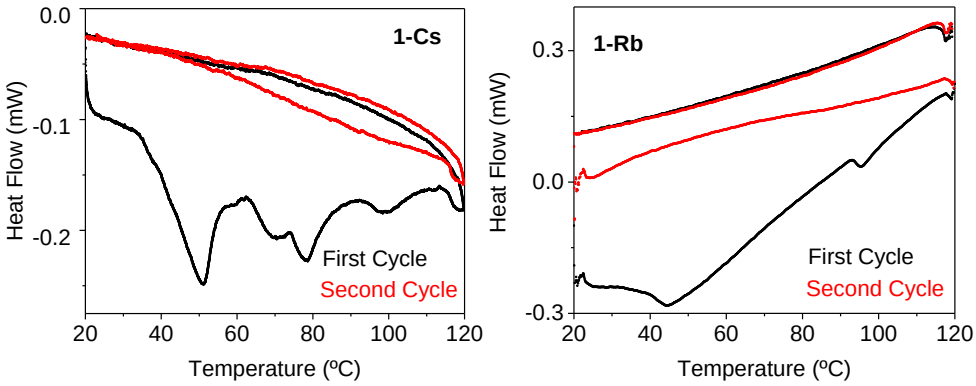

Figure 3.13. *DSC measurements for **1-Cs** and **1-Rb** in successive cycles within 20- 120ºC range at 1 K·min^{-1}.*

In the same direction, X-ray Diffraction from the same samples that were used for multiple thermal hysteresis measurements (four cycles in the 200-400 K range) confirms that the crystal structure is robust and preserved after these thermal treatment (Figure 3.14), and after partial dehydration, supporting that no major structural changes are occurring.

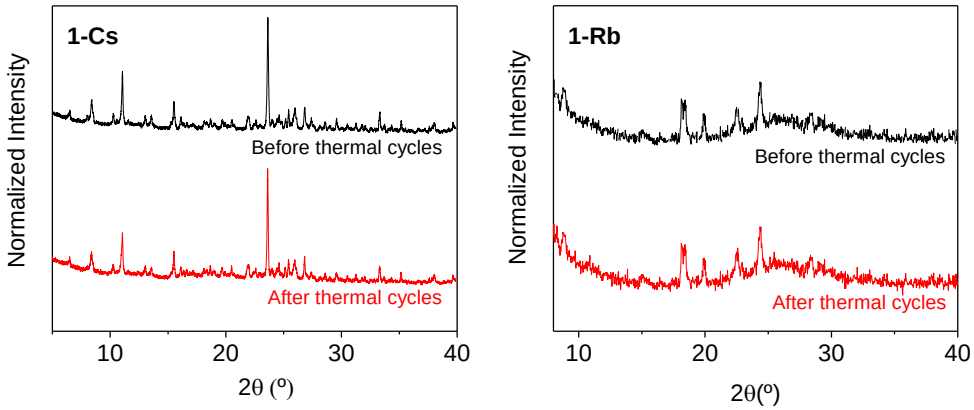

Figure 3.14. *PXRD pattern for **1-Cs** and **1-Rb** before and after multiple thermal cycles in 200 - 400 K range.*

3.3. Discussion

The polyanionic Fe^{II} trimer as cesium, rubidium or dimethylammonium salts show significant differences regarding the crystal packing. The crystal structure of cesium and rubidium salts show lower crystallographic disorder in the position of the cations due to the localization of these heavier atoms. This also localizes and strengthens the intermolecular interactions network in the crystal packing with strong and directional anionic interlayer interactions mediated by the Cs^+/Rb^+ cations, absent in the dimethyl ammonium salt. Additionally, the cesium salt presents stronger connectivity between intra-layer trimers, increasing the H-contacts from four up to six nearest neighbors, which involves higher interaction between trimers in all crystallographic directions.

Looking at the crystal structure, higher SCO cooperativity is expected in this order: Cs salt > Rb salt > $NH_2(Me)_2$ salt. This is in good agreement with the magnetic data, since cooperativity is related to abrupt spin transitions. **1-Cs** shows the most abrupt and complete SCO behavior, followed by **1-Rb** (Figure 3.15). Additionally, SCO behavior moves to lower temperatures in **1-Cs** complex. Cooperativity is also expected to increase the thermal hysteresis cycles. On the contrary, the thermal hysteresis width decreases from 80 K for (**1**) down to 50 K for **1-Cs**. This observation is counterintuitive, and does not follow the common correlations established for cooperative spin crossover materials.[57,58] This along with the unexpectedly high T_{TIESST} (record values in SCO phenomena) suggests the appearance of unknown factors not previously observed in these materials.

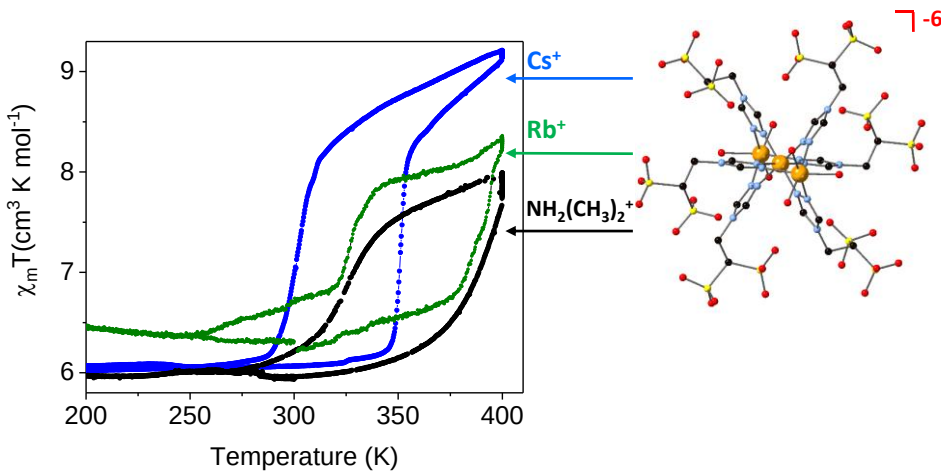

Figure 3.15. *Comparison of the hysteresis cycle at 0.3 K·min^{-1} for polyanionic Fe^{II} trimer with different cations (dimethyl ammonium, cesium or rubidium cations)*

3.4. Conclusions

Cesium and rubidium salts of the polyanionic trimer $[Fe_3(\mu\text{-}L_6)(H_2O)_6]^{6-}$ were isolated by complete substitution of the dimethyl ammonium cations by metathesis in solution with an excess of Cs^+ or Rb^+ cations, respectively. Their crystal structure revealed lower cation disorder and higher connectivity between trimers thanks to the localization of the heavier Cs^+/Rb^+ cations.

These compounds display distinct SCO behavior relative to the dimethyl ammonium salt, which we associate to stronger intermolecular connectivity. The **1-Cs** shows a two-step spin transition of the central Fe^{II} atom in each trimer, from the combination of an abrupt step above 350 K, and a gradual transition up to completeness at 400 K. The difference between heating and cooling branches showed a 47 K wide hysteresis cycle. The **1-Rb** also exhibits a two-step spin transition, a gradual transition down to 350 K and an abrupt and incomplete transition at higher temperatures. The cooling branch opens a quasi-static 55 K wide hysteresis loop in the abrupt regime. On the contrary, dimethyl ammonium salt (**1**) showed more gradual transition and wider hysteresis loop (> 85 K). The abrupt steps in the spin transition curves is attributed to an increase in the cooperativity in the Cs and Rb salts. However, this suggested higher cooperativity does not promotes a wider thermal hysteresis loop, as expected, provoking the opposite result, and suggesting that the observed hysteresis may not be exclusively related to the cooperativity phenomenon.

In line with previews studies with the dimethyl ammonium salt, our hypothesis deals with the appearance of intramolecular contributions being at the origin of the memory-like effects observed, that were thought to be irrelevant in SCO materials, precluding single-molecule memory effect in such materials. Further studies to confirm the appearance of single-molecule bistability in SCO are shown in chapter 4.

3.5. Experimental

3.5.1. Synthesis

All reagents were obtained from commercial sources and used without further purification. The ligand 4-(1,2,4-triazol-4yl)ethanedisulfonate (**L**), and the dimethylammonium salt $(Me_2NH_2)_6[Fe_3(\mu\text{-}L)_6(H_2O)_6]$ (**1**) were prepared according to the literature procedure.[49] $Cs_6[Fe_3(\mu\text{-}\mathbf{L})_6(H_2O)_6]\cdot 3H_2O$ (**1-Cs**) and $Rb_6[Fe_3(\mu\text{-}\mathbf{L})_6(H_2O)_6]\cdot 3H_2O$ (**1-Rb**) were obtained by metathesis from **1**. No proper yield was estimated, since only single crystals were used for further characterization, to assure complete purity of the samples.

$Cs_6[Fe_3(\mu\text{-}L)_6(H_2O)_6]\cdot 13H_2O$ (**1-Cs**). 180 mg (0.082 mmol, 1 eq.) of **1** and 275.6 mg (1.64 mmol, 20 eq.) of CsCl were separately dissolved in 5 mL of distilled water. Ascorbic acid (≈ 2 mg) were added to both solutions to avoid the oxidation of Fe (II) to Fe (III). Both solutions were mixed for 10 minutes under stirring. Afterwards, the solution was filtered off and ethanol vapor was slowly diffused into the solution to promote the growth of single crystals. After two days, single crystals of 2 were collected, filtered, washed with ethanol and dried in air.

$Rb_6[Fe_3(\mu\text{-}L)_6(H_2O)_6]\cdot 13H_2O$ (**1-Rb**). 100 mg (0.047 mmol, 1 eq.) of **1** and 115 mg (0.958 mmol, 20 eq.) of RbCl were separately dissolved in 5 mL of distilled water with ascorbic acid. Both solutions were mixed under stirring. An inner tube was introduced into the reaction solution to facilitate the formation of nucleation, was induced by ethanol vapor diffusion. After several days, pink crystal and powder appear in contact to the capillarity walls. They were collected and washed with ethanol.

3.5.2. Physical Methods

Thermogravimetric analyses (TGA) were performed using a TGA/SDTA851 Mettler Toledo with a MT1 microbalance.

Differential Scanning Calorimetry (DSC) analyses were performed with a Mettler Toledo /DSC822e instrument with a heating rate of 1°C min−1 in a nitrogen stream. Magnetic measurements were carried out on grained single crystals with a Quantum Design MPMS-XL SQUID magnetometer (Quantum Design, Inc, San Diego, CA, USA).

Magnetic susceptibility measurements were carried out under an applied field of 1000 Oe at different temperature scan rates within 200-400 K temperature range. The sample was introduce in a gel capsule with glass wool. A hole of around 1mm in diameter was done in the top part of the capsule to facilitate the purge inside the capsule. The diamagnetic contribution was corrected by Pascal constants. The magnetic data treatment are detailed explained in Annex II.

X-ray powder diffraction (PXRD) data were collected on a Siemens D5000 diffractometer (Bragg-Brentano parafocusing geometry and vertical θ-θ goniometer) fitted with a curved graphite diffracted-beam monochromator, incident and diffracted -beam Soller slits, a 0.06° receiving slit and scintillation counter as a detector. The angular 2θ diffraction range was between 5 and 40°. The data were collected with an angular step of 0.05° at 10s per step and sample rotation. A low background Si(510) wafer was used as sample holder. Cu kα radiation was obtained from a copper X-ray tube operated at 40 kV and 30 mA. The obtained XPRD patterns were fitted by Pawley profile by using the Topas software.[59]

Single crystal X-ray diffraction (SCXRD) measurements were performed on a Bruker-Nonius diffractometer with a APPEX 2 4K CCD area detector at 100 K. The total electron density in the unit cell was split up into two parts with associated contributions to $F_h = F_h1 + F_h2$. F_h1 is associated with the main molecule of interest,

$(Cation)_6$ $[Fe_3$ $(\mu\text{-}L)_6$ $(H_2O)_6]$, and F_h2 with the region where the non-coordination water molecules are disordered. The SQUEEZE approach [81] was used to determine the contribution from the F_h2 region. Crystal structure solution and refinement were performed using SHELXTL Version 6.10.

3.6. References

1. Raman, K. V. Kamerbeek, A. M., Mukherjee, A., Atodiresei, N., Sen, T.K., Lazić, P., Caciuc, V., Michel, R., Stalke, D., Mandal, S. K., Blügel, S., Münzenberg, M., *Moodera,* J. S. Interface-engineered templates for molecular spin memory devices. *Nature* **493**, 509–513 (2013).

2. Varghese, S., Elemans, J. A. A. W., Rowan, A. E., Nolte, R. J. M. Molecular computing: paths to chemical Turing machines. *Chem. Sci.* **6**, 6050–6058 (2015).

3. Castellano, M. Ruiz-García, R., Cano, J., Ferrando-Soria, J., Pardo, E., Fortea-Pérez, F. R., Stiriba, S. E., Barros, W. P., Stumpf, H. O., Cañadillas-Delgado, L., Pasán, J., Ruiz-Pérez, C., de Munno, G., Armentano, D., Journaux, Y., Lloret, F., Julve, M.. Metallosupramolecular approach toward multifunctional magnetic devices for molecular spintronics. *Coord. Chem. Rev.* **303**, 110–138 (2015).

4. Dunbar, K. R. Special issue on new horizons for magnetic solids based on molecules: From high-Tc magnets to nanomagnets to devices. *J. Solid State Chem.* **159**, 251–252 (2001).

5. Ma, L. Chen, C., Agnolet, G., Nie, Ji., Zhao, H., Dunbar, K.R. Electric transport properties of Mn12-acetate films measured with self-assembling tunnelling junction. *J. Phys. D. Appl. Phys.* **42**, (2009).

6. Muñoz, M. C., Real, J. A. Thermo-, piezo-, photo- and chemo-switchable spin crossover iron(II)-metallocyanate based coordination polymers. *Coord. Chem. Rev.* **255**, 2068–2093 (2011).

7. Avendano, C. Hilfiger, M. G., Prosvirin, A., Sanders, C., Stepien, D., Dunbar, K. R.. Temperature and Light Induced Bistability in a $Co_3[Os(CN)_6]_2{\cdot}6H_2O$ Prussian Blue Analog. *J. Am. Chem. Soc.* **132**, 13123–13125 (2010).

8. Bousseksou, A., Molnár, G., Salmon, L., Nicolazzi, W. Molecular spin crossover phenomenon: Recent achievements and prospects. *Chem. Soc. Rev.* **40**, 3313–3335 (2011).

9. Hilfiger, M. G. Chen, M., Brinzari, T. V., Nocera, T. M., Shatruk, M., Petasis, D. T., Musfeldt, J. L., Achim, C., Dunbar, K.R. An unprecedented charge transfer induced spin transition in an Fe-Os cluster. *Angew. Chemie - Int. Ed.* **49**, 1410–1413 (2010).

10. Li, Z. Y. Dai, J. W., Gagnon, K.J., Cai, H. L., Yamamoto, T., Einaga, Y., Zhao, H. H., Kanegawa, S., Sato, O., Dunbar, K. R., Xiong, R. G. A neutral Fe(III) compound exhibiting a two-step spin transition and dielectric anomalies. *Dalt. Trans.* **42**, 14685–14688 (2013).

11. Shatruk, M. Dragulescu-Andrasi, A., Chambers, K. E., Stoian, S. A., Bominaar, E. L., Achim, C., Dunbar, K. R. Properties of prussian blue materials manifested in molecular complexes: Observation of cyanide linkage isomerism and spin-crossover behavior in pentanuclear cyanide clusters. *J. Am. Chem. Soc.* **129**, 6104–6116 (2007).

12. Zhang, X., Xie, H., Ballesteros-Rivas, M., Wang, Z. X., Dunbar, K. R. Structural distortions of the spin-crossover material $[Co(pyterpy)_2](TCNQ)_2$ mediated by supramolecular interactions. *J. Mater. Chem. C* **3**, 9292–9298 (2015).

13. Hayami, S. Murata, K., Urakami, D., Kojima, Y., Akita, M., Inoue, K. Dynamic structural conversion in a spin-crossover cobalt(II) compound with long alkyl chains. *Chem. Commun.* 6510–6512 (2008).

14. Scheuermayer, S., Tuna, F., Bodensteiner, M., Scheer, M., Layfield, R. A. Spin crossover in phosphorus- and arsenic-bridged cyclopentadienyl- manganese(II) dimers. *Chem. Commun.* **48**, 8087–8089 (2012).

15. Halepoto, D. M. Holt, D., Larkworthy, L. F., Povey, D.C., Smith, G.W., Leigh, G. Jeffrey. Spin crossover in chromium(II) complexes. *Polyhedron* **8**, 1821–1822 (1989).

16. Klaeui, W., Eberspach, W., Guetlich, P. Spin-crossover cobalt(III) complexes: steric and electronic control of spin state. *Inorg. Chem.* **26**, 3977–3982 (2005).

17. Morgan, G. G., Murnaghan, K. D., Müller-Bunz, H., McKee, V., Harding, C. J. A manganese(III) complex that exhibits spin crossover triggered by geometric tuning. *Angew. Chemie - Int. Ed.* **45**, 7192–7195 (2006).

18. Clérac, R. Cotton, F. A., Daniels, L. M., Dunbar, K.R., Kirschbaum, K., Murillo, C. A., Pinkerton, A. A., Schultz, A. J., Wang, X. Linear tricobalt compounds with Di(2-pyridyl)amide (dpa) ligands: Temperature dependence of the structural and magnetic properties of symmetrical and unsymmetrical forms of $Co_3(dpa)_4Cl_2$ in the solid state. *J. Am. Chem. Soc.* **122**, 6226–6236 (2000).

19. Clérac, R. Cotton, F. A., Dunbar, K. R., Lu, T., Murillo, C. A., Wang, X. New Linear Tricobalt Complex of Di(2-pyridyl)amide (dpa), $[Co_3\ (dpa)_4(CH_3CN)_2][PF_6]_2$. *Inorg. Chem.* **39**, 3065–3070 (2002).

20. Gütlich, P., Gaspar, A. B., Garcia, Y. Spin state switching in iron coordination compounds. *Beilstein J. Org. Chem.* **9**, 342–391 (2013).

21. Koo, Y.-S., Galán-Mascarós, J. R. Spin Crossover Probes Confer Multistability to Organic Conducting Polymers. *Adv. Mater.* **26**, 6785–6789 (2014).

22. Kahn, O. Spin-Transition Polymers: From Molecular Materials Toward Memory Devices. *Science.* **279**, 44–48 (2002).

23. Marino, A. Chakraborty, P., Servol, M., Lorenc, M., Collet, E., Hauser, A. The role of

ligand-field states in the ultrafast photophysical cycle of the prototypical iron(II) spin-crossover compound $[Fe(ptz)_6](BF_4)_2$. *Angew. Chemie - Int. Ed.* **53**, 3863–3867 (2014).

24. Auböck, G., Chergui, M. Sub-50-fs photoinduced spin crossover in $[Fe(bpy)3]^{2+}$. *Nat. Chem.* **7**, 629–633 (2015).

25. Bertoni, R. Cammarata, M., Lorenc, M., Matar, S.F., Létard, J.F., Lemke, H.T., Collet, E. Ultrafast Light-Induced Spin-State Trapping Photophysics Investigated in $Fe(phen)_2(NCS)_2$ Spin-Crossover Crystal. *Acc. Chem. Res.* **48**, 774–781 (2015).

26. Manrique-Juarez, M. D. Mathieu, F., Shalabaeva, V., Cacheux, J., Rat, S., Nicu, L., Leïchlé, T., Salmon, L., Molnár, G., Bousseksou, A. A Bistable Microelectromechanical System Actuated by Spin-Crossover Molecules. *Angew. Chemie - Int. Ed.* **56**, 8074–8078 (2017).

27. Rat, S. Piedrahita-Bello, M., Salmon, L., Molnár, G., Demont, P., Bousseksou, A. Coupling Mechanical and Electrical Properties in Spin Crossover Polymer Composites. *Adv. Mater.* **30**, 1–6 (2018).

28. Lefter, C. Rat, S., Costa, J. S., Manrique-Juárez, M. D., Quintero, C. M., Salmon, L., Séguy, I., Leichle, T., Nicu, L., Demont, P., Rotaru, A., Molnár, G., Bousseksou, A. Current Switching Coupled to Molecular Spin-States in Large-Area Junctions. *Adv. Mater.* 7508–7514 (2016).

29. Molnár, G., Rat, S., Salmon, L., Nicolazzi, W., Bousseksou, A. Spin Crossover Nanomaterials: From Fundamental Concepts to Devices. *Adv. Mater.* **30**, 1–23 (2018).

30. Chen, J., M. A. Reed, A. M. RawLett, J. M. Tour. Large on-off ratios and negative differential resistance in a molecular electronic device. *Science.* **286**, 1550–1552 (1999).

31. Koudriavtsev, A. B., Linert, W. Spin crossover - An unusual chemical equilibrium. *J. Struct. Chem.* **51**, 335–365 (2010).

32. Craig, G. A. *Costa, J. S., Roubeau, O., Teat, S.J., Shepherd, H. J., Lopes, M., Molnár, G., Bousseksou, A., Aromí, G.*. High-temperature photo-induced switching and pressure-induced transition in a cooperative molecular spin-crossover material. *Dalt. Trans.* **43**, 729–737 (2014).

33. Shatruk, M., Phan, H., Chrisostomo, B. A., Suleimenova, A. Symmetry-breaking structural phase transitions in spin crossover complexes. *Coord. Chem. Rev.* **289–290**, 62–73 (2015).

34. Gütlich, P. Spin crossover - Quo vadis? *Eur. J. Inorg. Chem.* 581–591 (2013).

35. Šalitroš, I., Madhu, N. T., Boča, R., Pavlik, J., Ruben, M. Room-temperature spin-transition iron compounds. *Monatshefte fur Chemie* **140**, 695–733 (2009).

36. Brooker, S. Spin crossover with thermal hysteresis: Practicalities and lessons learnt. *Chem. Soc. Rev.* **44**, 2880–2892 (2015).

37. Ridier, K. Rat, S., Salmon, L., Nicolazzi, W., Molnár, G., Bousseksou, A. Scan-rate and vacuum pressure dependence of the nucleation and growth dynamics in a spin-crossover single crystal: The role of latent heat. *Phys. Chem. Chem. Phys.* **20**, 9139–9145 (2018).

38. Félix, G. Mikolasek, M., Peng, H., Nicolazzi, W., Molnár, G., Chumakov, A. I., Salmon, L., Bousseksou, A. Lattice dynamics in spin-crossover nanoparticles through nuclear inelastic scattering. *Phys. Rev. B - Condens. Matter Mater. Phys.* **91**, 1–5 (2015).

39. Mikolasek, M., Nicolazzi, W., Terki, F., Molnár, G., Bousseksou, A. Finite-size effects on the lattice dynamics in spin crossover nanomaterials. II. Molecular dynamics simulations. *Phys. Rev. B* **96**, 1–10 (2017).

40. Halder, G. J., Kepert, C. J., Moubaraki, B., Murray, K. S., Cashion, J. D. Guest-dependent spin crossover in a nanoporous molecular framework material. *Science (80-.).* **298**, 1762–1765 (2002).

41. Roubeau, O. Triazole-based one-dimensional spin-crossover coordination polymers. *Chem. - A Eur. J.* **18**, 15230–15244 (2012).

42. Luo, Y., Wen, G., Gu, L., Wang, M., Sun, B. Study of Spin Crossover in an Iron (II) Tris (diimine) System Tuned by Counter Anions. *Polyhedron* (2016).

43. Wang, S. Xu, W.T., He, W.R., Takaishi, S., Li, Y.H., Yamashita, M., Huang, W. Structural Insights into the Counterion Effects on the Manganese(III) Spin Crossover System with Hexadentate Schiff-Base Ligands. *Dalt. Trans.* **45**, 5676– 568 (2016).

44. Hostettler, M., Törnroos, K. W., Chernyshov, D., Vangdal, B., Bürgi, H. B. Challenges in engineering spin crossover: Structures and magnetic properties of six alcohol solvates of iron(II) tris(2-picolylamine) dichloride. *Angew. Chemie - Int. Ed.* **43**, 4589–4594 (2004).

45. Bartel, M. Absmeier, A., Jameson, G., Werner, F., Kato, K., Takata, M., Boca, R., Hasegawa, M., Mereiter, K., Caneschi, A., Linert, W. Modification of spin crossover behavior through solvent assisted formation and solvent inclusion in a triply interpenetrating three-dimensional network. *Inorg. Chem.* **46**, 4220–4229 (2007).

46. Nihei, M., Han, L.,Oshio, H. Magnetic bistability and single-crystal-to-single-crystal transformation induced by guest desorption. *J. Am. Chem. Soc.* **129**, 5312–5313 (2007).

47. Li, B. Wei, R. J., Tao, J., Huang, R. B., Zheng, L. S., Zheng, Z. Solvent-induced transformation of single crystals of a spin-crossover (SCO) compound to single crystals with two distinct SCO centers. *J. Am. Chem. Soc.* **132**, 1558–1566 (2010).

48. Feltham, H. L. C., Barltrop, A. S., Brooker, S. Spin crossover in iron(II) complexes of 3,4,5-tri-substituted-1,2,4-triazole (Rdpt), 3,5-di-substituted-1,2,4-triazolate (dpt−), and related ligands. *Coord. Chem. Rev.* **344**, 26–53 (2017).

49. Gómez, V. Sáenz De Pipaón, C., Maldonado-illescas, P., Waerenborgh, J. C., Martin, E., Benet-buchholz, J., Galán-mascarós, J. R. Easy Excited-State Trapping and Record High TTIESST in a Spin-Crossover Polyanionic FeII Trimer. *J. Am. Chem. Soc.* **137**, 11924–11927 (2015).

50. Sáenz de Pipaón, C., Maldonado-Illescas, P., Gómez, V., Galán-Mascarós, J. Spin Transition Kinetics in the Salt $[H_2N(CH_3)_2]_6[Fe_3(L)_6(H_2O)_6]$ (L = 4-(1,2,4-triazol-4-yl)ethanedisulfonate). *Magnetochemistry* **2**, 20 (2016).

51. Murnaghan, K. D. Carbonera, C., Toupet, L., Griffin, M., Dîrtu, M.M., Desplanches, C., Garcia, Y., Collet, E., Létard, J. F., Morgan, G. G. Spin-state ordering on one sub-lattice of a mononuclear iron(III) spin crossover complex exhibiting LIESST and TIESST. *Chem. - A Eur. J.* **20**, 5613–5618 (2014).

52. Aromí, G., Barrios, L. A., Roubeau, O., Gamez, P. Triazoles and tetrazoles : Prime ligands to generate remarkable coordination materials. *Coord. Chem. Rev.* **255**, 485–546 (2011).

53. Craig, G. A., Costa, S., Roubeau, O., Teat, S. J. Coupled Crystallographic Order – Disorder and Spin State in a Bistable Molecule : Multiple Transition Dynamics. 3120–3127 (2011).

54. Krober, J., Codjovi, E., Kahn, O., Grolibre, F., Jay, C. A Spin Transition System with a Thermal Hysteresis at Room Temperature. *J. Am. Chem. Soc.* **115**, 9810–9811 (1993).

55. Kulmaczewski, R. Olguín, J., Kitchen, J. A., Feltham, H. L C., Jameson, G. N L., Tallon, J. L., Brooker, S. Remarkable Scan Rate Dependence for a Highly Constrained Dinuclear Iron(II) Spin Crossover Complex with a Wide Thermal Hysteresis Loop. *J. Am. Chem. Soc* **136**, 878–881 (2014).

56. Paradis, N., Chastanet, G.,Létard, J. F. When stable and metastable HS states meet in spin-crossover compounds. *Eur. J. Inorg. Chem.* 3618–3624 (2012).

57. Hayami, S., Gu, Z. Z., Yoshiki, H., Fujishima, A., Sato, O. Iron(III) spin-crossover compounds with a wide apparent thermal hysteresis around room temperature. *J. Am. Chem. Soc.* **123**, 11644–11650 (2001).

58. Guionneau, P., Marchivie, M., Bravic, G., Létard, J.-F., Chasseau, D. Structural Aspects

of Spin Crossover. Example of the [$Fe^{II}Ln(NCS)_2$]. *Top Curr Chem* **234**, 97–128 (2004).

59. Coelho, A. A., Evans, J., Evans, I., Kern, A., Parsons, S. The TOPAS symbolic computation system. *Powder Diffr.* **26**, S22–S25 (2011).

Chapter 4

Molecular Magnetic Memory in Isolated SCO Fe^{II} Trimer

Abstract

In Spin-crossover (SCO) materials, memory effect (thermal hysteresis) arises from intermolecular cooperativity in the solid state, and hence, hysteretic behavior in an isolated SCO molecules is considered not possible. However, we have observed contradictory behavior in the SCO thermal bistability of the polyanionic iron triazole complex, $[Fe_3(\mu\text{-}L)_6(H_2O)_6]^{6-}$ (L^{2-} = 4-(1,2,4-triazol)-ethanedisulfonate) (**1**), that shows low cooperativity, but wide hysteresis. In this chapter we present further studies we performed with this complex to analyze the effect of cooperativity. Our results indicate that hysteresis appears in highly diluted samples: solid dilutions or liquid solutions; very similar to bulk data, suggesting the behavior has a dominant single-molecule origin. We assign this phenomena to the slow spin-state interconversion resulting in appearance of an energy barrier for the spin transition, analogous to the magnetic anisotropic barrier that opens the hysteresis cycle in single-molecule magnets (SMMs). These results indicate that magnetic SCO single molecules could be able to store information at room temperature, opening opportunities for molecular magnetic data storage.

4.1. Introduction

Electronic bistability at the single molecule level appears as the ultimate miniaturization limit for high-density information technologies. In this field, spin crossover (SCO) complexes are stimuli responsive molecules able to store information in their metastable high spin (HS) excited state.[1] Indeed, their spin switching between low spin (LS) and high spin (HS) state provide the interconversion into two electronic states that can be associated to a binary code, with the target of developing a molecular data storage switches.[2,3] In particular, the thermally driven spin switching acquire great importance for such applications due to the fact that the memory effect associated to thermal hysteresis become feasible at nearly room temperature.[4,5]

One limitation with thermally-induced SCOs materials is miniaturization, since memory effect at the single molecule level is not considered: thermal hysteresis appears exclusively in bulk when the spin transition is associated to a crystallographic phase transition via intermolecular cooperativity.[6,7] At the single molecule level, in absence of cooperativity, the non-interacting SCO molecules describe a thermal Boltzmann distribution following the overall vibronic levels of the ground LS and excited HS states,[8–10] resulting in a gradual spin conversion with no thermal hysteresis loop, and transition temperature defined by the energy differences between electronic states. This is well evidenced by theoretical and experimental studies with diluted SCO systems in solution[11–13] or in SCO-diluted solid systems incorporating non-SCO dopants.[14–23] In the latter cases, the hysteresis width significantly decreases upon dilution of SCO molecules, and finally disappears even at relatively low dopant concentration. For example, in the Fe_xM_{1-x}(pyrazine)$[Pt(CN)_4]$(M = Ni or Co) 3D-system, the initial hysteresis of 30 K (x = 1) vanishes at x < 0.4,[18] in $[Fe_xZn_{1-x}$(bapbpy)$(NCS)_2]$ (bapbpy = N6,N6-di(pyridin-2-yl)-2,2-bipyridine-6,6-diamine), the hysteresis disappears at x < 0.76[20] or in

$[Fe_xMn_{1-x}(dpp)_2(NCS)_2]\cdot py$ (dpp = dipyrido [3,2-a:2′,3′-c] phenazine (py = pyridine), the 40 K hysteresis (x = 1) is completely lost at just *x* = 0.88.[23] Remarkably, no hysteresis cycles remains below x ≤ 0.37, record threshold value for $[Fe_xCo_{1-x}(btr)_2\cdot(NCS)_2]\cdot H_2O$.[17]

One of the alternative strategy to achieve bistability in SCO single molecules is the use of photo-switchable ligands to induce the spin transition at the metal center. A photoreaction at the coordinated ligand (typically photo-isomerization) may trigger indirectly the spin conversion by: 1) changing the ligand field strength (phenomenon called Ligand-driven light-induced spin change, LD-LISC)[24–28]; 2) varying the coordination number (Light-driven coordination-induced spin-state switching, LD-CISSS)[29,30]; 3) altering the metal-metal antiferromagnetic coupling; or 4) promoting the intramolecular electron transfer (Ligand-Driven Light-Induced Valence Tautomerism, LD-LIVT).[31] With these possibilities, the memory effect of SCO molecules can be achieved at single molecular level, and in some cases, at constant room temperature.[25,28,29,31,32] However, the main disadvantage of these strategies is that the photoswitching through ligand-driven effects is almost limited to the liquid phase. Despite this clear limitation, some examples of rigorously unidirectional photoswitching in the solid state have been found,[33–35] and exceptionally, an Fe^{II} complex with a photoisomerizable diarylethene ligand have shown reversible photoswitching in solid state (spin conversion of ≈32%)[36] and recently, in thin films on Au(111) surface.[37]

Continuing with the aim of looking for memory effect at single SCO molecule, the polyanionic iron (II) trimer, $[Fe_3(\mu\text{-}L)_6(H_2O)_6]^{6-}$ (L = 4-(1,2,4-triazol-4-yl)ethanedisulfonate), described in previous chapters as dimethyl ammonium (**1**) or cesium salt (**1-Cs**), might be a very interesting SCO material in the miniaturization process down to molecular scale. In bulk, this complex presents wide thermal hysteresis for the HS - LS equilibria above room temperature, apparently not

associated to high cooperativity. This particular and counterintuitive behavior points towards different origin of the memory effect, that could be molecular. These reasons prompt us to further test the influence of cooperative interactions on the bistability of $(Me_2NH_2)_6$ $[Fe_3(\mu\text{-}L)_6(H_2O)_6]$ salt (**1**).

Here we present dilution experiments of this SCO complex by introducing diamagnetic dopant metal (Zn^{II} ion) and also in aqueous solution. Both dilutions lead to non-cooperative systems where the participation of molecule-lattice or intermolecular SCO interactions are negligible. The introduction of the magnetically silent Zn^{II} ion lead to the formation of the $(Me_2NH_2)_6[Fe_3(\mu\text{-}\mathbf{L})_6(H_2O)_6]_x[Zn_3(\mu\text{-}\mathbf{L})_6(H_2O)_6]_{(1-x)}$ series that were studied by magnetic susceptibility measurements. The spin transition in highly diluted solutions of **1** (4mM and 1mM) in different aqueous media (water-ethylene glycol and water-methanol) were followed by UV-vis spectroscopic measurements.

4.2. Results

4.2.1. Solid Dilution in a diamagnetic matrix

Synthesis and structural characterization

Crystals of **1**, $(Me_2NH_2)_6$ $[Fe_3(\mu\text{-}\mathbf{L})_6(H_2O)_6]$ ($\mathbf{L}^{-2}$ = 4-(1,2,4-triazol-4-yl)ethanedisulfonate), and its Zn^{II} analogue (**2**) were synthetized by following the reported procedure.[38] Both complexes are isostructural, with the same chemical structure of the polyanionic part (Figure 4.1) and identical cell parameters (Table 4.1), as SCXRD data shows. Therefore, they can form solid mixed solutions of Fe^{II} and Zn^{II} compounds.

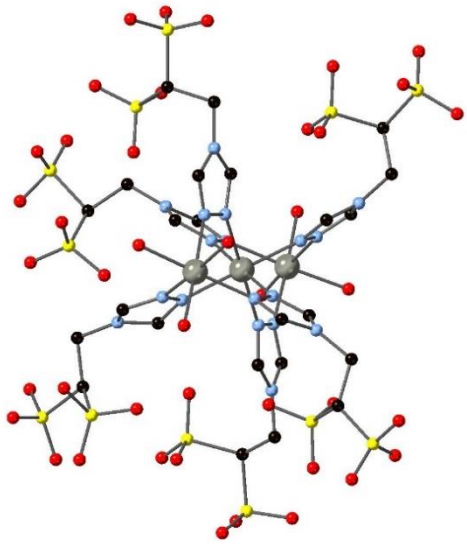

Figure 4. 1. *Molecular structure of $[M_3(\mu\text{-}L)_6(H_2O)_6]^{-6}$ (M = Fe, Zn). Color code: M = gray; S = yellow; O = red; N = blue; C = black. (H atoms have been omitted for clarity).*

Table 4. 1. *Crystallographic data for Fe Complex (**1**) and Zinc Comlex (**2**) complexes.*

	1	**2**
Chemical Formula	$C_{36}H_{100}Fe_3N_{24}O_{47}S_{12}$	$C_{36}H_{100}Zn_3N_{24}O_{47}S_{12}$
Formula weigh	2173.66	2202.24
T(K)	100(2)	100(2)
Crystal system	Triclinic	Triclinic
Space group	P –1	P –1
Crystal size	0.20x0.04x0.02	0.02x0.04x0.20
a(Å)	14.287(5)	14.2021(5)
b(Å)	15.1581(6)	15.1967(5)
c(Å)	21.3262(9)	21.5586(12)
α(°)	80.3780(14)	80.5586(12)
β(°)	84.2804(13)	84.6950(12)
γ(°)	83.7729(14)	81.8122(12)
V ($Å^3$)	4492.5(3)	4492.2(3)
Z	2	2
ρ_{calcd} (g cm^{-3})	1.607	1.636
μ (mm^{-1})	0.860	1.183
F (000)	2260	2284
Refl. collected	64559	7774
Ind.reflections	23819	23493
Abs. correction	Empirical	Empirical
θ range (°)	1.37-29.15	1.554-26.641
Index ranges	–19 ≤ h ≤ 18	–17 ≤ h ≤ 17
	–20 ≤ k ≤ 20	19 ≤ k ≤ 18
	–19 ≤ l ≤ 29	–26 ≤ l ≤ 26
Data/restr/para.	23819/3588/2115	18360/ 3524/1971
Goodnesss-of-fit	1.047	1.061
R1 (I>2σ(I))	0.0740	0.0915
wR2 (I>2σ(I))	0.2217	0.2367

The solid mixed *[(Fe$_3$)$_x$(Zn$_3$)$_{1-x}$]* compounds with the formula $(Me_2NH_2)_6[Fe_3(\mu\text{-}\mathbf{L})_6(H_2O)_6]_x[Zn_3(\mu\text{-}\mathbf{L})_6(H_2O)_6]_{(1-x)}$ (x = 1.0, 0.6, 0.4, 0.2 and 0.05) were obtained by fast precipitation with ethanol of the corresponding mixed aqueous solutions of the two pure salts in the desired ratio, see Experimental section for detailed information. This procedure affords solid powders with progressive pink – white color from higher to lower Fe content, Figure 4.2.

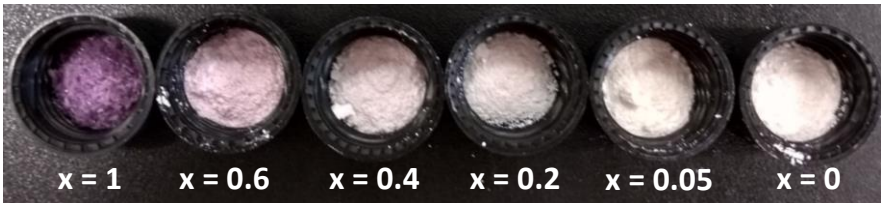

Figure 4.2. *Picture of solid mixed [(Fe$_3$)$_x$(Zn$_3$)$_{1-x}$] complexes with purple/white color depending on the Fe content.*

The effective iron and zinc fractions present in these diluted samples were determined from ICP-OES and ESEM-EDX analysis, both very close to the iron/zinc ratio during the synthesis, Figure 4.3. Despite that, the surface EDX analysis reveal higher values of Fe/Zn ratio than those obtained from ICP-OES analysis.

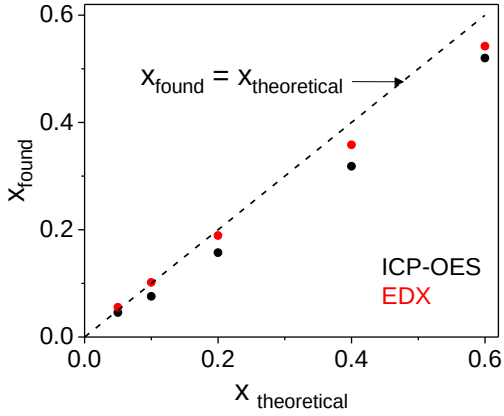

Figure 4.3. *Comparison between Fe fraction found in EDX and ICP-OES analysis (x found) as a function of Fe fraction expected (x theoretical) according to the synthesis of [(Fe$_3$)$_x$(Zn$_3$)$_{1-x}$] complexes.*

The EDX analysis together with back scattering ESEM images were performed in five distant areas of each sample (Figure 4.4), and the Fe and Zn content was calculated from the average atomic percent value, Table 4.2. This analysis not only reveals the Fe/Zn ratio but also evidence the homogenous spatial distribution of Fe and Zn over the samples.

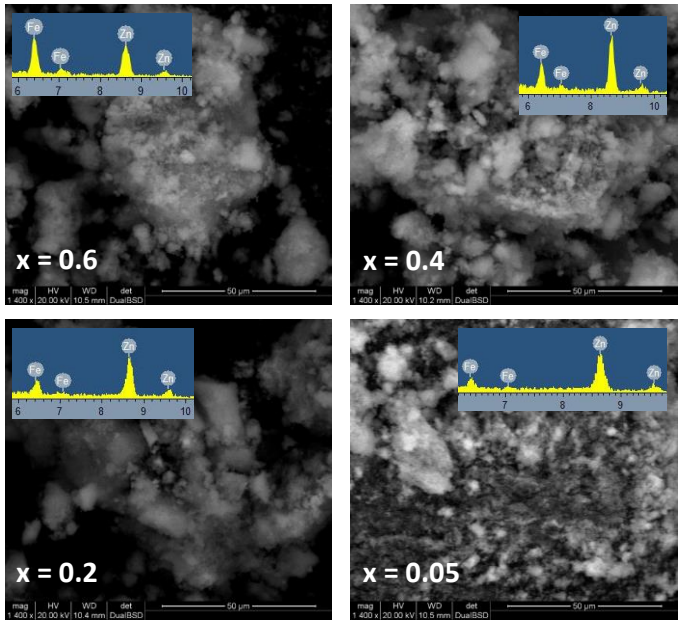

Figure 4.4. *Back scattering ESEM images and EDX spectra for $[(Fe_3)_x(Zn_3)_{1-x}]$ complexes.*

Table 4.2. *Fe and Zn fraction of $[(Fe_3)_x(Zn_3)_{1-x}]$ complexes from ESEM-EDX analysis.*

$X_{theoretical}$	Mean % Atomic EDX (Fe; Zn)	Standart Desviation (Fe; Zn)	X_{found} (EDX)
0.6	3.55; 3	0.17; 0.19	0.541
0.4	1.88; 3.37	0.2; 0.17	0.358
0.2	0.89; 3.82	0.28; 0.86	0.188
0.05	0.19; 3.36	0.15;0.58	0.055

The experimental powder X-Ray diffractograms were well-fitted by Pawley refinement with TOPAS software[39] (Figure 4.6), obtaining refined cell parameters in good agreement with SCXRD data for pure complexes. As expected for solid solutions of isostructural complexes, the cell parameters do not show significant variations upon metal dilution, Figure 4.5. This evidences that the crystalline structure of pure complexes is also retained in all mixed solids samples.

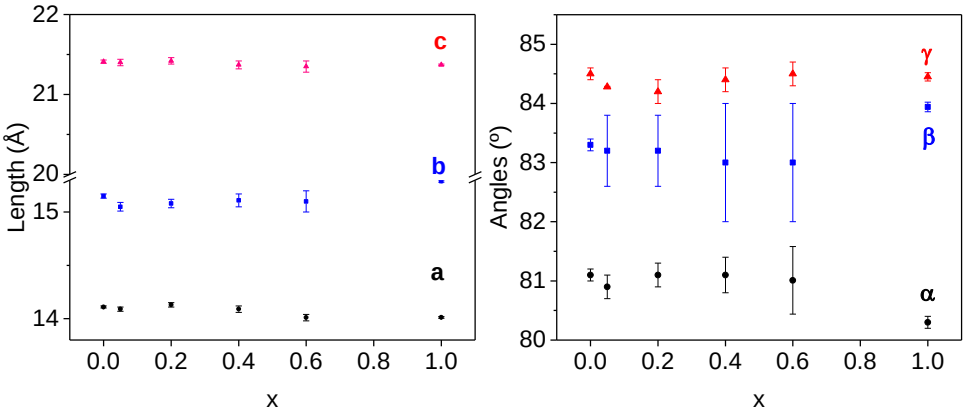

Figure 4.5. *Refined cell parameters from experimental XRD (shown in Figure 4.6) for the series of [$(Fe_3)_x(Zn_3)_{1-x}$] complexes.*

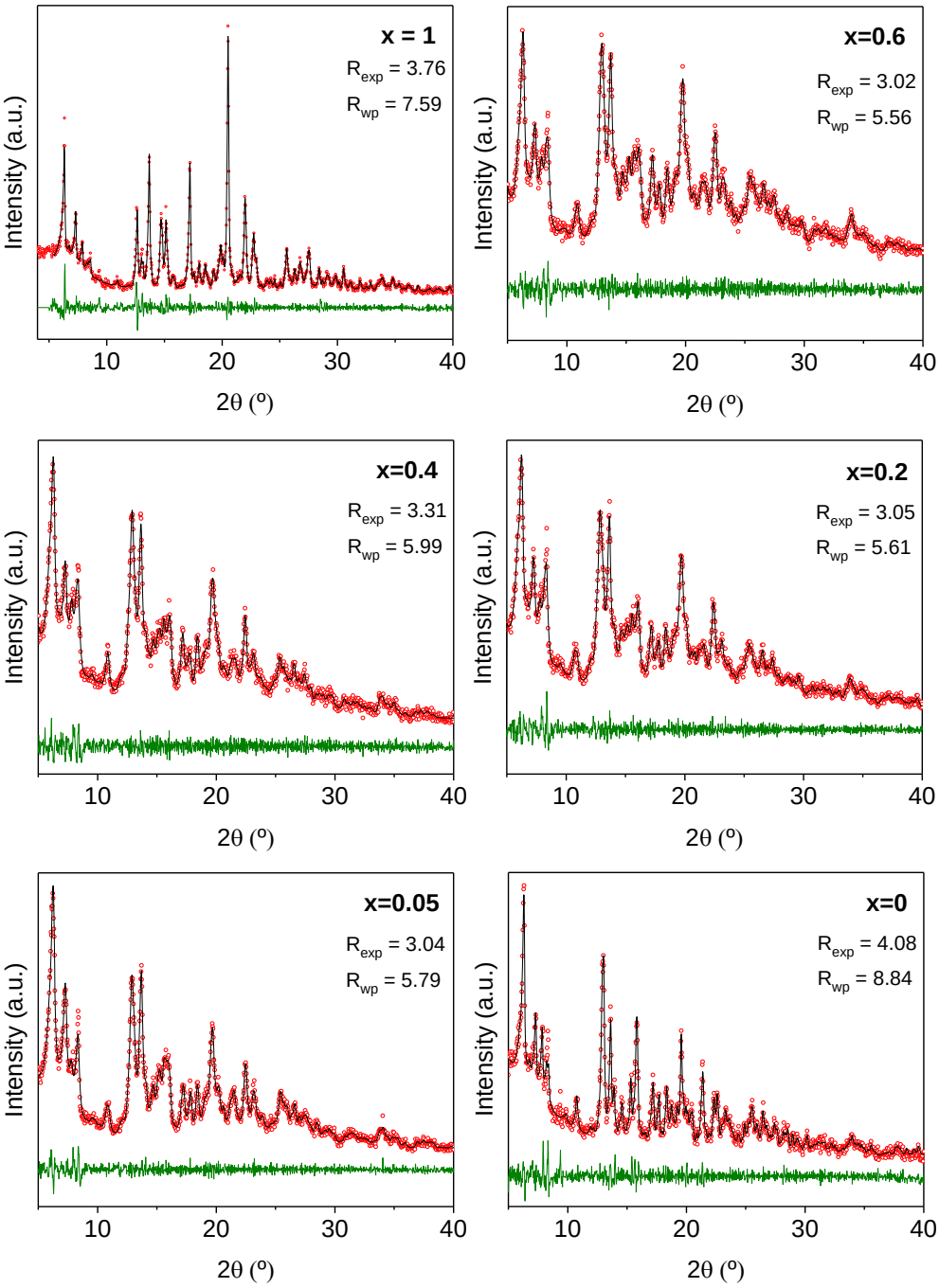

Figure 4.6. *Pawley refinement (black line) of PXRD patterns (red circles) for diluted $[(Fe_3)_x(Zn_3)_{1-x}]$ complexes. The difference between fitting and experimental data is represented by green line.*

Magnetic measurements

Variable temperature magnetic measurements were performed for $(Me_2NH_2)_6[Fe_3(\mu\text{-}\mathbf{L})_6(H_2O)_6]_x[Zn_3(\mu\text{-}\mathbf{L})_6(H_2O)_6]_{(1-x)}$ samples (Figure 4.7) at very slow scan rates (0.3 K/min) to avoid fast-scan artefacts.[4] The magnetic susceptibility was calculated per mol of Fe trimer ($mol_{(\mathbf{1})}$) and with the corresponding diamagnetic corrections from sample holder and Zn^{II} complex contributions (detailed information in Experimental section). In all samples, the $\chi_M T$ product at room temperature is within 7 - 7.5 $cm^3 \cdot (Fe_3mol)^{-1} \cdot K$ range. Considering Fe^{II}_{HS}-Fe^{II}_{SCO}-Fe^{II}_{HS} trimer configuration, the solid solution at room temperature present the 33 - 50% of the SCO centers in HS state. The $\chi_M T$ product increases from room temperature above 350 K, reaching saturation ($\chi_M T \approx 9$ $cm^3 \cdot (mol_{(\mathbf{1})})^{-1} \cdot K$ for Fe^{II}_{HS}-Fe^{II}_{HS}-Fe^{II}_{HS}) at 400 K after ≈ 8 hours. Afterwards, the $\chi_M T$ product decreases upon cooling, opening a wide hysteresis loop in all cases. Surprisingly, it is evident that the dilution has no apparent effect on the hysteresis width (90 ± 10 K) or transition temperatures ($T_{1/2}\uparrow$= 378 ± 3 K and $T_{1/2}\downarrow$= 290 ± 10 K), with all SCO parameters remaining consistent within experimental error, down to the most diluted sample (x = 0.05). All these parameters are summarized in Table 4.3.

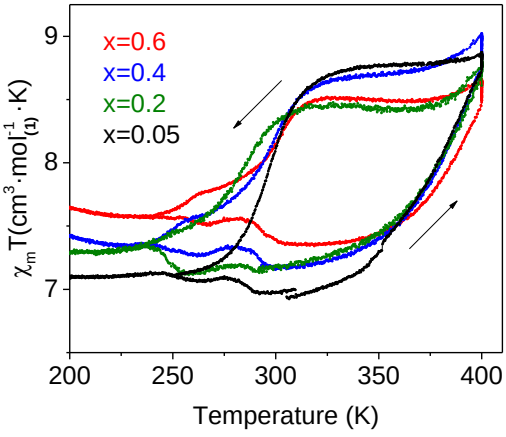

Figure 4.7. *Variable temperature magnetic data for $[(Fe_3)_x(Zn_3)_{1-x}]$ compounds with x= 0.6 - 0.05. Arrows indicate the scan direction.*

Table 4.3. *Transition temperatures and hysteresis width of thermal cycle at 0.3K/min for* $[(Fe_3)_x(Zn_3)_{1-x}]$ *compounds with x= 0.6 - 0.05.*

X calculated	$T_{1/2}\uparrow$ (K)	$T_{1/2}\downarrow$ (K)	Hysteresis Width (K)
0.6	381	299	82
0.4	380	289	91
0.2	378	282	96
0.05	375	296	79

These results are unique when compared with all previous metal dilution studies in the literature, where a drastic effect in the SCO behavior was found upon metal dilution. Particularly, the effect of dilution with Zn^{II} analogue has also been reported for different SCO complexes but it is not observed in the hysteresis cycles of our $(Fe_3)_x(Zn_3)_{1-x}$ compounds (x = 0.6 - 0.05). According to the statistical analysis provided by Martin et al.,[41] in highly diluted samples (x ≤ 0.04) there is a very high probability (≈ 0.9) to have each Fe^{II}_{SCO} center exclusively surrounded by Zn neighbors. Therefore, we can say that complex **1** maintains the hysteresis loop where the SCO centers can be considered isolated, suggesting that the hysteresis of **1** does not arise from intramolecular cooperatives forces, since there is no effect upon dilution.

We studied in more detail the dynamics of the most diluted sample $(Me_2NH_2)_6[Fe_3(\mu\text{-}\mathbf{L})_6(H_2O)_6]_x[Zn_3(\mu\text{-}\mathbf{L})_6(H_2O)_6]_{(1-x)}$ (x = 0.05). While the heating branch shows almost scan-rate independent dynamics, the cooling branch is highly scan rate dependent, as already observed in pure **1** (x = 1).[38] When cooling down at 2 K/min, the HS state is trapped, reaching a $\chi_M T$ product of 7.95 $cm^3 \cdot (mol_{(1)})^{-1} \cdot K$, which correspond to over 65 % of the SCO centers in HS state. Cooling down at 10 K/min, the $\chi_M T$ product at 200 K is still 8.7 $cm^3 \cdot (mol_{(1)})^{-1} \cdot K$, indicating almost quantitative trapping, with over 90 % of the Fe trimers quenched in the HS excited state, Figure 4.8 left. Once the metastable state is trapped at 200 K by faster cooling, the initial ground state can be recovered by slow warming at 0.3 K/min. From the derivative

of this $\chi_M T$ vs T curve, we determined the so-called Temperature Induced Excited Spin State Trapping (TIESST) temperature[19] around 250 K, Figure 4.8 right. It is worthy to mention that all solid solutions present the same characteristic T_{TIESST}, Figure 4.9, identical to that of bulk (**1**), indicating that this phenomena is not influenced by intermolecular cooperativity and that have a molecular origin.

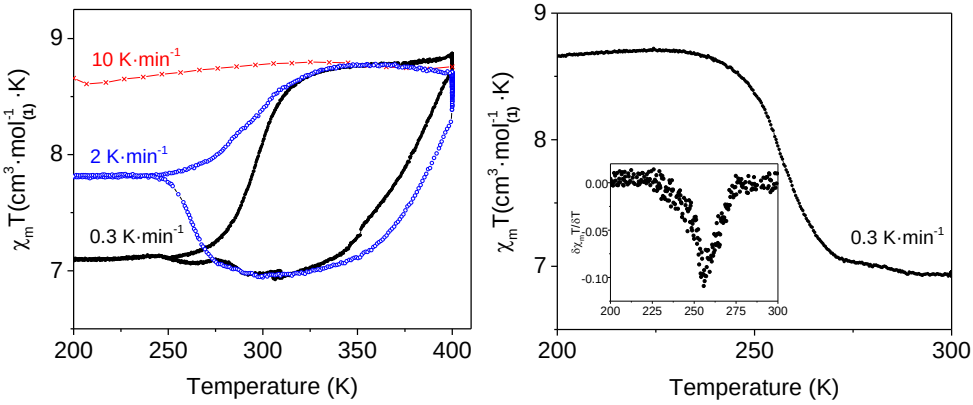

Figure 4.8. *(Left) Variable temperature magnetic data at different scan rates for $(Fe_3)_x(Zn_3)_{1-x}$ (x = 0.05) compound. (Right) Determination of the T_{TIESST} from the heating branch (0.3 K/min) of the trapped HS state as cooled down at 10 K/min.*

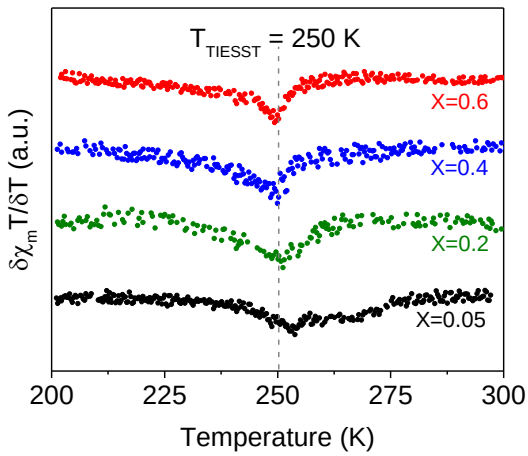

Figure 4.9. *Comparison of T_{TIESST} of the $(Fe_3)_x(Zn_3)_{1-x}$ complexes.*

We studied the kinetics of the isothermal relaxation process for quenched $(Fe_3)_x(Zn_3)_{(1-x)}$ (x = 0.05) samples at different temperatures, Figure 4.10 left. First, the samples were heated up to 400 K, and after saturation, the HS-HS-HS state was thermally trapped by fast cooling down to the desired temperature to study the relaxation kinetics to the ground state. The relaxation curves follow an exponential function (Equation 4.1), typical of non-cooperative system, where the relaxation rate constants for each isothermal process (k_{HL}) and the characteristic χT at infinite (χT_∞) can be extracted:

$$\chi T(t) = \chi T_\infty + (\chi T - \chi T_\infty)\exp(-k_{HL} \cdot t) \qquad \text{Equation 4.1}$$

The dependence of the rate constant with temperature shows a quite unique behavior (Figure 4.10 right): k_{HL} is constant above T_{TIESST}, and rapidly decreases below this temperature, analogous to bulk measurements of **1**.[42] This behavior is unprecedented in SCO materials, that typically show the opposite trend: constant rate constants below T_{TIESST}, and the thermally activation region occur at higher temperatures.[23,40,43,44]

In our case, an Arrhenius fit (Equation 4.2) in the thermally activated region below T_{TIESST} yields an estimated activation energy (E_a) of 3005 K (2088 cm^{-1}), which represents a large value for a molecular SCO complex.[23]

$$k_{HL}(T) = k_{HL}^{\infty}\exp(^{E_a}/_{k_B T}) \qquad \text{Equation 4.2}$$

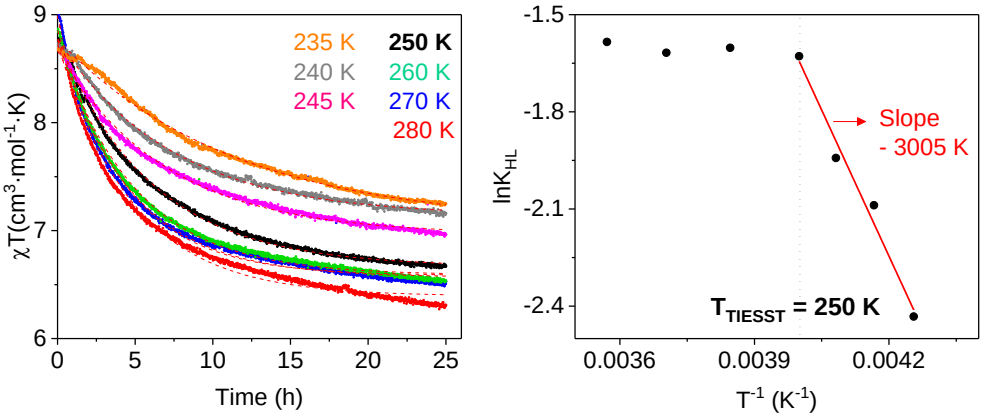

Figure 4.10. *(Left) Spin relaxation processes for the trapped HS state at different temperatures. (Right) ln*k_{HL} *vs* T^{-1} *plot (black points) and a linear fit of the thermally active region (red line) to estimate the activation energy from the slope.*

4.2.2. Liquid solutions

In the search for additional experimental evidences supporting (or discarding) the molecular origin of the magnetic features with memory effect exhibited by the $[Fe_3(\mu\text{-}\mathbf{L})_6(H_2O)_6]^{6-}$ polyanion, we decided to carry out experiments in liquid solutions, where cooperative effects are negligible, although other factors as solvation energy may play a role in the SCO dynamics. To reach a larger temperature range, we started our experiments with solutions of **1** in a water: ethylene glycol (3 : 4 % v.v) mixture. These solutions are colorless at room temperature, but become pink upon cooling, Figure 4.11. This visible color change is attributed to the spin-state conversion of the $[Fe_3(\mu\text{-}L)_6(H_2O)_6]^{6-}$ complex, by analogy with the bulk samples.

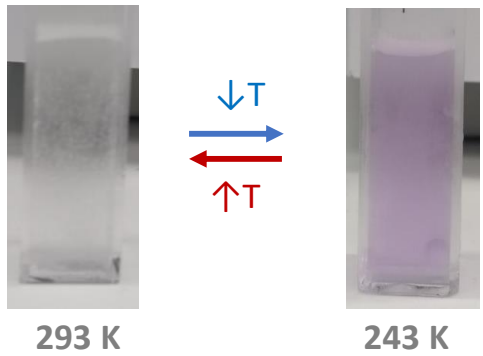

Figure 4.11. *Picture of 6 mM solution of **1** in water: ethylene glycol at 293 K (colorless solution) and at 243 K (pink solution).*

We used variable temperature UV-vis spectroscopy to follow the spin switching of **1** in solution. The absorption spectra for **1** (Solution 1; 4mM) dissolved in water: ethylene glycol (3:4 % v.v) mixture shows significant temperature-dependence in the absorbance intensity around 320 nm (Figure 4.12). This absorption peak may correspond to d–d transition bands of the LS iron^{II} species, arising from $^1A_1$ to $^1T_2$ transition.[8] Since this absorption peak is completely bleached at room temperature, the low spin fraction of complex **1** can be related to absorption intensity of this UV

peak. At 293 K, the solution appeared colorless and the absorption spectra do not exhibit a notable absorption band in ultraviolet region, which suggest that all the iron^{II} trimers are in the Fe^{II}_{HS}-Fe^{II}_{HS}-Fe^{II}_{HS} state. Upon cooling to 243 K the absorption significantly increases (Figure 4.12 left), which is attribute to a Fe^{II}_{HS}-Fe^{II}_{HS}-Fe^{II}_{HS} → Fe^{II}_{HS}-Fe^{II}_{LS}-Fe^{II}_{HS} transition. The opposite transition is observed during the warming process up to 293 K (Figure 4.12 right), pointing to a reversible spin transition process in solution within this temperature range.

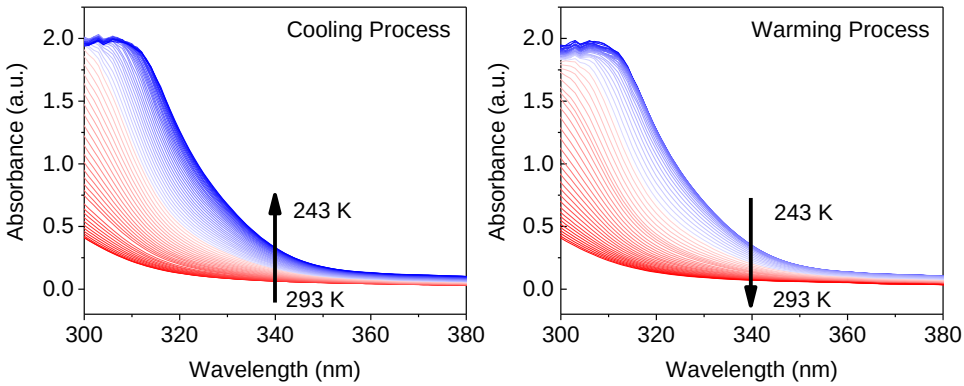

Figure 4.12. *Temperature-dependence absorption spectra for Solution 1 (4mM of **1** in water/ ethylene glycol (3:4 %v.v.)). The temperature rate is 0.5 K/min in the cooling (left) and warming process (right).*

Indeed, the evolution of absorbance at 320 nm as a function of temperature (Figure 4.13) reveals the appearance of irreversibility between cooling and warming branches. Remarkably, the thermal cycle shows an unexpected abrupt character in the LS → HS conversion, that does not correspond to a Boltzmann distribution, typical behavior of SCO in solution.[10] The transition temperature in LS → HS process is around $T_{1/2}(\downarrow)$ = 270 K, whereas the HS→LS transition during the cooling branch presents a more gradual character with a transition temperature $T_{1/2}(\downarrow)$ = 256 K, thus opening a 14 K wide hysteresis. Both branches converge above 273 K closing the hysteresis loop and evidencing a complete and reversible spin transition process in solution. The temperature dependent data was fitted to obtain Van´t Hoff

parameters for the cooling branch (ΔH = 81.8 KJ/mol ΔS = 307.9 J/mol·K) and the warming branch (ΔH = – 132.75 KJ/mol and ΔS = – 491.4 J/mol·K (according to Equation 4.8 and 4.9 detailed in Experimental section). The comparison of these thermodynamic parameters show the different thermodynamic nature of the spin transition between cooling and warming branches.

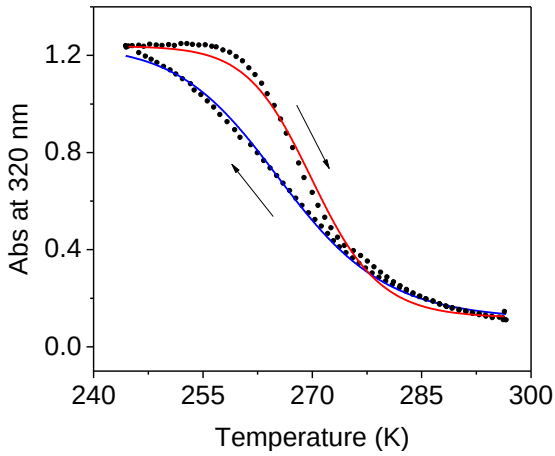

Figure 4.13. *Thermal evolution of the absorbance at 320 nm for 4 mM-solution of **1** in water/ethylene glycol (3:4% v.v.). The scan rate was 0.5 K/min (black points). Van´t Hoff fitting of the cooling branch (blue line) and warming branch (red line).*

The thermal cycles were also performed at slower scan rates, to preclude the influence of scan rate in the hysteresis opening. The hysteresis cycle (Figure 4.14) shows consistent behavior and repeatability even at very slow scan rates down to 0.16 K·min^{-1}, discarding the influence of thermal fluctuations or inertia.

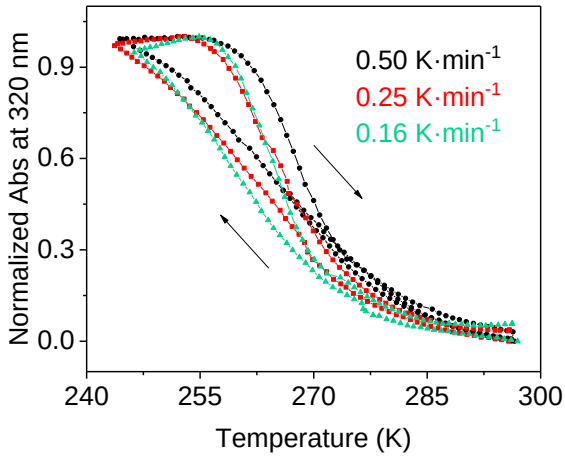

Figure 4.14. *Normalized 320nm-absorbance of solution 1 at different scan rates: 0.5, 0.25, 0.16 K/min. Arrow indicate the scan temperature direction.*

We also studied the relaxation process inside the hysteresis loop looking at the long time evolution of absorbance (at 260 K), in order to further confirm the genuine appearance of hysteresis, beyond dynamic effects (Figure 4.15). The relaxation processes, coming from a cooling branch (HS→LS) or warming branch (LS→HS), show intrinsic different kinetics and reach a stable and constant values just after one hour and maintaining a 6 % difference even after 5 hours. Additionally, the relaxation processes can be fitted to exponential asymptotic functions, yielding different populations at T_{∞}. This very slow spin-state interconversion in solution is similar to that observed in bulk, and in solid solutions, supporting again the intramolecular origin of the memory effect in this SCO compound.

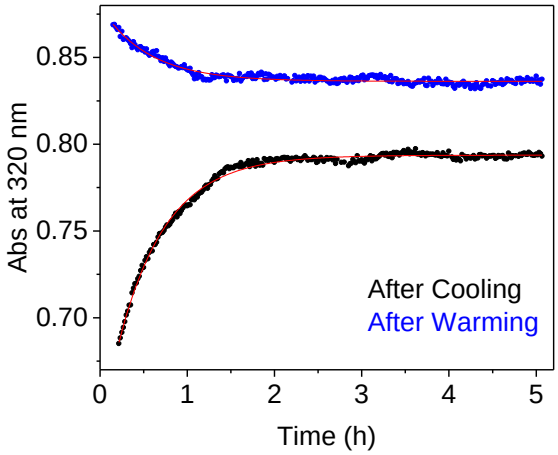

Figure 4.15. *Absorbance evolution in time at 260 K, after cooling (black points) and warming process (blue points) at 0.5 K/min. The red lines are the fitted asymptotic exponential function (Abs=A–B·C^{Time}, A =0.79, B = 0.16 and C = 0.16 after cooling and A = 0.83, B = – 0.04 and C = 0.16 after warming).*

In order to discard any agglomeration or solvation effect on the hysteresis loop, lower concentration solutions of **1** (1mM) in water/ethylene glycol (solution 2) and water/methanol (solution 3) were studied. At these dilutions, we followed more intense UV absorption bands, around 230 nm and 260 nm, which can also be attributed to the LS state, Figure 4.16.

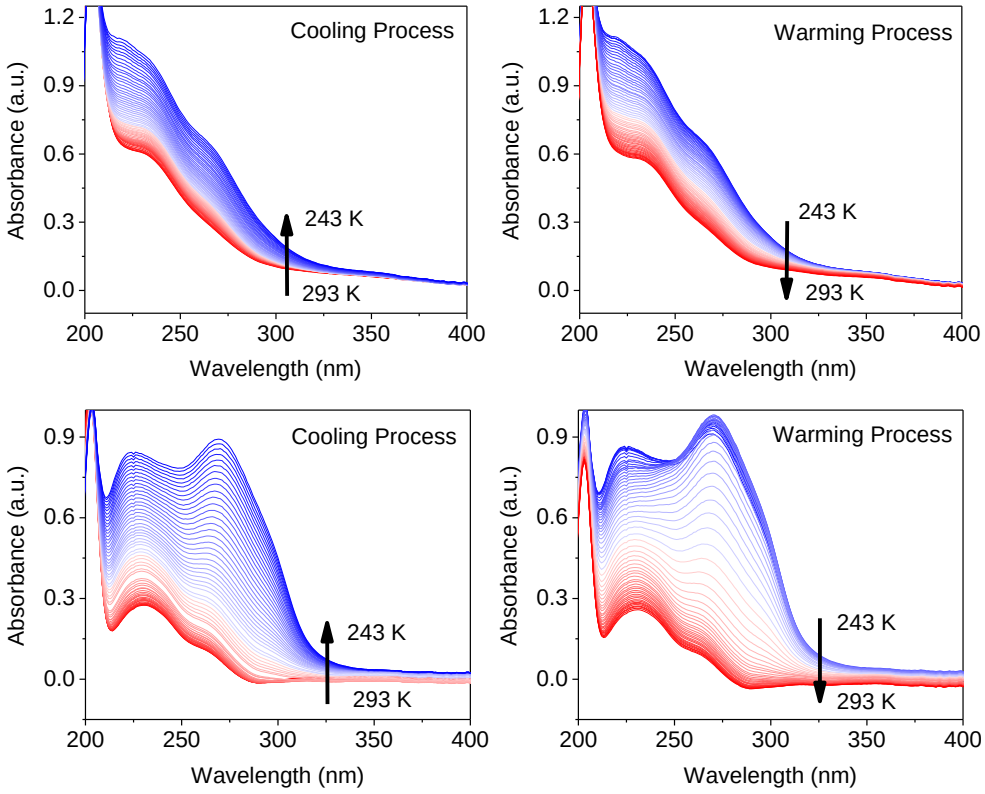

Figure 4.16. *Variable temperature absorption spectra for 1mM-solution of **1** dissolved in water /ethylene glycol (top) and water/methanol (3:4 %v.v.) mixture (bottom) in the cooling and warming process at 0.5 K/min.*

We did not find any significant changes upon more dilute samples, or upon incorporation of methanol (Figure 4.17). In light of these results, we discarded the solute-solute interaction and solvation effect (solute-solvent interaction, hydrogen bonding or intermolecular vibrational modes) as responsible for the appearance of the thermal hysteresis.

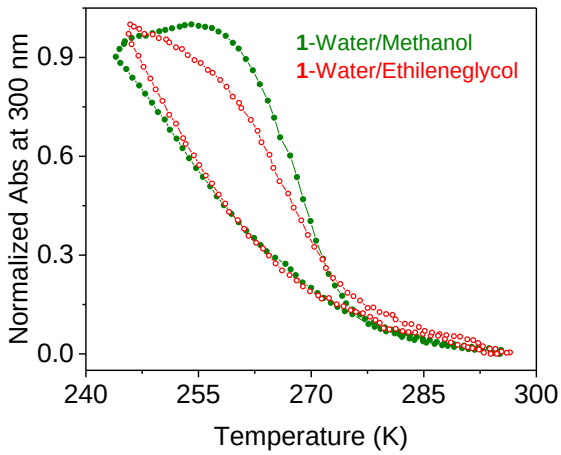

Figure 4.17. *Thermal hysteresis cycle at 0.5 K·min^{-1} for 1mM solution of **1** in water/ethylene glycol and water/methanol mixture.*

4.3. Discussion

All the experimental data, extracted from the study of reduced-cooperative systems based on dilution of **1**, reveal the appearance of a hysteretic SCO behavior with very slow spin-state interconversion (several hours at room temperature). Our studies supports the hypothesis that the observed hysteresis is not emerging due to intermolecular cooperative interactions, as the only accepted origin for such phenomena. Instead, all our experimental data points towards a kinetic hysteresis arising from the features of single molecules, probably due to the appearance of an intramolecular energy barrier causing an extremely slow spin-state interconversion rate. Our proposal can be well-explained by analogy to Single Molecule Magnets (SMMs), where the kinetic hysteresis is a consequence of the slow intramolecular relaxation due to a magnetic anisotropic barrier.[45,46]

We attribute the large barrier to spin transition in complex **1** to the large molecular rearrangement needed in this case, and that does not obey the simple configurational coordinate (scc) model,[47,48] due to the bulky and charged ligands, **L**. This concept was firstly proposed by Toftlund and McGarvey[49] that explained the long spin state lifetimes of light-induced SCO Fe^{II} complex with the hindrance provided by stiff ligands. Later, it was further explored in some trigonal prismatic $iron^{II}$ complexes with spin state lifetimes in the range of nanoseconds.[50,51]

Based on this idea, we propose that the reorganization of the twelve dangling anionic sulfonated groups on the periphery of the ligands during the SCO might represent the main contribution to intramolecular energy barrier in complex **1**, since these twelve negatively charged functional groups must approach one another upon the HS → LS transition, given the smaller radii of the centers Fe (LS) center. Indeed, SCXRD data at 100 K of complex **1**, Figure 4.18, reveals very short distances between the O atoms from close ligands, being the shortest distances 3.7 – 4.02 Å similar to the sum of their van der Waals radii (3.22 Å),[52] confirming the existence

of steric hindrance and electrostatic repulsion forces already in LS state. However, the LS→HS transition would not come with such tendency, since the sulfonate groups would be gaining additional space. This simple description fits very well the experimental data. We observed very strong scan rate dependence in the cooling branches (HS→LS), reaching easy quenching of the excited state, whereas the heating branches are almost scan rate independent.

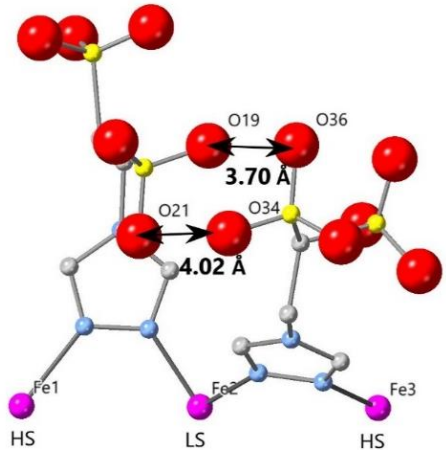

Figure 4.18. *Part of the chemical structure for **1** in Fe^{II}_{HS}-Fe^{II}_{LS}-Fe^{II}_{HS} configuration. Color code: Fe = pink; S = yellow; O = red; N = blue; C = gray. Four ligand and coordinating water molecules was removed for clarity.*

4.4. Conclusions

Here, we explore the influence of the cooperative interaction on the bistability of the thermally-induced Fe^{II} SCO complex (**1**) by performing dilution experiments in solid mixed Fe/Zn solution and in liquid solution.

The insertion of isostructural Zn^{II} complexes in **1** do not present significant effect on SCO properties, and remarkably, the hysteresis is still maintained at very low Fe^{II} concentration (less than 5% of Fe), contrary to all precedent materials. On the other hand, diluted liquid solutions of this complex show the appearance of thermal bistability, as monitored by spectroscopical measurements.

All these experimental data can be well-explained by the occurrence of magnetic bistability at the single molecule level in this SCO complex. By analogy with single-molecule magnets (SMMs), we assign this phenomenon to the appearance of an intramolecular activation barrier resulting in extremely slow spin-state interconversion (several hours at room temperature), probably related to the steric hindrance and electrostatic repulsion arising between the twelve $–SO^{3-}$ groups decorating the central iron cation, that need to contract/expand and reorganize during the SCO process. In this way, the ligand structure design appears as a strategy to control the spin state lifetime, opening unique and promising options to build molecular magnetic switches operating around room temperature.

4.5. Experimental

4.5.1. Synthesis

The ligand 4-(1,2,4-triazol-4-yl)ethanedisulfonate ($\mathbf{L^{2-}}$) was obtained as de dimethylammonium salt $(Me_2NH_2)_2\mathbf{L}$ following a literature procedure. [38]

$(Me_2NH_2)_6$ $[Fe_3(\mu\text{-}L)_6(H_2O)_6]$ (1) was synthetized according to procedure reported previously in our group[i]. Single crystals were hand collected and used for all further experiments.

$(Me_2NH_2)_6$ $[Zn_3(\mu\text{-}L)_6(H_2O)_6]$ (**2**). $Zn(ClO_4)_2{\cdot}6H_20$ (38 mg; 0.10 mmol), and $(Me_2NH_2)_2\mathbf{L}$ (90 mg; 0.24 mmol) were dissolved in water (5 ml total volume), obtaining a colorless solution. Ethanol vapor was slowly diffused into this aqueous solution to induce crystals growth. Single crystals of **2** were obtained after two days, filtered, washed with ethanol (3 × 15 mL) and dried in air. The crystals were characterized by single crystal X ray diffraction at 100 K confirming that **1** and **2** are isostructural.

Solid solutions $(Me_2NH_2)_6[Zn_3(\mu\text{-}L)_6(H_2O)_6]_{(1-x)}[Fe_3(\mu\text{-}L)_6(H_2O)_6]_x$ were prepared from mixed aqueous solutions of **1** and **2** in the desired molar ratios (see Table 4.4), with an excess of **Ligand** ((20 mg) 2.5 mmol/ mmol of **1** and **2**) in a total volume of 10 ml of water. Acid ascorbic was also added in order to avoid the Fe^{II} oxidation. After 10 minutes stirring, the mixed samples were obtained by fast precipitation with ethanol (20 ml). This suspension is centrifuged to collect the solid, that was filtered and washed with ethanol/ diethyl ether and dried in air. Yield: (37.2 mg) 63.37% for x = 0.6; (38.7 mg) 63.8% for x = 0.4; (40.1 mg) 65.4% for x = 0.2; (43.5 mg) 54.37% for x= 0.05.

Table 4.4. *Specific amount of 1 and 2 added to form the solid solution mixtures.*

Fe_xZn_{1-x}	mg (1)	mmol (1)	mg (2)	mmol (2)
X = 0.6	29.6	0.013	20	0.009
X = 0.4	19.7	0.009	30	0.013
X = 0.2	9.86	0.004	40	0.018
X =0.05	2.46	0.001	47.5	0.021

Liquid Solutions of $(Me_2NH_2)_6$ $[Fe_3(\mu\text{-}L)_6(H_2O)_6]$ was dissolved in aqueous mixture solution. yielding to **solution 1**, **2** and **3** with different concentrations. All these solutions was prepared under inert atmosphere in order to avoid the Fe^{II} oxidation.

Solution 1, 4mM concentration, was prepared dissolving complex **1** (30 mg; 0.014 mmol) in 3.4 ml of a mixture of water/ethylene glycol (3:4% v.v.).

Solution 2, 1mM in concentration, was prepared adding complex **1** (8 mg; 0.0038 mmol) to 3.4 ml of a mixture of water/ethylene glycol (3:4% v.v.).

Solution 3, 1mM, was prepared by dissolving complex **1** (8 mg; 0.0038 mmol) in 3.4 ml of a mixture of water/methanol (3:4% v.v.).

4.5.2. Physical measurements

ICP-OES was used to carry out elemental analysis with an Agilent 725-ES inductively coupled plasma optical emission spectrometer at University of Valladolid.

Electron microscopy (ESEM) images and analysis were obtained with a QUANTA600 equipment (FI) under high vacuum conditions with a Large-Field Detector at 20 kV.

Single crystal X-ray diffraction measurements (SCXRD) were performed on a Bruker-Nonius diffractometer equipped with an APEX II 4K CCD area detector, a FR591 rotating anode with MoK radiation, Montel mirrors as monochromator, a Kappa 4-axis goniometer and an Oxford Cryosystems low temperature device Cryostream 700 plus (T = -173 °C). Programs used were as follows: data collection with APEX II data reduction with Bruker Saint and absorption correction with SADABS. The crystal structure solutions was achieved using direct methods as implemented in SHELXTL and visualized using the program XP. Crystal data collection for **1** and **2** are given in Table 4.1.

X-ray powder diffraction measurements were made using a Siemens D5000 diffractometer (Bragg-Brentano para-focusing geometry and vertical θ-θ goniometer) fitted with a curved graphite diffracted-beam monochromator, incident and diffracted -beam Soller slits, a 0.06° receiving slit and scintillation counter as a detector. The angular 2θ diffraction range was between 5 and 40°. The data were collected with an angular step of 0.05° at 10s per step and sample rotation. A low background Si (510) wafer was used as sample holder. Cu kα radiation was obtained from a copper X-ray tube operated at 40 kV and 30 mA.

The obtained XPRD patterns were analyzed by Pawley profile analysis using the Topas software [39] and a Chebyshev function of seven terms was used to fit the background.

Magnetic measurements were carried out on grained solid powders with a Quantum Design MPMS-XL SQUID magnetometer (Quantum Design, Inc, San Diego, CA, USA) under an applied field of 1000 Oe at different temperature scan rates.

The experimental susceptibility was calculated per mol of iron trimer complex (Equation 4.3), where the diamagnetism from the sample holder (capsule and wool) was corrected, see Annex II.

$$\chi_{raw} = \frac{(M - M_{bag} - M_{wool}) \cdot Mm(mg/mmol)}{mg(Fe(II)trimer) \cdot H(Oe)} \qquad \text{Equation 4.3}$$

The extra diamagnetic contribution was experimentally obtained by fitting of the low temperature data (< 200 K) of each sample to a Curie-Weiss law with addition of a diamagnetic term:

$$\chi = \frac{C}{(T-\Theta)} + \chi_{DIA} \qquad \text{Equation 4.4}$$

Variable temperature absorption spectra were recorded in 1 cm quartz cells with an Agilent 8453 diode array spectrophotometer (λ =190–1100 nm). A cryostat from Unisoku Scientific Instruments was used for temperature control. A Pt100 sensor was inserted into the quartz cell to monitor the exact temperature in the solution. The measurements were carried out under inert atmosphere.

Temperature dependence of the absorbance was fitted using derived expression from Van´t Hoff expression (Equation 4.5):

$$\ln K_{eq} = -\frac{\Delta H}{RT} + \frac{\Delta S}{R} \qquad \text{Equation 4.5}$$

where K_{eq} is the equilibrium constant, ΔH enthalpy change and ΔS entropy change.

The equilibrium constant for cooling (HS → LS) and warming process (LS → HS) are expressed as,

$$K_{eq}(\text{cooling procces}) = (A(LT) - A_{obs})/(A_{obs} - A(HT)) \qquad \text{Equation 4.6}$$

$$K_{eq}(\text{warming procces}) = (A_{obs} - A(HT))/(A(LT) - A_{obs})) \qquad \text{Equation 4.7}$$

Where the Aobs is observed absorption and the high- and low-temperature limits of absorption are A(HT) and A(LT), respectively.

Therefore, the temperature dependence absorption spectra for cooling and warming branch of can be fitted with Equation 4.11 and Equation 4.12, respectively, by using the Van´t Hoff expression and the corresponding equilibrium constant for each process.

$$A_{obs} = \frac{e^{-\frac{\Delta H}{RT}+\frac{\Delta S}{R}} \cdot A(HT)+A(LT)}{e^{-\frac{\Delta H}{RT}+\frac{\Delta S}{R}}+1} \qquad \text{Equation 4.8}$$

$$A_{obs} = \frac{e^{-\frac{\Delta H}{RT}+\frac{\Delta S}{R}} \cdot A(LT)+A(HT)}{e^{-\frac{\Delta H}{RT}+\frac{\Delta S}{R}}+1} \qquad \text{Equation 4.9}$$

4.6. References

1. Gütlich, P., Hauser, A., Spiering, H. Thermal and Optical Switching of Iron(II) Complexes. *Angew. Chem. Int. Ed. Engl.* **33**, 2024–2054 (1944).

2. Bousseksou, A., Molnár, G., Salmon, L., Nicolazzi, W. Molecular spin crossover phenomenon: Recent achievements and prospects. *Chem. Soc. Rev.* **40**, 3313–3335 (2011).

3. Halcrow, M. A. Spin-crossover Compounds with Wide Thermal Hysteresis. *Chem. Lett.* **43**, 1178–1188 (2014).

4. Brooker, S. Spin crossover with thermal hysteresis: Practicalities and lessons learnt. *Chem. Soc. Rev.* **44**, 2880–2892 (2015).

5. Šalitroš, I., Madhu, N. T., Boča, R., Pavlik, J., Ruben, M. Room-temperature spin-transition iron compounds. *Monatshefte fur Chemie* **140**, 695–733 (2009).

6. Kahn, O., Martinez, C. J. Spin-Transition Polymers: From Molecular Materials Toward Memory Devices. *Science.* **279**, 44–48 (1998).

7. Im, M. Y. Fischer, P., Yamada, K., Sato, T., Kasai, S., Nakatani, Y., Ono, T. Symmetry breaking in the formation of magnetic vortex states in a permalloy nanodisk. *Nat. Commun.* **3**, 983–986 (2012).

8. Gütlich, P., Garcia, Y., Goodwin, H. A. Spin crossover phenomena in Fe(II) complexes. *Chem. Soc. Rev.* **29**, 419–427 (2000).

9. Moliner, N. Gaspar, A. B., Muñoz, M. C., Niel, V., Cano, J., Real, J. A. Light- and thermal-induced spin crossover in $\{Fe(abpt)_2[N(CN)_2]_2\}$. Synthesis, structure, magnetic properties, and high-spin ↔ low-spin relaxation studies. *Inorg. Chem.* **40**, 3986–3991 (2001).

10. Creutz, S. E., Peters, J. C. Spin-State Tuning at Pseudo-tetrahedral d6 Ions: Spin Crossover in $[BP_3]$FeII-X Complexes. *Inorg. Chem.* **55**, 3894–3906 (2016).

11. Luo, Y. H., Nihei, M., Wen, G. J., Sun, B. W., Oshio, H. Ambient-Temperature Spin-State Switching Achieved by Protonation of the Amino Group in $[Fe(H_2Bpz_2)2(bipy-NH_2)]$. *Inorg. Chem.* **55**, 8147–8152 (2016).

12. Mörtel, M. Witt, A., Heinemann, F. W., Bochmann, S., Bachmann, J., Khusniyarov, M.M. Synthesis, Characterization, and Properties of Iron(II) Spin-Crossover Molecular Photoswitches Functioning at Room Temperature. *Inorg. Chem.* **56**, 13174–13186 (2017).

13. Barett, S. A., Kilner, C. A., Halcrow, M. A. Spin Crossover in [Fe(3-bpp)2][BF4]2 in different solvents- A dramatic stabilisation of the low spin state in water. *Dalt. Trans.*

40, 12021–12024 (2011).

14. Sorai, M., Ensling, J., Gütlich, P. Mössbauer effect study on low-spin 1A1 ⇌ high-spin 5T2 transition in tris(2-picolylamine) iron chloride I. Dilution effect in [FexZn1-x(2-pic)3]Ch2 ·C2H5OH. *Chem. Phys.* **18**, 199–209 (1976).

15. Haddad, M. S., Federer, W. D., Lynch, M. W., Hendrickson, D. N. Spin-Crossover Ferric Complexes: Unusual Effects of Grinding and Doping Solids. *Inorg. Chem.* **20**, 131–139 (1981).

16. Ganguli, P., Gütlich, P., Müller, E. W. Effect of Metal Dilution on the Spin-Crossover Behavior in $[Fe_xM_{1-x}(phen)_2(NCS)_2]$ (M = Mn, Co, Ni, Zn). *Inorg. Chem.* **21**, 3429–3433 (1982).

17. Zarembowitch, J. M. J., Bousseksou, J. A., Dworkin, A., Haasnmt, J. G., Varretlb, F. Solid State Effects on Spin Transitions: Magnetic, Calorimetric, and Mossbauer-Effect Properties of $[Fe_xCo_{1-x}(4,4'\text{-bis-}1,2,4\text{-triazole})_2(NCS)_2]\cdot H_2O$ Mixed-Crystal Compounds. *Inorg. Chem.* **33**, 6325–6333 (1994).

18. Tayagaki, T. Galet, A., Molnár, G., Carmen Muñoz, M., Zwick, A., Tanaka, K., Real, J.A., Bousseksou, A. Metal dilution effects on the spin-crossover properties of the three-dimensional coordination polymer Fe(pyrazine)$[Pt(CN)_4]$. *J. Phys. Chem. B* **109**, 14859–14867 (2005).

19. Paradis, N., Chastanet, G., Létard, J. F. When stable and metastable HS states meet in spin-crossover compounds. *Eur. J. Inorg. Chem.* 3618–3624 (2012).

20. Zheng, S., Siegler, M. A., Costa, J. S., Fu, W. T., Bonnet, S. Effect of metal dilution on the thermal spin transition of $[Fe_xZn_{1-x}(bapbpy)(NCS)_2]$. *Eur. J. Inorg. Chem.* 1033–1042 (2013).

21. Paradis, N., Chastanet, G., Varret, F., Létard, J. F. Metal dilution of cooperative spin-crossover compounds: When stable and metastable high-spin states meet. *Eur. J. Inorg. Chem.* 968–974 (2013).

22. Baldé, C., Desplanches, C., Le Gac, F., Guionneau, P., Létard, J. F. The role of iron(ii) dilution in the magnetic and photomagnetic properties of the series $[Fe_xZn_{1-x}(bpp)_2](NCSe)_2$. *Dalt. Trans.* **43**, 7820–7829 (2014).

23. Paradis, N. Chastanet, G., Palamarciuc, T., Rosa, P., Varret, F., Boukheddaden, K., Létard, J. F. Detailed Investigation of the Interplay between the Thermal Decay of the Low Temperature Metastable HS State and the Thermal Hysteresis of Spin-Crossover Solids. *J. Phys. Chem. C* **119**, 20039–20050 (2015).

24. Boillot, M.-L., Roux, C., Audière, J.-P., Dausse, A., Zarembowitch, J. Ligand-Driven Light-Induced Spin Change in Transition-Metal Complexes: Selection of an

Appropriate System and First Evidence of the Effect, in Fe^{II} (4-styrylpyridine)$_4$ ($NCBPh_3$)$_2$. *Inorg. Chem.* **35**, 3975–3980 (1996).

25. Lallemand, J.-Y., Boillot, M.-L., Zarembowitch, J., Prunet, J., Chantraine, S. First ligand-driven light-induced spin change at room temperature in a transition-metal molecular compound. *New J. Chem.* **23**, 179–184 (2002).

26. Estrader, M. Salinas Uber, J., Barrios, L. A., Garcia, J., Lloyd-Williams, P., Roubeau, O., Teat, S.J., Aromí, G. A Magneto-optical Molecular Device: Interplay of Spin Crossover, Luminescence, Photomagnetism, and Photochromism. *Angew. Chemie - Int. Ed.* **56**, 15622–15627 (2017).

27. Nihei, M., Suzuki, Y., Kimura, N., Kera, Y., Oshio, H. Bidirectional photomagnetic conversions in a spin-crossover complex with a diarylethene moiety. *Chem. - A Eur. J.* **19**, 6946–6949 (2013).

28. Milek, M., Heinemann, F. W., Khusniyarov, M. M. Spin crossover meets diarylethenes: Efficient photoswitching of magnetic properties in solution at room temperature. *Inorg. Chem.* **52**, 11585–11592 (2013).

29. Venkataramani, S. Jana, U., Dommaschk, M., Sönnichsen, F. D., Tuczek, F., Herges, R. Magnetic Bistability of Molecules. *Science.* **331**, 445–449 (2011).

30. Heitmann, G., Schütt, C., Herges, R. Spin State Switching in Solution with an Azoimidazole-Functionalized Nickel(II)-Porphyrin. *European J. Org. Chem.* **2016**, 3817–3823 (2016).

31. Witt, A., Heinemann, F. W., Khusniyarov, M. M. Bidirectional photoswitching of magnetic properties at room temperature: ligand-driven light-induced valence tautomerism. *Chem. Sci.* **6**, 4599–4609 (2015).

32. Khusniyarov, M. M. How to Switch Spin-Crossover Metal Complexes at Constant Room Temperature. *Chem. - A Eur. J.* **22**, 15178–15191 (2016).

33. Tissot, A. Boillot, M. L., Pillet, S., Codjovi, E., Boukheddaden, K., Lawson Daku, L.M. Unidirectional photoisomerization of styrylpyridine for switching the magnetic behavior of an iron(II) complex: A MLCT pathway in crystalline solids. *J. Phys. Chem. C* **114**, 21715–21722 (2010).

34. Hasegawa, Y., Takahashi, K., Kume, S., Nishihara, H. Complete solid state photoisomerization of bis(dipyrazolylstyrylpyridine) iron(II) to change magnetic properties. *Chem. Commun.* **47**, 6846–6848 (2011).

35. Takahashi, K. Hasegawa, Y., Sakamoto, R., Nishikawa, M., Kume, S., Nishibori, E., Nishihara, H. Solid-state ligand-driven light-induced spin change at ambient temperatures in bis(dipyrazolylstyrylpyridine)iron(II) complexes. *Inorg. Chem.* **51**,

5188–5198 (2012).

36. Rösner, B. Milek, M., Witt, A., Gobaut, B., Torelli, P., Fink, R. H., Khusniyarov, M. M. Reversible Photoswitching of a Spin-Crossover Molecular Complex in the Solid State at Room Temperature. *Angew. Chemie - Int. Ed.* **54**, 12976–12980 (2015).

37. Poggini, L. Milek, M., Londi, G., Naim, A., Poneti, G., Squillantini, L., Magnani, A., Totti, F., Rosa, P., Khusniyarov, M.M., Mannini, M. Room temperature control of spin states in a thin film of a photochromic iron(II) complex. *Mater. Horizons* **5**, 506–513 (2018).

38. Gómez, V. Sáenz De Pipaón, C., Maldonado-Illescas, P., Waerenborgh, J.C., Martin, E., Benet-Buchholz, J., Galán-Mascarós, J. R. Easy Excited-State Trapping and Record High TTIESST in a Spin-Crossover Polyanionic FeII Trimer. *J. Am. Chem. Soc.* **137**, 11924–11927 (2015).

39. Coelho, A. A., Evans, J., Evans, I., Kern, A., Parsons, S. The TOPAS symbolic computation system. *Powder Diffr.* **26**, S22–S25 (2011).

40. Hauser, A., Gutlich, P., Spiering, H. High-Spin → Low-Spin Relaxation Kinetics and Cooperative Effects in the $[Fe(ptz)_6](BF_4)_2$ and $[Zn_{1-x}Fe_x(ptz)_6](BF_4)_2$ (ptz = 1-Propyltetrazole) Spin-Crossover Systems. *Inorg. Chem.* **25**, 4245–4248 (1986).

41. Martin, J. P., Zarembowitch, J., Dworkin, A., Haasnoot, J. G., Codjovi, E. Solid-State Effects in Spin Transitions: Influence of Iron(II) Dilution on the Magnetic and Calorimetric Properties of the Series $[Fe_xNi_{1-x}(4,4'\text{-bis}(1,2,4\text{-triazole}))_2(NCS)_2]\cdot H_2O$. *Inorg. Chem.* **33**, 2617–2623 (1994).

42. Sáenz de Pipaón, C., Maldonado-Illescas, P., Gómez, V., Galán-Mascarós, J. Spin Transition Kinetics in the Salt $[H_2N(CH_3)_2]_6[Fe_3(L)_6(H_2O)_6]$ (L = 4-(1,2,4-triazol-4-yl)ethanedisulfonate). *Magnetochemistry* **2**, 20 (2016).

43. Bonhommeau, S. Brefuel, N., Palfi, V. K., Molnar, G., Zwick, A., Salmon, L., Tuchagues, J.P., Sanchez Costa, J., Letard, J.F., Paulsen, H., Bousseksou, A. High-spin to low-spin relaxation kinetics in the $[Fe(TRIM)_2]Cl_2$ complex. *Phys. Chem. Chem. Phys.* **7**, 2909–2914 (2005).

44. Lebedev, G. Pillet, S., Baldé, C., Guionneau, P., Desplanches, C., Létard, J. F. Kinetics of photo-induced phase transition and relaxation in the spin-crossover complexes $[Fe_xZn_{1-x}(phen)_2(NCS)_2]$, influence of metal dilution. *IOP Conf. Ser. Mater. Sci. Eng.* **5**, (2009).

45. Brown, A. J., Pinkowicz, D., Saber, M. R., Dunbar, K. R. A trigonal-pyramidal Erbium(III) single-molecule magnet. *Angew. Chemie - Int. Ed.* **54**, 5864–5868 (2015).

46. Wu, D. Q. Shao, D., Wei, X. Q., Shen, F. X., Shi, L., Kempe, D., Zhang, Y. Z., Dunbar, K.

R., Wang, X. Y. Reversible On-Off Switching of a Single-Molecule Magnet via a Crystal-to-Crystal Chemical Transformation. *J. Am. Chem. Soc.* **139**, 11714–11717 (2017).

47. Buhks, E., Navon, G., Bixon, M., Jortner, J. Spin Conversion Processes in Solutions. *J. Am. Chem. Soc.* **102**, 2918–2923 (1980).

48. Hauser, A. Light-Induced Spin Crossover and the High-Spin→Low-Spin Relaxation. *Top. Curr. Chem* 155–198 (2004).

49. Fabre, B. Ferrocene-terminated monolayers covalently bound to hydrogen-terminated silicon surfaces. Toward the development of charge storage and communication devices. *Acc. Chem. Res.* **43**, 1509–1518 (2010).

50. Hauser, A., Enachescu, C., Daku, M. L., Vargas, A., Amstutz, N. Low-temperature lifetimes of metastable high-spin states in spin-crossover and in low-spin iron(II) compounds: The rule and exceptions to the rule. *Coord. Chem. Rev.* **250**, 1642–1652 (2006).

51. Stock, P. Deck, E., Hohnstein, S., Korzekwa, J., Meyer, K., Heinemann, F. W., Breher, F., Hörner, G. Molecular Spin Crossover in Slow Motion: Light-Induced Spin-State Transitions in Trigonal Prismatic Iron(II) Complexes. *Inorg. Chem.* **55**, 5254–5265 (2016).

52. Bondi, A. Van der waals volumes and radii. *J. Phys. Chem.* **68**, 441–451 (1964).

UNIVERSITAT ROVIRA I VIRGILI
BISTABLE MOLECULAR MATERIALS: TRIAZOLE-BASED COORDINATION CHEMISTRY OF FIRST ROW TRANSITION METALS
Andrea Moneo Corcuera

Chapter 5

Nanostructuring the SCO Fe^{II} Trimer on surfaces

Abstract

The interesting SCO behavior of $[NH_2(CH_3)_2]_6[Fe_3(\mu\text{-}L)_6(H_2O)_6]$ (**1**) complex and the experimental evidence of molecular memory effect (shown in chapter 4) makes this system very promising for molecular data storage applications. Here, we present our first attempt to grow nanostructures of 1 onto a proper surface (either fused silica or gold) in order to explore possible applications in SCO-based devices. On one hand, we have been able to obtain homogeneous films of **1** onto fused silica substrate with control over the thickness in the ≈ 450 – 5 nm range by combining drop casting and spin coating method. All the films exhibit comparable SCO behavior with extremely slow spin interconversion and the resulting bistability within wide temperature range around room temperature. On the other hand, we have studied the deposition of molecules of **1** on Au (111) surface via controlled pulsed liquid injection in ultra-high vacuum which allowed to prepare homogeneous sub-monolayer with well-defined orientation over large range. Indeed, in-situ Scanning Tunneling Microscopy (STM) images reveal that the material form well-ordered structures that predominantly nucleate in the herringbone dislocations of the Au (111) substrate. This represents a promising starting point to investigate the individual magnetic properties of one single molecule on the surface.

5.1. Introduction

Spin crossover (SCO) complexes are promising systems proposed for multiple applications such as data storage, molecular electronics or spintronics.[1] The realization of SCO-based application would require the manipulation of these SCO materials at reduced length scales. Therefore, great efforts have been recently done towards the preparation of nano-sized SCO materials such as coordination nanoparticles,[2–4] thin films[5–7] or nano-patterning on surfaces.[8–10] Indeed, the synthesis of these nanoscale materials,[11] the study of their spin switching properties[12] and the development of new processing procedures have contributed to renew the interest in this field, opening new technological perspectives through the integration of SCO complexes in nano-devices.[13]

In particular, one of the most appropriate configurations of nano-sized SCO materials for their incorporation in devices would be continuous thin films, whose thickness can be tuned with nanometer precision. With this purpose, several procedures have been developed to transfer intact SCO molecules on solid surface. Simple deposition methods such as dip coating, drop casting, [14] spin coating[15] or vacuum sublimation[5,7,16–18] have been extended to a large variety of materials and allowed the formation of homogeneous film with thickness in the nanometer scale. On the other hand, more dedicated deposition strategies such as Langmuir-Blodgett technique, [19,20] chemical deposition[21] or in-situ UHV deposition[22] are required in order to form ultra-thin film with fine-tuned thickness precision. [23]

An important challenge in this context is to preserve the bistability of the SCO materials after deposition onto solid surface, since the spin switching phenomenon can be critically altered due to 1) molecule – surface interaction[24–26] and 2) differing cooperative phenomena relative to the bulk. Regarding to the latter case, it is well-known that the “macroscopic” SCO behavior is very sensitive to molecular environment changes (e.g. solvent molecules, packing, etc…) and the memory effect

(thermal hysteresis) is directly attributed to cooperative contribution.[27] The nano-structuration process involves a reduction in the number of interacting centers (cooperativity), leading to an inevitable change in the SCO properties, and typically, the complete loss of memory effect at certain finite dimension in which cooperativity becomes ineffective. Accordingly, it is still uncertain that the hysteretic behavior may exists at single molecule level in monolayer or sub-monolayer systems. Indeed, this was experimentally demonstrated by Wolfgang Kuch et al. in the study of thermal–induced spin transition curves of $[(Fe(H_2B(pz)_2)_2(2,2`\text{-bipy})]$ complex on graphite surface. The authors observed that modulating the film thickness from multilayer to sub-monolayer resulted in apparent anti-cooperative behavior for sub-monolayer coverage.[28]

In order to exploit SCO bistability in ultra-thin films, several alternative strategies have been proposed in the literature. On the one hand, the light-induced metastable spin trapping (LIESST) phenomenon is independent of cooperative effects, finding this phenomenon in sub-monolayers of $[(Fe(H_2B(pz)_2)_2(bipy)]$[29] and $[Fe^{II}((3,5\text{-}(CH_3)_2Pz)_3BH)_2]$ (Pz : 1,4 – pyyrazolyl) complexes.[30] Another remarkable example of SCO bistability is the voltage-induced spin switching that was found by Wulf Wulfhekel et al. in Fe-phen single molecules deposited on CuN/Cu(100) surface.[24] However, in all these cases low temperatures are still needed, which is incompatible with room temperature applications.

The thermal-induced SCO complex, $[NH_2(CH_3)_2]_6[Fe_3(\mu\text{-}L)_6(H_2O)_6]$ (**1**), appear as an ideal candidate to overcome this limitation. Complex **1** exhibit large hysteresis in bulk (over 85 K) above room temperature, and also, experimental observations in **1**-diluted systems suggested memory effect at single molecular level. For all these reasons, the study of the SCO behavior of these molecules in nanostructured systems are particularly attractive with promising perspectives in molecule-based data storage application.[31]

In this chapter we prepared films of **1** onto fused silica substrate with controlled thickness in the range of 450 – 5 nm via combined drop casting/spin coating-based method. We report on the thermal-induced spin crossover around room temperature for all these films investigated by variable temperature UV-spectroscopy. Furthermore, we also obtain well-ordered arrangement of molecules of **1** over long range of Au (111) surface via controlled pulsed liquid injection into UHV chamber. The surface was characterized by current-constant Scanning Tunneling Microscopy (STM) images at room temperature, whereas further characterization and the investigation of their SCO properties are under progress.

5.2. Results and discussion

5.2.1. Thin Films of 1 on fused silica substrate

Our first attempts to obtain thin films by a simple drop casting method from aqueous solutions of **1** on fused silica substrate were not successful to reach a few nanometer thick films. We found direct relationship between solution concentration and film thickness after evaporation in film **A**, **B** and **C** (Table 5.1), with a minimum thickness of 120 ± 20 nm. Lower concentrations did not yield homogeneous films, and a different preparation method had to be attempted.

Direct spin coating of aqueous solutions of **1** did not result in homogeneous films. Spin coated films show very low surface coverage since the high solubility of molecules in aqueous solutions and the slow evaporation rate of water promote the elimination of the molecules during the spinning.

Then, we tested a combination of both methods, starting with drop casting the solution of **1**, and then spin coating this silica substrate after a resting period of time, to allow an initial solvent evaporation before spinning. This successive procedure allowed us to obtain thinner films with controllable thickness depending on the resting time before the spinning (

Table **5.2**). With this strategy, we have able to obtain thinner films, with minimum thickness over 5 ± 1 nm for an optimum 15 min resting time.

Table 5.1. *Drop-casted films of 1 as a function of solution concentration.*

Film	Thickness (nm)	Concentration (1) (mg/ml)
A	450 ± 40	10
B	350 ± 30	5
C	120± 20	1

Table 5.2. *Drop-casted/Spin coated films of **1** as a function of resting time before spinning.*

Film	Thickness (nm)	Resting Time (min)
D	70 ± 10	90
E	35 ± 2	60
F	5 ± 1	15

The thickness of films **A** - **F** was estimated by Atomic Force Microscopy (AFM) scratching technique. For that, the deposited films were locally removed and the scratched area was imaged to get a representative cross-section profile, Figure 5.1 and Figure 5.2). The thickness was obtained by subtracting the height of the bare silica substrate (revealed after removing the deposited film) from the total height of the layer. The cross-section profiles were performed in the central region of the substrate, being the most representative zone in the film.

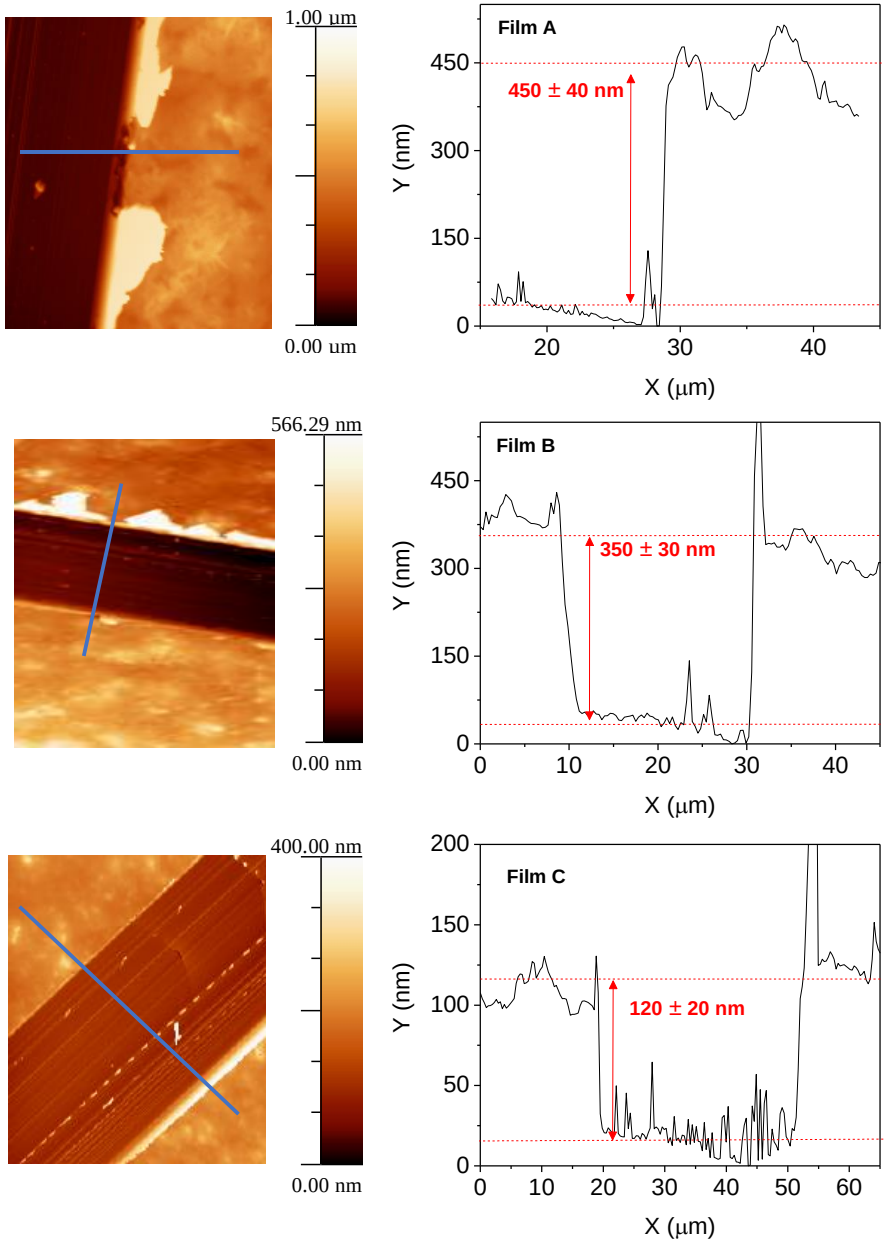

Figure 5.1. *(Left) AFM images showing a scratch region of the drop casted films **A** - **C** (Right) Representative cross-section profile across the scratch (Blue line).*

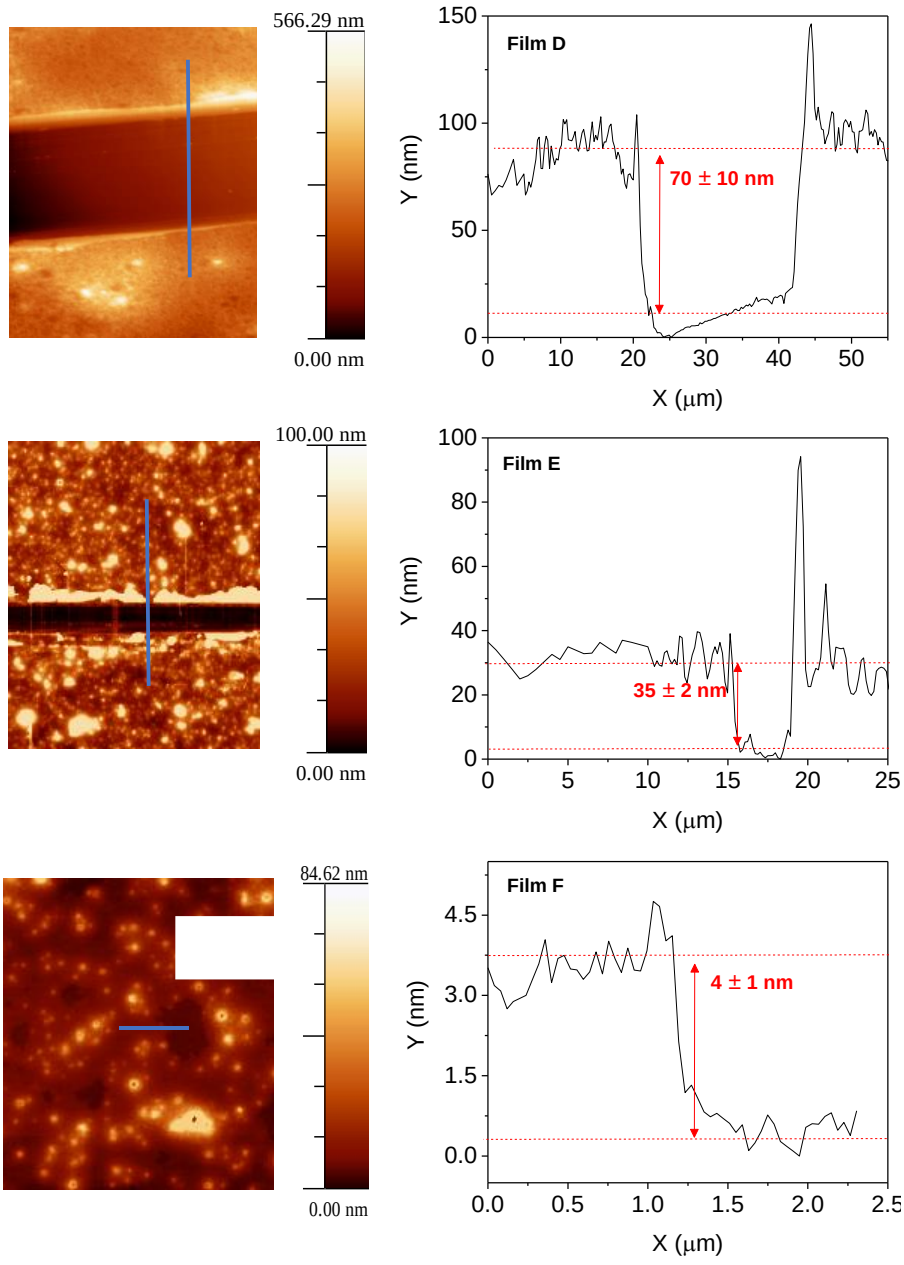

Figure 5.2. *(Left) AFM images showing a scratch region of the drop-casted/spin coated films* ***D*** *-* ***F****. (Right) Representative cross-section profile across the scratch (Blue line).*

The morphology and topography of the deposited films were analyzed through AFM images at room temperature. In all films, the substrate was homogeneously covered by the deposited layer, with lower agglomeration and surface roughness for thinner films. This difference can be easily observed in Figure 5.3, which shows AFM images for the most representative films (the thickest (**A**) and thinnest (**F**) film). The surface roughness was extracted from 100 x 100 μm^2 AFM images, obtaining average roughness (R_a) parameter of 64 nm for film **A** and 6.2 nm for film **F**.

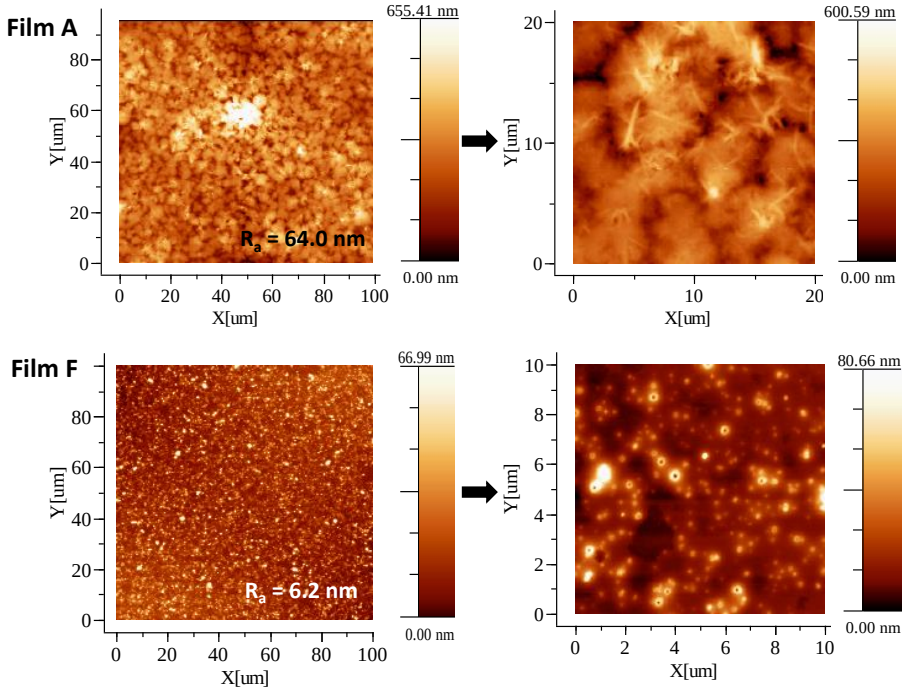

Figure 5.3. *100 x 100 μm^2 AFM images for film **A** (top) and film **F** (bottom) and the corresponding zoom AFM image.*

Regarding the thinnest film **F**, more detailed AFM images collected over 10 x 10 μm^2 area (Figure 5.4 Top) reveal very thin layer with mean thickness around 5 ± 1 nm, despite some nucleation points with average height of 35.6 ± 0.6 nm randomly distributed on the surface, Figure 5.4 Bottom. The error were calculated from variance analysis (ANOVA).

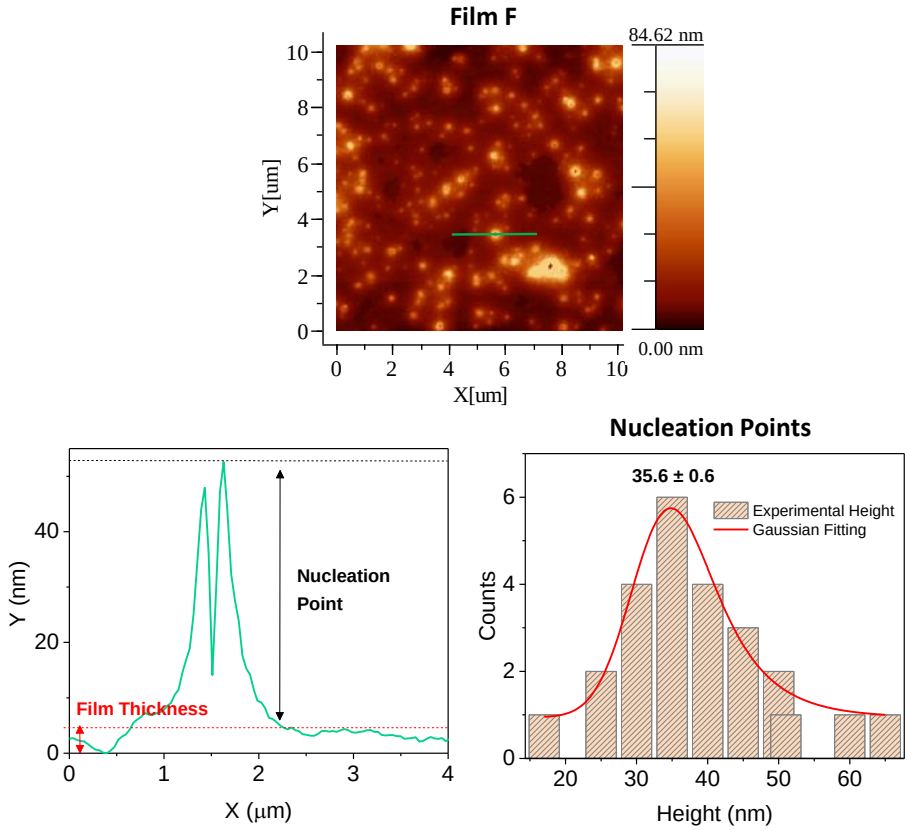

Figure 5.4. *(Left) 10x10 μm² AFM images of film **F**. (Middle) Representative analysis profile showing the film thickness and nucleation point dimensions. (Right) Height distribution of nucleation points.*

Taking the advantage of the absorption properties of LS species of **1**, films **A** - **F** were also characterized by UV absorption spectroscopy. This provides a proportional relation between the absorption intensity and the absorptive species, which allows us to verify the thickness extracted from AFM images.[32,33] UV absorption spectra were collected for film **A** – **F** at 270 K, where the trimers are in Fe^{II}_{HS}-Fe^{II}_{LS}-Fe^{II}_{HS} ground state. All the films exhibit a clear absorption peak centred at 278 nm (Figure 5.5 Left), which could be assigned to $^1A_1 \rightarrow {}^1T_2$ transition for Fe^{II} in LS state. The 278

nm absorbance (Abs) is lineally proportional to the estimated thickness (*x*), in good agreement with the Lambert-Beer Law,

$$Abs = \varepsilon \cdot x \qquad \text{Eq 5.1}$$

According to that equation, the molar absorption coefficient (Ɛ) of complex **1** in films was determined obtaining a value of $12 \cdot 10^3$ cm^{-1}, extracted from the lineal fit of *Abs (278 nm) vs thickness* plot, Figure 5.5 right.

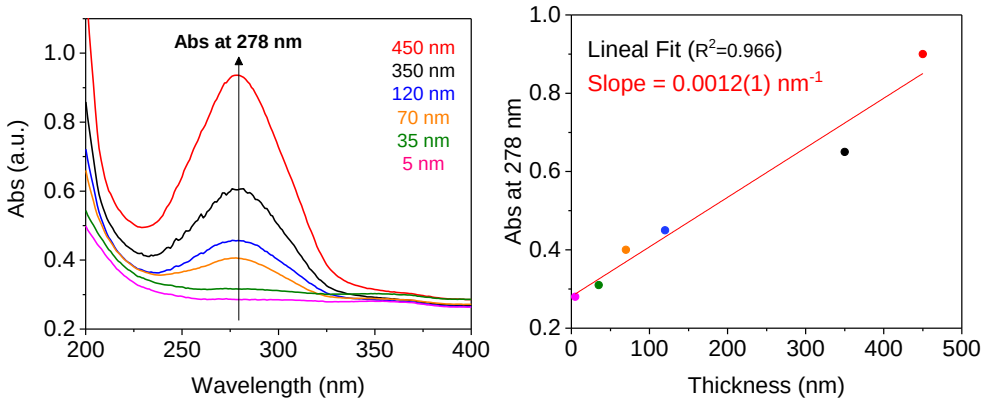

Figure 5.5. *Absorbance vs film thickness plot of films A-F. Red line is the linear fit of the experimental data (black dot). The inset is the linear fit data.*

We investigated the existence of the spin transition phenomena of **1** in the films **A** - **F**. The magnetic response of these films cannot be studied directly with magnetic measurements, due to their very small size and the contribution from the Si support. As an alternative method, variable temperature UV absorption spectroscopy was used to study the spin transition, taking advantage of the signature spectroscopy differences between high spin (HS) and low spin (LS) states for this material.

As expected, films **A** – **F** show significant temperature-dependence in the absorption peak centred at 278 nm. Figure 5.6 show these UV absorption spectra for thicker film (**A**) during warming and cooling process within 265 – 400 K range. Upon heating process, the absorption peak remarkably decrease, assigned to the spin transition

from LS to HS state of the central Fe^{II} ion. An opposite behavior is observed during cooling process, but the initial absorption spectra is not immediately reached during this process.

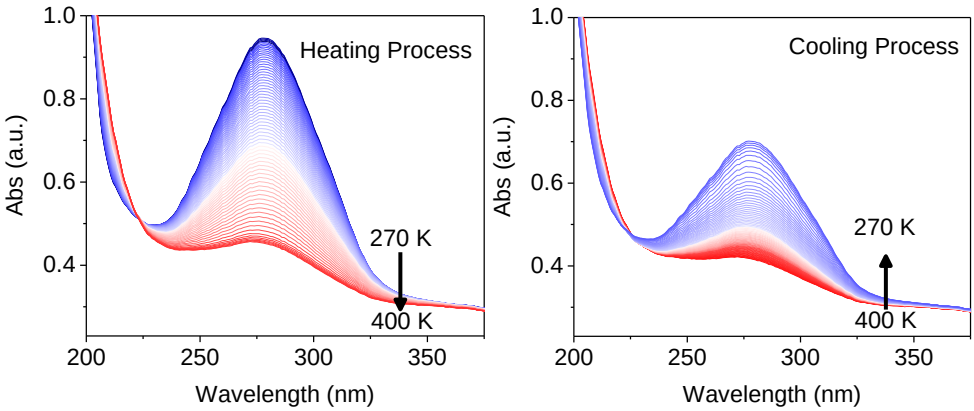

Figure 5.6. *Variable-temperature UV absorption spectra for film **A** upon heating (left) and cooling process (right).*

Similar temperature-dependence of the UV absorption spectra is observed in all the films. The normalized 278 nm-absorbance evolution as a function of temperature (Figure 5.7) reveals that the film thickness do not affect the spin crossover behavior. Indeed, the SCO memory effect were preserved for the thinnest film (around 5 nm od mean thickness). These observations are often not consistent with size reduction effect studies,[34] when thermal hysteresis is diminished, and eventually lost, via nano-structuration.

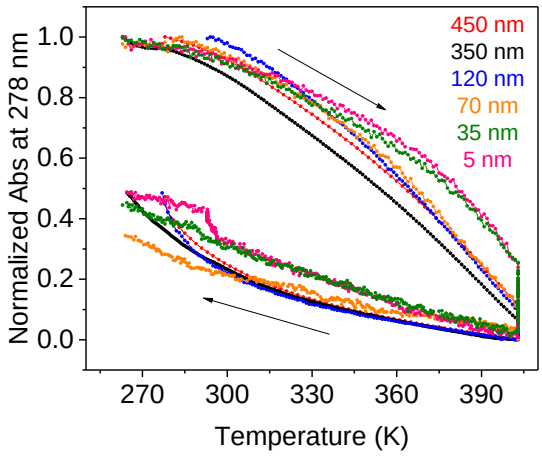

Figure 5.7. *Evolution of 278 nm-absorbance within 270 – 400 K for films **A** – **F**.*

Focussing on the SCO behaviour of the thinnest film (Figure 5.8 left) we observed a continuous decrease in the absorbance value up to 400 K, at a scan rate of 1K/min and even a further decrease when the temperature was hold for one hour at 400 K until reaching saturation (Figure 5.8 inset). The HS population rate at 400 K follows an exponential function [Abs = 0.281 + 0.0021·exp(0.041·T)], typical of non-cooperative materials. The films were cooled down at a slower rate (0.5K/min), to avoid any dynamic effects, and we found that absorbance keeps increasing slowly. At the minimum temperature achieved (265K), the absorbance of the films kept decreasing, needing 6 hours to recover the original LS ground state, Figure 5.8 right. The spin relaxation kinetics can be well-fitted to exponential function [Abs = 0.287 - 0.0072·exp(-0.44·T)], leading to a non-cooperative spin transition. All these experimental observation already suggest the appearance of a reversible spin transition with memory effect at room temperature, and also extremely slow kinetics of the spin interconversion processes, as previously observed in bulk and in diluted systems of **1**.

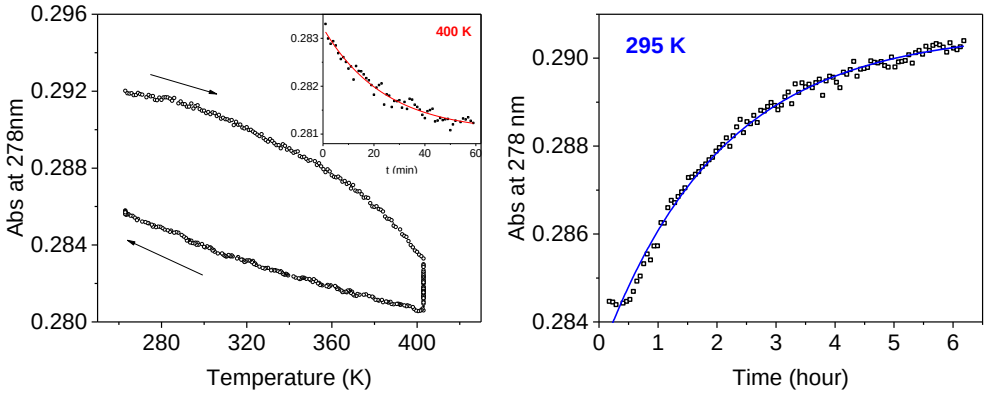

Figure 5.8. *(Left) Thermal evolution of 278 nm-absorbance for film **F**. (Inset) The absorbance evolution rate at 400 K (Black squares) and at 293 K with the corresponding fit functions (full lines). Arrows indicate the scan direction.*

Moreover, this thermal cycle was reproducible and robust in successive cycles, Figure 5.9.

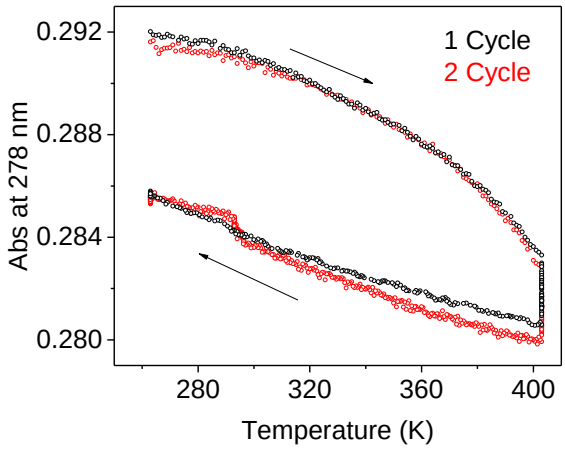

Figure 5.9. *Two successive thermal cycles for film **F**. Arrows indicate the scan direction.*

5.2.2. Study of the deposition of 1 on Au (111) substrate

We studied the deposition of molecules of **1** onto gold surface in ultra-high vacuum (UHV). The Au (111) substrate was selected due to the expected high affinity of the sulfonated groups of **1** for gold surface. between the surface and the sulfonated groups of the molecules.[35,36]

Before deposition, the surface topography of the bare Au (111) substrate was characterized by constant current mode Scanning Tunneling Microscopy (STM) at room temperature. Figure 5.10 shows typical Au (111) surface with characteristic herringbone pattern referred to the surface atomic reconstruction.[37,38] The herringbone pattern appears in the STM images as bright pair of lines (soliton walls), which separate alternatively Hexagonally Close-Packed (HCP) and Face-Centered Cubic (FCC) regions with a width of 4.1 and 3.3 nm, respectively. The intersection of the soliton walls (called “elbows”) are separated with a periodicity of ≈ 18.7 nm. The Au (111) surface also presents step-edge with height of 2.5 ± 0.5 Å, that correspond to a monoatomic Au step.[39] The observation of these features on the surface (herringbone reconstruction and monoatomic steps) is often considered as criteria of cleanliness. Moreover, these dislocations typically play a critical role on the deposition of material over the surface. Indeed, previous deposition studies show that the “elbows” and step-edges are the most reactive regions of the surface since the materials predominantly nucleate at these regions.[39–41]

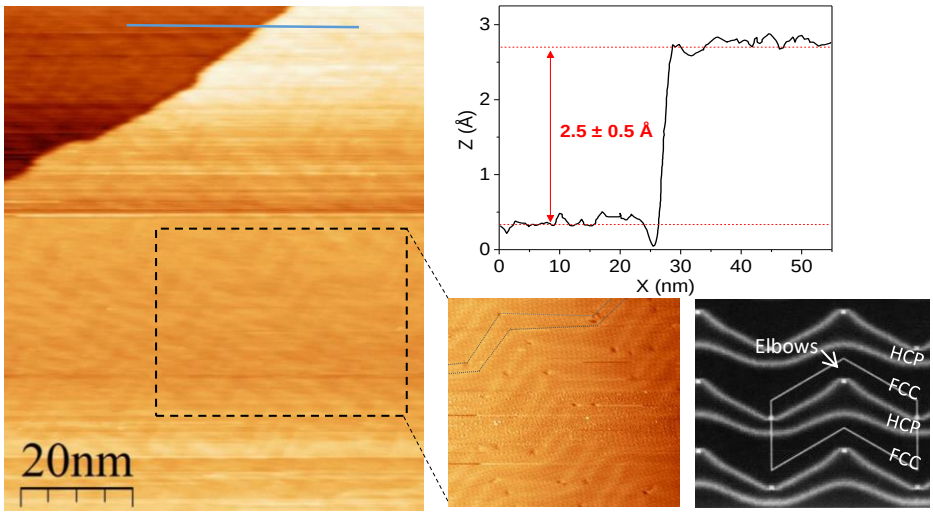

Figure 5.10. *(Left) STM image (V = 1 V; I = 0.057 nA) of bare Au (111) surface with a zoom showing the herringbone pattern. (Top right) Cross-section profile across the step-edge (blue line). (Bottom right) Representation of a herringbone reconstruction highlighting the fcc, hcp and elbow regions.*

Complex **1** was deposited onto clean Au (111) surface via controlled pulsed injection of highly diluted aqueous solution of **1** (0.35 mM) in UHV. This deposition method is based on pulsed fast-valve that allow to introduce small droplets of solution in UHV chamber where the substrate is placed (see experimental section for detailed information). After the deposition, the surface were characterized by in-situ STM images, observing that the molecular coverage can be controlled as a function of pulses number. Indeed, the increase of injection pulses number (from 2 to 12 pulses) suppose a progressive coverage of molecules at the surface, Figure 5.11 Top. The STM images of the substrate after 2 injection pulses reveal islands of material in the FCC regions along the herringbone reconstruction and in the step-edges of the Au (111) surface, in good agreement with previous deposition onto this surface.[40,41] Some of these entities are isolated with 1.1 – 1.8 nm in diameter (see blue arrows), which approximately coincide to the molecular dimensions of the iron (II) trimer.[42] With 8 injection pulses, the deposited material grow in the FCC region from the

nucleation points at the dislocations of the herringbone reconstruction. The STM images of the substrate after 12 injection pulses show significant higher surface coverage and molecular arrangement with apparent deviation from the initial herringbone pattern.

In order to achieve smaller diffusion rate and to ensure the complete removal of the solvent, these samples were kept overnight in the UHV chamber. The resulting STM images (Figure 5.11 Bottom) remarkably reveal the appearance of higher ordered structures on the surface relative to freshly-prepared samples. In particular, this difference is more notorious in sample with 8 and 12 injection pulses, showing molecular arrangement with well-defined orientation in long – range. In 8 pulses sample, this orientation follow the herringbone pattern, while 12 pulses sample present considerable deviation from the initial pattern.

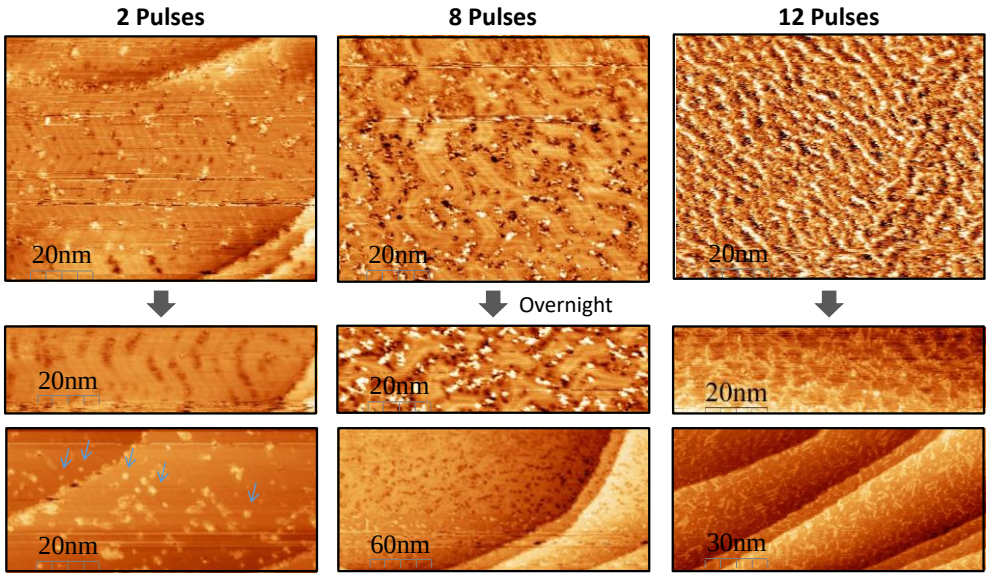

Figure 5.11. *STM images of **1** film on Au (111) after 2 pulses (V = -1 V; I =0.032 nA), 8 pulses(V = -1 V; I =0.032 nA) and 12 pulses (V = 1 V; I = 0.028 nA and V = -1.33 V; I = 0.035 nA), injection of **1**-solution.*

Taking advantage of this observation, we have able to obtain highly homogeneous and ordered sub-monolayer via two-step deposition process. As first step, a solution of **1** (0.35 mM) was injected in 4 pulses of 5 ms into the UHV chamber. After keeping the substrate overnight, the second deposition step of 4 injection pulses were performed on the same position of the substrate. The resulting STM images of this sample reveals that the deposited material form fiber-like shape structures with well-defined orientation on a large scale, Figure 5.12. The preferential orientation appear as parallel fibers with no tendency towards zig-zag reconstruction pattern, Figure 5.12 Bottom. In some regions close to step-edges, the material start to deposit in perpendicular directions to the preferential direction, resulting in an ordered branchy network, Figure 5.12 Top.

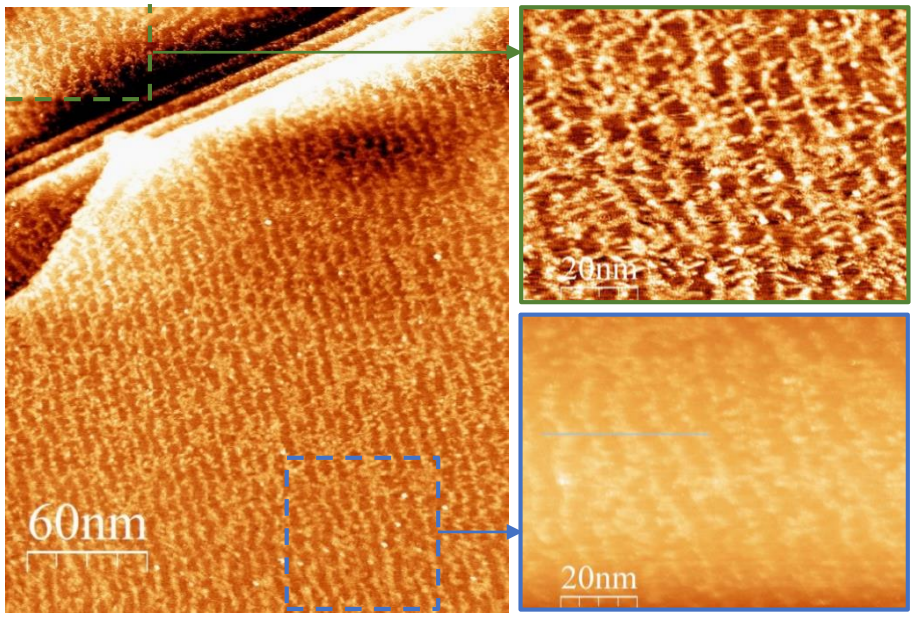

Figure 5.12. *(Left) STM image (V = -1 V; I = 0.026 nA) of Au (111) after two-step deposition of 8 total injection pulses. (Right) STM images (V = -1 V; I = 0.026 nA) showing the two preferential orientations of the deposited material.*

Preferential orientation of parallel fibers are further analyzed by using a representative constant current mode STM image of this sample, Figure 5.13. Cross-sectional profiles along the deposited fibers show a mean width of the fibers of 3.5 ± 0.3 nm and the mean periodicity perpendicular to the fibers of 6.9 ± 0.3 nm, which is in good agreement to the value obtained from Fourier Transform of 3 x 3 µm STM image (7.1 ± 0.3 nm). This data does not correspond to the width of FCC and HCP region from the reconstruction of the bare substrate, suggesting a variation of the herringbone pattern, probably due to the molecule-surface interaction.

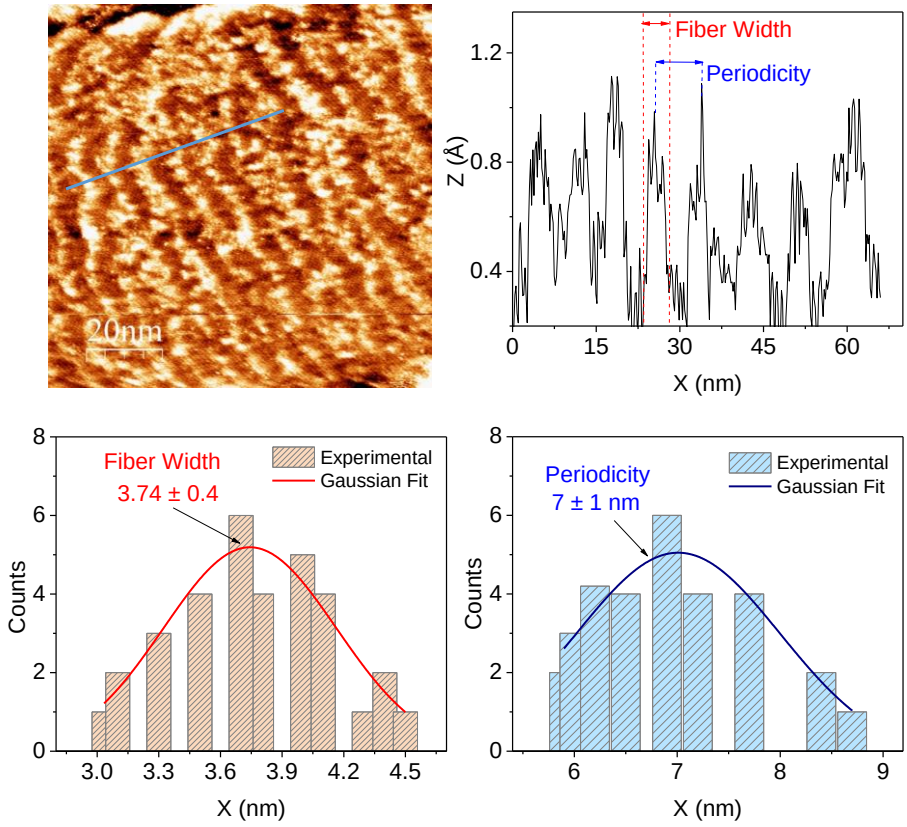

Figure 5.13. *(Top, Left) STM image (V = -1 V; I = 0.035 nA) of preferential orientation after two-step deposition of **1** on Au (111). (Top, right) Cross section profile along blue line in the STM images. (Bottom) Distance distribution of the fiber width and the periocity*

corresponding to different cross section of the STM image. The error were calculated by variance analysis (ANOVA).

In order to discard any solvent effect, a blank solution (water no containing complex **1**) was also deposited on clean Au (111) substrate. The resulting STM images after the injection showed clean bare substrate with any features. This verifies that the features previously shown are due to adsorbed molecules of **1** and not to a residual solvent effect.

5.3. Conclusions

In summary, we have prepared nanostructured films of $[NH_2(CH_3)_2]_6[Fe_3(\mu\text{-}L)_6(H_2O)_6]$ (**1**) complex onto fused silica substrate with control over the thickness (range between 450 nm and 5 nm) by combining drop casting and spin coating methods. We have investigated their SCO properties, observing the preservation of the thermal hysteresis in all these nanostructured films. Contrary to typical SCO materials in films, negligible thickness effect (associated to cooperativity effect) was found in the spin transition behavior, and indeed, the thinnest film obtained (mean thickness of 5 ± 1 nm) also show wide hysteresis loop and extremely slow spin state interconversion at room temperature as in the bulk and diluted systems. Therefore, this particular SCO material open interesting perspectives towards the development of SCO single molecule memories.

With this perspective, we have deposited molecules of **1** on Au (111) substrate under high vacuum system via controlled liquid injection system. The molecules on the surface arrange with well-defined orientation and they can form homogenous and ordered sub-monolayer over long range. These results are actually the first step toward further investigations of spin transition of a single molecule attached on a surface.

5.4. Experimental

5.4.1. Film Preparation onto fused silica substrate

The films were deposited onto fused silica substrates, which were cleaned with acetone and isopropanol to remove contaminants.

Drop-casted films (**A**, **B** and **C**). Complex **1** was dissolved in Milli Q water under nitrogen atmosphere at different concentrations (10.5, and 1 mg/ml). 30 µl of these aqueous solutions were drop-casted onto the clean fused silica substrate. Afterwards, solvent was evaporated at room temperature to yield films **A**,**B** and **C**, respectively.

Drop-Casted/Spin-Coated films (**D**, **E** and **F**). Complex **1** (10 mg) was dissolved in Milli Q water (1 mL) under nitrogen atmosphere. 30 µl of this aqueous solution were drop-casted onto a fused silica substrate. After letting the substrate to stand at room temperature (15, 30 and 90 min), the silica substrate was spinned at a 3000 rpm for one min to yield samples **D**, **E** and **F**, respectively.

5.4.2. Film Preparation onto Au (111) substrate

These experiments were carried out in the ICMM-CSIC in ESISNA group. The Au(111) substrates were cleaned under UHV by multiple alternating Ar^+ sputtering (1 keV / 15µA) and thermal annealing at (470 ^oC) cycles of 10 minutes.

The deposition of complex **1** onto Au (111) substrate was performed in ultrahigh vacuum chamber by controlled liquie¡d injection. The solution of complex **1** was introduced into UHV chamber through Liquid Injection Valve (LIV), properly connected to a vacuum pre-chamber ($5 \cdot 10^{-9}$ mbar), Figure 5.14.[43] This deposition method combine a fast injection of opening/closing time of 5 millisecond (variable pulses number) and a vacuum technology (turbo molecular pump and a vacuum

gauge). The pre-chamber pressure is recorded by a Pirani-Pening vacuum gauge and mass quadrupole spectrometer.

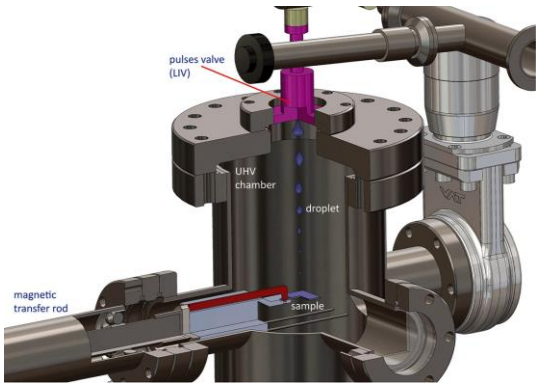

Figure 5.14. Scheme of the LIV valve for controlled liquid injection into high vacuum chamber.

5.4.3. Physical methods

Atomic Force Microscopy (AFM). The AFM images were acquired in Laboratoire de Chimie de Coordination (LCC-CNRS) in Toulouse with SmartsSPM-1000 Scanning Probe Microscope with a silicon tip (HQNSC15-AlBS, 325 Khz; 40N/m). AFM measurements were performed by using tapping mode at room temperature. Film thickness was estimated by using a scratching technique, which consist in imaging a scratched area of the films to directly measure the depth profile. The surface topographical images were treated with the WSxM 5.0 Develop 9.1. image processing software.[44]

Ultraviolet Visible (UV-vis) spectroscopy. Temperature dependent UV absorption spectra were acquired in the 200–400 nm range with a Cary 50 spectrophotometer and a Linkam FTIR-600 liquid nitrogen cryostat. The sample chamber was purged with nitrogen. The UV absorption spectra were collected in LCC-CNRS institute in the team P.

Scanning Tunneling Microscopy (STM). The experiments were conducted in an ultrahigh vacuum (UHV) STM chamber ($1 \cdot 10^{-10}$ mbar) equipped with a liquid injection valve for the deposition and in-situ room temperature STM from OMICRON. The STM images were recorded in the constant current mode at stabilization bias voltages between -1.5 and 1.5 V. W tips, prepared in situ by thermal annealing and field emission, were used. The STM images were analyzed by WSxM. These experiments were carried out in the ICMM-CSIC in ESISNA group.

5.5. References

1. Létard, J.-F., Guionneau, P., Goux-Capes, L. Towards Spin Crossover Applications. *Spin Crossover Transit. Met. Compd. III* **1**, 221–249 (2006).

2. Boldog, I. Gaspar, A. B., Martínez, V., Pardo-Ibañez, P., Ksenofontov, V., Bhattacharjee, A., Gütlich, P., Real, J. A. Spin-crossover nanocrystals with magnetic, optical, and structural bistability near room temperature. *Angew. Chemie - Int. Ed.* **47**, 6433–6437 (2008).

3. Coronado, E., Galán-Mascarós, J. R., Monrabal-Capilla, M., García-Martínez, J., Pardo-Ibáñez, P. Bistable spin-crossover nanoparticles showing magnetic thermal hysteresis near room temperature. *Adv. Mater.* **19**, 1359–1361 (2007).

4. Durand, P. Pillet, S., Bendeif, E., Carteret, C., Bouazaoui, M., El Hamzaoui, H., Capoen, B., Salmon, L., Hébert, S., Ghanbaja, J., Aranda, L., Schaniel, D. Room temperature bistability with wide thermal hysteresis in a spin crossover silica nanocomposite. *J. Mater. Chem. C* **1**, 1933–1942 (2013).

5. Shi, S. Schmerber, G., Arabski, J., Beaufrand, J. B., Kim, D. J., Boukari, S., Bowen, M., Kemp, N. T., Viart, N., Rogez, G., Beaurepaire, E., Aubriet, H., Petersen, J., Becker, C., Ruch, D. Study of molecular spin-crossover complex $Fe(phen)_2(NCS)_2$ thin films. *Appl. Phys. Lett.* **95**, 2–5 (2009).

6. Naggert, H. Bannwarth, A., Chemnitz, S., Von Hofe, T., Quandt, E., Tuczek, F. First observation of light-induced spin change in vacuum deposited thin films of iron spin crossover complexes. *Dalt. Trans.* **40**, 6364–6366 (2011).

7. Shalabaeva, V. Rat, S., Manrique-Juarez, M. D., Bas, A. C., Vendier, L., Salmon, L., Molnár, G., Bousseksou, A. Vacuum deposition of high-quality thin films displaying spin transition near room temperature. *J. Mater. Chem. C* **5**, 4419–4425 (2017).

8. Cavallini, M., Biscarini, F., Gomez-Segura, J., Ruiz, D., Veciana, J. Multiple Length Scale Patterning of Single-Molecule Magnets. *Nano Lett.* **3**, 1527–1530 (2003).

9. Molnár, G. Cobo, S., Real, J. A., Carcenac, F., Daran, E., Vieu, C., Bousseksou, A. A combined top-down/bottom-up approach for the nanoscale patterning of spin-crossover coordination polymers. *Adv. Mater.* **19**, 2163–2167 (2007).

10. Cavallini, M. Bergenti, I., Milita, S., Kengne, J. C., Gentili, D., Ruani, G., Salitros, I., Meded, V., Ruben, M. Thin deposits and patterning of room-temperature-switchable one-dimensional spin-crossover compounds. *Langmuir* **27**, 4076–4081 (2011).

11. Senthil Kumar, K., Ruben, M. Emerging trends in spin crossover (SCO) based functional materials and devices. *Coord. Chem. Rev.* **346**, 176–205 (2017).

12. Molnár, G., Rat, S., Salmon, L., Nicolazzi, W., Bousseksou, A. Spin Crossover Nanomaterials: From Fundamental Concepts to Devices. *Adv. Mater.* **30**, 1–23 (2018).

13. Bousseksou, A., Molnár, G., Salmon, L., Nicolazzi, W. Molecular spin crossover phenomenon: Recent achievements and prospects. *Chem. Soc. Rev.* **40**, 3313–3335 (2011).

14. Galyametdinov, Y. Ksenofontov, V., Prosvirin, A., Ovchinnikov, I., Ivanova, G., Gütlich, P., Haase, W. First example of coexistence of thermal spin transition and liquid-crystal properties. *Angew. Chemie - Int. Ed.* **40**, 4269–4271 (2001).

15. Matsuda, M., Tajima, H. Thin film of a spin crossover complex [Fe(dpp)2](BF4)2. *Chem. Lett.* **36**, 700–701 (2007).

16. Gopakumar, T. G. Matino, F., Naggert, H., Bannwarth, A., Tuczek, F., Berndt, R. Electron-induced spin crossover of single molecules in a bilayer on gold. *Angew. Chemie - Int. Ed.* **51**, 6262–6266 (2012).

17. Miyamachi, T. Gruber, M., Davesne, V., Bowen, M., Boukari, S., Joly, L., Scheurer, F., Rogez, G., Yamada, T. K., Ohresser, P., Beaurepaire, E., Wulfhekel, W. Robust spin crossover and memristance across a single molecule. *Nat. Commun.* **3**, 936–938 (2012).

18. Ossinger, S. Naggert, H., Kipgen, L., Jasper-Toennies, T., Rai, A., Rudnik, J., Nickel, F., Arruda, L. M., Bernien, M., Kuch, W., Berndt, R., Tuczek, F. Vacuum-Evaporable Spin-Crossover Complexes in Direct Contact with a Solid Surface: Bismuth versus Gold. *J. Phys. Chem. C* **121**, 1210–1219 (2017).

19. Bodenthin, Y., Pietsch, U., Möhwald, H., Kurth, D. G. Inducing spin crossover in metallo-supramolecular polyelectrolytes through an amphiphilic phase transition. *J. Am. Chem. Soc.* **127**, 3110–3114 (2005).

20. Ruaudel-Teixier, A., Barraud, A., Coronel, P., Kahn, O. Spin transition in a magnetic Langmuir-Blodgett film. *Thin Solid Films* **160**, 107–115 (1988).

21. Cobo, S., Molnár, G., Real, J. A., Bousseksou, A. Multilayer sequential assembly of thin films that display room-temperature spin crossover with hysteresis. *Angew. Chemie - Int. Ed.* **45**, 5786–5789 (2006).

22. Otero, G. Biddau, G., Sánchez-Sánchez, C., Caillard, R., López, M.F., Rogero, C., Palomares, F. J., Cabello, N., Basanta, M. A., Ortega, J., Méndez, J., Echavarren, A. M., Pérez, R., Gómez-Lor, B., Martín-Gago, J. A. Fullerenes from aromatic precursors by surface-catalysed cyclodehydrogenation. *Nature* **454**, 865–868 (2008).

23. Cavallini, M. Status and perspectives in thin films and patterning of spin crossover

compounds. *Phys. Chem. Chem. Phys.* **14**, 11867–11876 (2012).

24. Miyamachi, T. Gruber, M., Davesne, V., Bowen, M., Boukari, S., Joly, L., Scheurer, F., Rogez, G., Yamada, T. K., Ohresser, P., Beaurepaire, E., Wulfhekel, W. Robust spin crossover and memristance across a single molecule. *Nat. Commun.* **3**, 936–938 (2012).

25. Gruber, M. Davesne, V., Bowen, M., Boukari, S., Beaurepaire, E., Wulfhekel, W., Miyamachi, T. Spin state of spin-crossover complexes: From single molecules to ultrathin films. *Phys. Rev. B - Condens. Matter Mater. Phys.* **89**, 1–9 (2014).

26. Wiedemann, D., Grohmann, A. Bulk spin-crossover in the complex [FeL(NCS)$_2$] of a tris(pyridyl)ethane-derived N4-ligand - A temperature-dependent crystallographic study. *Dalt. Trans.* **43**, 2406–2417 (2014).

27. Brooker, S. Spin crossover with thermal hysteresis: Practicalities and lessons learnt. *Chem. Soc. Rev.* **44**, 2880–2892 (2015).

28. Kipgen, L. Bernien, M., Ossinger, S., Nickel, F., Britton, A.J., Arruda, L. M., Naggert, H., Luo, C., Lotze, C., Ryll, H., Radu, F., Schierle, E., Weschke, E., Tuczek, F., Kuch, W. Evolution of cooperativity in the spin transition of an iron(II) complex on a graphite surface. *Nat. Commun.* **9**, 1–8 (2018).

29. Warner, B. Oberg, J. C., Gill, T.G., El Hallak, F., Hirjibehedin, C. F., Serri, M., Heutz, S., Arrio, M. A., Sainctavit, P., Mannini, M., Poneti, G., Sessoli, R., Rosa, P. Temperature- and light-induced spin crossover observed by X-ray spectroscopy on isolated Fe(II) complexes on gold. *J. Phys. Chem. Lett.* **4**, 1546–1552 (2013).

30. Bairagi, K. Iasco, O., Bellec, A., Kartsev, A., Li, D., Lagoute, J., Chacon, C., Girard, Y., Rousset, S., Miserque, F., Dappe, Y.J., Smogunov, A., Barreteau, C., Boillot, M. L., Mallah, T., Repain, V. Molecular-scale dynamics of light-induced spin cross-over in a two-dimensional layer. *Nat. Commun.* **7**, 1–7 (2016).

31. Khusniyarov, M. M. How to Switch Spin-Crossover Metal Complexes at Constant Room Temperature. *Chem. - A Eur. J.* **22**, 15178–15191 (2016).

32. Swinehart, D. F. The Beer-Lambert law. *J. Chem. Educ.* **39**, 333–335 (1962).

33. Larena, A., Pinto, G., Millán, F. Using the Lambert-Beer law for thickness evaluation of photoconductor coatings for recording holograms. *Appl. Surf. Sci.* **84**, 407–411 (1995).

34. Volatron, F. Catala, L., Rivière, E., Gloter, A., Stéphan, O., Mallah, T. Spin-crossover coordination nanoparticles. *Inorg. Chem.* **47**, 6584–6586 (2008).

35. Nordyke, L. L., Buttry, D. A. Redox Surfactants Are Chemical Probes of Electrode Surface Functionalization Derived from Disulfide Immobilization on Gold. *Langmuir*

7, 380–388 (1991).

36. Leventis, N., Sotiriou-Leventis, C., Chen, M., Jain, A. Electrochemical evidence for the affinity of n-alkyl sulfonate group-modified viologens to gold. *J. Electrochem. Soc.* **144**, 9–10 (1997).

37. Barth, J. V., Behm, R. J., Brune, H., Ertl, G. Scanning tunneling microscopy observations on the reconstructed Au(111) surface: Atomic structure, long-range superstructure, rotational domains, and surface defects. *Phys. Rev. B* **42**, 9307 (1990).

38. Narasimhan, S., Vanderbilt, D. Elastic stress domains and the herringbone reconstruction on Au(111). *Phys. Rev. Lett.* **69**, 1564–1567 (1992).

39. Jewell, A. D., Tierney, H. L., Sykes, E. C. H. Gently lifting gold's herringbone reconstruction: Trimethylphosphine on Au(111). *Phys. Rev. B - Condens. Matter Mater. Phys.* **82**, 1–6 (2010).

40. Cullen, W. G., First, P. N. Island shapes and intermixing for submonolayer nickel on Au(111). *Surf. Sci.* **420**, 53–64 (1999).

41. Wang, Z. T. Darby, M.T., Therrien, A. J., El-Soda, M., Michaelides, A., Stamatakis, M., Sykes, E., Charles H. Preparation, Structure, and Surface Chemistry of Ni-Au Single Atom Alloys. *J. Phys. Chem. C* **120**, 13574–13580 (2016).

42. Gómez, V. Sáenz De Pipaón, C., Maldonado-illescas, P., Waerenborgh, J. C., Martin, E., Benet-buchholz, J., Galán-mascarós, J. R. Easy Excited-State Trapping and Record High TTIESST in a Spin-Crossover Polyanionic Fe^{II} Trimer. *J. Am. Chem. Soc.* **137**, 11924–11927 (2015).

43. Sobrado, J. M., Martín-Gago, J. A. Controlled injection of a liquid into ultra-high vacuum: Submonolayers of adenosine triphosphate deposited on Cu(110). *J. Appl. Phys.* **120**, 1–10 (2016).

44. Horcas, I. Fernández, R., Gómez-Rodríguez, J. M., Colchero, J., Gómez-Herrero, J., Baro, A. M. WSXM: A software for scanning probe microscopy and a tool for nanotechnology. *Rev. Sci. Instrum.* **78**, (2007).

General Conclusions

In the present doctoral thesis, the basic molecular magnetism of coordination compounds based on the di-anionic ligand (**L^{-2}** = 4-(1,2,4-triazol-4-yl)ethanedisulfonate) have been explored. In particular, the spin crossover (SCO) phenomenon has been studied in different dimensions scales, from bulk to single molecule, ending with application-oriented surface engineering.

- In Chapter 2, we have selectively synthetized linear trinuclear complexes with the formula $[NH_2Me_2]_6[M_3(\mu\text{-}\mathbf{L})_6(H_2O)_6]$ (M = Mn^{II}, Co^{II}, Ni^{II}, Fe^{II} and Cu^{II}) by the reaction of the ligand (**L**) with the metal precursors. These trimers presented dominant intra-trimer antiferromagnetic interactions, promoted by the triazole bridging mode. We extracted the magnetic exchange parameters (*J*) from the magnetic susceptibility data, finding slightly lower *J* values when compared with analogous trimers in the literature, which we attributed to a higher local distortion of metal octahedral in our compounds.
- In Chapter 3, we describe how simple cation-exchange yields new salts of the polyanionic Fe^{II} trimer $[Fe_3(\mu\text{-}L_6)(H_2O)_6]^{6-}$, where different SCO behavior was found. The substitution of dimethyl ammonium by heavy alkaline mono-cations as Cs^+ and Rb^+ resulted in more abrupt transitions. We correlate this behavior to stronger intermolecular connectivity (i.e. higher cooperativity) in these materials. Remarkably, this increase in cooperativity does not promote wider thermal hysteresis, as expected, which suggests that the observed hysteresis in this series may be not exclusively associated to bulk cooperativity.
- In Chapter 4, we present our studies upon magnetic dilution of this $[Fe_3(\mu\text{-}L_6)(H_2O)_6]^{6-}$ trimer. Our results indicate that the thermal hysteresis is preserved even in highly diluted systems: in Fe/Zn solid solutions and also in liquid solution. The observation of hysteresis in such diluted materials, where the cooperative forces are negligible, are unprecedented in SCO materials. By analogy to single

molecule magnets, we assign the occurrence of SCO memory at the molecular level to the appearance of an intramolecular activation barrier to the relaxation process, resulting in extremely slow spin-state interconversion. These results open the opportunity to exploit this SCO-active molecules in molecular data storage.

- In Chapter 5, we exploit the molecular memory effect of this SCO Fe^{II} complex to fabricate nanometer film on fused silica with intact SCO bistability, even in 5nm-thick film. Furthermore, we were also able to push the miniaturization process beyond nanometer size by growing well-ordered sub-monolayer of this SCO complex on Au (111) surface. These results suppose our first step toward the investigation of the spin transition of this single SCO molecule as deposited on a surface.

Annex I

Basic Molecular Magnetism Concepts

In order to understand the magnetic properties of transition metal coordination complexes is required to know some definitions and basic concepts about molecular magnetism.[1–3] Here, we emphasize the importance of the number of unpaired electrons in the resultant magnetic properties, focusing our attention on temperature-dependent magnetic behavior.

Magnetic susceptibility and magnetization

Definition and Units

When a homogeneous magnetic field (H) interact with a molecular compound (1 mol), it acquires a molar magnetization (M). The way in which M vary with H is described as,

$$\frac{\delta M}{\delta H} = \chi \qquad \text{Equation 6.1}$$

Where χ represent the molar magnetic susceptibility of the compound.

When the magnetic field is weak enough, the susceptibility becomes independent to the magnetic field,

$$\frac{M}{H} = \chi \qquad \text{Equation 6.2}$$

The units of these magnitudes are often defined by the CGS system. Where H is magnetic field strength expressed in Gauss (*G*), M is expressed in $cm^3 \cdot G \cdot mol^{-1}$, and represents the molar magnetic susceptibility (χ) have the molar volume units ($cm^3 \cdot mol^{-1}$).

Diamagnetism and paramagnetism

The magnetic susceptibility can be described as the magnetic response of a material to an applied magnetic field. According to this concept, there are diamagnetic and paramagnetic substances with different behavior into an applied field.

On one hand, the diamagnetism is a common property of all the matter and it arises from the interaction between the motion of the electrons in their orbits and the magnetic field. The diamagnetism is related to materials with filled electronic shells (i.e. paired electrons). The diamagnetic materials are repelled by the magnetic field, showing negative and small values of the magnetic susceptibility, generally in -1 to $100 \cdot 10^{-6}$ $cm^3 \cdot mol^{-1}$ range. Moreover, the diamagnetic susceptibility is independent to the temperature.

On the other hand, the paramagnetism is related to unpaired electrons and it is generated from the interaction of this electrons with the magnetic field. The paramagnetic materials concentrate the density of the magnetic lines of force. The magnetic susceptibility of this substances present typically positive values, highly dependent on the temperature.

Coordination transition metal complexes present a combination of both diamagnetic and paramagnetic contribution through this algebraic sum,

$$\chi = \chi^D + \chi^P \qquad \text{Equation 6.3}$$

Where χ^D and χ^P are the diamagnetic and paramagnetic contribution to the total magnetic susceptibly of the complexes (χ).

Since, in most cases, the paramagnetic susceptibility is the interested variable, diamagnetic corrections have to be carried out in the treatment of variable temperature magnetic susceptibility data.

Fundamental Equations. Van Vleck Formula

When a magnetic field perturb a material, their magnetic moment vary in function to the energy of their populated states (E),

$$M = \frac{\delta E}{\delta H} \qquad \text{Equation 6.4}$$

The macroscopic magnetization is result of the sum of microscopic magnetization ($\mu_n = -\delta E_n/\delta H$) according to Boltzmann distribution for the population of energy levels.

$$M = \frac{N\sum_n\left(\frac{\delta E_n}{\delta H}\right)\exp\left(-\frac{E_n}{kT}\right)}{kT\sum_n exp\left(-\frac{E_n}{kT}\right)} \qquad \text{Equation 6.5}$$

Where N is the Avogadro Numbers, K is the Boltzmann constant, T the temperature and $E_n^{(x)}$ is the energy of different states (x).

This is a fundamental equation in the molecular magnetism field, from which other important expressions have been deduced. For example, the Van Vleck Formula (Equation 6.6) is based on this equation and in several approximations:

- The first approximation was the energy expressed as polynomial function with the magnetic field,

$$E_n = E_n^{(0)} + E_n^{(1)}H + E_n^{(2)}H^2 \ldots$$

$$\mu_n = -\frac{\delta E_n}{\delta H} = -E_n^{(1)} - 2E_n^{(2)}H \ldots$$

- Second approximation was very weak magnetic fields, H/kT<<<1

$$\mu_n = -E_n^{(1)} - 2E_n^{(2)}H$$

- Moreover, non-spontaneous magnetization (M=0 when H=0) and the lineal dependence of magnetization with respect to H.

Thus, the equation 6.5. and previous approximations lead to the development of Van Vleck Formula,

$$\chi = \frac{N\sum_n\left(\frac{E_n^{(1)2}}{kT} - 2E_n^{(2)}\right)\exp(E_n^{(0)}/kT)}{\sum_n \exp\left(-E_n^{(0)}/kT\right)} \qquad \text{Equation 6.6}$$

If the energy vary lineally with the magnetic field, $E_n^{(2)}$=0, then the Van Vleck Formula can be simplified as,

$$\chi = \frac{N\sum_n E_n^{(1)2} exp E_n^{(0)}/kT}{kT\sum_n exp E_n^{(0)}/kT} \qquad \text{Equation 6.7}$$

The Curie Law

The Curie Law was proposed from experimental data in 1910 before the quantum mechanics. The Curie Law suppose that the ground state has no angular momentum and the excited states are very well-separated to the ground state. This law describes that the paramagnetic susceptibility (χ) vary inversely with the temperature through the Equation 6.8, where C is the Curie Constant expressed in $cm^3 \cdot K \cdot mol^{-1}$.

$$\chi = \frac{C}{T} \qquad \text{Equation 6.8}$$

Thus, the Curie constant can be extracted from experimental data of fitted χ^{-1} *vs T plot*, where the slope is C^{-1}, Figure 6.1.

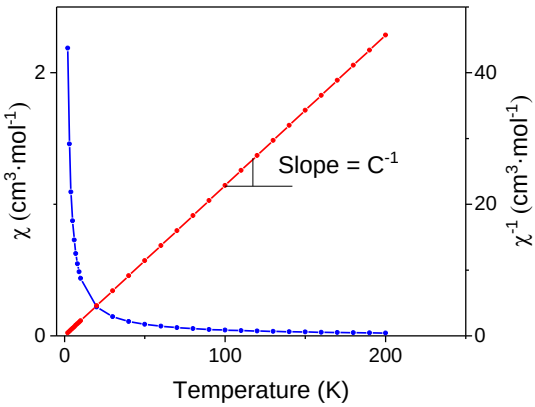

Figure 6.1. *χ vs T plot and χ^{-1} vs T plot for an example with C=4.37 $cm^3 \cdot mol^{-1} \cdot K$.*

On the other hand, the Curie constant can be also determined theoretically. We use the simplified Van Vleck formula and the equation of the energy levels ($E_n = M_S g \beta H$, with $E_n^{(0)} = 0$) leading to Equation 6.9 and 6.10,

$$\chi = \frac{Ng^2\beta^2}{kT} \sum_{M_s=-S}^{+S} M_s^2/(2S+1) \qquad \text{Equation 6.9}$$

$$\chi = \frac{Ng^2\beta^2}{3kT} S(S+1) \qquad \text{Equation 6.10}$$

Finally, applying the Curie thermal dependence of the magnetic susceptibility, the Curie constant can be expressed as,

$$C = \frac{Ng^2\beta^2}{3k} S(S+1) \approx \frac{g^2 S(S+1)}{8} \qquad \text{Equation 6.11}$$

Where N is the Avogadro`s number ($6.022 \cdot 10^{23}$ mol^{-1}), g is the g-factor (typically g = 2 for ideal isotropic situation), k is the Boltzmann constant ($9.27 \cdot 10^{-24}$ J/T), β is the Bohr magneton and S is the total spin.

The Curie-Weiss Law

The Curie Law is only applicable to ideal system when the magnetization vary lineally with the magnetic field. Therefore, most magnetic system do not strictly obey the Curie Law. This deviation can be caused by the population variation within measured temperature range and/or the magnetic coupling between paramagnetic centers. To take into account these deviations, a correction term is introduced in Curie Law, leading to the called Curie-Weiss Law,

$$\chi(T) = \frac{C}{(T-\theta)} \qquad \text{Equation 6.12}$$

Where C is the Curie constant and θ is a correction term or also called Weiss constant, with temperature units (K). Both parameters can be obtained empirically from linear fit of χ^{-1} vs T plots, where the slope correspond to C^{-1} value and the abscissa intercept is - θ/C value.

$$\chi^{-1} = \frac{T}{C} - \frac{\theta}{C} \qquad \text{Equation 6.13}$$

The χ^{-1} vs T line for systems following this law do not intercept the origin as ideal systems, see Figure 6.2. Typically, negatives values of Weiss constant involve antiferromagnetic interactions, while positives values are associated to ferromagnetic interactions.

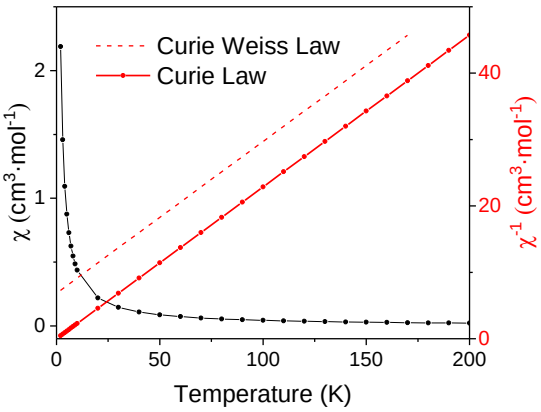

Figure 6.2. *Comparison of the magnetic material that follow the Curie and the Curie-Weiss Law.*

Magnetization. Brillouin Function

The magnetization data can be described as,

$$M_{(\mu_B)} = N\, g\, \beta S \cdot B_s(x) \qquad \text{Equation 6.14}$$

Where N is the number of centers with spin (S), g is the g-factor and $B_s(x)$ is the Brilluoin Function:

$$B_s(x) = \frac{2S+1}{2S}\coth\left(\frac{2S+1}{2S}\, y\right) - \frac{1}{2S}\coth\left(\frac{1}{2S}\, y\right) \qquad \text{Equation 6.15}$$

$$x = g\beta SH/kT$$

Being β the Bohr magneton (5.7888 eV·T^{-1}), H the external magnetic field applied (Teslas), g the g-factor and kT is the Boltzmann constant (8.6173 eV·K^{-1}).

According to this magnetization description, when H/kT is small, the magnetization is lineal with the magnetic field, while when H/kT is big enough the Brillouin Function tends to the unity and the magnetization reach a saturation value ($M_s = Ng\beta S$). The magnetization curve for g = 2 and different values of spins are shown in Figure 6.3.

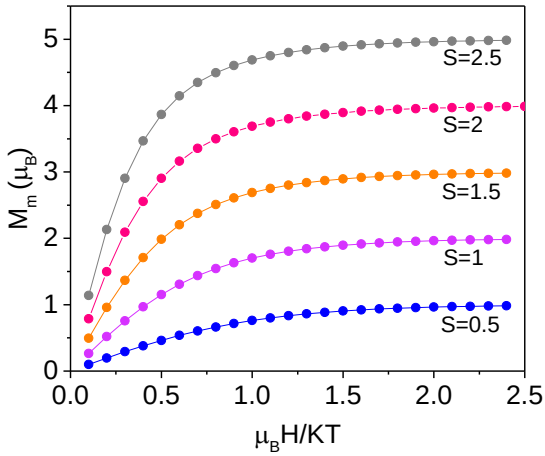

Figure 6.3. *Magnetization with g=2 for Cu^{II} (S=0.5), Ni^{II} (S=1) Co_{HS}^{II} (S=1.5) and Mn_{HS}^{II} (S=2.5).*

Magnetic Superexchange

The interaction between magnetic centers is probably one of the most important source of magnetic exchange in transition metal ions. Typically, the general model for coordination transition metal complexes is paramagnetic metal ions with uncorrelated spins separated by diamagnetic atoms from the ligands. Therefore, the spins of the metal centers can interact each other through atoms of ligands. The strength of this spin-spin interaction depends on several factors including the orbitals overlapping. This spin-spin exchange interaction is also called magnetic superexchange.

To express the spin-spin exchange interaction, we use a general Hamiltonian expression, called isotropic or Heisenberg Hamiltonian,

$$H_{ex} = -2\sum J_{ij} S_i \cdot S_j \qquad \text{Equation 6.16}$$

Where S are the spins of the different metal centers (i,j) and J is the exchange constant expressed in Kelvins, which measure the character and strength of the interaction. A negative value of J is attributed to antiferromagnetic interactions and a positive value is associated to ferromagnetic interaction.

In particular, the lineal trinuclear complexes shown in Chapter 2 have been modulated as centrosymmetric linear trimer with exchange coupling parameter (J) between neighboring and terminal metal centers. We assume that the exchange pathway between the neighboring metal are identical ($J = J_{12} = J_{23}$) and the coupling between the terminal metal centers is zero ($J_{13} = 0$), Figure 6.4. Moreover, the effective g-factor was considered to be identical for all the metal centers in the trimer.

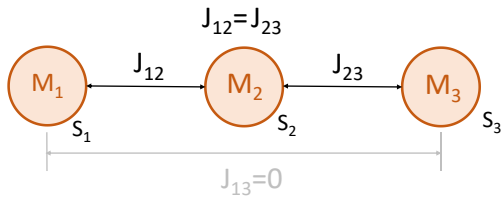

Figure 6.4. *Simplified scheme of magnetic coupling for a lineal trimer system*

The magnetic exchange interactions in this simplified model is expressed by the isotropic Hamiltonian,

$$H_{ex} = -2J(S_1 \cdot S_2 + S_2 \cdot S_3) = -2J(S_2(S_1 + S_3)) \qquad \text{Equation 6.17}$$

Where S_1, S_2 and S_3 are the spins of the metal centers. If we describe $S_A = S_1 + S_3$ and $S_T = S_A + S_2$,

$$H_{ex} = -2J(S_2 \cdot S_A) = -J(S_T^2 - S_A^2 - S_2^2) \qquad \text{Equation 6.18}$$

The energies have been expressed in function of J,

$$E_n = -J(S_T(S_T + 1) - S_A(S_A + 1)) \qquad \text{Equation 6.19}$$

According to that energy equation, the energy levels were calculated in function to J for Mn^{II}, Ni^{II} and Cu^{II} trimers, shown in Table 6.1.

Table 6.1. *Energy levels for trimers of Mn^{II}, Ni^{II} and Cu^{II}.*

Complexes	n	S_A	S_T	E_n
M = Mn^{II}	1	5	15/2	-55 J (-33.75)
	2	5	5/2	-30 J (-8.75)
	3	0	5/2	0 (+21.25)
M = Ni^{II}	1	2	3	-10 J (-6)
	2	2	1	-6 J (-2)
	3	0	1	0 (+4)
M = Cu^{II}	1	1	3/2	-3 J (-7/4)
	2	1	1/2	-2 J (-3/4)
	3	0	1/2	0 (+5/4)

Therefore, if J is negative, the fundamental state is antiferromagnetic and if J is positive the ferromagnetic state would be the lower energy level, see Figure 6.5.

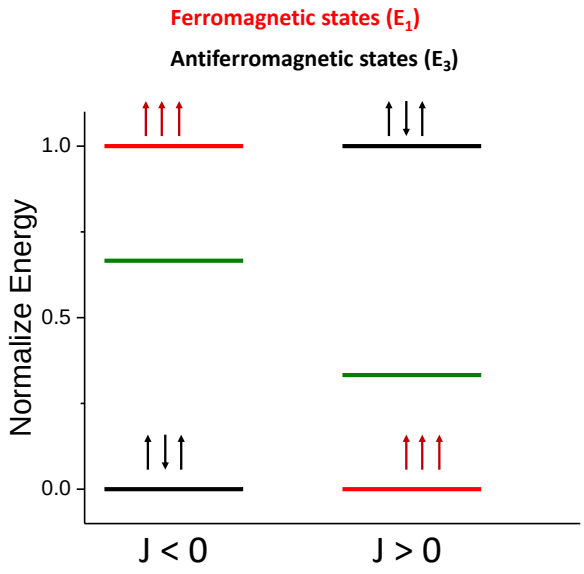

Figure 6.5. *Energy diagram for negative or positive J parameter.*

References

1. Miller, J. S. & Drillon, M. *Magnetism: Molecules to Materials*. *Magnetism: Molecules to Materials* **1**–**5**, (2003).

2. Miller, J. S. Molecular Materials I. Molecular materials mimic inorganic network solids. *Adv. Mater.* **2**, 98–99 (2004).

3. Kahn, O. *Molecular Magnetism (Kahn, Olivier)*. *Journal of Chemical Education* **72**, (2009).

Annex II

Magnetic Measurements

Magnetic measurements

MPMS SQUID Magnetometer and functional parts

Magnetic measurements were performed in a Quantum Design Magnetic Property Measurement System (MPMS) SQUID magnetometer. This analytical instrument is able to study magnetic properties with high sensibility of small solid samples in wide range of temperature and magnetic field. The principal components are shown in Figure 7.1 and the most important functional components are:

- Temperature Control Module (TCM) that offer a regulated and precise range of operation between 1.9 K and 400 K.
- Superconducting magnet with two Josepshon junction able to generate high and uniform magnetic fields between -7 to 7 Teslas. There are several modes to control the magnetic field, the Oscillate Mode, no overshoot mode and high and low resolution mode.
- SQUID (Superconducting Quantum Interference Device) detector system that consist in SQUID sensing loops, superconducting transformer with a RFI shield, and the SQUID sensor. The detector is designed to reject the magnetic field from the magnet.
- Liquid Helium system to refrigerate the superconducting detector, magnet and to operate down to 1.9 K.

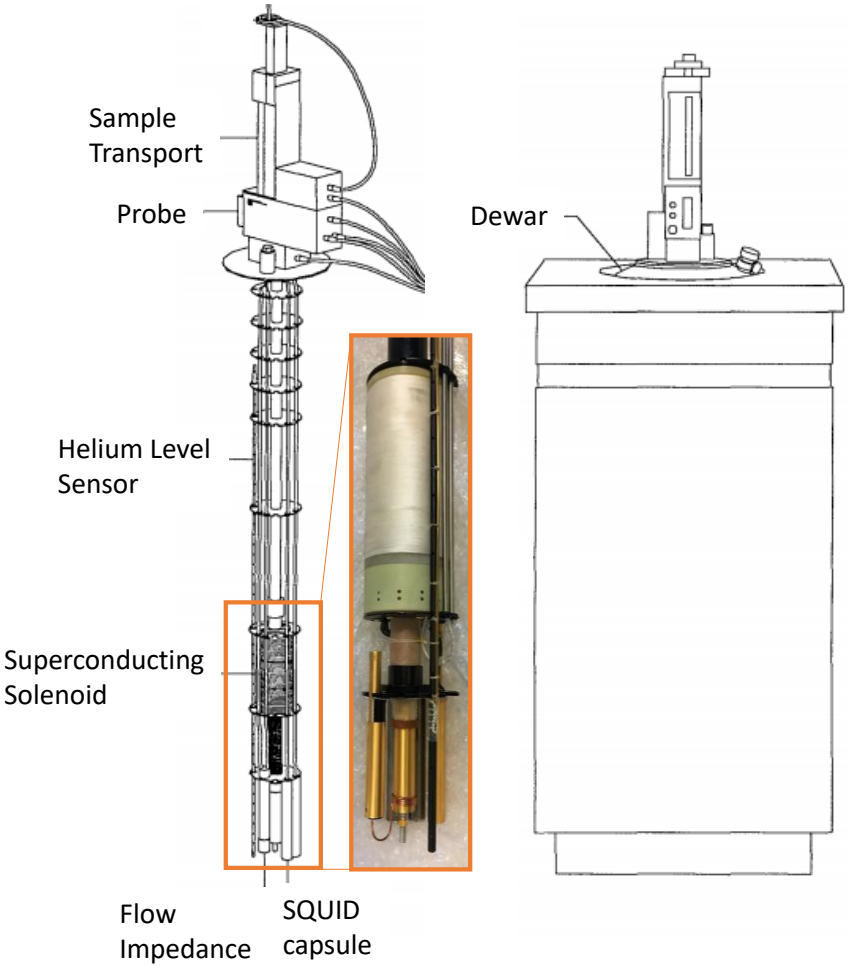

Figure 7.1. *MPMS System Components*

Sample Preparation

The MPSMS system was mainly use in this thesis to measure the magnetic properties of several samples in variable temperature magnetic susceptibility measurements and in magnetization measurements.

The grained-crystals or homogeneous powder, with known weight, was introduced in a diamagnetic gel capsule. Glass wool was later introduced to hold the powder. A hole of around 1mm in diameter was done in the top part of the capsule to facilitate the purge inside the capsule. Kapton® polyimide film is fixed around the capsule to avoid the separation of the two parts of the capsule. Finally, the capsule is placed in a plastic tube (Figure 7.2), which is introduced in the pre-chamber of the instrument. Cycles of vacuum and helium gas are performed in the pre-chamber in order to avoid air and humidity. Afterwards, the sample is transported to the chamber where the magnetic measurements takes places.

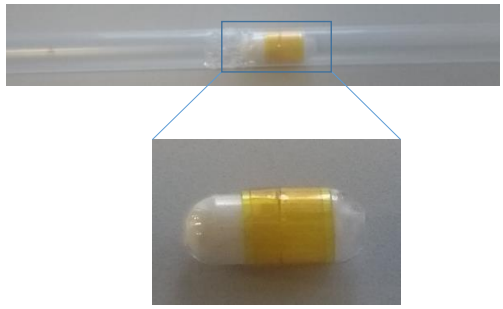

Figure 7.2. *Picture of a sample ready to measure*

Sample Detection

The magnetic moment of the sample is detected through a superconducting detection coil that is connected to the SQUID detector (Figure 7.3), which transform the current intensity into magnetic moment signal.

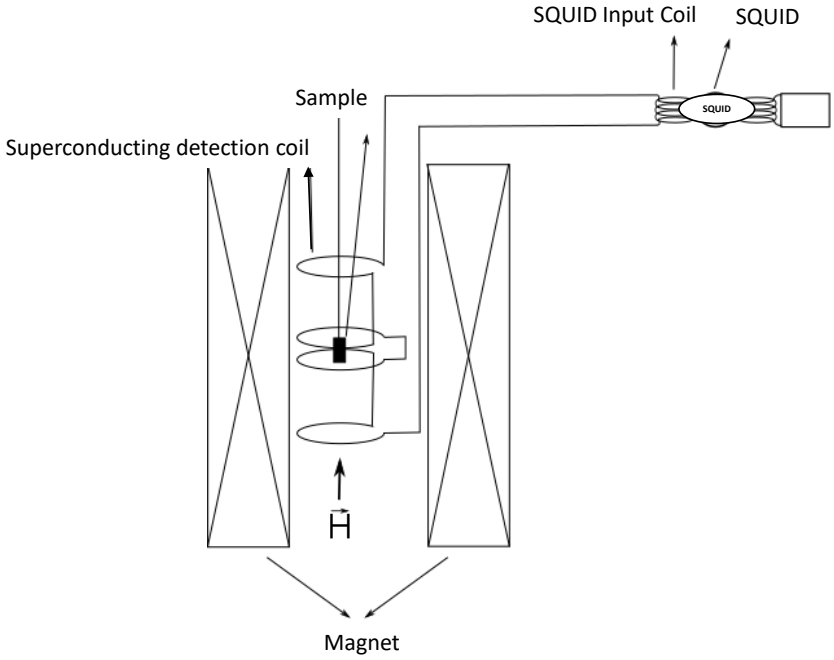

Figure 7.3. *Scheme of the detection of the magnetic response of the sample.*

The sample is place inside a superconducting detection coils and the movement of the sample changes the magnetic flux of the detections coils, ΔΦ, causing a proportional induced intensity, ΔI. This ΔI can be related to ΔΦ through the circuit impedance, L:

$$\Delta I = \frac{\Delta \Phi}{L} \qquad \text{Equation 7.1}$$

The superconducting detection coil and the SQUID Input Coin form a close-circuit, which is connected to SQUID detector. SQUID detects the intensity in the superconducting coils and it generates a proportional potential difference (V). Therefore, the potential difference is also proportional to the magnetic response of

the sample. The instrument mathematically transform the potential difference into magnetization (M), expressed in emu or cm^3.

The RSO option was used to perform variable temperature magnetic susceptibility measurements. RSO option measure the sample by moving it rapidly through the SQUID pickup coils. The sample movement is not stopped in the data reading. This RSO measurements offer high sensitivity around $5 \cdot 10^{-9}$ emu.

Sample Centering

Before the measurements, the sample have to be centered with respect to the SQUID pickup coils to ensure that all the magnetic moment of the sample will be read by the coins. For that, the magnetic response of the sample is measured while it is moving vertically through the complete length of the sample transport's travel paths, Figure 7.4. The maximum voltage detected correspond to the middle of the magnet, where the sample is adjusted.

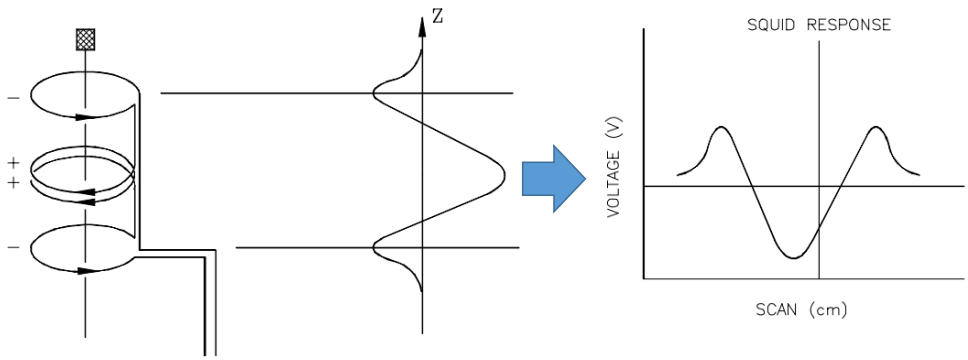

Figure 7.4. *DC Centering Measurement and Measured SQUID Voltage Response*

Magnetic data treatment

Variable-temperature magnetic susceptibility data

Magnetic susceptibility measurements were performed within 2 – 400 K temperature range at applied magnetic field of 1000 Oe.

This equipment give us magnetization data expressed in emu or cm^3. As mentioned in Annex I, the total magnetic susceptibility can be calculated from the magnetization value through,

$$\chi = \frac{M}{H} \qquad \text{Equation 7.2}$$

Taking into account the magnetization generated by sample holder (M_{bag} and M_{wool}), the molar magnetic susceptibility (χ) of the sample is determined by equation 7.4,

$$\chi_m = \frac{(M_{raw} - M_{bag} - M_{wool}) \cdot Mm}{mass \cdot H} \qquad \text{Equation 7.3}$$

Where the M_m is the molar weight of the compound (mg/mmol), H is the magnetic field expressed in Oe and mass is the exact weight of the sample (mg) and M_{bag} and M_{wool} are the diamagnetic contribution of the sample holder:

$$M_{bag}(cm^3) = H \cdot mg(bag) \cdot \left(-2.0188 \cdot 10^{-4} \cdot H - 2.63066 + \frac{2.96773}{T}\right) 10^{-10}$$

$$M_{wool}(cm^3) = H \cdot mg(wool) \cdot \left(\frac{3.0461}{T}\right) \cdot 10^{-8}$$

Typically, the variable temperature magnetic susceptibility measurements are shown as χ·T product vs T plots in order to explore the magnetic response of the sample without general thermal paramagnetic dependence.

Variable-field magnetization data

Magnetization measurements were performed for variable magnetic field from 0 to 7 Teslas at 2 Kelvin.

The magnetization expressed as Bohr magneton are calculated from the measured magnetization (M_{raw}) through,

$$M = \frac{M_{raw} \cdot M_m}{mass \cdot \beta} \qquad \text{Equation 7.4}$$

Where the M_{raw} is the measured magnetization expressed in emu, mass is the exact weight of the sample (mg) and β is the Bohr magneton (5584.8 emu/mol).

UNIVERSITAT ROVIRA I VIRGILI
BISTABLE MOLECULAR MATERIALS: TRIAZOLE-BASED COORDINATION CHEMISTRY OF FIRST ROW TRANSITION METALS
Andrea Moneo Corcuera

UNIVERSITAT ROVIRA I VIRGILI
BISTABLE MOLECULAR MATERIALS: TRIAZOLE-BASED COORDINATION CHEMISTRY OF FIRST ROW TRANSITION METALS
Andrea Moneo Corcuera

UNIVERSITAT ROVIRA I VIRGILI
BISTABLE MOLECULAR MATERIALS: TRIAZOLE-BASED COORDINATION CHEMISTRY OF FIRST ROW TRANSITION METALS
Andrea Moneo Corcuera

UNIVERSITAT ROVIRA I VIRGILI
BISTABLE MOLECULAR MATERIALS: TRIAZOLE-BASED COORDINATION CHEMISTRY OF FIRST ROW TRANSITION METALS
Andrea Moneo Corcuera

UNIVERSITAT
ROVIRA i VIRGILI